Coronary Segmentation in Intravascular Optical Coherence Tomography

Kai-Pin TUNG

A dissertation submitted in partial fulfilment of the requirements for the degree of

Doctor of Philosophy

of

Imperial College London

February 2014

Department of Computing

Imperial College London

Abstract

Cardiovascular disease (CVD) is a fatal disease of the heart or blood vessels. The greatest number of deaths from CVD is coronary heart disease (CHD). It is characterised by thickening of the arterial vessel wall due to atheromatous plaque which may result in narrowing or even occlusion of arterial lumen.

Currently, intravascular optical coherence tomography (IVOCT) has been increasingly used in the clinic for the diagnosis of CHD because it permits high-resolution direct tomographic visualisation of cross-sectional images. With IVOCT techniques, stenosis and restenosis caused by plaques and neointima can be detected and analysed.

The first main contribution of the thesis is a technique for the automatic segmentation of the lumen border when the guide-wire artifacts are noticeable. The proposed segmentation technique is capable of eliminating guide-wire artifacts and generating accurate lumen borders from IVOCT sequences. Compared to commercially available systems, the proposed method is robust and accurate.

The second main contribution of this thesis is an approach for the stent strut detection that can detect stent struts when their intensity responses are weak. This technique is based on stent strut shadow detection. The innovative aspect of our technique is that, for every detected strut shadow, a-priori probability map is applied to estimate the stent strut position. With the detected stent struts, a stent area can be estimated to analyse the neointimal hyperplasia (NIH) thickness in IVOCT sequences.

The thesis also proposes an approach for the neointima segmentation without any information

of the stent but instead with the lumen border. The approach is a combination of a multi-atlas based segmentation approach and a patch-based segmentation approach. With the approach, the neointima label can be obtained by fusing labels from atlases. Compared to other label fusion approaches, a significant increase in segmentation accuracy can be observed.

Acknowledgements

Declaration of Originality

This thesis is dedicated to my family to their emotional and financial support, especially to my father and mother for instilling the importance of hard work and higher education; to my wife, my brother, my sisters in law and my parents in law for supporting me each step of the way.

Copyright Declaration

Glossaries

A-line axial line. 9, 90, 91

ACS , acute coronary syndrome, means that any group of symptoms attributed to obstruction of the coronary arteries.. 6

AMI , acute myocardial infarction (commonly known as a heart attack), results from the partial interruption of blood supply to a part of the heart muscle, leading the heart to be damaged or die.. 5, 8, 45

BM3D , block-matching 3D, a denoising approach. 93, 99

BMS , bare metal stent, is a vascular stent used to reopen the narrowed artery. 6, 8

CABG , coronary artery bypass graft surgery, is a surgical procedure performed to reduce the risk of death from coronary artery disease. 2

CC , cross-correlation, a metric of image similarity. 37, 38, 117, 124, 139

CHD , coronary heart disease, is a disease that plaque builds up inside the coronary arteries. i, 1, 2, 4–6, 14, 17, 20, 54, 58, 62, 88, 90, 137, 141, 142

CT computerised tomography. 11, 15, 31

CTA computerised tomography angiography. 9, 15, 16, 25, 26

CVD , cardiovascular disease, is a class of diseases that include the heart or blood vessels. i, 1, 4

CWT continuous wavelet transform. 60, 63

DES , drug-eluting stent, is a coronary stent placed into narrowed, diseased coronary arteries that slowly releases a drug to block cell proliferation. 8

ECV extracellular volume. 31, 32

EM , expectation maximisation, is an iterative approach for finding maximum likelihood estimates of parameters in a statistic model where it depends on unobserved variables. 18, 22, 26–28, 40, 43, 44, 51, 65, 66, 68–71, 80, 81, 83, 85, 138

FDOCT , frequency-domain OCT, an image modality. 20, 79

GC , graph-cuts, is the process of partitioning a directed or undirected graph into disjoint sets. 18, 22, 26, 28, 30–32, 43, 44, 65, 66, 68, 70, 71, 80, 81, 83, 85, 138

GMM , Gaussian mixture model, is an approach that assumes an image can be represented as a combination of Gaussians. 26, 66–69, 80

IRTK , image registration toolkit, is a cross-platform software tool for image analysis developed by Professor Daniel Rueckert and the Biomedical Image Analysis (BioMedIA) group at Imperial College London. 66, 79, 99, 123, 170

ISA , incomplete stent apposition (also known as stent malapposition), is defined by a separation of at least one stent strut from the intimal surface of the arterial wall with evidence of blood behind the strut, without involvement of side branches. 90

ISR , in-stent restenosis, means restenosis occurs after a stent is embeded. 111

IVOCT , intravascular optical coherence tomography, is a high resolution catheter-based imaging modality intended to optimise visualisation of coronary artery lesions.. i, iii, 1, 2, 8–11, 13, 14, 16–19, 21, 33, 36, 44, 45, 52, 54, 58–66, 71, 72, 79–82, 90, 92, 94–96, 99, 102, 113, 114, 116, 123, 126, 131, 137, 138, 140–142

NIR near-infrared. 9, 45

NMI , normalized mutual information, a metric of image similarity. 37, 39, 117

NSTEMI non ST-segment elevation myocardial infarction. 6

OCT , optical coherence tomography, an image modality. 1, 10, 11, 19, 20, 22, 44, 53–57, 61

ONH optic nerve head. 54, 58

PARS , post-angioplasty restenosis, is a case when restenosis happens following balloon angioplasty. 111

PCA principal component analysis. 52, 113

PCI , percutaneous coronary intervention (known as coronary angioplasty or angioplasty), is a non-surgical procedure used to treat the narrowed coronary arteries of the heart. 13, 19

PDA posterior descending artery. 4

PDFs probability density functions. 50–52

PNN probabilistic neural network. 60

PSV , peri-stent volume, is the vessel segment volume without the stent implantation. 81, 87

PTCA , percutaneous transluminal coronary angioplasty, is a procedure to open a narrowed coronary artery. This allows better blood flow through the artery and to the heart muscle. It is often done with a balloon that is passed through a special catheter. 6, 8, 88, 89, 111

RCA right coronary artery. 4, 45

RNFL retinal nerve fiber layer. 53–56

RV right ventricle. 3, 44

SSD , sum of square differences, a metric of image similarity. 37, 38, 117

STEMI ST-segment elevation myocardial infarction. 6, 8

SVM , support vector machine, is a supervised learning model used for classification and regression analysis. 56, 57

TDOCT , time-domain OCT, an image modality. 20

XA x-ray angiography. 141, 142

Contents

List of Tables

List of Figures

Chapter 1

Introduction

Cardiovascular disease (CVD), also known as heart and circulatory disease, is a disease of the heart or blood vessels. It is the major cause of premature death in the Western countries [Perk et al., 2012]. The greatest number of deaths from CVD is coronary heart disease (CHD) [Roger et al., 2012]. It is characterised by thickening of the arterial lumen border due to atheromatous plaque which may result in narrowing or even occlusion of arterial lumen. Currently, intravascular ultrasound (IVUS) is increasingly used in the clinic for the diagnosis of CHD because it permits direct tomographic visualisation of cross-sectional images of the lumen border, stent struts and neointima. However, the spatial resolution of IVUS is inadequate to accurately distinguish the thickness of the plaques and neointima. Optical coherence tomography (OCT) is a newly emerging optical-based technology that can provide real-time, high-resolution, three dimensional (3D) images with micrometer resolution. Intravascular optical coherence tomography (IVOCT) is a type of OCT. It is used for intravascular imaging and evaluation of vulnerable plaques. With IVOCT techniques, stenosis and restenosis caused by atheroma and neointima can be detected and analysed. This thesis addresses some of the image analysis challenges for quantitative IVOCT in CHD.

1.1   Background and Motivation

The cardiovascular system [Katz, 2005] is the core blood distribution system which circulates blood around the body of the circulatory system. It consists of the heart and two networks of blood vessels: the pulmonary circulation, which moves deoxygenated blood from the heart to the lungs and returns oxygenated blood back to the heart; and the systemic circulation, which carries oxygenated blood from the heart to the body's organs and tissues and returns oxygen-depleted blood back to the heart. The basic anatomy and function of the heart are further reviewed in section 1.1.1.

CHD is a disease that the coronary arteries become narrowing or blockage, usually caused by atherosclerosis. Atherosclerosis is the buildup of fatty deposits (plaque) on the inner walls of the coronary arteries. These plaques can restrict blood flow to the heart muscle by physically clogging the artery or by causing abnormal artery function. This can cause chest pain. If the blood supply to a portion of the heart muscle is cut off entirely, or if the energy demands of the heart become much greater than its blood supply, a heart attack may occur.

Treatment of CHD depends on the severity of CHD. Coronary angioplasty is a non-surgical treatment: a collapsed balloon is passed through the blood vessels until it reaches the arteries of the heart. The balloon is inflated to widen the narrowed coronary artery. A stent (flexible mesh tube) is sometimes inserted to keep the artery open afterwards. The treatment of the most serious case of CHD is usually via coronary artery bypass graft surgery (CABG). A healthy artery or vein, for example from the chest or the leg, is connected or grafted to the blocked coronary artery. The grafted artery or vein bypasses the blocked portion of the coronary artery. This creates a new path for oxygen-rich blood to flow to the heart muscle.

A patient-specific coronary model from preoperative cardiac IVOCT sequences can be used to provide an analysis of restenosis and lead to better understanding of CHD. In addition, the patient-specific coronary model can be used to assist the diagnosis of CHD and prevent late stent thrombosis (LST).
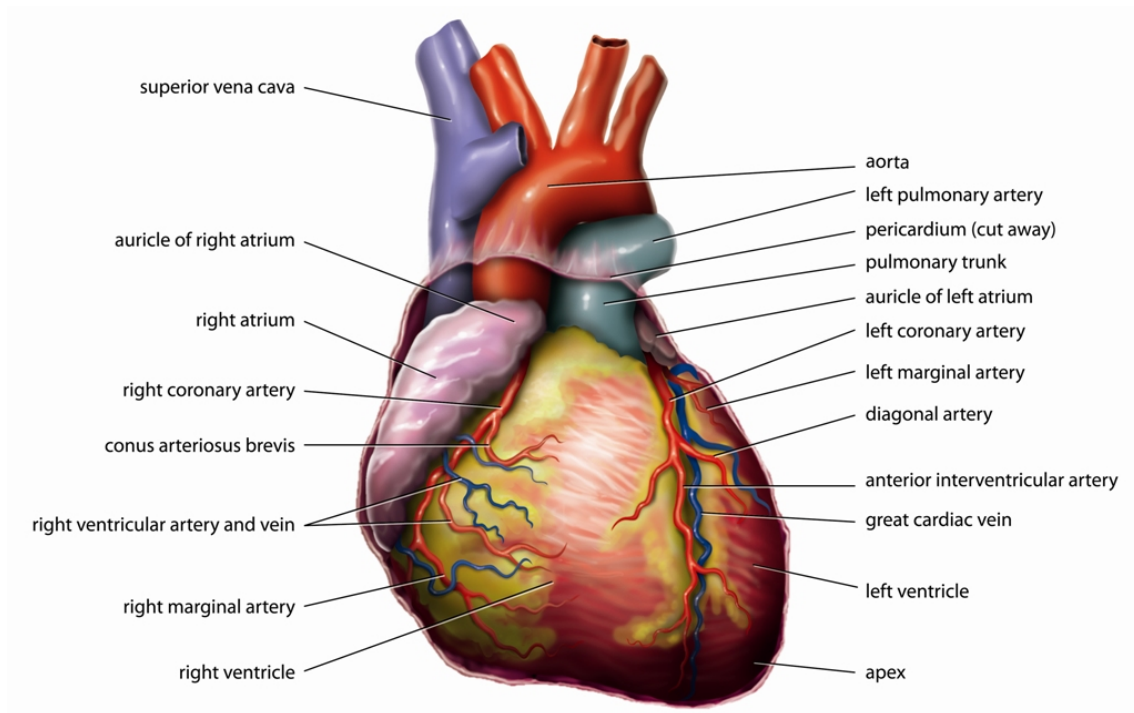
Figure 1.1: This figure shows the anatomy of the human heart. From [Tvanbr, 2010].

1.1.1 Anatomy of the Heart

The heart (Figure 1.1) contains four chambers. The upper chambers are called left and right atria, and the lower chambers are the left and right ventricles. The left atrium (LA) receives oxygenated blood from the lungs through the pulmonary vein. As the contraction triggered by the sinoatrial node progresses through the atria, the blood passes through the mitral valve into the left ventricle (LV). The LV receives oxygenated blood and pumps it to the body through the aorta which is the main artery that carries oxygen-rich blood to the body. The right atrium (RA) receives venous blood from the body and passes it through the right ventricle (RV) where the blood is pumped to the lungs (pulmonary circulation) for oxygenation. At the same time the left atrium receives oxygenated blood from the lungs and the LV pumps it out to the rest of the body (systemic circulation).

The four chambers of the heart are separated from each other and the rest of the body by four sets of valves. The bicuspid (or mitral) and tricuspid atrioventricular valves separate the left and right atria and ventricles respectively, while the aortic valve separates the LV from the aorta, and the pulmonary valve separates the RV from the pulmonary artery. Thin chords

Type of CVD	Deaths (in %)
Coronary heart disease	49.9
Stroke	16.5
High blood pressure	7.5
Congestive heart failure	7.0
Diseases of the arteries	3.4
Other	15.6

Table 1.1: Percentage breakdown of deaths of CVD [Roger et al., 2012].

called the chordae tendineae are attached to the atrioventricular valves and projections of the ventricular muscle known as the papillary muscle. During the ventricular contraction, the papillary muscles contract and prevent the valves from inverting into the atrium. The septum separates the left and right atria as well as the left and right ventricles.

The Coronary Circulation

The heart muscle needs oxygen-rich blood to survive and the blood is supplied to the heart by its own vascular system, called the coronary circulation (Figure 1.1). The aorta (the main blood supplier to the body) branches off into two main coronary blood vessels: left coronary artery (LCA) and right coronary artery (RCA). The LCA consists of the left anterior descending artery (LAD), left circumflex artery (LCX) and left marginal artery (LMA). The RCA consists of the posterior descending artery (PDA) and right marginal artery (RMA). These coronary arteries supply oxygen-rich blood to the entire heart muscle. If coronary artery occlusions occur, the endocardial regions of the heart have become to infarction since the oxygen-rich blood can not reach the endocardial regions of the heart. The diseases caused by the blockage of coronary artery are discussed in the next subsection.

1.1.2   Cardiovascular Diseases

A percentage breakdown of the deaths of CVD in USA is shown in Table. 1.1 [Roger et al., 2012]. From the table, the greatest proportion of deaths of CVD is CHD.
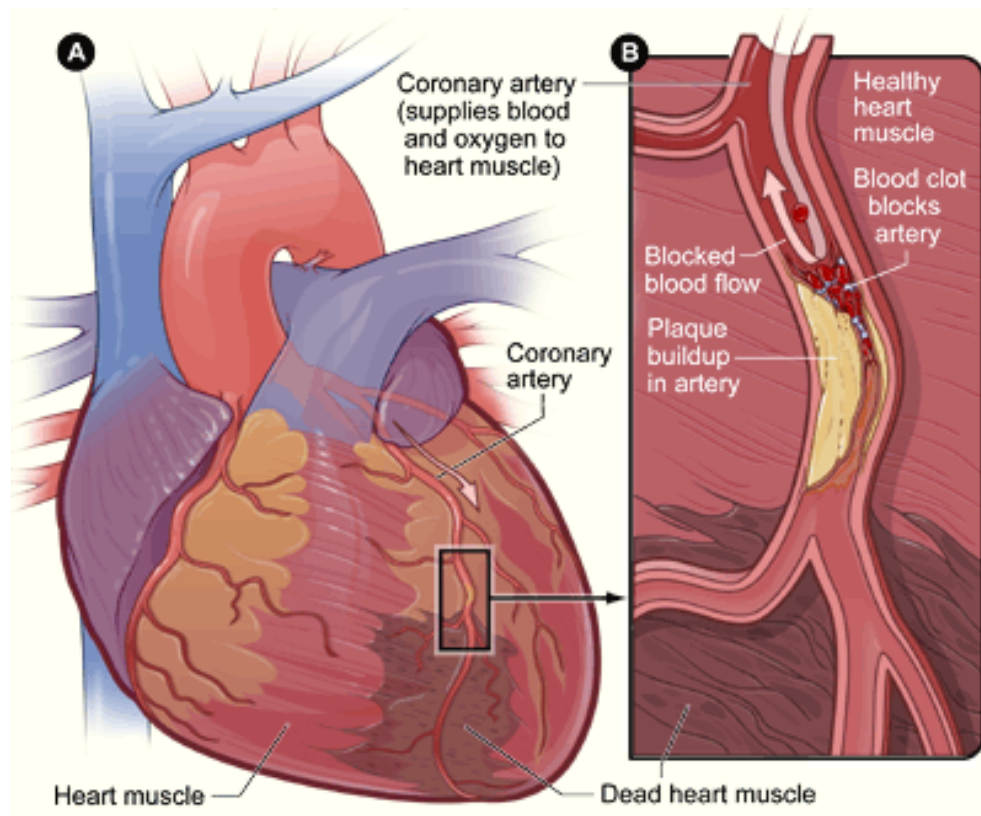
Figure 1.2: a) shows an overview of a heart and coronary artery showing damage (dead heart muscle) caused by a heart attack. b) shows a cross-section of the coronary artery with plaque buildup and a blood clot. From [NHLBI, 2012a].

Coronary Heart Disease

CHD refers to the fact that the heart's blood supply is blocked or interrupted by a build-up of fatty substances in the coronary arteries (Figure 1.2). This is caused by the build-up on the walls of the coronary arteries. This process is known as atherosclerosis and the fatty deposits are called atheroma. If the coronary arteries narrow due to a build-up of atheroma, the blood supply to the heart will be restricted. This will cause angina, atherothrombosis and acute myocardial infarction (AMI).

Angina, also known as angina pectoris, refers to chest pain due to clogging of the coronary arteries. It occurs when there is an imbalance between the heart's oxygen demand and supply. This imbalance arises from an increase in demand (e.g. during exercise) without a proportional increase in supply. When the symptoms of coronary occlusive disease do not change over time, the patient is said to have stable angina pectoris.

Athero-thrombus occurs when the plaque ruptures. The ruptured area occludes blood flow and results in unstable angina. When the partially occluded coronary arteries enlarge, the patient will suffer chest pain, often radiating to the left arm or angle of the jaw, pressure-like in character and associated with nausea and sweating. These symptoms can be referred to acute coronary syndrome (ACS). If a significant portion of the heart muscles is damaged, the heart may stop beating regularly.

ACS refers to any group of symptoms attributed to the obstruction of the coronary arteries (normally chest-pain). A heart attack can be divided into non ST-segment elevation myocardial infarction (NSTEMI) and ST-segment elevation myocardial infarction (STEMI). In NSTEMI, the blood clot only partly occludes the artery and as a result only a portion of the heart muscle being supplied by the affected artery may die. In STEMI, the coronary artery is completely blocked off, and as a result virtually all of the heart muscle being supplied by the affected artery may die. The most serious cases (ACS, unstable angina, NSTEMI and STEMI) of CHD are caused by plaque rupture and thrombosis. A treatment of CHD is discussed in section 1.1.3.

1.1.3   Coronary Stenting

A coronary stent is a tube-like structure placed in the coronary arteries in order to keep the arteries open. This is often used in the treatment of CHD. Stenting is used to prevent vessel closure during percutaneous transluminal coronary angioplasty (PTCA) and reduces the incidence of angiographic restenosis which has an occurrence rate of 30-40% [Serruys et al., 2006]. In 1999, stenting made 84.2% of all percutaneous coronary interventions [Serruys et al., 2006].

However, as the stent is a foreign object, it often incites an immune response that leads to further narrowing near to or inside the stent. The growth of scar tissue across the stent is known as neointimal hyperplasia (NIH) and it may cause the stented artery (using a standard stent (bare metal stent (BMS))) becomes blocked (known as restenosis, Figure 1.3). BMS has been associated with a 20-30% restenosis rate requiring reintervention [Moliterno, 2005, Arjomand et al., 2003]. This phenomenon is clinically evident within the first 6-9 months after
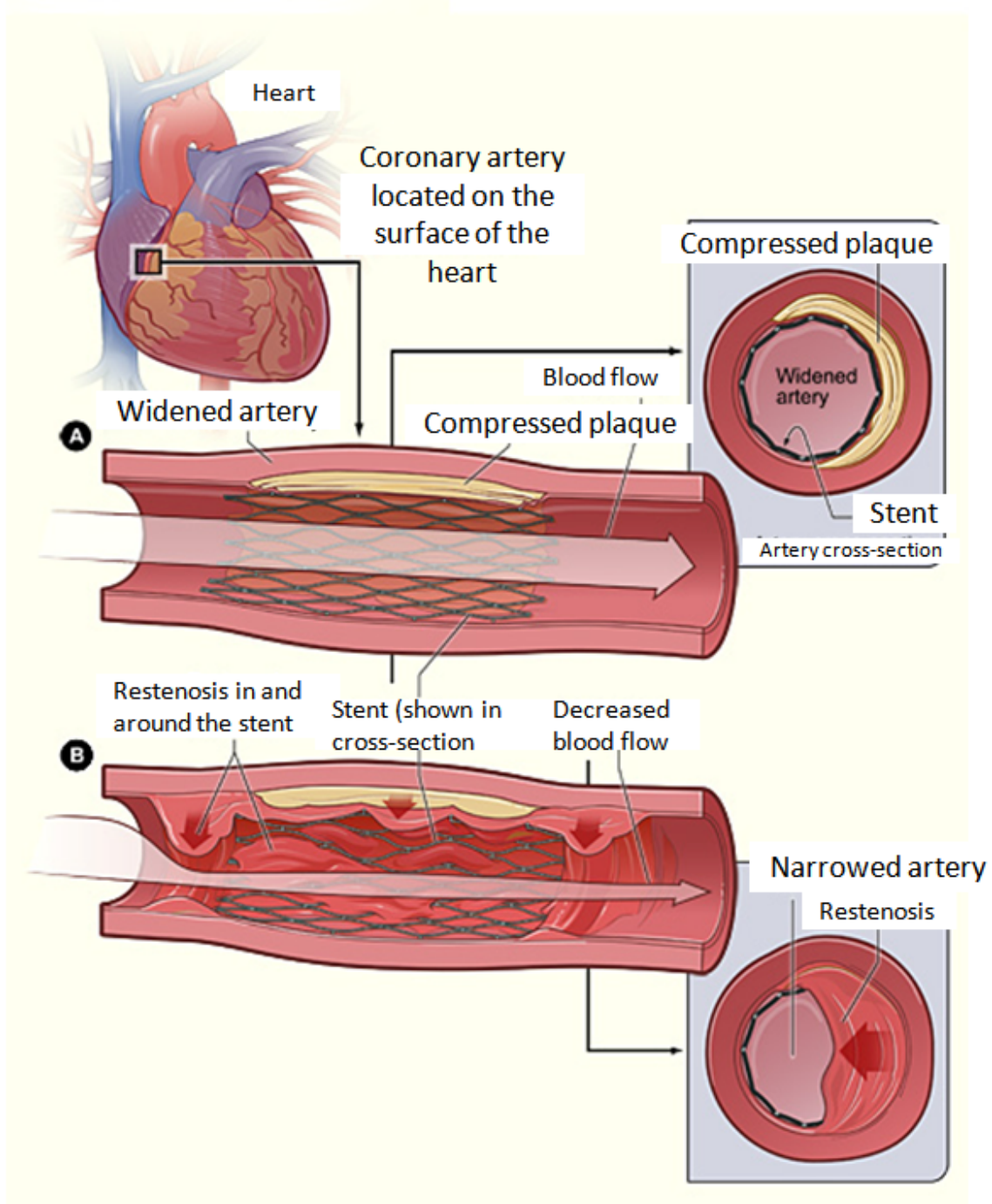
Figure 1.3: The illustration shows the restenosis of a stent-widened coronary artery. a) shows how the expanded stent compresses the plaque, allowing normal blood flow. The inset image shows a cross-section of the compressed plaque and stent-widened artery. b) shows how over time, scar tissue grows through and around the stent. This causes a partial blockage of the artery and abnormal blood flow. The inset image shows a cross-section of the tissue growth around the stent. From [NHLBI, 2012b].

stent placement, and occurs in response to strut-associated injury and inflammation [Moliterno, 2005].
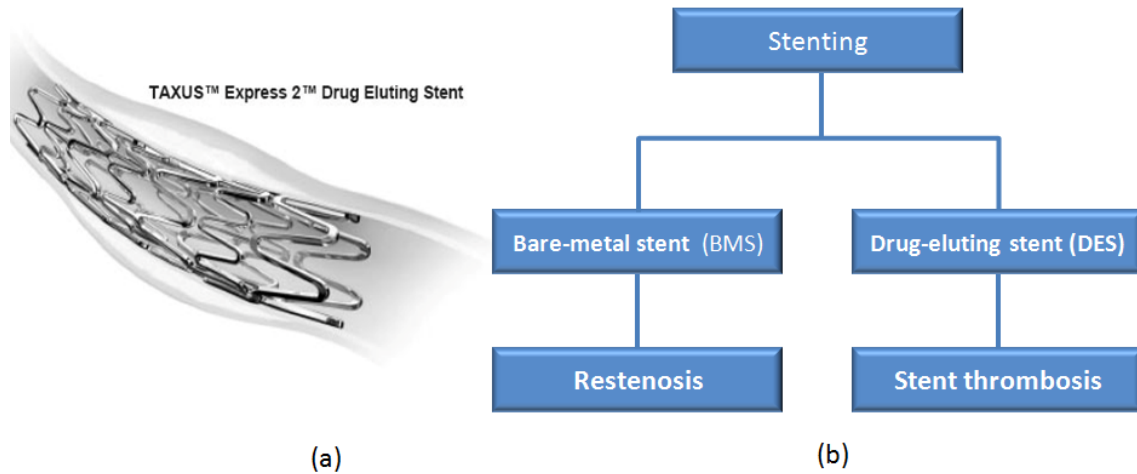
Figure 1.4: (a) a drug-eluting stent. From [USFDA, 2012]; (b) the BMS results in restenosis after stent placement [Tsimikas, 2006]. The DES reduces the case of renarrowing but cause stent thrombosis [Virmani et al., 2004, Tsimikas, 2006, Pfisterer et al., 2006].

In addition to restenosis, PTCA and BMS implantation also cause exaggerated endothelial injury and inflammation, rendering both the stent and vessel highly thrombogenic [Gawaz et al., 1996, Caramori et al., 1999]. A fibrinogen layer covers the stent surface, further inducing platelet activation and thrombosis. In 2001, drug-eluting stent (DES) was introduced as a strategy to minimise restenosis and requirement for reintervention [Pfisterer et al., 2006]. An example of DES is shown in Figure 1.4(a).

Despite the enthusiasm that resulted from the advent of DES, incomplete endothelialisation and stent thrombosis continue to cause problems. Stent thrombosis is an uncommon but serious complication of coronary artery stents that almost always causes death or a large non-fatal AMI, usually with STEMI. Several analyses [Virmani et al., 2004, Tsimikas, 2006, Pfisterer et al., 2006] that tracked patient outcomes over several years after stent placement showed that blood clots were more likely to form inside DES than inside BMS. The consequential and long-term outcomes following stent implantation are summarised in Figure 1.4(b).

To prevent coronary restenosis and stent thrombosis, intravascular image modalities such as IVOCT and IVUS are used to observe the clinical symptoms such as plaque/neointima growth and stent malapposition. These modalities will be discussed in the next section.

1.2 Coronary Artery Imaging

In this section, we introduce the medical imaging techniques that can be used to image the coronary arteries. We will describe the most frequently used image modalities such as IVOCT, IVUS, biplane x-ray angiograms, magnetic resonance angiography (MRA) and computerised tomography angiography (CTA).

1.2.1 Intravascular Optical Coherence Tomography

Plaques that possess (a) a thin fibrous cap ($<65\mu m$), (b) a large lipid pool and (c) activated macrophages near the fibrous cap are prone to rupture and cause acute coronary events [Jang et al., 2002]. Since many of the determinants of plaque vulnerability are structural abnormalities, a high-resolution imaging technique may offer promise as a method of detecting vulnerable plaques. Catheter-based diagnostic imaging techniques, however, can provide structural information with higher resolution than non-invasive imaging methods.

IVOCT has been proposed as a high-resolution imaging method for plaque characterisation of the coronary artery [Bezerra et al., 2009, Sampson and Hillman, 2004, Huang et al., 1991]. It is an interferometric optical imaging modality, somewhat analogous to ultrasound, that provides cross-sectional and 3D (2D+time) images of biological tissue with extremely high resolutions reaching down to the micron scale. Multiple axial line (A-line) scans are continuously acquired as the image-wire rotates and a full revolution creates a complete cross section of the vessel (B-scan) [Bezerra et al., 2009]. Figure 1.5 shows an example of IVOCT in a coronary artery.

IVOCT acquisition is performed similar to IVUS: The imaging catheter acquires cross-sectional images of the coronary artery by emitting near-infrared (NIR) light instead of ultrasound towards the lumen border in a radial manner while the transducer is rotating and the catheter is pulled back with high and constant speed. IVOCT allows an acquisition speed of 100-160 frames per second and a very fast pullback speed (15-25 mm/s) which greatly decreases the imaging time; on the other hand, it results in a large number of images for each single pro-
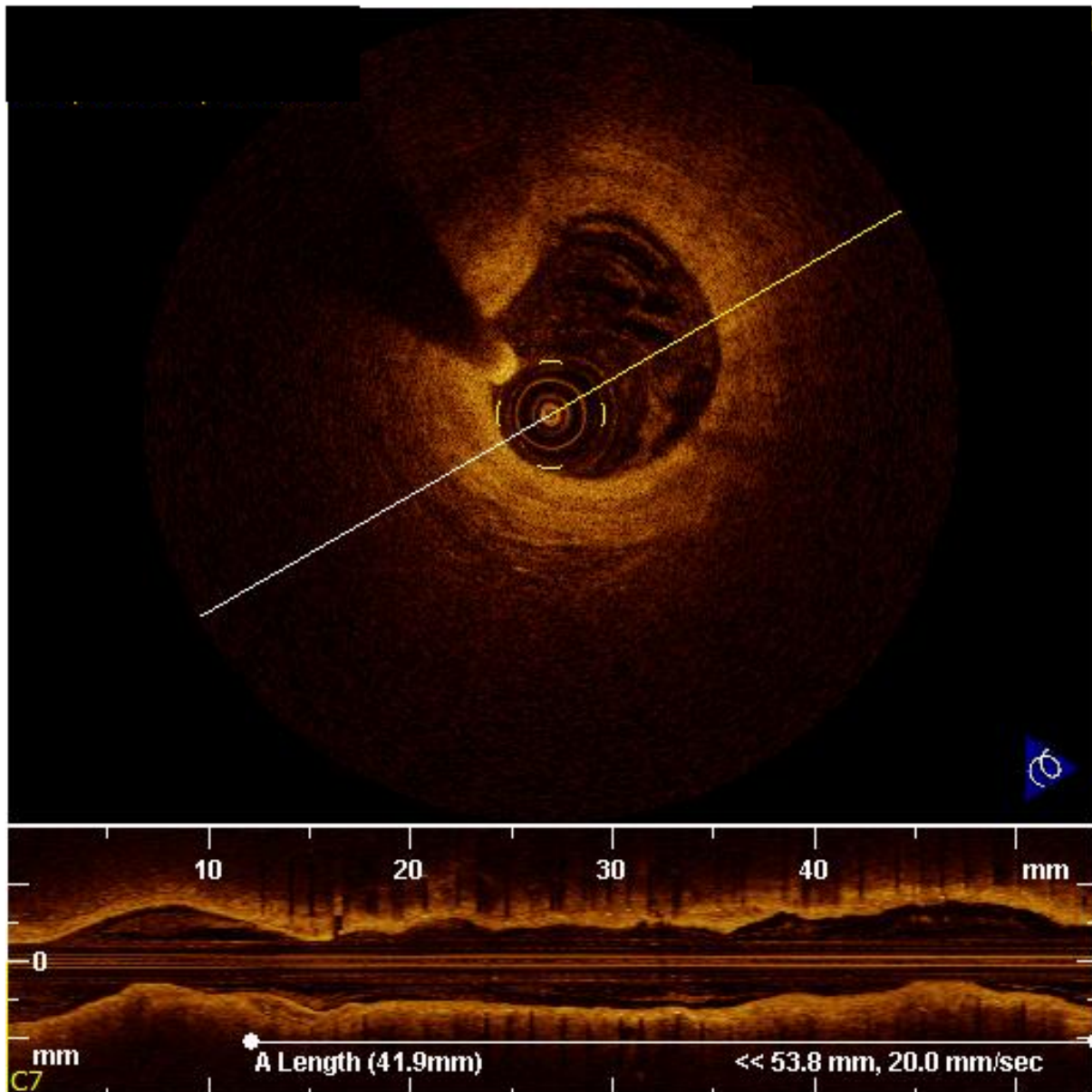
Figure 1.5: Upper image is a cross-sectional image of a coronary artery. Bottom image is the longitudinal view of the coronary.

cedure. The latest IVOCT acquisition system is the C7-XR system. Images acquired by this system is a frequency domain OCT (FDOCT) images. A brief introduction of the system can be found in section 1.5.1.

Vitro studies have shown that the resolution of IVOCT ($10\mu m$-$20\mu m$) can be used to analyse the components of plaque and thickness of plaque/neointima [Jang et al., 2002]. The intrinsic optical properties of typical plaque constituents have provided sufficient contrast to differentiate between lipid, calcium and fibrous tissue [Jang et al., 2002]. When IVOCT has been used to
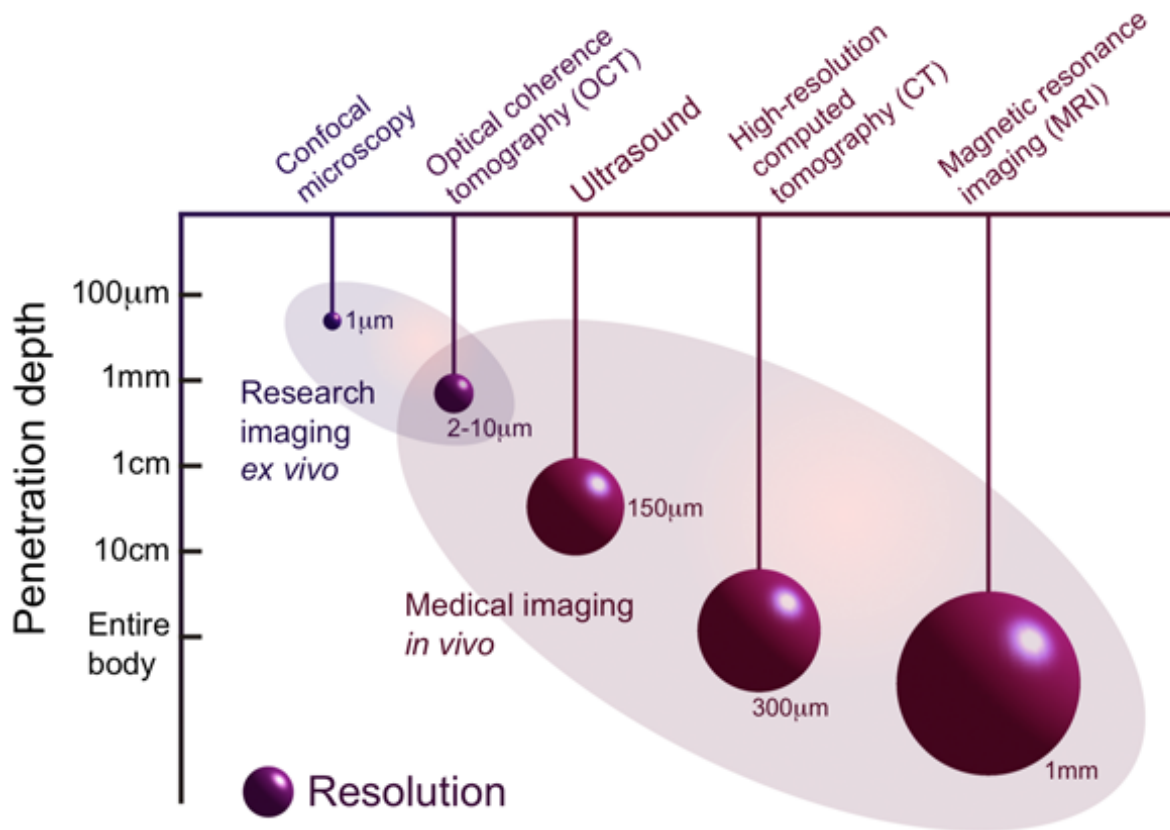
Figure 1.6: Comparison of OCT resolution and imaging depths to those of alternative image modalities; the "pendulum" length represents imaging depth, and the "sphere" size represents resolution. From [OBEL, 2012].

assess stented arterial segments, it can accurately differentiate stent struts and the vascular tissue surrounding them. Therefore, IVOCT may be a valuable tool to assess appropriate healing of stented coronary segments and therefore guide pharmacological therapy to prevent LST.

In addition, OCT can be directly compared with alternative techniques in terms of several different criteria: resolution, imaging depth, acquisition time, complexity and sample intrusiveness. With regard to the first two, OCT occupies a niche represented in Figure 1.6. Its imaging depth is typically limited to a few millimeters, less than ultrasound, magnetic resonance imaging (MRI) or computerised tomography (CT), but its resolution is greater. Like ultrasound, the acquisition time of OCT is short enough to support tomographic imaging at video rates, making it much more tolerant to subject motion than either CT or MRI.

1.2.2   Other Modalities

Intravascular Ultrasound

IVUS is widely used in interventional cardiology. It is a medical imaging technology that uses a specially designed catheter with a miniaturised ultrasound probe attached to the distal end of the catheter. The proximal end of the catheter is attached to computerised ultrasound equipment. It allows the application of ultrasound technology to see from inside blood vessels out through the surrounding blood column, visualising the endothelium (inner wall) of blood vessels.

The guide-wire is kept stationary and the ultrasound catheter tip is pulled backwards, usually under motorised control at a pullback speed of 0.5 mm/s. The sound waves emitted from the catheter tip are usually in the 20-40 MHz range. The catheter also sends the return echo information out to the external computerised ultrasound equipment, which constructs and displays a real time ultrasound image of a thin section of the blood vessel currently surrounding the catheter tip. Usually, the frame rate is 30 frames/second.

IVUS is used in the coronary arteries to determine the amount of atheromatous plaque built up at any particular point in the epicardial coronary artery. The progressive accumulation of plaque within the artery wall over decades is the setup for vulnerable plaque which, in turn, leads to heart attack and stenosis (narrowing) of the artery (known as coronary artery lesions). IVUS is of use for determining both plaque volume within the wall of the artery and/or the degree of stenosis of the artery lumen. It can be especially useful in situations in which angiographic imaging is considered unreliable; such as for the lumen of ostial lesions or where angiographic images do not visualise lumen segments adequately, such as regions with multiple overlapping arterial segments. It is also used to assess the effects of treatments of stenosis such as with hydraulic angioplasty expansion of the artery, with or without stents, and the results of therapy over time. Figure 1.7 shows IVUS examples of a stented coronary artery.

IVUS is rarely done alone or as a strictly diagnostic procedure. It is usually done at the same
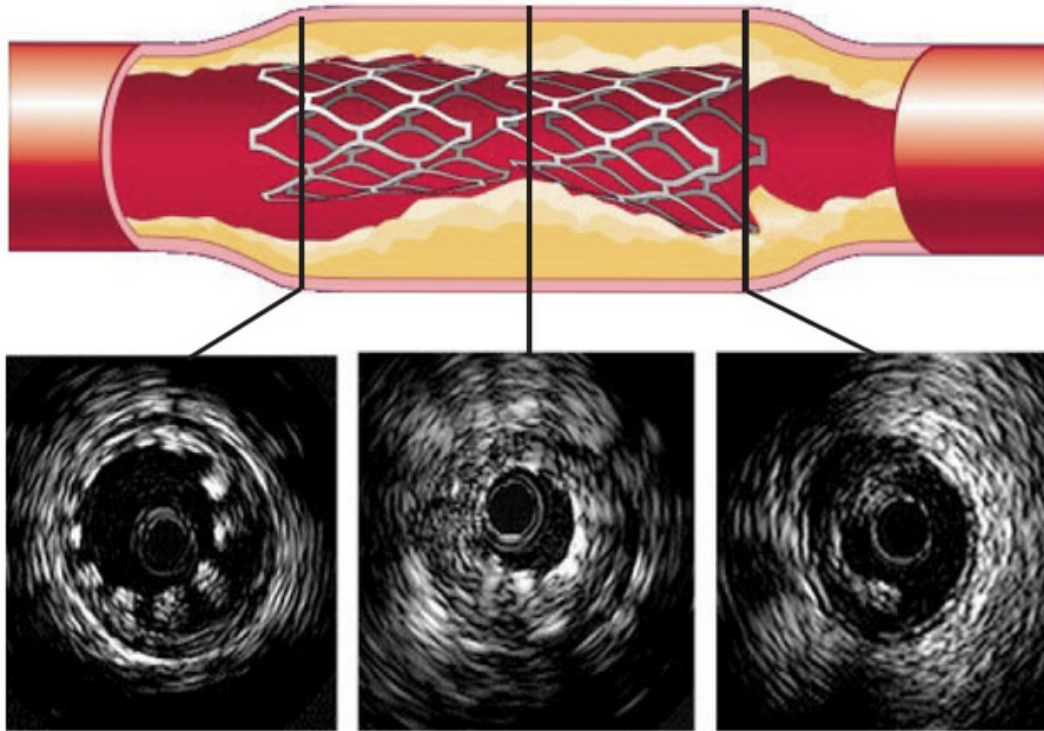
Figure 1.7: This figure shows incomplete apposition, incomplete expansion and edge tear in IVUS. From [Buckley, 2011].

time that a percutaneous coronary intervention (PCI), such as angioplasty, is being performed. However, owing to its relatively low resolution (100-150μm), IVUS does not provide detailed structural information that could improve our understanding of the mechanisms of acute complications and restenosis. Additionally, the high echogenicity of stent struts makes it difficult to evaluate adjacent structures such as small dissections and tissue prolapse.

To sum, IVUS provides useful information regarding vessel size, plaque area and morphology for stent implantation. However, the resolution of IVUS (100-150μm), limits the ability of IVUS to detect detailed structures such as thrombus, stent malapposition and tissue prolapse during stent implantation. By contrast, the high resolution of IVOCT allows visualisation of fine coronary structures. This imaging modality may be useful not only for detecting different types of coronary plaque, but also for facilitating PCI procedures with stent malapposition, strut distribution and stent edge dissection.

A comparison between the IVOCT C7-XR system and the IVUS imaging system is shown in Figure 1.8. The comparison shows that the strength of IVUS is tissue penetration. However, it

Performance Comparison: FD-OCT vs. IVUS
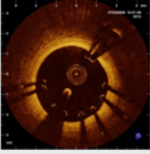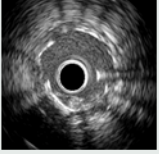
	C7-XR	IVUS
Axial Resolution	15 – 20 µm	100 – 200 µm
Beam Width	20 – 40 mm	200 – 300 mm
Frame Rate	100 frames/s	30 frames/s
Pullback Speed	20 mm/s	0.5 - 1 mm/s
Max. Scan Diameter	10 mm	15 mm
Tissue Penetration	1.0 - 2.0 mm	10 mm
Lines per Frame	500	256
Lateral Resolution	19 µm	225 µm
Guide-Wire Probe	Yes	Yes
Blood Clearing	Required	Not Required

Figure 1.8: This figure shows a comparison between IVOCT system (C7-XR system, frequency-domain OCT) and IVUS system. IVUS system has better tissue penetration and does not need to clean blood when it is used to acquire images. From [Gonzalo, 2010].

is easy to notice that IVOCT has more advantages than IVUS. Therefore, IVOCT has become the more popular image modality in the analysis of CHD and restenosis.

Biplane X-ray Angiography

X-ray angiography is one of the primary modalities used for assessment of the anatomy and function of the vascular system [Hoffmann et al., 1999]. It is a type of X-ray imaging used to examine blood vessels. The images are created using a radiopaque substance, or contrast medium, to make the blood vessels visible under X-ray. Biplane X-ray angiograms acquire two images at different angles simultaneously with a single contrast injection compared to mono-plane X-ray angiograms. Figure 1.9 shows an example of a pair of biplane X-ray angiograms of the coronary arteries. Biplane X-ray systems can be used both pre-operatively and intra-operatively. However, the major drawback of biplane angiography is its invasive nature and the lack of 3D information. A separate 3D reconstruction step of the vascular structures is
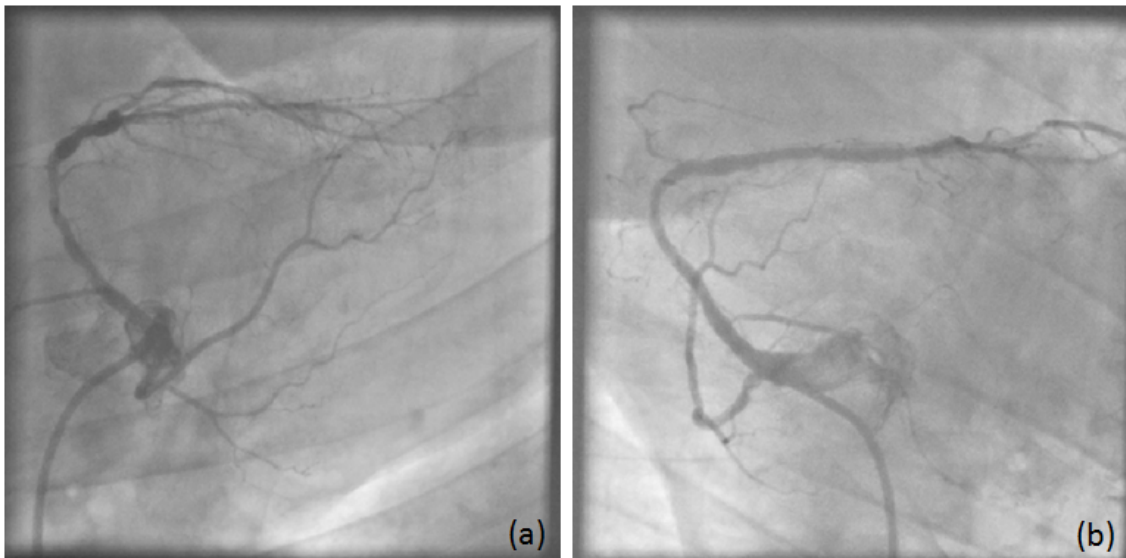
Figure 1.9: Biplane X-ray angiograms of coronaries: (a) view 1 of angle 40 and (b) view 2 of angle 45.

essential after acquiring biplane X-ray angiograms.

Computed Tomography Angiography

CTA is a Computed Tomography technique based on x-rays used to visualise arterial and venous vessels throughout the body. It combines the technology of a conventional CT scan with that of traditional angiography to create detailed images of the blood vessels in the body. It is used to evaluate stenosis, occlusion or aneursyms in the coronary arteries. A CTA scan is performed simultaneously with a high-speed medium contrast injection into a small peripheral vein. The entire CTA exam may be completed within a few seconds. Figure 1.10 shows an example of a CTA scan of a patient. For further details about CTA see [Schuijf et al., 2006, Bluemke et al., 2008].

Magnetic Resonance Angiography

MRI is a detailed tomography imaging technology used to visualise internal structures of the body by using magnetic fields and radio frequency waves. MRA is a variant of MRI specially for imaging vasculature structures. MRA is often used for the arteries in the brain,
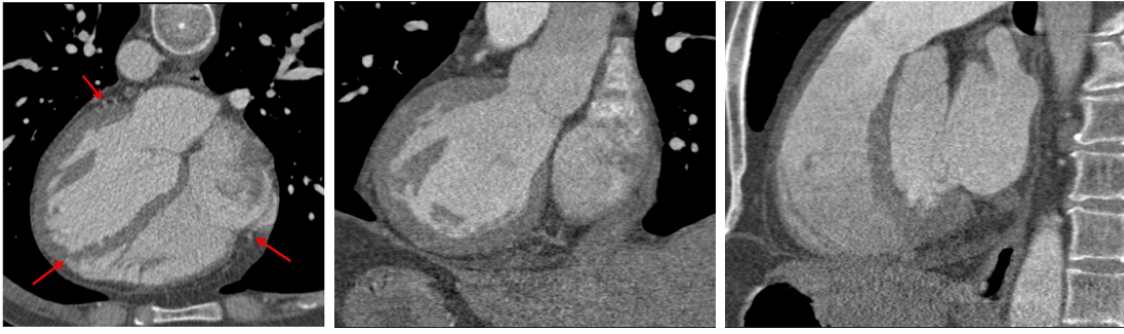
Figure 1.10: CTA images in transversal, coronal and sagittal views. Red arrows point to the right coronary artery; yellow arrow shows the left coronary. From [Zhang, 2010].
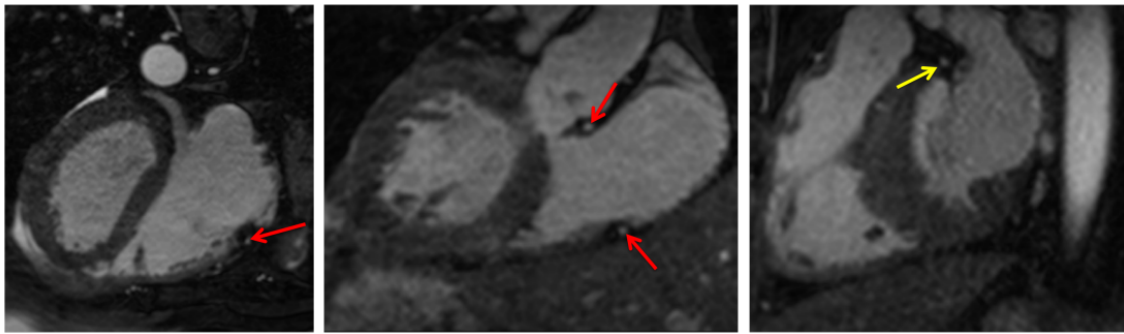
Figure 1.11: MRA images in transversal, coronal and sagittal views. Red arrows point to the right coronary artery; yellow arrow shows the left coronary. From [Zhang, 2010].

neck, abdomen and legs where less motion is presented. When it is used for imaging coronary arteries, navigator-based respiratory gating techniques are used to eliminate respiratory motion [Stenhning et al., 2007]. An example of an MRA is shown in Figure 1.11. MRA lacks the resolution and real-time imaging of angiography. In addition, MRA imaging times are longer than CTA (normally one hour or longer).

1.3   Objectives and Challenges

IVOCT has become the modality of choice for coronary restenosis and LST image analysis as it has a number of advantages over other imaging techniques. It is capable of differentiation among different plaque components [Yabushita et al., 2002]. Additionally, IVOCT is capable of restenosis and stent thrombosis observation [Ikenaga et al., 2010]. The goal of our work is to construct a patient-specific coronary model from preoperative cardiac IVOCT sequences. Knowledge about the segmented lumen and stent can be valuable in the management

of CHD (atherosclerosis). In addition, with the segmented neointima, our model can be useful in the diagnosis of restenosis and prevent LST. These objectives can be achieved by addressing the following technical challenges:

- The first challenge is the guide-wire shadow artifacts elimination. When IVOCT is acquired by using the C7-XR system, the catheters are advanced over a guide-wire using a short rail section at the catheter tip. The guide-wire runs outside parallel to the imaging segment resulting in a shadow artifact in the image. If the guide-wire shadow artifacts are not eliminated, these artifacts will cause inaccurate lumen segmentation since the lumen border and the surrounding tissue are covered by the guide-wire shadow artifacts. However, most existing approaches do not explicitly address the problem of guide-wire shadow artifacts elimination.

- The second challenge is the stent struts detection while the intensities of stent struts are weak. Stent struts segmentation is used to identify malapposed stent struts, apposed stent struts and neointima covered stent struts. In general, a stent is often placed at the site of blockage to permanently open the artery during angioplasty (stent apposition). If it does not reach the arterial wall, malapposition occurs and may cause LST. Covered stent struts provide information about restenosis. Most existing algorithms focus on the detection of the strut position without dealing with the weak intensity responses of stent struts.

- Finally, the severity of restenosis is based on the thickness of neointima which is estimated from the lumen area and the stent area. However, the dependency on the thickness of the neointima may cause inaccurate restenosis analysis when an inaccurate stent area is used. A challenge for this neointima segmentation is to develop an alternative approach that segments NIH when knowledge of stent properties such as the positions of the stent struts and stent area estimation are not available.

1.4   Contributions

The focus of the research presented in this thesis is the use of IVOCT imaging for coronary restenosis analysis. The work presented in this thesis makes three main technical contributions to the analysis of coronary restenosis in the context of image segmentation. The main contributions of the thesis are contained in chapters 4-6:

- A fully automatic lumen border segmentation technique is developed. The proposed segmentation technique is capable of generating an accurate lumen border segmentation from IVOCT image acquisitions. This method can be used to eliminate guide-wire shadow and accurately estimate the lumen border. The estimation of the position of the guide-wire is the key concept for the elimination of guide-wire shadow artifacts. After identification of the artifacts, a geometrically-based method which can be applied to IVOCT cross-sectional images to remove the artifacts is proposed. The segmentation approach is based on a novel combination of expectation maximisation (EM)-based segmentation and graph-cuts (GC)-based segmentation. Compared to lumen border estimation with commercial systems (the C7-XR system and the Odeirena system, designed by [Ughi et al., 2011]), the approach has achieved high overlap accuracy with respect to ground truth obtained from the C7-XR system in terms of lumen area estimation.

- A novel method for stent struts detection in IVOCT in-stent-restenosis images is proposed. IVOCT can accurately differentiate the most superficial layers of the lumen border as well as stent struts and the vascular tissue surrounding them. This method not only detects the strut shadow zone but also accurately segments and reconstructs the stent struts in 3D. The estimation of the position of the strut shadow zone is the key requirement which enables the strut segmentation. After identification of the shadow zone, an a-priori probability map is used to estimate the stent strut positions in every detected shadow zone. This method can be applied to cross-sectional IVOCT images to detect the struts including apposed struts, malapposed struts and covered struts. The comparison against manual expert segmentation demonstrates that the proposed strut identification

is accurate but the stent area is over-estimated because of the sensitivity of strut shadow identification.

- A multi-atlas based neointima segmentation method is proposed since NIH plays a decisive role in coronary restenosis after stenting. The novel aspect of the method is that neointima can be segmented without stent area estimation but instead with lumen border segmentation. The approach can be considered as a classification method since each atlas acts as a classifier and the neointima tissue labels from all atlases are fused. The atlases are selected by measurements of stenosis and image similarity. A probability map is then used to estimate neointima tissue in the unseen image. To account for registration errors, a patch-based label fusion is applied. Compared to other label fusion approaches, a significant increase in segmentation accuracy can be observed.

A list of publications arising from the work in this thesis can be found in Appendix B.

1.5 System Environment

This section describes the system environment including the IVOCT imaging system and the image data used in this work.

1.5.1 Imaging System

The image sequences used in the thesis were acquired by a commercial system (the latest ImageWire C7-XR^{TM} system, Lightlab imaging, Westford, MA, USA) used for PCI (Figure 1.4(a)). This C7-XR system is the frequency-domain OCT (FD-OCT) imaging system which consists of an OCT imaging catheter (a C7 dragonfly imaging catheter, Figure 1.4(b)) and an imaging operating console. The catheter is advanced distally into the coronary artery via a standard angioplasty guide-wire (0.014″) and an imaging probe integrated in the catheter [Terashima et al., 2012]. Cross-sectional images are acquired by an automated IVOCT pullback during contrast injection through the guide catheter. The high pullback speed (20 mm/s) allows imaging
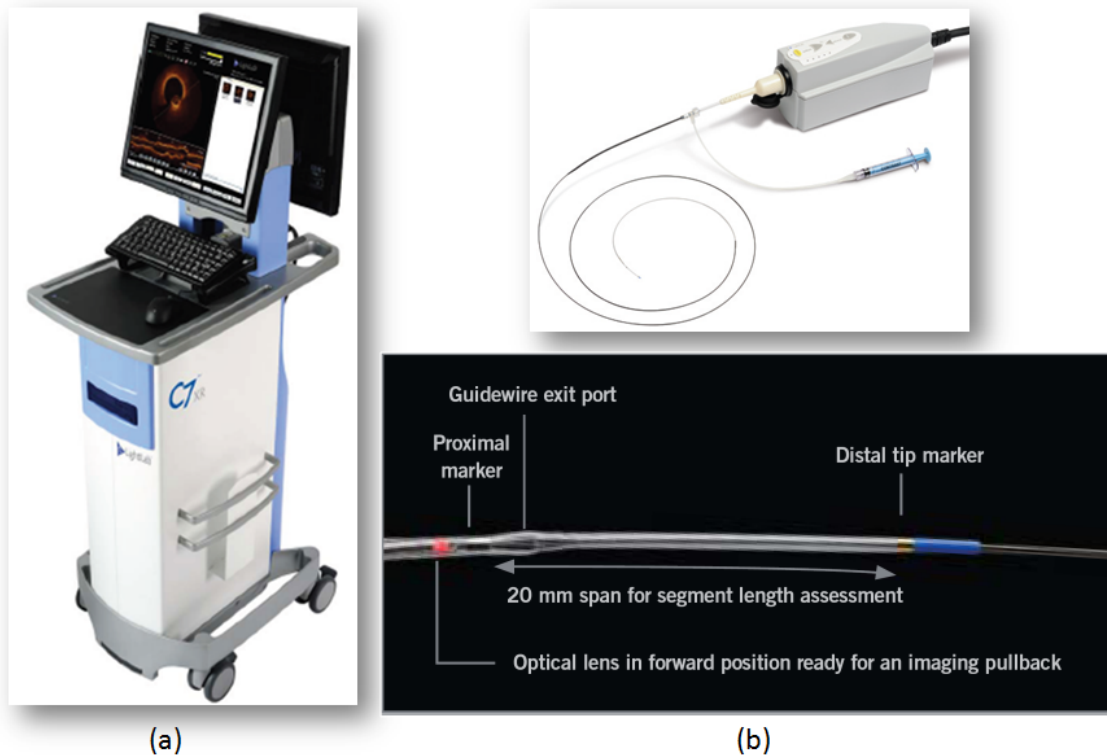
Figure 1.12: (a) imaging system (C7-XR system) and (b) its catheter. From [Gonzalo, 2010]. The catheter has one optical lens and two marks: proximal marker and distal tip marker. The segment length of the imaging procedure is about 20mm.

of long coronary segments in few seconds while the speed is about 10-25x increased compared to the previous OCT systems such as the time-domain OCT systems (ImageWire M2/M3, Lightlab imaging, Westford, MA, USA) and the IVUS system [Terashima et al., 2012].

The comparison between the C7-XR frequency-domain OCT (FDOCT) system and its previous M2/M3 time-domain OCT (TDOCT) systems is shown as Figure 1.13. Although images acquired from the previous time-domain OCT systems do not have obvious guide-wire artifacts, the acquisition procedure is slow since the additional procedure (balloon occlusion) is required to temporarily stop the blood flow. In addition, the lower pullback speed and poor image quality are the other drawbacks. Therefore, since 2010, the C7-XR system has become the popular CHD/restenosis diagnosis system [Terashima et al., 2012].
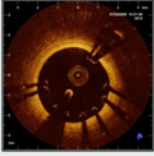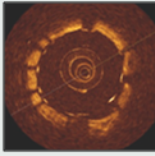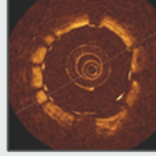
Figure 1.13: A comparison of OCT systems. From [Gonzalo, 2010]. The C7-XR system (frequency domain OCT) provides better image resolution and a rapid imaging procedure than the previous time-domain OCT system.

1.5.2 Materials

In the thesis, the total eighteen IVOCT sequences were obtained from Royal Brompton Hospital by Dr. Ranil and Dr. Hiroto. The sequences were acquired in the right coronary artery by using the C7-XR system since the system provides high resolution images for plaque classification and stent struts distribution. Each sequence is considered as an independent patient sequence with different severity of in-stent restenosis and artery stenosis (mild narrow, moderate narrow and severe narrow). In addition, the sequences were grouped by lumen percent diameter stenosis (LPDS) [Vos et al., 1997, Abizaid et al., 1998] and verified by Dr. Hiroto (Table 1.2). The length of stented segments of each patient is about $45.5mm$. The stenting timescales and the related diagnoses are not available. Every sequence is acquired during a pullback rate of 20.0 mm/s and has between 268/271 frames. The field of view of all sequences is 512x512 pixels. An overview of all sequences can be found in Appendix A.2.

Table 1.2: This table shows the severity of artery stenosis of the patient data.

Narrow	Patient ID
Mild	P1, P6, P12, P13, P14, P15, P17, P18
Moderate	P2, P3, P5, P7, P8, P9, P11, P16
Severe	P4, P10

1.6   Overview of thesis

In the following chapters, we review the segmentation approaches that are used in our system (Chapter 2). Image segmentation approaches used in IVUS and OCT images are reviewed in Chapter 3. The methods and algorithms that have been developed during our research are presented in the subsequent chapters. In Chapter 4, we develop a method for lumen border segmentation using the EM-GC-based method and geometric methods. In Chapter 5, a comprehensive stent struts detection approach using probability maps of stent strut position estimations is developed. In Chapter 6, we introduce a multi-atlas based method to segment neointimal tissue without information of stent struts. Finally, in Chapter 7, we summarise the work presented in this thesis and discuss future work.

1.7   Statement of originality

The material in this thesis has not previously been submitted for a degree at any university, and to the best of my knowledge contains no material previously published or written by another person except where due acknowledgement is made in the thesis itself.

Chapter 2

Review of Image Segmentation Algorithms

2.1 Introduction

Image segmentation can be defined as the task of distinguishing objects from background in unseen images. Typically this division is based on low-level approaches such as intensity-based segmentation approaches or high-level segmentation approaches such as active contours. The aim of this chapter is to review the related segmentation methods used in the thesis.

We review the image enhancement methods in section 2.2 and present low-level/high-level approaches in section 2.3 and section 2.4, respectively. Atlas-based segmentation approaches are also reviewed in section 2.5. In section 2.6, recent popular methods, especially multi-atlas and patch-based segmentation, are discussed.

2.2 Image Enhancement

Image enhancement, either a pre-processing step for tubular structure segmentation or as a technique to improve the visualisation of 2D (line-) or 3D (tube-like) structures, is widely used

in medical image analysis. Once tube-like structures are segmented, they can be quantified and further assessed. In this section, we review the state-of-the-art technique of Hessian-based enhancement.

2.2.1 Hessian-based Filtering

Hessian-based filtering is a class of tubular enhancing filters that are based on second-order intensity information. These filters exploit the amount of intensity variation after an image is smoothed with a Gaussian filter. To extract the intensity variation, the second derivative of the Gaussian is computed. The Hessian matrix $H(x)$ defines the second derivatives at each voxel in the image $I(x)$:

$$H(x) = \begin{bmatrix} \frac{\partial^2 I}{\partial x^2} & \frac{\partial^2 I}{\partial x \partial y} & \frac{\partial^2 I}{\partial x \partial z} \\ \frac{\partial^2 I}{\partial y \partial x} & \frac{\partial^2 I}{\partial y^2} & \frac{\partial^2 I}{\partial y \partial z} \\ \frac{\partial^2 I}{\partial z \partial x} & \frac{\partial^2 I}{\partial z \partial y} & \frac{\partial^2 I}{\partial z^2} \end{bmatrix} \tag{2.1}$$

The Hessian matrix can be decomposed into eigenvalues $(\lambda_1, \lambda_2, \lambda_3)$ and eigenvectors $(\vec{v_1}, \vec{v_2}, \vec{v_3})$ using eigen-decomposition. The eigenvalues can be used to determine the likelihood of the voxel x belonging to a vessel. Assuming an ordering of the eigenvalues of the Hessian as $|\lambda_1| \leq |\lambda_2| \leq |\lambda_3|$, the magnitude of the eigenvalues are proportional to the amount of intensity variation and the corresponding eigenvectors indicate the directions of these variations. For an ideal bright line on a dark background, the maximum intensity variation is expected in the two orthogonal directions $\vec{v_2}$ and $\vec{v_3}$ and the minimum intensity variation is found in $\vec{v_1}$.

Frangi et al. [Frangi et al., 1998] proposed the use of rations of the eigenvalues for distinguishing line- and tube-like structures. They proposed a vesselness response filter $v(x, \sigma)$ on the basis of the Hessian matrix:

$$v(\delta) = \begin{cases} 0, & \text{if } \lambda_2 > 0 \text{ or } \lambda_3 > 0 \\ (1 - e^{-\frac{A^2}{2\alpha^2}}) e^{-\frac{B^2}{2\beta^2}} (1 - e^{-\frac{S^2}{2\gamma^2}}), & \text{otherwise} \end{cases} \tag{2.2}$$

where

$$A = \frac{|\lambda_2|}{|\lambda_3|}, B = \frac{|\lambda_1|}{\sqrt{|\lambda_2\lambda_3|}}, S = \sqrt{\lambda_1^2 + \lambda_2^2 + \lambda_3^2} \tag{2.3}$$

The weighting factors α, β, γ in Eq. (2.2) are used to determine the influence of parameters A, B and S. Controlled by α, the parameter A discriminates plate- from line-like structures; B (dominated by β) accounts for any deviation from blob-like structures and S (controlled by γ) differentiates between high-contrast region and low-contrast region such as a bright vessel structure in dark background.

With a multi-scale framework, the vesselness responses are calculated at a range of scales ($\sigma_{min} \leq \sigma \leq \sigma_{max}$) by computing the Hessian matrix at each scale. Different scales can be used to detect different sizes of vessels. Frangi et al. [Frangi et al., 1998] proposed that the largest vesselness response and its corresponding scale can be selected across scales. The multi-scale Hessian-based vessel enhancement filter is then defined as:

$$V(x) = \max_{\sigma}(v(x, \sigma)) \tag{2.4}$$

Here x is a voxel in the image I, v represents the filter response at a specific scale and σ is the scale for calculating Gaussian derivatives in order to derive the Hessian matrix. By calculating $V(x)$ for all voxels in image I, a vessel enhanced image is obtained. The corresponding scale σ for voxel x can be used to approximate the radius of the vessel at that voxel.

An evaluation of three Hessian-based filters [Frangi et al., 1998, Sato et al., 1998, Lorenz et al., 1997] for the enhancement of the central axis of coronary arteries in multi-detector CTA images acquired with contrast injection is presented in [Olabarriaga et al., 2003]. The average filter response obtained with different parameter configurations was measured at fixed distances from a reference central axis determined manually. Results were compared according to two objective measures: the response decay rate at the centre and the overall response within the largest radius for coronary arteries. It was noted that Frangi's design [Frangi et al., 1998] provided the best central vessel axis enhancement.

A drawback of Hessian-based filtering methods for the enhancement of tubular structures is the

high computational cost particularly when a multi-scale framework is used. The Hessian matrix must be computed and decomposed for each voxel at each scale before measuring the vesselness. Orlowski et al. [Orlowski and Orkisz, 2009] presented guidelines for efficient computation of multi-scale filters based on eigenanalysis of the Hessian matrix applied to 3D medical images of blood vessels.

Except for the drawback of computational speed, Hessian-based vessel enhancement filters have been shown to be applicable to various imaging modalities such as digital subtracted angiography [Lorenz et al., 1997, Frangi et al., 1998], CTA [Sato et al., 1998, Olabarriaga et al., 2003], MRA [Sato et al., 1998, Frangi et al., 1998, Wink et al., 2002] and several types of vessels (cerebral [Lorenz et al., 1997, Sato et al., 1998], peripheral [Frangi et al., 1998], hepatic [Sato et al., 1998], pulmonary [Sato et al., 1998] and cardiac [Olabarriaga et al., 2003, Wink et al., 2002]).

2.3   Low-Level Image Segmentation Methods

Image segmentation can be considered as the process of segmenting the image into groups of connected pixels. In general, pixels that are grouped together have similar properties such as color, texture, intensity etc. Algorithms for low-level image segmentation can be categorised into either non-graph based or graph-based algorithms. In this section, we review a popular nongraph-based clustering algorithm (EM algorithm [Dempster et al., 1977]) and a graph-based algorithm (GC algorithm [Boykov et al., 2001b, Boykov and Jolly, 2001]).

2.3.1   Expectation-Maximisation (EM) Algorithm

A well known statistical approach used for image segmentation is the EM algorithm [Dempster et al., 1977]. It models the image intensities using a Gaussian mixture model (GMM) [Moon, 1996] which assumes that an image can be represented as a combination of Guassians. EM is used to estimate the parameters of Gaussians (mean, variance and convergence) of different

classes and determines the class of each voxel in the image.

The general EM algorithm is comprised of the following simple steps: a) initialisation, b) expectation (E-step) and c) maximisation (M-step). Steps (b) and (c) are iteratively repeated until convergence.

Since a Gaussian mixture model is a probabilistic model, the mixture model of voxel i is represented by:

$$f(x_i|\Theta) = \sum_{k=1}^{K} \alpha_k G(x_i|\theta_k) \qquad (2.5)$$

Here $f(x_i|\Theta)$ is a K components Gaussian mixture model; x_i represents the intensity of the voxel i; K is the number of classes that need to be extracted from an image; $\theta_k, k = 1, 2, ..., K$ is a parameter vector of class k given by mean μ_k and standard deviation σ_k. α_k is the mixing proportion of class k ($\alpha_k > 0$ and $\sum_{k=1}^{K} \alpha_k = 1$); $\Theta = \{\alpha_1, ..., \alpha_k; \mu_1, ..., \mu_k; \sigma_1, ...\sigma_k\}$ is the parameters vector of the mixture model. The Gaussian model $G(x_i|\theta_k)$ of the voxel x_i can be written as:

$$G(x_i|\theta_k) = \frac{1}{\sqrt{2\pi\sigma}} \exp(\frac{-(x - \mu_i)^2}{2\sigma_i}) \qquad (2.6)$$

The EM algorithm is applied to find the optimal parameter Θ by maximising the log-likelihood function $L(\Theta)$:

$$
\begin{aligned}
L(\Theta^*) &= \arg\max f(x_1, x_2, ..., x_n|\Theta) \\
&= \arg\max \log[\prod_{i=1}^{n} f(x_i|\Theta)] \\
&= \arg\max \sum_{i=1}^{n} \log \sum_{j=1}^{k} \alpha_j f(x_i|\theta)
\end{aligned}
\qquad (2.7)
$$

Here $\prod_{i=1}^{n} f(x_i|\Theta)$ is the likelihood function; Θ^* is the maximum log-likelihood estimator of Θ.

At each iteration, the E-step calculates the expected posterior probability $p^{(t+1)}(k|x_i, \theta_k)$ that voxel i belongs to class k:

$$p^{(t+1)}(k|x_i, \theta_k) = \frac{\alpha_k G(x_i|\theta_k^{(t)})}{\sum_{k=1}^{K} \alpha_k G(t)(x|\theta_k^{(t)})} \qquad (2.8)$$

Here $p^{(t+1)}(k|x_i, \theta_k)$ is the probability of pixel i given from class k at the $t + 1$-th iteration;

$G(x_i|\theta_k^{(t)})$ is the probability of voxel i given it is a member of class k.

The M-step updates parameter vector based on the result of E-step:

$$
\begin{aligned}
\mu_k^{(t+1)} &= \frac{\sum_{i=1}^{N} x_i p^{(t+1)}(k|x_i, \theta_k^{(t)})}{\sum_{i=1}^{N} p^{(t+1)}(k|x_i, \theta_k^{(t)})} \\
(\sigma_k^{(t+1)})^2 &= \frac{\sum_{i=1}^{N} p^{(t+1)}(k|x_i, \theta_k^{(t)})(x_i - \mu_k^{(t+1)})^2}{\sum_{i=1}^{N} p^{(t+1)}(k|x_i, \theta_k^{(t)})} \\
\alpha_k^{(t+1)} &= \frac{\sum_{i=1}^{N} p^{(t+1)}(k|x_i, \theta_k^{(t)})}{N}
\end{aligned}
\tag{2.9}
$$

The EM algorithm terminates when it satisfies the stopping criterion:

$$
\frac{L(\Theta^{(m+1)} - L(\Theta^{(m)})}{L(\Theta^{(m)})} \leq \epsilon
\tag{2.10}
$$

Here, ϵ is the tolerance parameter which is usually set to 10^{-5}.

The EM algorithm works well in image segmentation especially when an image can be represented by well-characterised Gaussian density functions [Saeed et al., 1998]. Applications of the EM algorithm for segmenting lumen border in IVUS images are explained in section 3.1.3.

2.3.2   Graph-Cuts Algorithm

The task of segmenting an image into structures can be transformed into a labeling problem produced by optimisation of the posterior energy function [Wolz et al., 2010]. A GC [Boykov et al., 2001b, Boykov and Jolly, 2001]) is the process of partitioning a directed or undirected graph into disjoint sets. It is a method that constructs a graph to optimise energy functions which can be characterised as markov random field (MRF) [German and German, 1984]. The MRF-based model is a probabilistic model which captures contextual constraints to model a-priori belief about the continuity of image features such as region labels, textures and intensities. The concept of optimality of such cuts is usually introduced by associating an energy to each cut. In general, GC performs segmentation in a global optimisation framework to a binary problem and guarantees a globally optimal solution for a wide class of energy functions.

Considering a weighted graph G=<V,E> where V is a set of vertices/nodes and E is a set of weighted edges connecting the vertices, we assume V corresponds to a set of image pixels P plus additional vertices called terminals s (source/object) and t (sink/background). E consists of edges connecting neighbouring pixels (n-links) and those connecting the pixels to the terminals (t-links). An *s-t* cut is a set of edges that completely separates the source node from the sink node leading to a segmentation of the image into foreground and background.

Let N denotes a set of all unordered pairs $\{i, j\}$ of neighbouring pixels in the image I (2D: 8-connected neighbourhood system; 3D: 26-connected neighbourhood system). The aim is to find the best labeling f (optimal segmentation) by minimising the following energy function (using min-cut/max-flow algorithm [Boykov et al., 2001b]):

$$E(f) = \lambda \sum_{i \in I} D_i(f_i) + \sum_{i,j \in N} V_{i,j}(f_i, f_j) \tag{2.11}$$

Here f_i is the label ("foreground" or "background") assigned to the pixel i; the data term $D_i(f_i)$ shows the likelihood probability that pixel i belongs to foreground or background. The smoothness term $\sum_{i,j \in N} V_{i,j}(f_i, f_j)$ penalties the neighbouring pixels when their labels are different. λ is a weighting term used to balance the two energy terms. If λ is too small, an oversegmentation of an image tends to occur; if λ is too large, an undersegmentation typically occurs. The selection strategy can be referred to [Peng and Veksler, 2008].

The smoothness term is defined as:

$$V_{i,j}(f_i, f_j) = \exp(-\frac{(x_i - x_j)^2}{2\sigma^2}) \cdot (\frac{1}{\|i - j\|}) \tag{2.12}$$

Here $\|i - j\|$ denotes the distance between two pixels, σ is the standard deviation of the intensities and x_i, x_j are the intensity of pixels i, j. For the data term D_i, an a-priori probability definition is used to compute the weight of the t-links between all the pixels and both terminals as follows:

$$D_i(f_i) = -\ln Pr(x_i|f_i) \tag{2.13}$$

The weight $Pr(x_i|f_i)$ represents the likelihood of foreground and background at pixel i. The

value is closed to zero when the label of the pixel belongs to the foreground or the background; otherwise, the value is increasing when the probability of the label of the pixel belonged to the background decreases.

A drawback of the GC is that the found optimal solution is only satisfied with a binary problem (foreground/background problem). Boykov et al. [Boykov et al., 2001b] proposed approximation algorithms (α-expansion and α-β swap) for the multiple label energy minimisation problem (local minimisation).

The main idea of the α-expansion algorithm is to segment all α and non-α pixels with GC and the algorithm will change the value of α at each iteration. The algorithm will iterate through each possible label for α until it converges. At each iteration, the α region P_α can only expand. This changes somehow the way of setting the graph weights. Also when two neighbouring nodes do not currently have the same label, an intermediate node is inserted and links are weighted so that they are relative to the distance to the α label.

The α-expansion algorithm can only be used when the smoothness term is metric. The description of metric is that the amount of constrains has been satisfied by the smoothness term. These constrains include 1) $V(\alpha, \beta) = 0 \Leftrightarrow \alpha = \beta$ or $V(\alpha, \beta) \neq 0 \Leftrightarrow \alpha \neq \beta$, 2) $V(\alpha, \beta) = V(\beta, \alpha) \geq 0$ and 3) $V(\alpha, \beta) \leq V(\beta, \gamma) + V(\gamma, \beta)$. The first two terms tell that an energy between two different labels α and β should be non-zero. If it is zero, that means the two labels are the same. The last term defines the triangle rule. A shortcut is always cheaper or similar than taking the whole path. If the smooth term only satisfies the first two terms, it is said a semi-metric term. If the last term is also satisfied, it is said a metric term.

The smoothness term of the α-β swap algorithm is semi-metric. The main idea of the α-β swap algorithm is to separate all α pixels from β pixels with GC and the algorithm changes the α-β combinations at each iteration. The algorithm iterates through each possible combination until it converges.

Another drawback of the GC is the memory usage [Lerme et al., 2010]. Larger neighbourhood systems yield better image segmentations but at the expense of both increased running time

and memory consumption [Lombaert et al., 2005]. To address this problem, some approaches have been proposed to reduce the computational costs of the GC methods [Lombaert et al., 2005, Li et al., 2004].

GC has risen to become an extremely popular algorithm for image segmentation [Sinop and Grady, 2006]. For example, [Lin et al., 2005] proposed a method for integrating model-based a priori information into the GC formulation. A 4D model prior of the LV is calculated from an average of historically analysed cases. This is scaled and rotated to the given case and a 2D spatial prior is calculated for each image. The spatial prior is then combined with the pixel intensity and the edge information in the GC optimisation.

[Funka-Lea et al., 2006] proposed a method to segment all the chambers of the heart together as a single object, separated from the surrounding physiology in CT images. In addition, the method efficiently segments the blood pools and muscle of the heart as a single 3D region. [Lombaert and Cheriet, 2010] proposed a method for heart segmentation in 4D MRI data sets. The method utilities a GC method for the segmentation of the heart by simultaneously exploiting motion and region cues. A 4D graph is constructed to find a moving object with a uniform intensity from a static background.

[Lang et al., 2011] presented three real-time registration approaches for model-enhanced guidance, exploring different regions of the heart and both surface-based and intensity-based registration. The surface-based registrations employ a GC for surface extraction, while the image-based registration relies on intelligent image subsampling to reduce computational requirements.

[Dikici and Orderud, 2010] proposed a hybrid edge detection approach using GC and step criterion (STEP) edge detectors and its integration into a Kalman-filter [Orderud and Rabben, 2008] based LV tracking framework. The hybrid edge detection approach is the weighted combination of these techniques and is determined by the size of the tracked endocardial mesh.

[Chen et al., 2012] proposed a method to evaluate the potential of low-dose cardiac CT for the measurement of myocardial whole heart extracellular volume (ECV) fraction. ECV is altered under conditions of increased myocardial fibrosis. The method consists of three steps: Firstly,

myocardium and blood pool on post-contrast image are segmented by a shape-constrained GC method; Secondly, the symmetric demons deformable registration method is applied to register pre-contrast to post-contrast images to establish the correspondences between the voxels from pre-contrast to post-contrast images; Finally, the whole heart ECV value was computed.

Applications of GC in different areas (stereo, image restoration, texture synthesis and image segmentation) can be found in [Camilus and Govindan, 2012].

2.4   High-Level Image Segmentation Methods

The low-level segmentation algorithms presented so far are mainly intensity driven. This makes the segmentation flexible, but can also result in unrealistic segmentations due to noise, artifacts and low-contrast boundaries presented in the image. High-level segmentation algorithms avoid these problems by incorporating additional a-priori information, e.g. about the shape and appearance of the object of interest.

2.4.1   Deformable models

Deformable models are physically motivated, model-based techniques for delineating region boundaries. These boundaries can be described by closed parametric curves or surfaces that deform under the influence of internal and external forces. To delineate an object boundary in an image, a closed curve or surface must first be placed towards the desired boundary and is then allowed to undergo an iterative relaxation process. Internal forces are computed across the curve or surface to keep it smooth throughout the deformation process. External forces are usually derived from the image to drive the curve or surface toward the desired feature of interest, e.g. edges or corners.

There are two types of deformable models: parametric deformable models [Kass et al., 1987, Cohen et al., 1992, Xu and Prince, 1998] and geometric deformable models [Malladi et al., 1995, Osher and Sethian, 1988]. Parametric deformable models [Kass et al., 1987, Cohen et al.,

1992] represent curves and surfaces explicitly in their parametric forms. This representation allows direct interaction with the model and can lead to a compact representation for fast real-time implementation. Adaptation of the model topology, however, such as splitting or merging parts during the deformation, can be difficult using parametric models. Geometric deformable models [Malladi et al., 1995, Osher and Sethian, 1988] based on the level-set method can handle topological changes using only geometric measures. Their parameterisations are computed only after completed deformation, thereby enabling the topology to change dynamically. Despite this fundamental difference, the underlying principles of both methods are very similar.

An extension of the parametric deformable models is the incorporation of additional prior knowledge into the models (active shape models (ASM) [Cootes et al., 1995]). Use of prior knowledge in a deformable model can lead to more robust and accurate results when a structure has similar shape across a large number of subjects. Incorporation of prior knowledge requires a training step to accumulate information on the variability of the object shape being delineated.

More details about the use of deformable models used in medical imaging can be found in [Hegadi et al., 2010]. In the following, we review an active contours approach that is a type of parametric deformable model in more detail since it has been widely used to segment lumen border in IVUS and IVOCT image sequences [Katouzian et al., 2012].

Active Contours

The basic premise of the energy minimising formulation of deformable contours is to find a parameterised curve that minimises the weighted sum of some internal energy and external energy. The internal energy specifies the tension or the smoothness of the contour. The external energy is defined over the image domain and typically possesses local minima at intensity edges in the image occurring at object boundaries. Minimising the total energy yields internal forces and external forces. Internal forces hold the curve together (elasticity forces) and keep it from bending too much (bending forces). External forces attract the curve toward the desired object boundaries. To find the object boundary, parametric curves are initialised within the image domain, and are forced to move toward the energy minima under the influence of both these

forces.

An active contour is a parametric contour embedded in the image plane $(x, y) = \Re^2$. The contour $v(s)$ is represented as $v(s) = (x(s), y(s))$ where x and y are the coordinates of the point s on the curve and $s \in [0, 1]$ is the parametric domain. The shape of the contour subject is dictated by a minimised energy function of the contour:

$$E(v) = E_{int}(v) + E_{ext}(v) \tag{2.14}$$

Here the $E_{int}(v)$ is the internal deformation energy:

$$E_{int}(v) = \int_0^1 \alpha(s)|\frac{\partial v}{\partial x}|^2 + \beta(s)|\frac{\partial^2 v}{\partial x^2}|^2 ds \tag{2.15}$$

Here $|\frac{\partial v}{\partial x}|$ and $|\frac{\partial^2 v}{\partial x^2}|$ represent the first and second derivatives of the curve. $E_{int}(v)$ characterises the deformation of a flexible contour. Two physical parameter functions dictate the simulated physical characteristics of the contour: $\alpha(s)$ controls the tension of the contour while $\beta(s)$ controls its rigidity. The values of the non-negative functions $\alpha(s)$ and $\beta(s)$ determine the extent to which the snake can stretch or bend at any point s on the curve.

The external energy $E_{ext}(v)$ couples a snake to the image:

$$E_{ext}(v) = \int_0^1 E_{ext}(v(s))ds \tag{2.16}$$

$E_{ext}(v)$ is typically a combination of energy functions: $\omega_{line}E_{line}$ and $\omega_{edge}E_{edge}$. E_{line} means the intensity of the image. E_{edge} attracts the curve to edges or areas with large image gradients. The weight ω_{line} attracts the contour to dark lines or light lines depending on the sign of the weight. ω_{edge} is the weight which adjusts the attraction to edges.

A snake that minimises E must satisfy Euler-Lagrange equation:

$$\alpha v''(s) - \beta v''''(s) - \nabla E_{ext} = 0 \tag{2.17}$$

This can be viewed as a force balance equation:

$$F_{int} + F_{ext}^1 = 0 \tag{2.18}$$

Here $F_{int} = \alpha x''(s) - \beta x''''(s)$ and $F_{ext}^1 = -\nabla E_{ext}$. The internal force F_{int} discourages stretching and bending while the external force F_{ext}^1 pulls the snake toward the desired image features.

To find a solution/minimisation of Eq. (2.17), the snake treats the curve v as function of time t as well as s (i.e., $v(s,t)$) and Eq. (2.17) has become as following:

$$v(s,t) = \alpha v''(s) - \beta v''''(s) - \nabla E_{ext} \tag{2.19}$$

When the snake has converged to a minimum, its derivative to time will be zero, and so the equation above is satisfied. This can be viewed as a gradient-descent minimisation [Kass et al., 1987]. When the boundary conditions of Eq. (2.19) are given by two separate end points of the curve, the shape of the curve is a straight line. Otherwise, the snake shrinks to a point when the boundary conditions are given by a closed curve [Toennies, 2012].

Since the curve $v(s)$ can be defined as a finite number of locations $0 \le s_1 < s_2 < ... < s_n < 1$, an iterative scheme for the optimisation of the active contour model can be developed. If a node position $v(s)$ vary with time, the location at time t is $v(s,t)$ with $v(s,t) = (x(s,t), y(s,t))$. The active contour stops moving if a local minimum of the energy function has been found ($x(s,t+1) - x(s,t) = 0$ and $y(s,t+1) - y(s,t) = 0$). Thus, the current point $v(s,t+1)$ on the curve can be estimated from the previous point $v(s,t)$ using gradient-descent minimisation:

$$v(s,t+1) = v(s,t) - \gamma \nabla E(v(s,t)) \tag{2.20}$$

Here, γ controls the size of step at each iteration. $\nabla E(v(s,t))$ is the gradient of the energy function of the point s at time t. It can be denoted as:

$$\nabla E(v(s,t)) = \{\nabla E(v(x_1,y_1,t)), ..., \nabla E(v(x_n,y_n,t))\} \tag{2.21}$$

A drawback of the active contour is that the energy function has many local minima. It is not guaranteed that the iterative procedure fits the active contour to the desired object boundary. Hence, most active contour methods require the user to place the model contour sufficiently close to the object to be segmented.

Applications of snakes to segment lumen border in IVUS and IVOCT datasets can be found in section 3.1.2 and section 3.2.2.

2.5   Atlas-based Segmentation

In general, an atlas incorporates the locations, shapes of anatomical structures and the spatial relationships between the structures. An atlas can, for example, be generated by manually segmenting a selected image (single atlas). It can also be obtained by integrating information from multiple segmented images, for example from different atlases. Given an atlas, an image can be segmented by mapping its coordinate space to that of the atlas in an anatomically meaningful way, a process commonly referred to as registration. Labeling an image by mapping it to an atlas is consequently known as atlas-based segmentation, or registration-based segmentation. The idea is that, given an accurate coordinate mapping (registration) from the image to the atlas, the label for each image voxel can be determined by looking up the structure at the corresponding location in the atlas under that mapping. Obviously, computing the image registration between the image and atlas is the critical step in any such method.

Atlas-based segmentation strategy includes four different types: segmentation with one single atlas, segmentation with the most similar atlas, segmentation with an average shape atlas and simultaneous segmentation with multiple atlases. A schematic graphical comparison of the four types is shown as Figure 2.1.

A straightforward strategy is to use one individual atlas. The atlas selected in this strategy can be random or based on image quality, lack of artifacts or normality of the imaged subject (Fig-
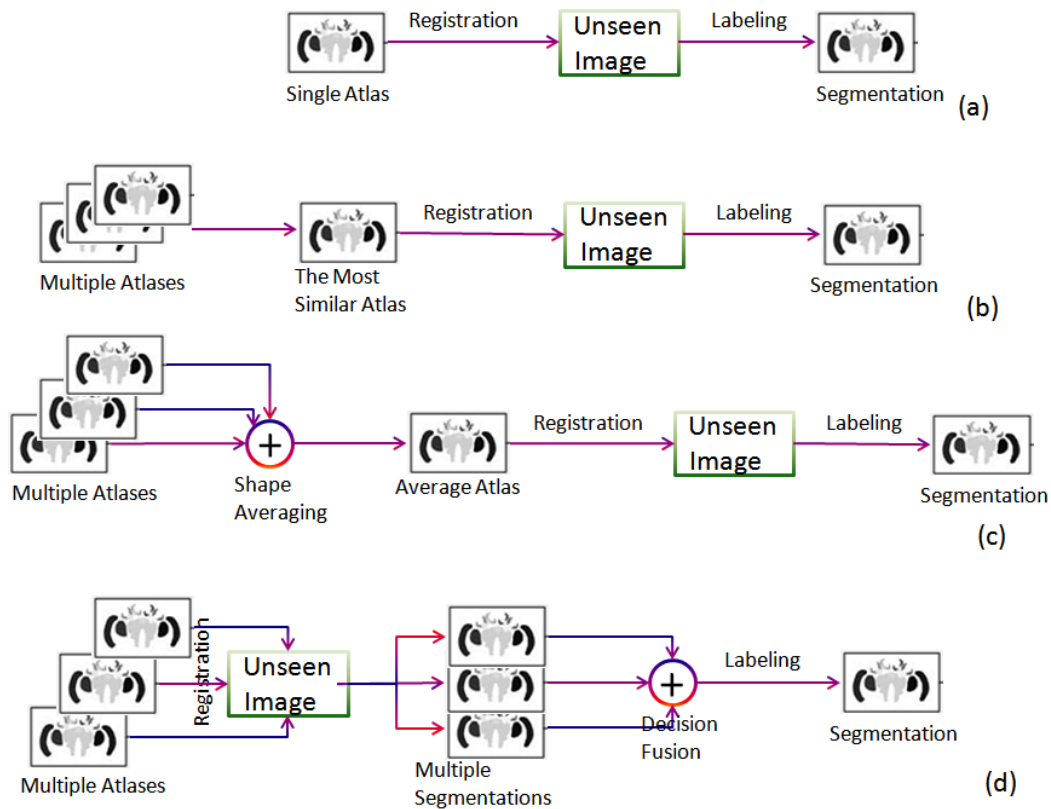
Figure 2.1: Atlas-based segmentation with (a) a single atlas, (b) the most similar atlas from atlases, (c) an average shape atlas obtained from shape averaging of atlases and (d) multiple atlases. From [Rohlfing et al., 2005].

ure 2.1(a)). If the atlas is derived from an individual subject, segmenting other subjects using this atlas becomes a problem since this atlas may be totally different from the other subjects. A better strategy is to use an atlas that is as similar to as many atlas as possible. Such atlas can be generated by creating an average over many atlases (Figure 2.1(c)).

Instead of using just one random single atlas, one similar atlas can be chosen to provide more reliable segmentations. For each image that we are segmenting, there is one atlas that will produce the best segmentation accuracy among all available atlases (Figure 2.1(b)). To select the most similar atlas, image similarity can be expressed using a variety of metrics including sum of square differences (SSD), cross-correlation (CC), mutual information (MI) and normalized mutual information (NMI) [Hajnal et al., 2001]. We briefly describe these measures in the next few paragraphs.

Given two images, a reference I_R and a source I_S, and a transformation $\mathbf{T}$, the similarity of two images can be measured by the sum of the intensity differences at each corresponding voxel

location x over the image domain Ω. Assuming $I_R(x)$ denotes the image intensity of the voxel x in the reference image, $I_S(\mathbf{T}(x))$ is the intensity of the transformed voxel position $\mathbf{T}(x)$ in the source image, the SSD of two images is defined as:

$$S_{SSD} = \sum_{x \in \Omega} (I_R(x) - I_S(\mathbf{T}(x)))^2 \tag{2.22}$$

If the two images are exactly the same, this metric will have the minimum value of zero.

CC assumes that a linear relationship exists between the intensity values of corresponding voxels in the two images. It is defined as:

$$S_{CC} = \frac{\sum_{x \in \Omega} (I_R(x) - \overline{I_R}) \cdot (I_S(\mathbf{T}(x)) - \overline{I_S(\mathbf{T})})}{\sqrt{\sum_{x \in \Omega} (I_R(x) - \overline{I_R})^2} \cdot \sqrt{\sum_{x \in \Omega} (I_S(\mathbf{T}(x)) - \overline{I_S(\mathbf{T})})^2}} \tag{2.23}$$

where $\overline{I_R}$ and $\overline{I_S(\mathtt{T})}$ represent the mean intensities of the two images. If the two images are more similar, the value of CC increases. However, this metric is sensitive to local differences of the brightness and the contrast in the two images.

Instead of comparing voxel intensities directly, mutual information [Viola and Wells, 1995, Collignon et al., 1995] (MI) measures how much information one image contains about the other instead of comparing voxel intensities directly. It is based on marginal entropy of each image and the joint entropy of the image pair. The marginal entropy of an image I is defined as:

$$H(I) = -\sum_{i \in I} p(i) \log p(i) \tag{2.24}$$

Here $p(i)$ is the probability of voxels with intensity i appearing in image I. The joint entropy of two images I_S and I_R is given by

$$H(I) = -\sum_{i_R \in I_R} \sum_{i_S \in I_S} p(i_R, i_S) \log p(i_R, i_S) \tag{2.25}$$

Here $p(i_R, i_S)$ is the joint probability density function of images I_R and I_S and i_R, i_S represent intensity respectively. When the anatomical structures in two images are similar, the joint

entropy decreases. Thus, the mutual information of two images is denoted as:

$$S_{MI} = H(I_R) + H(I_S) - H(I_R, I_S) = \sum_{i_R \in I_R} \sum_{i_S \in I_S} p(i_R, i_S) \log \frac{p(i_R, i_S)}{p(i_R) \cdot p(i_S)} \qquad (2.26)$$

If the information that one image contains about the other one increases, the mutual information also increases. To normalise the probability in $[0, 1]$, NMI [Studholme et al., 1999, Pluim et al., 2003] has been proposed:

$$S_{NMI} = \frac{H(I_R) + H(I_S)}{H(I_R, I_S)} \qquad (2.27)$$

When the normalised mutual information increases, one image contains lots of information about the other one.

The last group of atlas-based segmentation is multi-atlas based segmentation (Figure 2.1(d)). We can look at an atlas combined with a coordinate mapping from an unseen image as the output of a classifier. The input of the classifier is a coordinate within the domain of the unseen image. The classifier output, determined internally by transforming that coordinate and looking up the label in the atlas at the transformed location, is the label that the classifier assigns to the given unseen image coordinate. We will discuss this multi-atlas based segmentation in the next section in more detail.

Atlas-based segmentation method has been successfully applied in cardiac imaging [Lorenzo-Valdes et al., 2004, Zhuang et al., 2010]. The construction of an atlas of the heart can be based either on the segmentation of a single individual [Lorenzo-Valdes et al., 2002, Zhuang et al., 2010] or on a probabilistic model, usually representing the average segmentation obtained in a population of subjects [Lorenzo-Valdes et al., 2003, Lorenzo-Valdes et al., 2004]. For example, [Lorenzo-Valdes et al., 2002] proposed to construct a subject-specific atlas for each subject from the end diastolic phase and propagate this atlas to all other cardiac phases of the same subject. A non-rigid registration [Rueckert et al., 1999] was used to accomplish this purpose. The process is illustrated in Figure 2.2. The limitation of this work is that the subject-specific atlas can only be applied to images from the same subject. Hence, this approach is not fully automated.
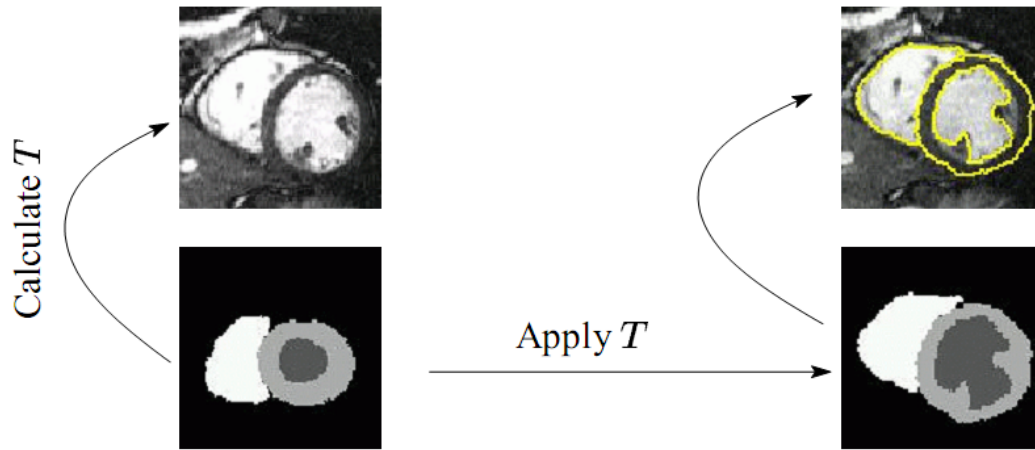
Figure 2.2: Atlas based segmentation by calculating the transformation T between the atlas and an image and then apply T to deform the atlas. From [Lorenzo-Valdes et al., 2002].

[Lorenzo-Valdes et al., 2003, Lorenzo-Valdes et al., 2004] proposed an approach that used a probabilistic atlas to initialise as tissue classification based on the EM algorithm. It is notable that the probabilistic atlas used is a 4D spatio-temporal atlas. The purpose of using the probabilistic atlases is to automatically estimate the initial parameters (mean and variance) for each class (structure) and to provide spatially and temporally varying a-priori information about the likelihood of different anatomical structures. This spatial alignment corrects for differences due to position, size and orientation of the anatomy. The probabilistic atlases have been constructed by blurring the segmented image corresponding to each structure with a Gaussian kernel and subsequent averaging. The segmentation obtained after convergence of the EM algorithm is refined to integrate spatial information through a MRF.

The atlas-based segmentation approaches presented above are more flexible compared to deformable models. A single registration from the atlas to an unseen image is required to obtain segmentation. However, the registration may fail if the anatomy in the unseen image is too different from the anatomy in the atlas in terms of morphology. In some cases, the registration may also fail if the anatomy in the unseen image contains some pathological changes that lead to locally varying image contrast. For example, the intensities in the myocardium can change due to infarction. Both of these difficulties may cause errors in the resulting registration between the atlas and the unseen image.

2.6   Multi-atlas and Patch-based Segmentation

To overcome the problems of the atlas-based segmentation discussed above and to make the segmentation more robust, [Rohlfing et al., 2004, Heckemann et al., 2006, Aljabar et al., 2009] proposed segmentation methods by using different atlases. Each atlas is registered to the unseen image and the resulting segmentations are then fused into a consensus segmentation. It has been recently shown that using multiple atlases can yield more accurate results for the segmentation of brain MRI [Artaechevarria et al., 2009], neck images [Han et al., 2008] and aortic images [Isgum et al., 2009].

Figure 2.3 represents a multi-atlas based segmentation framework that includes three steps: Firstly, the atlas selection step will select a subset of atlases that are most similar to the subject in order to reduce complexity and increase robustness. Secondly, the atlas propagation step will propagate the selected atlases to the unseen image using affine and/or non-rigid registration. Finally, the decision fusion step is used to combine the segmentations from multiple atlases into a final segmentation of the unseen image. If the number of atlases equals to one or the atlases are fused into an average image, the framework can be reduced to the single atlas-based segmentation method.

In the selection step, [Aljabar et al., 2009] proposed to use a subset of the most similar atlases during the atlas selection step. The authors showed that selecting the most similar subset of atlases for each unseen subject provides more accurate subcortical segmentations than those using a non-selective combination of random atlas subsets or all atlases. In their work, the selection is based on an image similarity measure between the atlas and the unseen image. The results suggest that the multi-atlas segmentation performs better than single atlas-based segmentation.

In the fusion step, fusion strategies such as global weighted voting (majority voting and weighted voting) or locally weighted voting can be used. The majority voting method [Kittler et al., 1998] counts the votes for each label from each warped atlas and chooses the label receiving the most
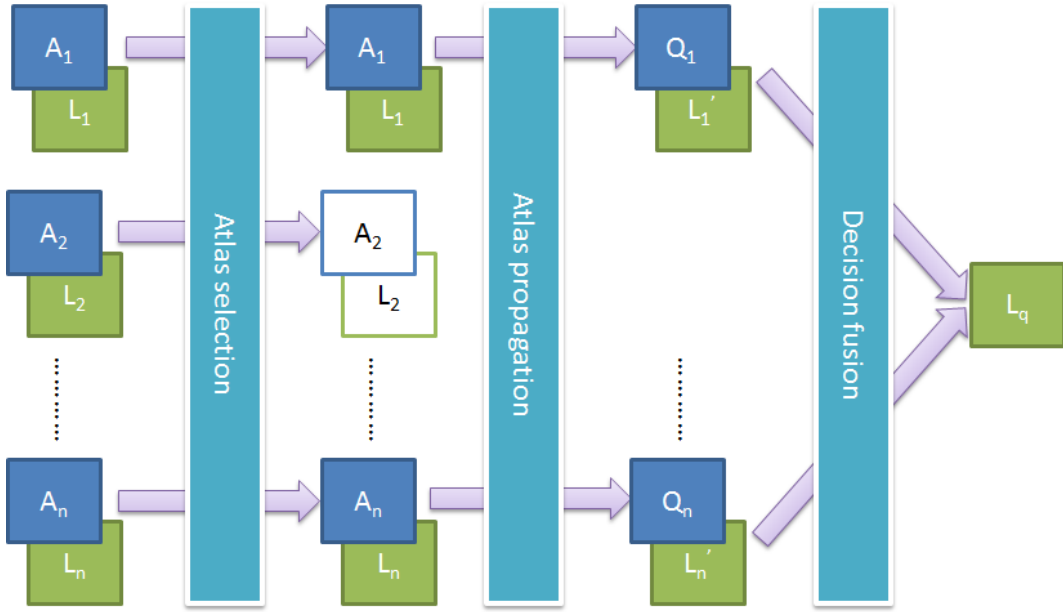
Figure 2.3: The framework of the multi-atlas segmentation. From [Shi, 2012]. It includes atlas selection, non-linear propagation and decision fusion.

votes to produce the final segmentation $\hat{S}_T$:

$$\hat{S}_T(x) = \arg \max_{l \in 1...L} \sum_{i=1}^{n} S_i^l(x) \tag{2.28}$$

Here l indexes through labels and L is the number of all possible labels; x indexes through image pixels. $S_i^l(x)$ is the vote for label l produced by the i-th atlas, defined by:

$$S_i^l(x) = \begin{cases} 1, & \text{if } S_i(x) = l \\ 0, & \text{otherwise} \end{cases} \tag{2.29}$$

The majority voting is the most frequently used approach in papers including [Rohlfing et al., 2004, Heckemann et al., 2006, Aljabar et al., 2009]. [Rohlfing et al., 2004] proposed to use registration to unseen images from a database of individual atlas images with subsequent multi-classifier decision fusion. The multi-classifier decision fusion strategy used in the paper is a majority voting with a partial volume interpolation. [Heckemann et al., 2006] showed that multi-atlas segmentation performs at levels of accuracy approaching those of expert human raters in terms of the Dice overlap [Dice, 1945] values obtained. The Dice overlap (Eq. (2.30)) is a measure computed by using different areas that include automatically segmented (Aa),

manually segmented (Am), and their intersection (Aam). The value of Dice is between 0 and 1. The higher Dice value indicates a better match between automatic and manual segmentations.

$$Aam = \frac{2\|A_a \cap A_m\|}{\|A_a\| + \|A_m\|} \tag{2.30}$$

Global weighted voting means that the weighting is generated by the similarity between the transformed atlas and the unseen image. Although image similarity does not necessarily correlate with registration accuracy, compared to majority voting, higher accuracy of global weighted voting is achieved [Artaechevarria et al., 2008]. In addition, in global fusion strategies, the weights for the different atlases are fixed for the whole image. This means that using global weighting is difficult to accommodate partly successful registrations [Artaechevarria et al., 2008].

[Artaechevarria et al., 2009, Commowick et al., 2009, Sabuncu et al., 2010] proposed to use a local weighted voting strategy instead of the global weighted voting. Instead of assigning a single weight to all voxels in the atlas, each voxel can have a different weight. Each voxel between the atlas and the unseen image is weighted by measuring the similarity between the local patches. [Lotjonen et al., 2010] proposed to construct the final segmentation using an EM or GC based optimisation after local weighted voting. The weight is used as a-priori probability for a subsequent EM-based image segmentation. In addition, they proposed to use the intensity differences after intensity normalisation to speed up the registration process which is one of the most time consuming aspects of multi-atlas propagation. The results showed a three-fold improvement in terms of computational speed as well as improved accuracy.

In the atlas propagation step, the registration is usually constrained to ensure one-to-one correspondences between the unseen image and the atlas. This restriction ensures a realistic deformation and preserves the topology of the anatomical structures in the unseen image. However, this also restricts the ability of the registration to capture large, local variations in terms of shape. When the registration fails for small structures, it is likely that the correct correspondence can be found within the local neighbourhood. Unfortunately, most decision fusion strategies mentioned above cannot deal with these residual mis-registrations between

the images and the atlas.

To address this short-coming, [Coupe et al., 2011] proposed a non-local patch-based approach during the decision fusion step. Here, "non-local" denotes that the weight of a patch is only dependent on the intensity similarity and it is regardless of its distance to a voxel of interest. The proposed patch-based method achieves the labeling of each voxel individually by comparing the patch surrounding at this voxel with other patches in atlases within a certain spatial neighbourhood. Using this method, several patches from each atlas can be used during the decision fusion. This enables a large increase in the number of sample patches and reduces the influence of registration errors. The authors used the local weighted fusion with intensity similarity after intensity normalisation. The proposed patch-based approach outperforms the above multi-atlas based methods for the segmentation of small structures like the hippocampus in terms of segmentation accuracy. More recently, [Bai et al., 2012] proposed a method using the idea of patch-based segmentation [Coupe et al., 2011] to reduce the registration errors in the multi-atlas based RV segmentation.

2.7   Summary

This chapter has presented a review of segmentation techniques that are relevant to this thesis. We reviewed the Hessian-based filter, the EM algorithm and the GC approach in the sections of intensity enhancement methods and intensity-based segmentation methods, respectively. Deformable model based segmentation methods, atlas-based segmentation and multi-atlas based segmentation are presented as well. The works reviewed in this chapter form the basis of our work developed in the following chapters.

The next chapter specifically reviews some segmentation approaches used in IVUS, OCT and IVOCT modalities. We utilise these approaches to build our proposed frameworks for lumen border segmentation, stent struts detection and neointima segmentation in chapter 4- 6.

Chapter 3

Image Segmentation in Intravascular Ultrasound and Optical Coherence Tomography

Narrowing of coronary arteries (atherosclerosis) may reoccur after balloon angioplasty, atherectomy or bypass surgery and the accurate diagnosis of vulnerable plaques and their thickness are critical. A reason that makes atherosclerosis one of the deadliest disease is not the stenosis alone but the failure of the detection and proper treatment of the vulnerable plaques that will lead to AMI [Katouzian et al., 2012]. Therefore, imaging modalities such as IVUS, IVOCT and NIR signals [Binder, 2002] have been developed to characterise atherosclerotic plaque components, distinguish the thickness of plaques and identify vulnerable ones.

In this chapter, we review state-of-the-art segmentation algorithms that detect either both the vessel wall (media adventitia (MA)) and the lumen borders simultaneously or one of them. Automatic detection of the vessel wall and the lumen borders is required to quantify the degree of stenosis and measure the lumen area in which blood flows in IVUS and IVOCT. Generally, IVUS and IVOCT catheters are advanced into the left or right coronary artery and possibly in some side-branches using a guide-wire coming out of a guiding catheter inserted in the femoral artery. Acquisition of cross-sectional ultrasound/optical images of the RCA, LCA, and LCX
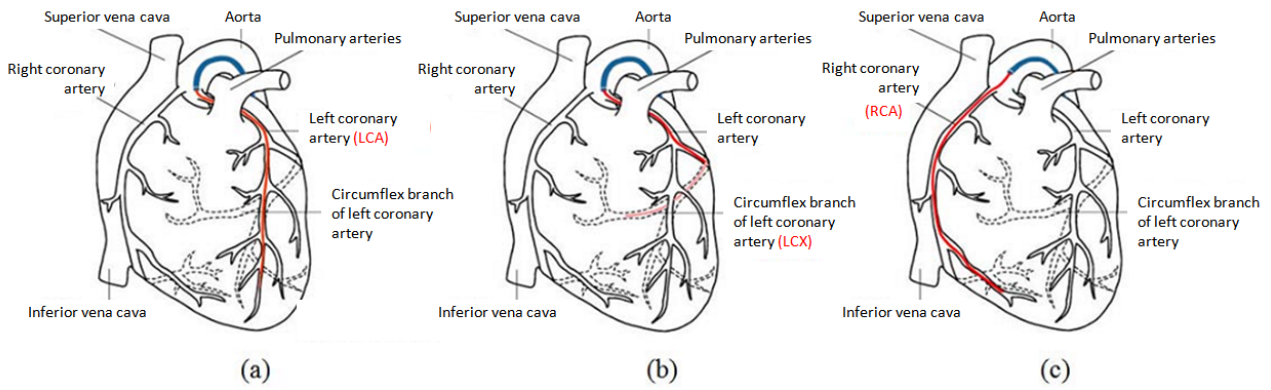
Figure 3.1: Schematic illustration of advanced catheter (red) into (a) LCA (b) LCX and (c) RCA. From [Katouzian et al., 2009].

coronary arteries (Figure 3.1) can be performed with a rotating single-element transducer or a phased array transducer. In addition, we review some segmentation approaches that are used in Ophthalmology to characterise clinically important features such as damage to the fovea and optic nerve. These methods can be categorised based on their clinical application, the domain of analysis, the transducer center frequency, dimensionality and underlying image processing framework.

3.1 Review of Lumen Border Segmentation in Intravascular Ultrasound

The invention and proliferation of IVUS imaging has been introduced for in-vivo assessment of coronary atherosclerosis [Katouzian et al., 2012]. The lumen border is at the innermost surface of atherosclerotic plaques. The illustration of structures such as blood, tissues and plaques in the artery reflect sound waves differently because of differences in density (Figure 3.2) [Kimura et al., 1995].

To detect the lumen border, researchers have developed several algorithms which will be discussed in the next few subsections.
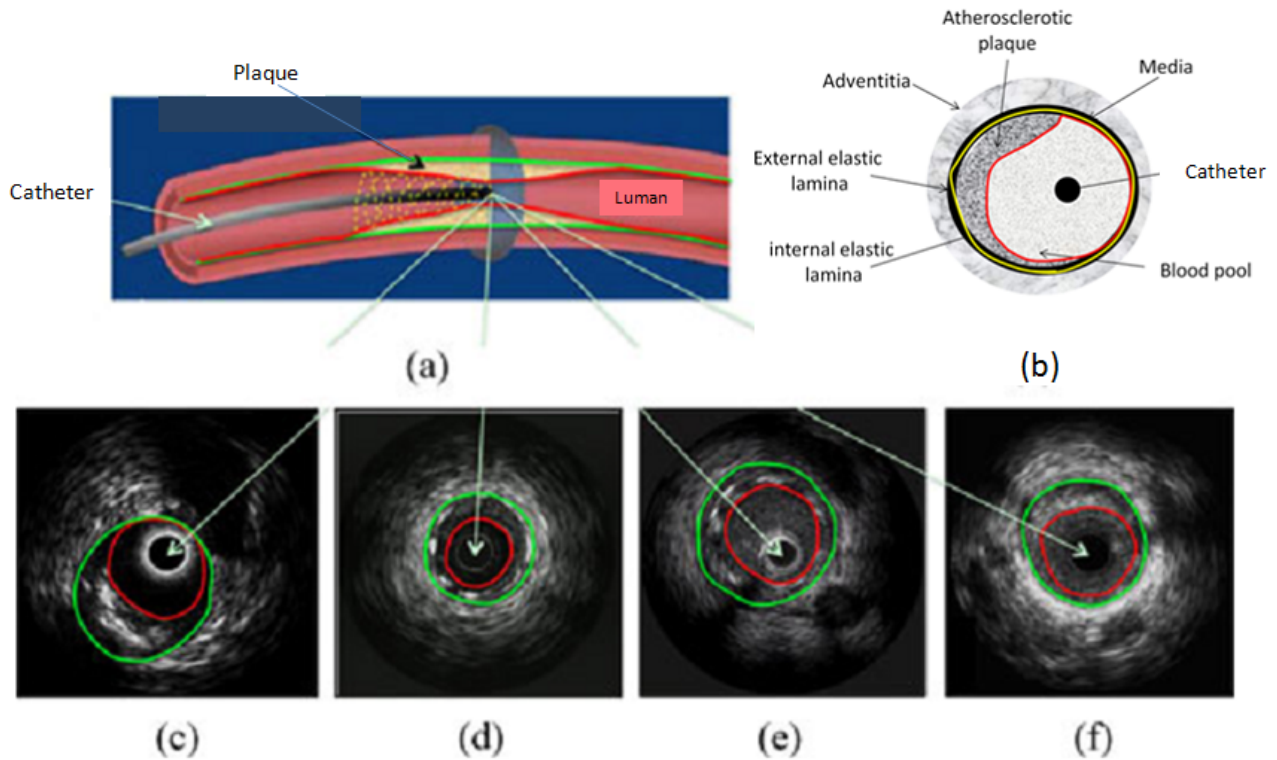
Figure 3.2: (a) Schematic of an artery, catheter, atherosclerotic plaque, and a cross-sectional IVUS image. The yellow spiral dashed line depicts the trajectory of transducer scan lines. (b) Cross-sectional diagram of the anatomy of the arterial wall. Four distinct IVUS frames acquired with (c) 20-MHz, (d) 30-MHz, (e) 40-MHz, and (f) 45-MHz transducers. Green and red borders represent the vessel wall and lumen borders, respectively. From [Katouzian et al., 2012].

3.1.1 Edge-Tracking and Gradient-Based Techniques

The first category of the segmentation approaches is edge-tracking and gradient-based techniques. Edges of the vessel wall and lumen borders in IVUS rarely represent clean borders due to scattering effects within the lumen, discontinuities in intensities and image noise. Hence, further refinement (e.g., smoothing for noise reduction) and hybrid algorithms have been designed to assemble edge features into desirable target boundaries (boundary enhancement).

The IVUS segmentation techniques usually require precise initialisation and rely on an energy minimisation framework. Herrington et al. [Herrington et al., 1992] developed the first semi-automatic algorithm based on such a principle. Later, Sonka et al. [Sonka et al., 1995] introduced one of the earliest comprehensive approaches for the detection of the internal and
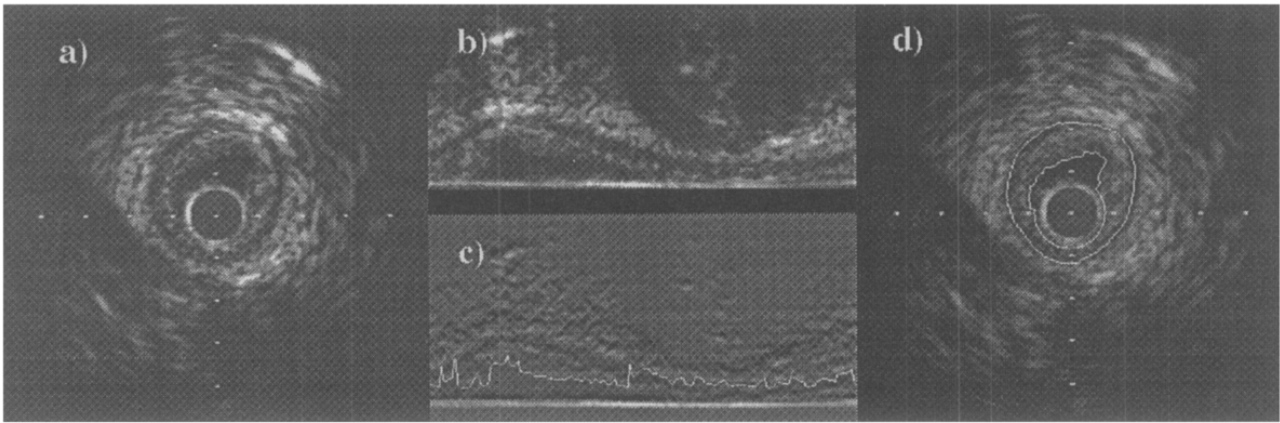
Figure 3.3: IVUS images with a 30 MHz, 1.17mm diameter intracoronary IVUS catheter depict the stages of segmentation process in [Meier et al., 1997]. (a) the original image, (b) polar transform, (c) the gradient image of polar transform with segmented but unfiltered luminal outline and (d) the resulting luminal and medial-adventitial outlines in Cartesian coordinates after post-processing. From [Meier et al., 1997].

external elastic laminae borders as well as lumen borders. The cost functions for each border were minimised by using a graph-search technique [Sonka et al., 2007] and incorporated a-priori knowledge such as shape models and edge patterns. [Li et al., 1994, von Birgelen et al., 1996] presented a similar semi-automatic methodology using dynamic programming to find the optimal path within the vessel and detect both MA and lumen borders in polar coordinates from delineated contours. The minimum cost path search was performed between end points interactively selected in reconstructed longitudinal images at the intersection of two perpendicular cut planes.

Meier et al. [Meier et al., 1997] proposed a fully automatic segmentation method for the detection of both MA and lumen borders along the circumferential direction in polar coordinates. Speckle noise reduction by applying iterative nonlinear spatial median filters was also presented in their work. Three different segmentation techniques were applied to detect the lumen borders: 1) thresholding of gradient maps obtained by convolving the polar image with gradient kernels in the radial direction; 2) adaptive region growing from a seed point (after the detection of the catheter); and 3) the deformation of a gradient-based parametric deformable model to search for connected outline points and detect the MA borders. Post-processing was required to remove the remaining outliers and refine the final segmentation (Figure 3.3).

The main limitation of the above mentioned methods is the difficulty of processing curved

vessels or a vessel that does not appear as horizontal in an image.

3.1.2 Active Contour-Based Techniques

Katouzian et al. [Katouzian et al., 2012] reported that active contours have been widely used in many medical image segmentation applications and most of the IVUS studies adopted the traditional formulation of a parametric snake [Kass et al., 1987, Williams and Shah, 1997]. The parametric model formulation is more intuitive and better suited for IVUS border detection applications since the topology of the boundaries is simple and therefore the underlying parametrisation remains simple and computationally efficient.

Due to the intrinsic non-vessel image features (the presence of guide-wires, calcified plaques, side branches and motion artifacts from the catheter and the heart), the vessel borders are not well distinguished in IVUS image, since the features obstructs the direct application of the classical deformable model. A fine-tuning of parameters and an accurate initialisation are required when ordinary features such as image gradients and intensities, which are sensitive to noise, are employed.

Several approaches have been proposed to overcome these drawbacks by modifying the energy terms or incorporating pre-processing techniques prior to the use of a deformable model. For example, Kovalski et al. [Kovalski et al., 2000] removed the elasticity term from the internal energy. To control the smoothness of the contour, they introduced a-priori information on the final desired shape via regularisation along the longitudinal direction, and a balloon force to control the motion only along the radial direction. The contours evolved towards the features of interest driven by intensity-based external forces. Finally, they extended the algorithm to 3D for the automatic detection of MA and lumen borders.

The authors in [Shekhar et al., 1999] developed a semi-automatic 3D segmentation framework, an active surface model (an extension of a 2D digital dynamic model technique [Lobregt and Viergever, 1995]), for the detection of both borders. The internal force consisted of distinct tangential and radial components derived from the corresponding transverse and longitudinal
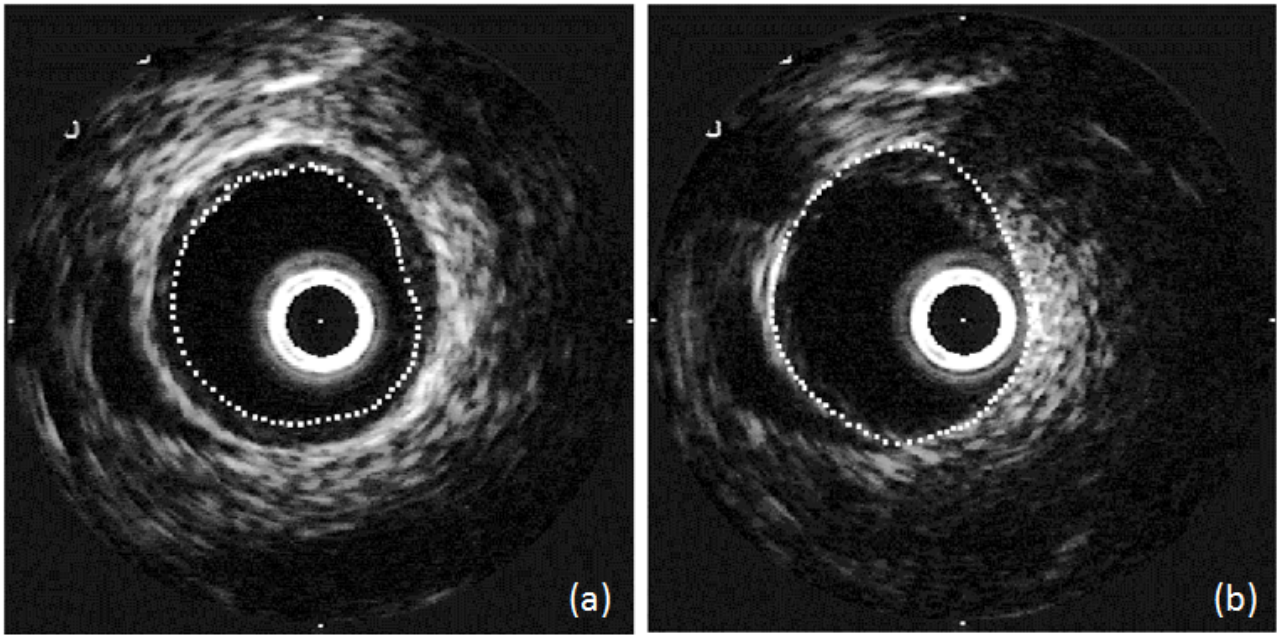
Figure 3.4: Segmentation examples from [Shekhar et al., 1999] showing (a) the luminal border and (b) the adventitial border in two different datasets with 30 MHz transducers.

curvature vectors. The external force was based on the gradient of a 3D potential field defined by convolving the image volume with a 3D Sobel-like kernel. A damping force was used to control the convergence of the model to its final shape. The algorithm required user intervention to initialise the template every other frame. The results demonstrated robust segmentation with negligible variability (Figure 3.4).

3.1.3   Statistical- and Probabilistic-Based Techniques

Statistically driven approaches are generally based on the assumption that intensities corresponding to lumen and plaque (intima) regions are generated from two different distributions of reflectors. These approaches can be modeled parametrically (e.g. using Rayleigh or mixture of Gaussians probability density functions (PDFs)) [Haas et al., 2000, Zhu et al., 2002, Brusseau et al., 2004, Cardinal et al., 2005, Pujol and Radeva, 2002] or non-parametrically [Unal et al., 2008].

In many cases, this is a valid assumption to differentiate blood (speckles) from tissue and to detect the lumen borders. The authors in [Gil et al., 2000b, Gil et al., 2000a] took advantage

of this property and developed the very first region-based technique for detection of the lumen borders by thresholding in polar coordinates. They incorporated the probabilities of intensities that correspond to lumen and non-lumen areas into a deformable model framework, generated corresponding edge images, and delineated borders automatically in Cartesian coordinates with elliptical shape constraints.

Haas et al. [Haas et al., 2000] modeled the expected contour in 3D with a-priori knowledge using Markov processes [Besag, 1974]. The final contour and parameters associated with the Rayleigh distribution were found in an iterative fashion employing a maximum a posteriori (MAP) estimator. A Rayleigh distribution can model the gray level distribution of the ultrasonic speckle pattern in a uniform scattering tissue in B-mode imaging where B-mode imaging represents a cross-sectional image [Wagner et al., 1983]. Similarly, Brusseau et al. [Brusseau et al., 2004] used a Rayleigh model for the image intensity appearance and estimated the final contour position with a MAP estimator and a constraint on the first zero crossing of image derivatives. The presented technique was fully automatic for 2D images. The possibility of extension of the algorithm to 3D was also studied by propagating 2D contours between adjacent frames.

Cardinal et al. [Cardinal et al., 2006] modeled the intensities in IVUS pullback images as a mixtures of Rayleigh PDFs corresponding to the lumen, the intima, the media and the adventitia. They incorporated this mixture model into an extension of the fast-marching framework [Sifakis et al., 2002] for multiple-front propagation. They initialised the regions from manually traced lumen and media borders in several frames on longitudinal image planes. Then, the initialised fronts propagated with different speeds proportional to each PDFs. The unknown PDFs parameters were estimated via the EM algorithm. The authors evaluated the algorithm performance with different initialisations and in comparison with a 3D gradient-based fast-marching technique. Statistical analysis was then performed by comparing automatic lumen and MA borders with corresponding manual ones for every other frame. The analysis demonstrated the robustness of the proposed methodology and obtained small Hausdorff distances with different initialisations.

The authors in [Mendizabal-Ruiz et al., 2008] also presented a 2D semi-automatic approach using a parametrisation of the lumen region with a mixture of Gaussian PDFs to smooth the lumen contour. The curve was then deformed through the optimisation of a Bayesian cost function, comprising likelihoods of intensities corresponding to blood and non-blood regions. A-priori information corresponding to blood and non-blood areas, in form of normalised histograms computed from manually selected regions, was employed to estimate the likelihood function.

Unal et al. [Unal et al., 2008] presented an automatic 2D algorithm, implemented in a polar coordinate system, which built a statistical shape space through principal component analysis (PCA). Once the shape space was built, an initial contour was obtained by a region-based non-parametric probabilistic energy function described in [Paragios and Deriche, 2002]. The authors also estimated the probability distribution inside and outside the lumen using intensity profiles from a training dataset and delineated the lumen borders automatically (see Figure 3.5). For MA border detection, edge information was used to evolve the curve.

3.1.4   Summary

The techniques that were described in this section allow the measurements of lumen and plaque areas, which are required prior to tissue characterisation or balloon angioplasty and stent implantation. The intensity distributions corresponding to blood and non-blood regions in images acquired with low-frequency transducers (20-30 MHz) are assumed to be separable. In such a situation, a thresholding-based technique with empirically tuned values [Taki et al., 2008] outperforms more sophisticated algorithms (such as methods in [Unal et al., 2008, Katouzian et al., 2010]). However, this assumption is no longer valid for images acquired with high-frequency transducers (40 MHz and above) because the separation between blood and non-blood intensities vanishes when the transducer centre frequency increases [Katouzian, 2011]. Among these methods, parametric active contours have also been used in IVOCT lumen border segmentation. The discussion is presented in section 3.2.2.
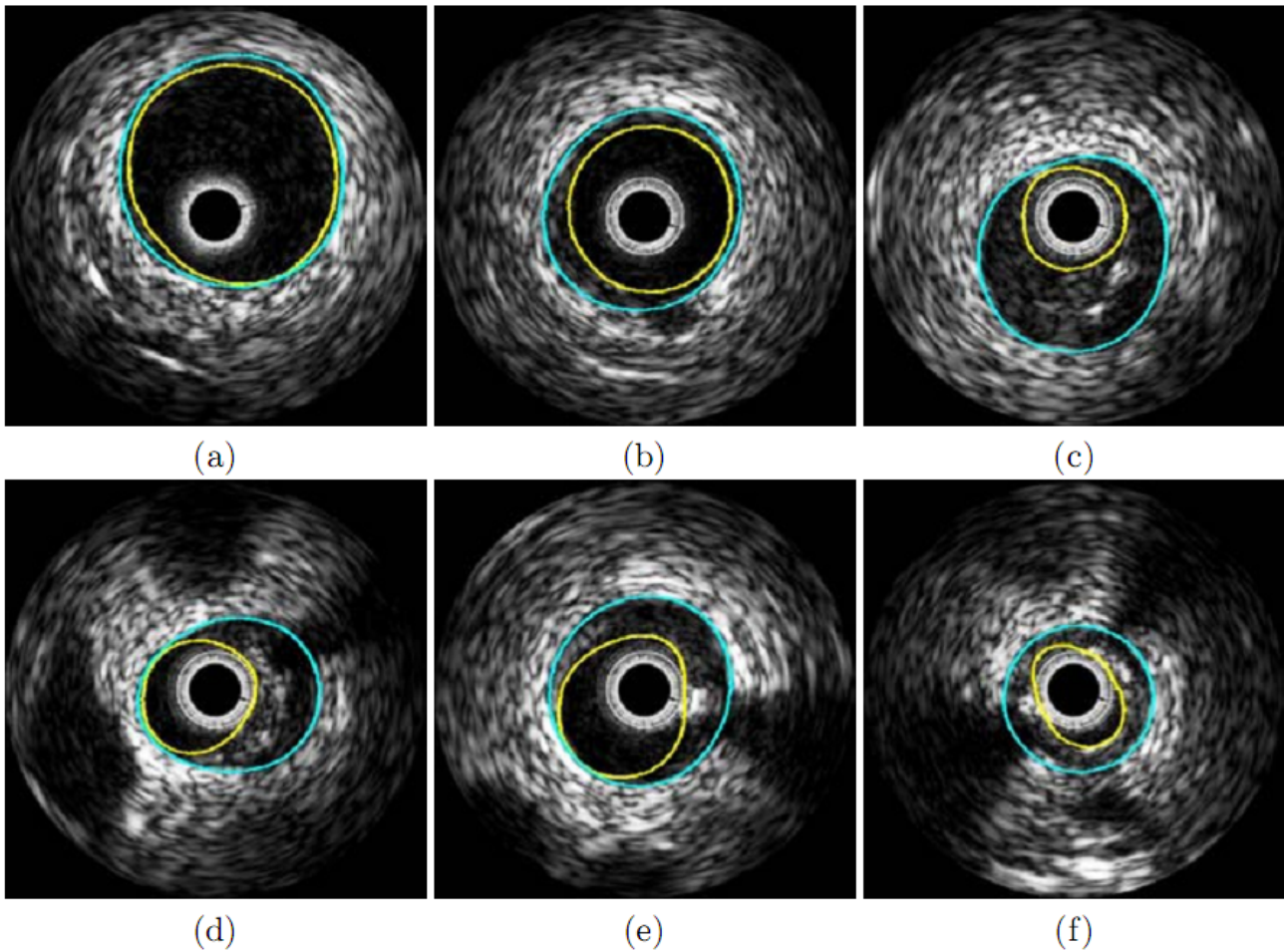
Figure 3.5: Six examples (using a 20 MHz transducer) of automatically computed lumen and media/adventitia contours, including the cases of (a) healthy artery without plaque (b) catheter (c) small lumen with spurious noise between lumen and media/adventitia and (d)-(f) calcification with shadows. From [Unal et al., 2008].

3.2 Review of Image Segmentation in Optical Coherence Tomography

OCT is a non-invasive and non-contact imaging technique. It is used in many different biomedical applications, with retinal imaging being the most successful application for which numerous commercial instruments are on the market. It can be used to obtain detailed images from within the retina [Fercher et al., 2003] and characterise clinically important features (e.g. damages to the fovea and optic nerves) in Ophthalmology [DeBuc, 2011]. For instance, glaucoma is characterised by the progressive loss of ganglion cells and axons in the retinal nerve fiber layer (RNFL). Thus, the thickness of the RNFL reduces and leads to peripheral and subsequently

central vision loss [Cabrera-Fernandez et al., 2005].

IVOCT is a catheter-based, invasive and OCT imaging technique that has been used in interventional cardiology to help diagnose certain types of CHD [Bezerra et al., 2009]. Segmentation approaches for IVOCT images are normally used to segment the lumen border and to detect stent struts. Therefore, in this section, we review segmentation approaches that are used in IVOCT and applications of OCT in Ophthalmology.

3.2.1   OCT Segmentation in Ophthalmology

Intensity-Based Methods

Lee et al. [Lee et al., 1995] proposed the first segmentation method based on intensity difference to measure retina and RNFL thickness. They used a 1D edge detection [Marr and Hildreth, 1980] method to compute the derivative of the reflectivity versus axial distance for each A-scan in an OCT image. In [Koozekanani et al., 2001], the authors introduced a MRF model for extracting the inner and outer retinal boundaries from radial scans of the macula. The problem of this model is that it simply relies on connecting 1D points, which makes it sensitive to noise.

Herzog et al. [Herzog et al., 2004] proposed a method to automatically extract the optic nerves and retinal boundaries from axial OCT scans through the optic nerve head (ONH). The boundaries are obtained by maximising the number of edges that lie on the boundary while minimising the boundary's average rate of change. In general, the algorithm identified the correct vitreal-retinal boundary in the images except in regions where the OCT signal was severely attenuated due to shadowing.

Shahidi et al. [Shahidi et al., 2005] segmented three retinal segments by using a simple search of peaks corresponding to high- and low-intensity bands. A modified median filter and an adaptive thresholding method based on the reflectivity histogram of each A-scan line to segment four layer structures within the retina was used in [Ishikawa et al., 2005]. The authors in [Ishikawa et al., 2005] mentioned that the thicknesses of the innermost layers in the macula had diagnostic
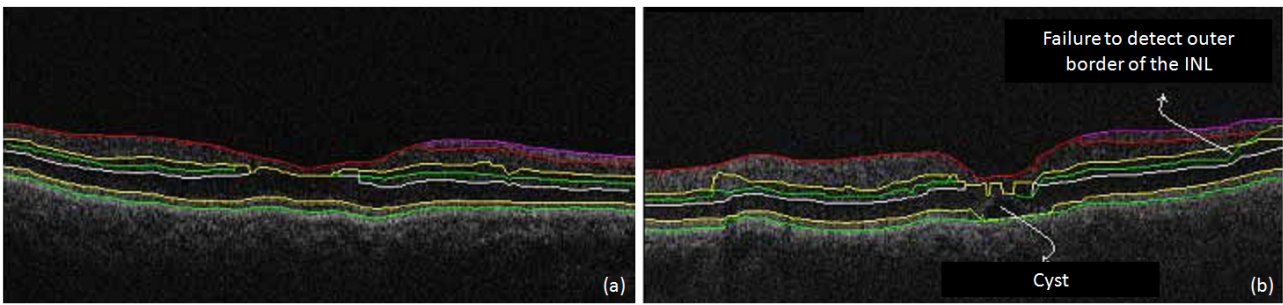
Figure 3.6: (a) The automatic segmentation algorithm is able to extract the 7 cellular layers in Glaucomatous case and (b) the algorithm is able to fairly extract the cellular layers in almost the whole macula except in the region enclosing the cyst where the layer structure is totally corrupted by the presence of abnormal fluid. From [Cabrera-Fernandez et al., 2005].

power comparable with that of RNFL in glaucoma studies. Using a 2D gradient approach in a dynamic programming framework confirmed that glaucoma primarily affected the thicknesses of the inner retinal layers (RNFL, ganglion cell layer and inner plexiform layer) in the macula was proposed in [Tan et al., 2008].

Cabrera-Fernandez et al. [Cabrera-Fernandez et al., 2005] used diffusion filtering [Gilboa et al., 2004] to reduce speckle noise without blurring retinal structures. A peak finding algorithm based on local coherence information of the retinal structure was used to determine seven intraretinal layers in an automatic/semi-automatic framework (Figure 3.6).

A different approach based on active contour models has been used to quantify structural irregularities in OCT retinal images. Cabrera-Fernandez et al. [Cabrera-Fernandez, 2005] proposed a method using a nonlinear anisotropic diffusion filter to remove strong speckle noise. A gradient vector flow snake model was also employed to extract fluid-filled regions in the retinal structure. Mujat et al. [Mujat et al., 2005] used deformable splines to assess the thickness of the RNFL. Although all the model parameters were set based on a large number of OCT scans in different retinal areas, a good contour initialisation was still the major problem because the initialisation must be close to the true boundary location. Even though the sensitivity to initialisation was not reported in this study, the approach was highly vulnerable to the existence of blood vessels and other morphological retinal features.

One advantage of this automatic snake methodology was that it was able to provide larger area maps of the RNFL thickness facilitating the correct registration of region of interest with visual
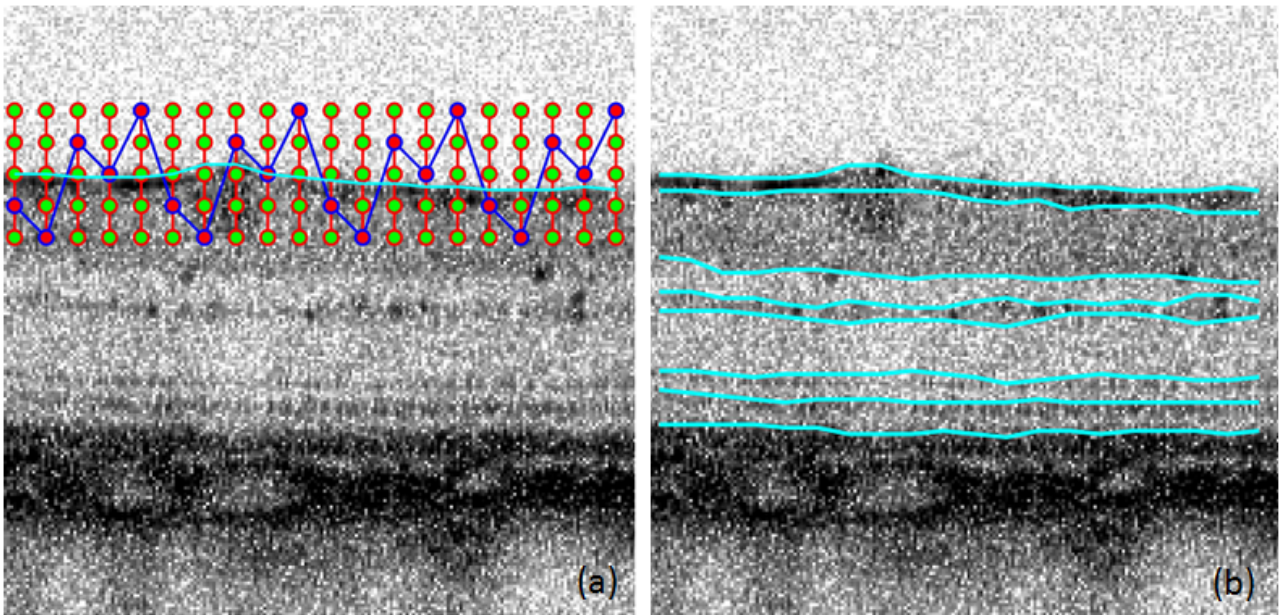
Figure 3.7: (a) Demonstration of the precise layer boundary optimisation step on an OCT image. The dense trellis (red lines with green nodes) for a particular retinal layer is overlaid on the OCT image. Cyan line shows that the approximate location of the retinal layer used as an initial condition for the optimisation. Blue line shows that a possible solution for a retinal layer. (b) The approximate locations of the retinal layers (cyan lines) overlaid on the OCT image. From [Mishra et al., 2009].

field defects which could allow better longitudinal evaluation of RNFL thinning in glaucoma studies. In later work, Mishra et al. [Mishra et al., 2009] also presented a modified active contour algorithm based on a sparse dynamic programming method and a two-step kernel based optimisation scheme. Although this effective algorithm achieved accurate intra-retinal segmentation on rodent OCT images under low image contrast and in the presence of irregularly shaped structural features, results on images including the foveal pit region were not given and no quantitative evaluation using a large data set was provided (Figure 3.7).

In contrast to the edge detection approaches mentioned above, a multi-resolution hierarchical support vector machine (SVM) was used in a semi-automatic approach to calculate the thickness of the retina and the photoreceptor layer along with the volume of pockets of fluid in 3D OCT data [Fuller et al., 2007]. In this approach, the SVM included scalar intensity, gradient, spatial location and the mean of the neighbours as features. Although the SVM method performed well on both healthy and diseased OCT data, a major drawback was that some voxels were misclassified resulting in scattered noise in the thickness maps. In addition, this
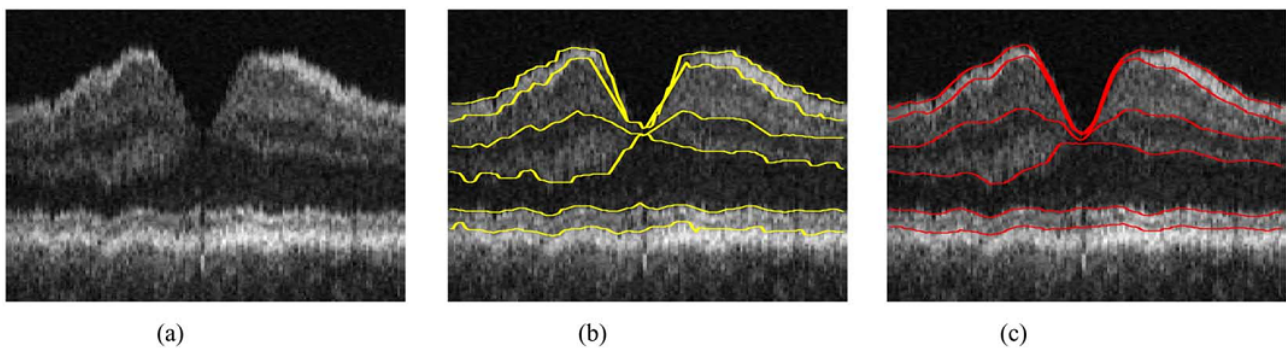
Figure 3.8: (a) An original image; (b) segmented borders; (c) manual segmented layers. From [Garvin et al., 2008].

method required that the user paints the areas of interest in any slice of the volume. Thus, the training data set grew through painting increasing the complexity of the SVM classifier, and as a result more time was required to complete the segmentation task.

Graph-Search Based Methods

A more complex approach to OCT retinal layer segmentation using gradient and intensity information in a 3D context was presented by Haecker et al. [Haeker et al., 2006]. The authors generated a 3D image from radial lines and performed a 3D graph-search [Sonka et al., 2007]. The basic idea of this graph-based approach is to break a graph into paths or fragments, which are utilised as filtering features in graph-search. This approach was further developed into a multilayer segmentation (from 2 layers to multi-layers) [Garvin et al., 2008] showing superior results for high quality OCT data. This graph-search approach potentially increased the accuracy of the segmentation by using weights describing both edge and regional information to segment the volume.

Even though this elegant method can guarantee to find the global minimum when compared to deformable models, its computational complexity can increase the computation time if more complex constraints are required to segment diseased retinal images showing common structural irregularities and a less ideal foveal pit.

Lee et al. [Lee et al., 2010] presented an improved and fully automatic method based on a similar methodology using graph-search combined with a k-nearest neighbour classifier. To
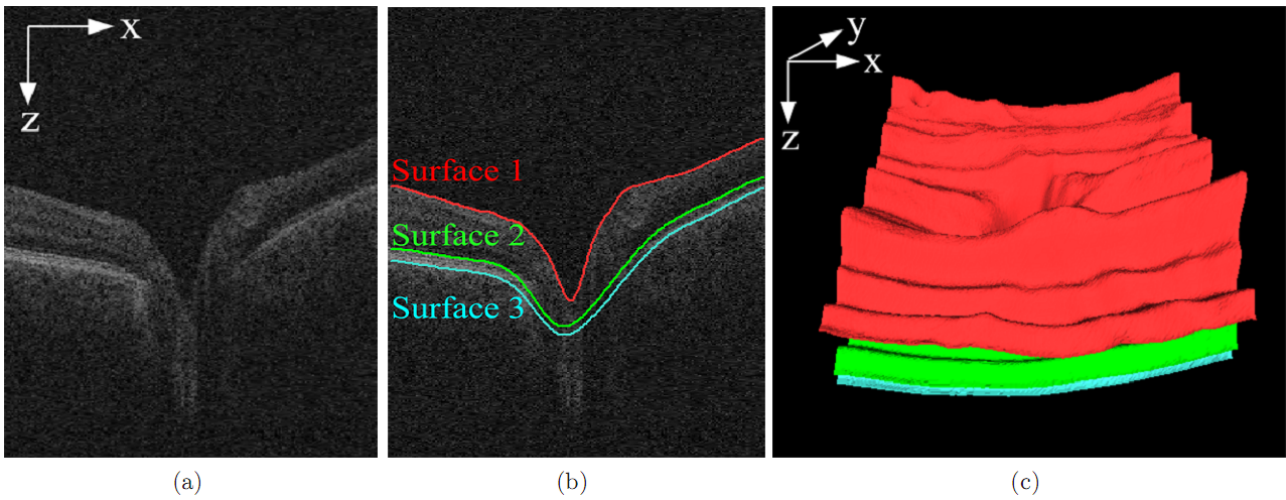
Figure 3.9: (a) X-Z image of the original OCT volume. (b) Segmentation results of 3 retinal surfaces. (c) 3D rendering of the segmented retinal surfaces. From [Lee et al., 2010].

segment the ONH cup and rim, contextual information combined with a convex hull-based fitting procedure were employed. In general, the methodology shows good performance but additional processing steps to compensate for the presence of vessels in and around the ONH are required to both reduce misclassified A-scans on the vessels and increase the accuracy of the ONH rim or cup contour segmentation (Figure 3.9).

In addition, Chiu et al. [Chiu et al., 2010] reported an interesting approach based on graph theory and dynamic programming. The proposed method significantly reduced the processing time required for image segmentation and feature extraction. It was able to address sources of instability such as the merging of the layers at the fovea, uneven tissue reflectivity, vessel hypo-reflectivity and the presence of pathology. Interestingly, the approach incorporated an automatic initialisation that bypasses the need for manual endpoint selection.

In this subsection, we briefly introduced segmentation approaches used in Ophthalmology to detect glaucoma. Approaches that are relative to the disease can be found in [DeBuc, 2011].

3.2.2   IVOCT Lumen Border Segmentation

IVOCT is one of the most frequently used medical imaging modality for CHD. It not only characterises different atherosclerotic plaque components by their distinctive signal patterns
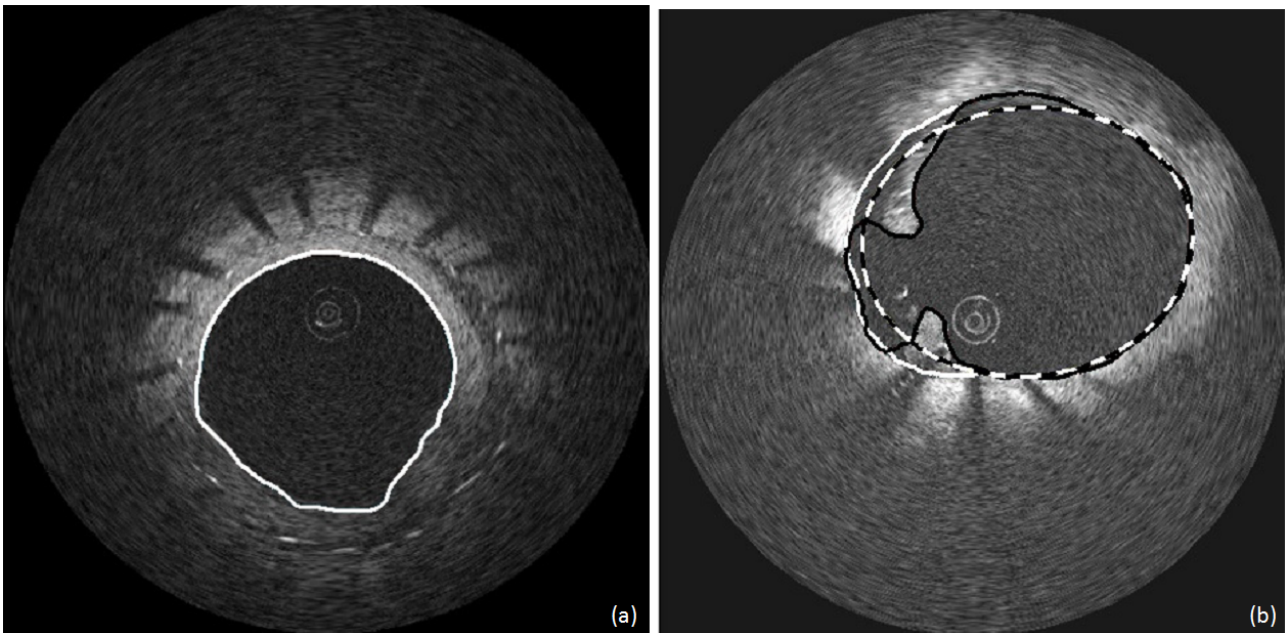
Figure 3.10: (a) an example of a good automatic segmentation result, and a failed segmentation example in (b). A fitting ellipse (dotted line in (b)) and a step for user correction (white line in (b)) are used to segment the lumen border (black line in (b)). Images were acquired by M2 system. From [Dubuisson et al., 2009].

but also provides information of NIH after stent implantation. The fundamental step in plaque and NIH detection is the lumen border segmentation. This subsection will describe some of the recently proposed segmentation approaches for lumen border segmentation.

Dubuisson and Kauffmann [Dubuisson et al., 2009, Kauffmann et al., 2010] proposed that the lumen border could be segmented by a combination of morphological and active contour models. They firstly applied an Otsu filter [Otsu, 1979] to obtain a binary IVOCT set and this binary set was used to find an approximation of the lumen border by morphological processes. The lumen border was then used to initialise an active contour to obtain the final shape of the lumen border (Figure 3.10(a)). In addition, they used ellipse-fitting [Fitzgibbon et al., 1998] to correct the inaccurate lumen border shape caused by stent malapposition (Figure 3.10(b)).

Gurmeric et al. [Gurmeric et al., 2009] proposed a combination of thresholding and Catmull-Rom splines [Catmull and Rom, 1974] to automatically estimate lumen border and stent area. Thresholding and a Gaussian filter were used to denoise a cross-sectional image. A Catmull-Rom spline was then used to estimate the contours of the lumen border and the stent area. The interaction and initialisation of this spline were well-suited to the problem of correcting of
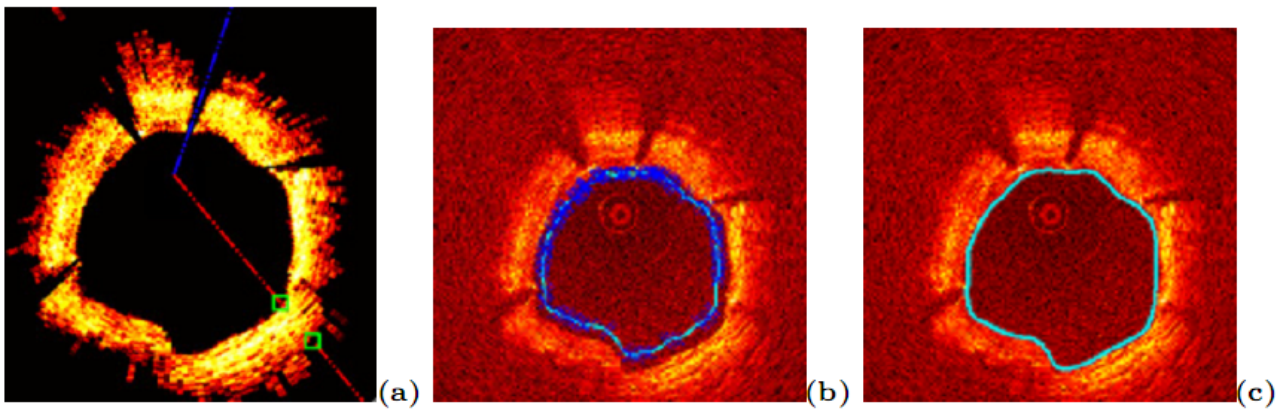
Figure 3.11: Segmentation results from [Gurmeric et al., 2009]. Images were acquired by M3 system. (a) Ray shooting in pre-filtered image; (b) Initial spline on ray intersection points; (c) Spline evolution and segmented lumen region.

both contours (see Figure 3.11).

Tsantis et al. [Tsantis et al., 2012] proposed an automatic lumen extraction method based on a MRF model and continuous wavelet transform (CWT) analysis. The MRF model was employed for lumen area identification. Image intensities and wavelet coefficients derived from the CWT analysis for each pixel were engaged as the input to the MRF model. In addition, after lumen segmentation, stent struts were detected by strut wavelet responses and probabilistic neural network (PNN) classification.

Moraes et al. [Moraes et al., 2012] presented an alternative approach to the automatic lumen segmentation based on wavelets and mathematical morphology to segment the lumen border of IVOCT sequences. The methodology can be summarised as follows: First, a wavelet decomposition was performed to discriminate the tissue from an image. An Otsu filter [Otsu, 1979] was then applied to obtain lumen region. Finally, mathematical morphology was used to correct, refine and estimate the information previously provided, so that a binary version of the lumen shape and its contour could be accurately obtained.

3.3   Summary

This chapter has reviewed segmentation approaches that are used in IVUS, OCT and IVOCT images. The applications of these methods consist of lumen border segmentation (in IVUS and IVOCT images) and retina layer segmentation (in OCT images). In the view of retina layer segmentation, intensity-based methods can be used to differentiate the layers of the retina when each layer of the retina has different intensity response. However, the drawback of intensity-based methods is that these methods can not cope with the multi-layer segmentation of retina. Therefore, graph-search based methods are proposed to segment the intra-layers of the retina.

In the aspect of lumen border segmentation, if the intensities of the lumen border and the vessel wall are clear, the lumen border and the vessel wall can be distinguished by edge-tracking and gradient-based techniques. With a good initialisation of the shape of the lumen border, active contour-based techniques can be used for estimating the lumen border. Supposing that intensities of lumen and plaque regions can be differentiated from different distributions of reflectors, statistical and probabilistic-based techniques can be used to recognise the lumen border.

In most cases, the lumen border can be well-estimated by these lumen border segmentation methods if acquired IVOCT sequences do not have obvious guide-wire shadow artifacts. If the artifacts exist, the lumen borders are obstructed. This means that the artifacts can cause a failure of the boundary segmentation of the lumen borders. Therefore, we propose a method that can automatically segment the lumen border even though in the presence of guide-wire shadow artifacts (Chapter 4).

Chapter 4

Lumen Border Segmentation

4.1 Introduction

Atherosclerosis, or arteriosclerotic vascular disease, is a condition where the arteries become narrowed and hardened due to an excessive build up of plaques around the artery wall. Plaque is made up of fat, cholesterol, calcium and other substances found in the blood. Over time, the plaque hardens and narrows the arteries. The arteries lose their elasticity which leads to a reduction of blood flow through the vessels. This potentially causes blood clots that can result in life-threatening conditions such as heart attack and stroke [Ross, 1993]. Figure 4.1 shows the differences between atherosclerosis and a health coronary artery.

Visualisation and quantitative analysis of intravascular coronary arteries is an important step in the diagnosis of CHD, stenosis grading, surgical planning, blood flow simulation and post-surgery monitoring. Lumen border segmentation can be useful for quantification, e.g., stenosis grading or determining the dimension of stents to be used in the following interventions.

Knowledge about lumen border properties is valuable in the management of CHD [Pearson, 1994]. Recent studies [Dubuisson et al., 2009, Gurmeric et al., 2009, Kauffmann et al., 2010, Gonzalo, 2010, Moraes et al., 2012, Tsantis et al., 2012] have proposed several methods for detecting the lumen border and stent struts by analyzing endovascular IVOCT sequences.
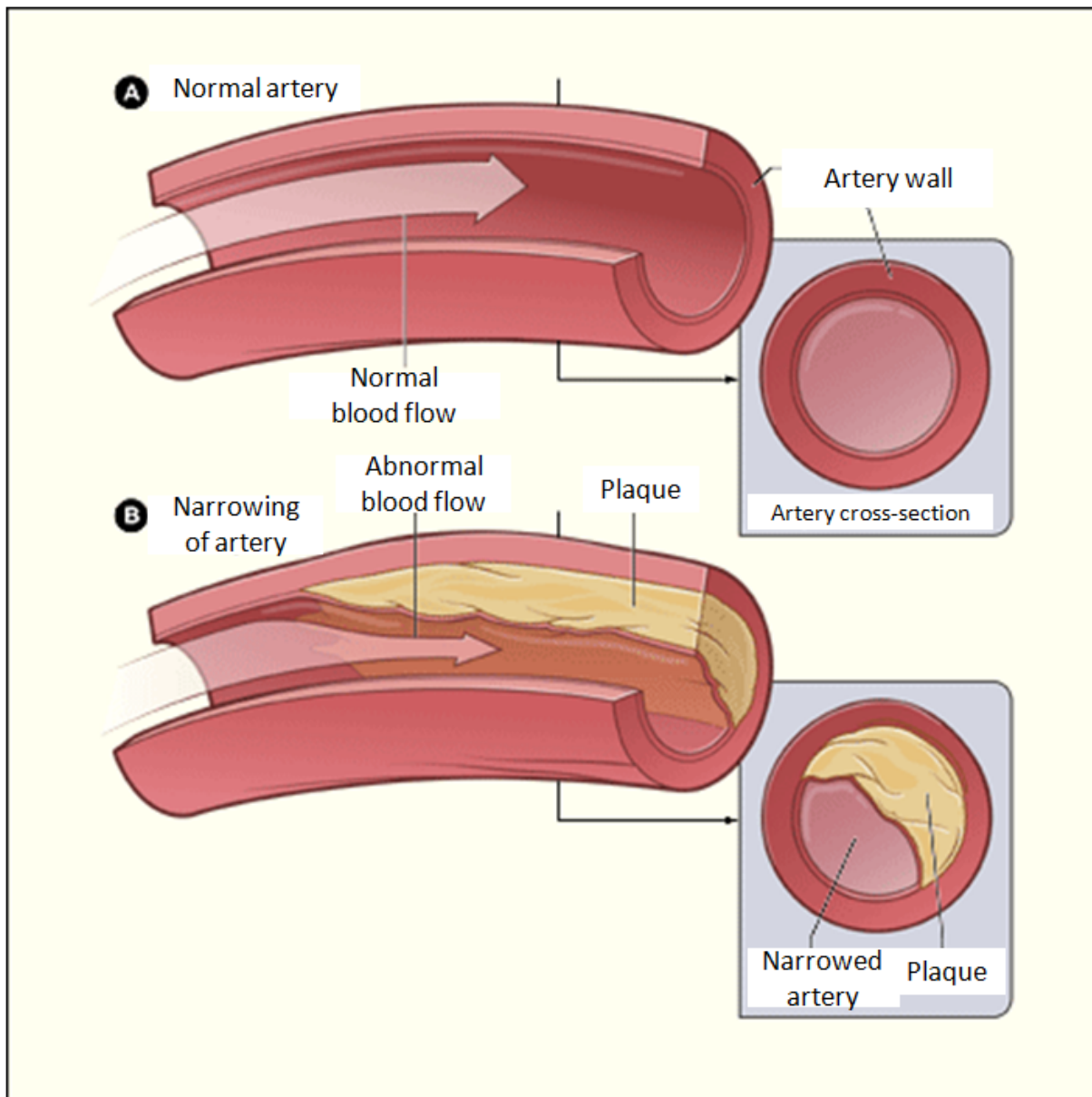
Figure 4.1: This figure shows the differences between (A) healthy coronary artery and (B) narrowing coronary artery. From [NHLBI, 2008].

Dubuisson and Kauffmann [Dubuisson et al., 2009, Kauffmann et al., 2010] proposed that the lumen border can be segmented by combined morphological and active contour models. Gurmeric et al. [Gurmeric et al., 2009] used thresholding and Catmull-Rom splines to estimate the shape of the lumen border and stent struts. Moraes et al. [Moraes et al., 2012] presented an automatic lumen segmentation approach, based on wavelets and mathematical morphology to segment the lumen border of IVOCT sequences. Tsantis et al. [Tsantis et al., 2012] proposed an automatic lumen extraction method based on a MRF model and CWT analysis.
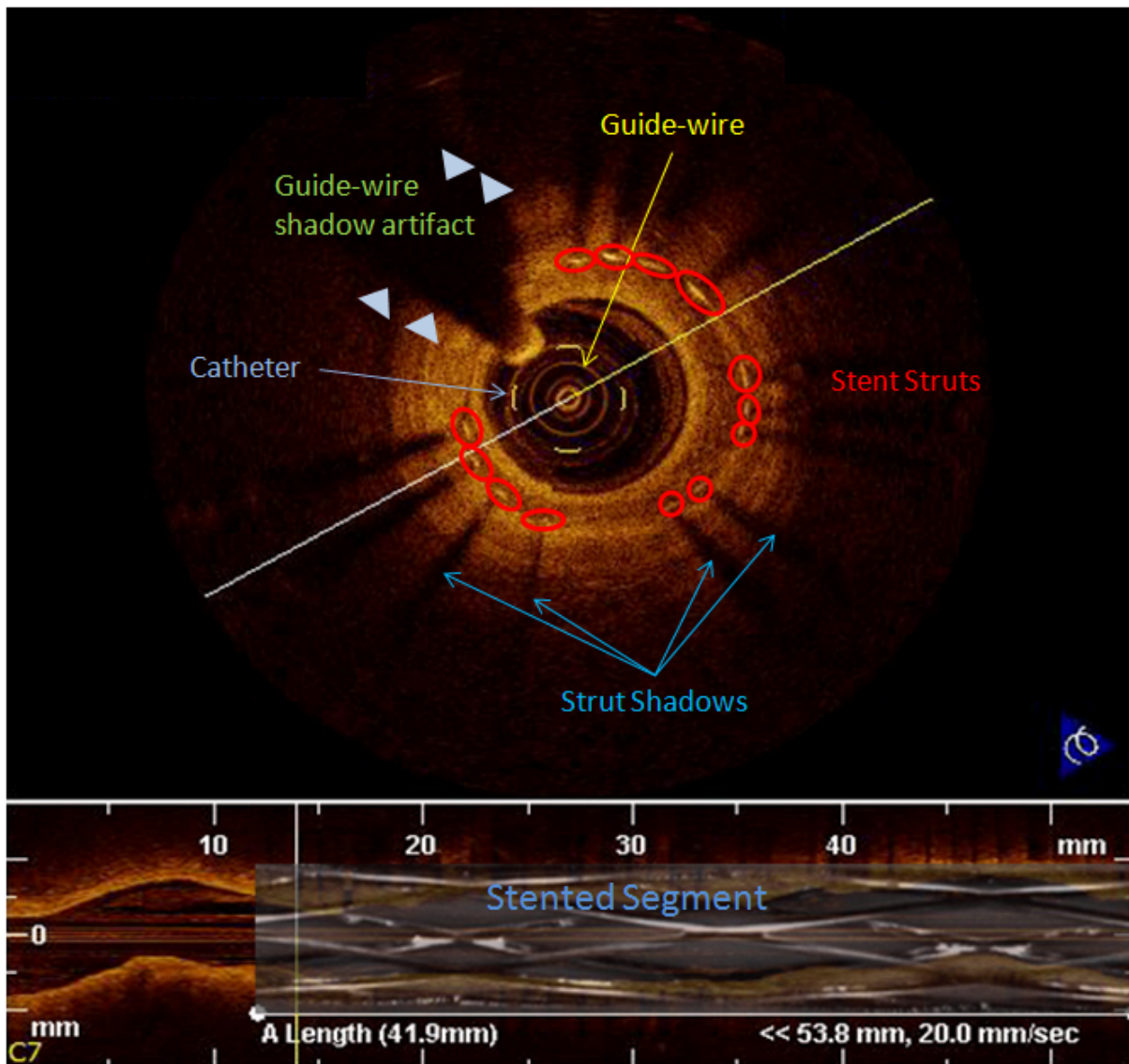
Figure 4.2: This figure shows a cross-sectional image in IVOCT (top) sequence and a longitudinal view of the image sequence (bottom). The guide-wire shadow artifact is visible from the 10 to 11 o'clock position.

However, these algorithms work well only in IVOCT images without the existence of guide-wire shadow artifacts (images acquired by commercial M2/M3 systems). If this artifact exists (images acquired by a commercial C7-XR system), regions of the lumen border, vessel wall and lipid tissue will be hidden and this will cause inaccurate lumen border segmentation. An example of guide-wire shadow artifacts can be observed in Figure 4.2.

In this chapter, we propose an automatic algorithm for the identification of the vessel lumen, enabling accurate and robust segmentation despite the presence of guide-wire shadow artifacts. The estimation of the position of the guide-wire is the key concept for the elimination of guide-
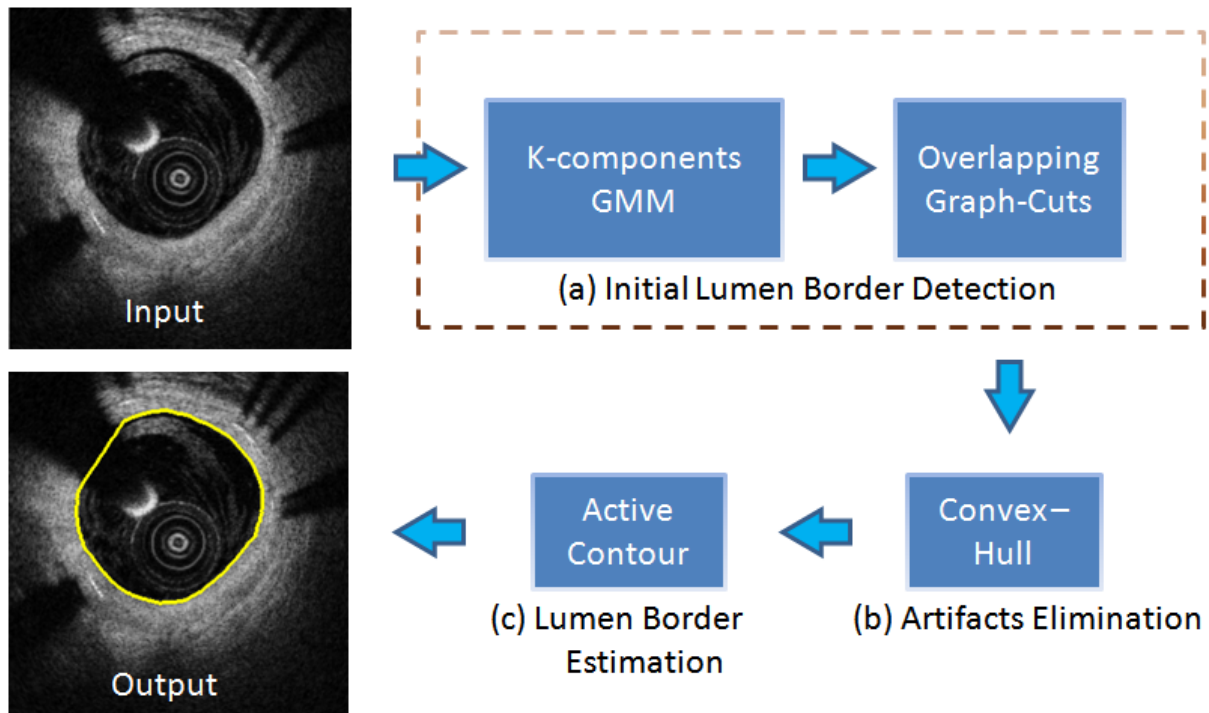
Figure 4.3: OCT image undergoes (a) initial lumen border detection; (b) artifacts elimination and (c) contour correction and smoothing to estimate the hidden region of the lumen border.

wire shadow artifacts. After identification of the artifacts, we propose a geometrically-based method which can be applied to IVOCT cross-sectional images to remove the artifacts. The segmentation approach is based on a combination of EM-based segmentation and GC-based segmentation. The approach will be described in detail in the following section. Section 4.3 illustrates the segmentation results from 18 patients. Finally, Section 4.4 summarises the results and concludes this chapter.

4.2 Lumen Border Segmentation

The proposed approach consists of three steps: (a) initial lumen border detection, (b) elimination of guide-wire shadow artifacts and (c) final lumen border estimation. A flowchart is shown in Figure 4.3. An initial estimation of the lumen border is obtained using a combination of EM and GC. After this initial segmentation, a convex hull estimation [de Berg et al., 1997] is used to eliminate guide-wire shadow artifacts. In the final step, an active contour model is used to correct and smooth the contour of the lumen border. This three-steps approach is implemented

by matrix laboratory (MATLAB) and image registration toolkit (IRTK). A brief introduction
of these two tools can be found in Appendix A.1.

4.2.1   Initial Lumen Border Detection

In IVOCT images corrupted by guide-wire shadow artifacts, the boundary of the lumen border
is difficult to segment by thresholding. We propose a combined EM-based estimation [Demp-
ster et al., 1977, Moon, 1996, Zhang et al., 2001, Lorenzo-Valdes et al., 2004] and GC refine-
ment [Boykov et al., 2001b, Boykov and Jolly, 2001] to obtain an accurate initial lumen border
segmentation. The EM-based estimation is used to assign a class/label to each voxel via GMM
since the intensity of the lumen border is relative homogeneous. However, image noise or the
intensity of the guide-wire may cause mislabelling of voxels. To overcome the mislabelling prob-
lem, we utilise multiple Gaussians to represent one label of each voxel. After the probability of
each voxel's label has been obtained, we use GC to refine the lumen border segmentation since
the EM algorithm lacks information from neighbouring voxels. Each step of this algorithm will
be described in detail in the following subsections.

EM Segmentation

Traditionally, the intensities in an image can be represented as a combination of Gaussian dis-
tributions. However, one Gaussian distribution may not be sufficient to describe heterogeneous
intensity distributions. In order to model the intensity distribution more accurately, for each
voxel i, we use multiple Gaussian distributions (GMM) to represent the label/class of this voxel.
The mixture of Gaussians model of the voxel i is represented in Eq. (2.5).

The parameters (mean, standard deviation and covariance) of each Gaussian model are es-
timated by EM. It utilises the maximum log-likelihood estimator to determine the optimal
parameters (Eq. (2.7)). Once the parameters are found, the label of each voxel in the image
can be easily determined by computing the probability of the label of this voxel in the image.

In our approach, the EM algorithm is used to estimate the optimal parameters by executing

two steps iteratively: The E-step computes the probability that voxel x_i belongs to the label k and the M-step re-estimates the model parameters. The equations of the E-step and M-step are denoted as:

E-step:

$$p_{ik}^{(m+1)} = \frac{\alpha_{ik}^{(m)} G(x_i, \mu_k^{(m)}, \sigma_k^{(m)})}{\sum_{k=1}^{K} \alpha_{ik}^{(m)} G(x_i, \mu_k^{(m)}, \sigma_k^{(m)})} \tag{4.1}$$

M-step:

$$\begin{aligned}
\mu_k^{(m+1)} &= \frac{\sum_i p_{ik}^{(m+1)}(x_i)}{\sum_i p_{ik}^{(m+1)}}, \\
(\sigma_k^{(m+1)})^2 &= \frac{\sum_i p_{ik}^{(m+1)}(x_i - \mu_k^{(m+1)})^2}{\sum_i p_{ik}^{(m+1)}}, \\
\alpha_k^{(m+1)} &= \frac{\sum_i p_{ik}^{(m+1)}}{N}
\end{aligned} \tag{4.2}$$

Here $p_{ik}^{(m+1)}$ denotes the posterior probability of i-th voxel belonging to the label k at the $(m+1)$ iteration; x_i denotes the intensity of the i-th voxel; $G(x_i, \mu_k^{(m)}, \sigma_k^{(m)})$ denotes the probability of voxel i belonging to label k at the m-th iteration.

However, it is possible that one component of GMM can not clearly identify whether a voxel belongs to the lumen border tissue (lF) or the background label (lB). To avoid mislabelling, we utilise multiple Gaussians to present each voxel's label. Let $Pr(x_i|lB)$ and $Pr(x_i|lF)$ denote the probability that a voxel i belongs to the lumen border tissue (lF) or the background label (lB) of one component k of GMM:

$$\begin{aligned}
Pr(x_i|lB) &= \frac{\sum_{k=1}^{n} p_{ik}}{n} \\
Pr(x_i|lF) &= \frac{\sum_{k=n+1}^{K} p_{ik}}{K - n}
\end{aligned} \tag{4.3}$$

Here, p_{ik} is the probability of the i-th voxel belonging to the component k; x_i means the intensity of the i-th voxel; K denotes the total number of components in the GMM; n and $(K - n)$ are the number of components used to estimate the voxel's label. The probability maps of the background and the lumen border tissue of an example image are shown in Figure 4.4.
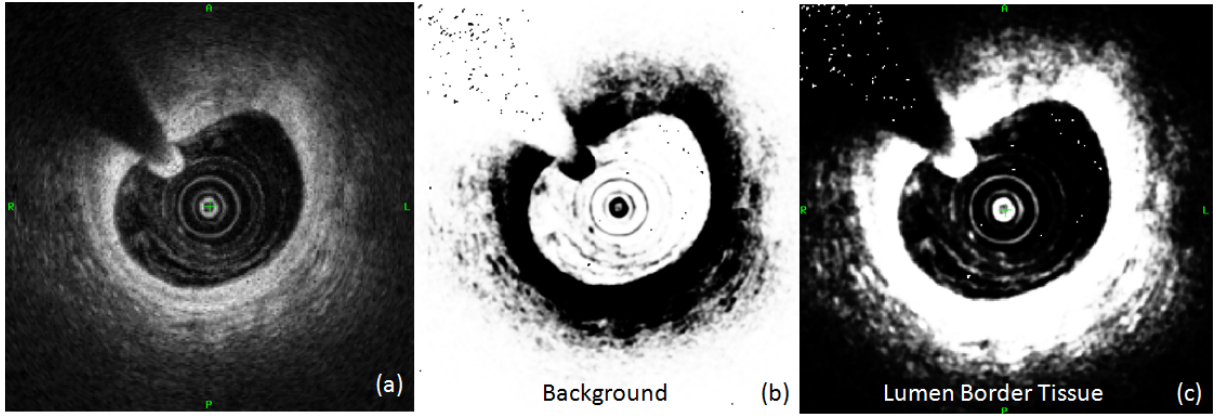
Figure 4.4: Example probability maps of (b) the background and (c) the lumen border tissue in an OCT image (a).

Graph-Cuts Refinement

The EM algorithm classifies each voxel into different labels (the lumen border tissue (lF) and the background (lB)) but it lacks information about spatial correlation between neighbouring voxels. For example, voxels in the background region should be classified as the same label lB but if the intensity of a voxel in this region is closer to the mean of the lumen border tissue label lF, the classifier would incorrectly classify the voxel as belonging to class lF. The drawback is due to the fact that EM algorithm is based on the GMM which assumes that all voxels distributions are identical and independent.

To overcome this, we use GC [Boykov et al., 2001b, Boykov and Jolly, 2001] to refine the segmentation. The energy function defined by MRF is denoted as:

$$
\begin{aligned}
E(L) &= E_{data}(L) + E_{smooth}(L) \\
&= \lambda \sum_{i \in I} D_i(l_i) + \sum_{\{i,j\} \in N} V_{i,j}(l_i, l_j)
\end{aligned}
\tag{4.4}
$$

Here, the energy function consists of a data term (D_i) and a smoothness term ($V_{i,j}$) and assigns binary labels (the lumen border tissue (lF) and the background (lB)) to each voxel using either a standard 8 or 26 neighbourhood system (Figure 4.5(a))); N denotes the neighbourhood of voxels within an image; $L = \{l_i | i \in I\}$ is a labelling (segmentation) of a volume image I where l_i can be either lumen border tissue (lF) or the background (lB) [Boykov et al., 2001b, Boykov
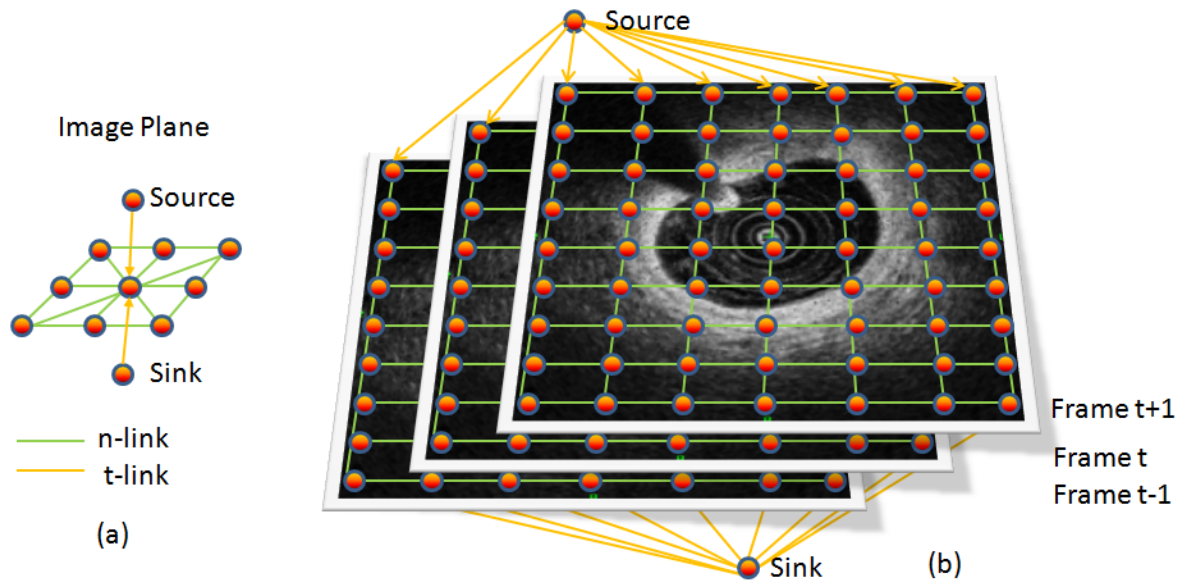
Figure 4.5: (a) An example of 2D neighbourhood system. A node/voxel connects 8 neighbour nodes and plus 2 terminal nodes (source and sink nodes); (b) An image is represented as a set of nodes. Each node has edges to link its neighbourhood and terminal nodes. The edges that connect to the terminal nodes are called t-link (yellow lines). Green lines are the edges connecting neighbouring voxels (n-links).

et al., 2001a].

The data term $D(l_i)$ (also called data likelihood term) represents the likelihood of lumen border tissue and background region presence at voxel i. $V_{i,j}(l_i, l_j)$ is a smoothness (spatial coherence) term that favours similar labels at neighbouring voxels. The parameter λ governs the trade-off between the data and smoothness terms.

To optimise Eq. (4.4), an undirected weighting graph G=<V,E> with a node $v \in V$ for each voxel i is defined to present an image (see Figure 4.5(b)). Each edge $e \in E$ consists of connections between node v and two terminal nodes F and B (source and sink nodes) as well as connections between neighbouring voxels. The terminal nodes F and B represent the two labels describing the lumen border tissue and the background, respectively. Determining a minimum cut on the graph G can be used to minimise the energy function in Eq. (4.4) [Boykov et al., 2001b]. After the optimisation, the desired segmentation can be obtained.

In our approach, the data term $E_{data}(L)$ is estimated using the EM segmentation which uses multi-GMMs to compute the probabilistic models of background and the lumen border tissue

of the voxel i. The weights of the t-links (edges between voxel i and source/sink nodes) are computed as $E(lB) = -\ln(Pr(x_i|lB))$ and $E(lF) = -\ln(Pr(x_i|lF))$. The value of this data term is close to zero if the probability of a voxel belonging to the lumen border or the background is high and it increases with decreasing probability [Toennies, 2012].

The smoothness term is used to set the weights of edges between neighbouring voxels and it is defined by the following equation:

$$V_{i,j}(l_i, l_j) = \exp(-\frac{(x_i - x_j)^2}{2\sigma^2 + \epsilon}) \cdot (\frac{1}{\|i - j\|}) \qquad (4.5)$$

Here $\|i - j\|$ is the distance between two voxels, σ is the standard deviation of the intensities, ϵ is a small constant added for numerical stability and x_i, x_j are the intensities of voxels i, j.

Combination of EM segmentation and GC refinement

After EM segmentation and GC refinement, the initial lumen border segmentation can be obtained. However, the main challenge of the combination of these two approaches is the memory requirements. This is because the memory usage for segmenting high-resolution data using GC is prohibitive. In general, GC requires $24n + 14m$ bytes to construct a graph [Lerme et al., 2010]. Here n and m are the number of nodes and edges in the graph.

Larger neighbourhood systems of GC yield better segmentations since a larger neighbourhood captures the precise mix of lumen border tissue and background at each voxel [Cour et al., 2005]. However, larger neighbourhoods come at the expense of both running time and memory consumption increases [Lombaert et al., 2005]. For example, if we formulate our 3D image in a graph and perform the combination of EM&GC (using a 26-neighbourhood system), over 10 GB memory is required to represent the graph. Since this is not feasible on a standard PC, we have proposed a two-step approach to address this problem. The first step is to divide a volumetric image into several overlapping subsets (s_i) and obtain the segmentation via EM&GC in each subset.

The second step is to guarantee that the segmentation of each subset is estimated via 3D GC

because the segmentations of the overlapping frames of each subset are not estimated by using a 26-neighbourhood system (3D GC). To overcome this problem, a straightforward method is to replace the segmentations of the overlapping frames from the corresponding frames in the neighbouring subsets. After these two steps, a binary segmentation can be integrated from the segmentations of subsets at the end of the procedure.

In practice, we divide the IVOCT sequence into several subsets and each subset contains p frames. Neighbouring subsets are overlapped by q frames. We then iterate the estimation process until the IVOCT sequence has been segmented. Generally, the sequence (n frames) can be divided into $N = \frac{n}{p-q} + 1$ subsets. Figure 4.6(a) illustrates an example that a sequence is firstly divided into 6 overlapping subsets and the number of frames of the subset s_6 is less than or equal to p frames ($\leq p$). It is because the value n is not exactly divisible in most cases. After running the segmentation via EM&GC on each subset, a partial lumen segmentation ($S_i, i = 1, ..., N$) can be obtained.

We then check that the segmentations of overlapping frames between neighbouring subsets (S_1 and S_2, S_2 and S_3, ..., S_{N-1} and S_N) are obtained via 3D GC (Figure 4.6(b1)-(b5), marked by blackish green). For example, Figure 4.6(b1) illustrates the neighbouring subsets S_1 and S_2 are overlapped by 2 frames (q=2). Once the segmentation of the frame p in S_1 is not estimated via 3D GC, it can be replaced by the segmentation of the q-th (the 2nd) frame in S_2. Similarly, the first frame in S_2 can be substituted for the (p-q+1)-th frame in S_1. This strategy can guarantee that the segmentation of each frame is obtained via 3D GC.

The initial lumen border segmentation of the IVOCT sequence is then obtained by the sum of each subset lumen border segmentation $S_{LB} = \sum_{i=1}^{N} S_i$. The pseudo-code for the initial lumen border detection is shown as algorithm 1. Finally, Figure 4.7(a) shows the result of the initial lumen border segmentation. We can clearly notice segmentation errors due to the presence of the guide-wire (denoted by the light blue circle in Figure 4.7(a)). The next section explains how these segmentation errors can be corrected.

Algorithm 1 Initial lumen border segmentation

Input: A n frames patient sequence P
Output: The segmented binary sequence S_{LB}

Set the sequence P (n frames) is divided into the subsets s_i of p frames and neighbouring subsets overlap by q frames.
Set the number of subsets equals to $N = \frac{n}{p-q} + 1$.
for $i = 1$ *in* N **do**

> Run EM segmentation
> Set the resulted probability maps of the lumen border tissue and the background as the data likelihood term of GC
> Run GC refinement
> Set the outcome of partial lumen segmentation equals to S_i

end
for $i = 1$ *in* $N - 1$ **do**

> Set $S_{p,i}$ denotes the segmentation of the frame p in the partial lumen segmentation S_i
> $S_{p,i} = S_{q,i+1}$
> $S_{1,i+1} = S_{p-q+1,i}$

end
Set the binary segmentation $S_{LB} = \sum_{i=1}^{N} S_i$.

4.2.2   Elimination of Guide-Wire Artifacts

The artifacts in the IVOCT images cause a failure of the boundary detection of the lumen border since it is occluded by shadows from the guide-wire. To remove the artifacts, we have used a convex hull approach [de Berg et al., 1997] to identify the portion of the lumen border which is affected by the artifacts. This identification is implemented in 2D since the artifacts of each slice can appear at the different locations.

In practice, we first construct the convex hull of the initial lumen border points. The convex hull is the smallest convex set that includes the total initial lumen border points (red pluses in Figure 4.7(a)). The convex hull is generated by the Matlab function (convhull). The method for computing the convex hull is based on the gift-wrapping algorithm [Cormen et al., 2001]. The method starts by finding the starting point in the initial lumen border points. The starting point is generally set by finding a point whose vertical coordinate is minimum in the initial lumen border points (marked as A, Figure 4.8(a)). By scanning through all the
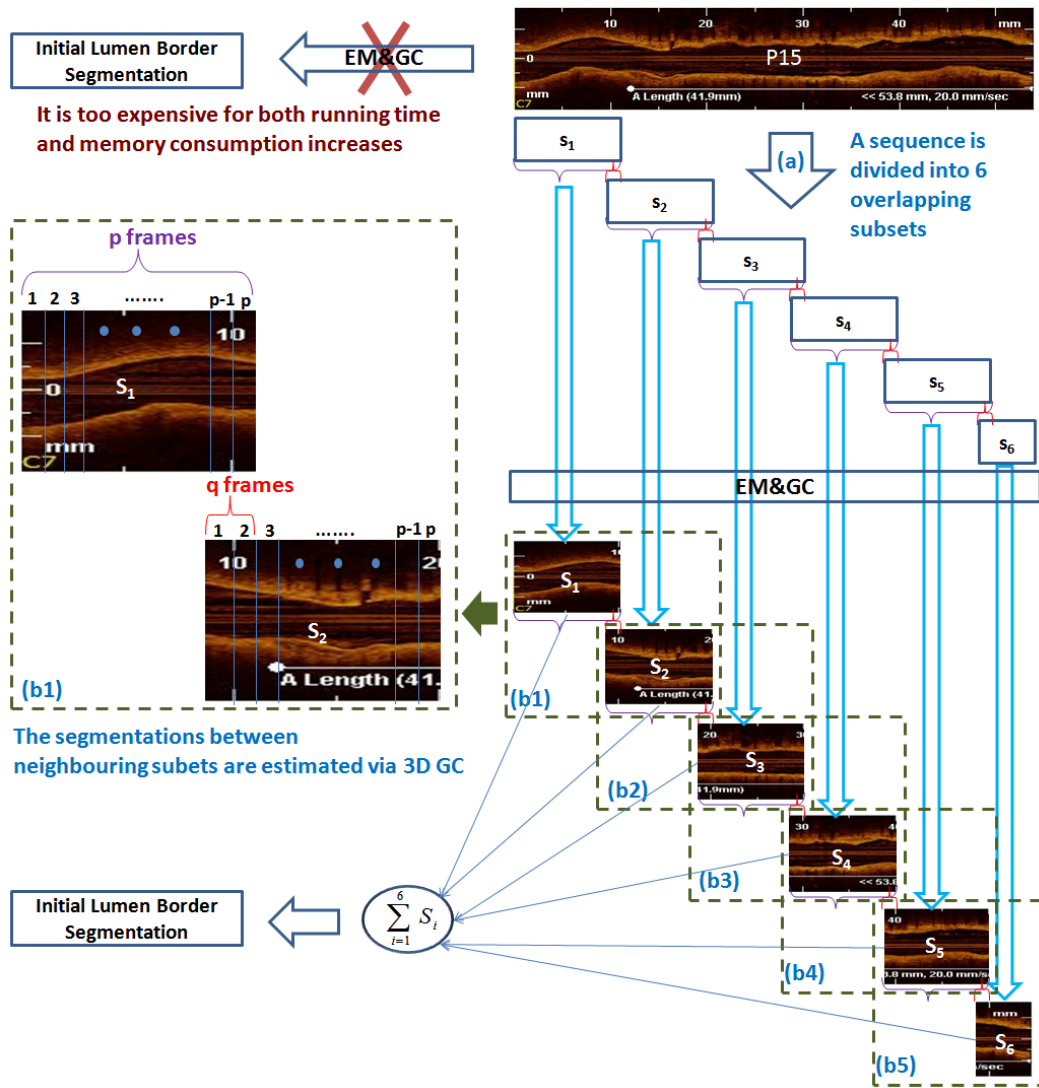
Figure 4.6: An image sequence (P15) is hard to be segmented by the combined EM&GC approach since it is too expensive for both running time and memory consumption increases. To overcome this problem, we have proposed a two-step approach. Firstly, (a) the sequence (n frames) is divided into the subsets of p frames ($s_i, i = 1, ..., 6$). The number of frames of s_6 is less than p since the total number of frames n is not exact divisible. The neighbouring subsets are overlapped by q frames. Afterwards, the combined EM&GC approach is used in each subset to obtain the partial lumen border segmentation ($S_i, i = 1, ..., 6$). Secondly, (b) after the segmentations are obtained, we check the segmentations of overlapping frames in each subset are estimated via 3D GC (marked by blackish green, (b1)-(b5)). Since the segmentations of overlapping frames of each subset are not estimated via 3D GC, a straightforward method is to replace the segmentations of overlapping frames from the corresponding frames in the neighbouring subset. For example, (b1) shows that the neighbouring subsets S_1 and S_2 are overlapped by 2 frames (q=2) and the frame p in S_1 corresponds to the q-th frame (the 2nd frame) in S_2. Therefore, to guarantee the segmentation is obtained via 3D GC, the segmentation of the frame p in S_1 can be replaced by the 2nd frame in S_2. Similarly, the segmentation of the 1st frame in S_2 can be replaced by the (p-1)-th frame in S_1. The value of the correlation is calculated by (p-q+1). After (a) and (b) steps, the initial lumen border segmentation can be integrated by combining the partial lumen border segmentations.
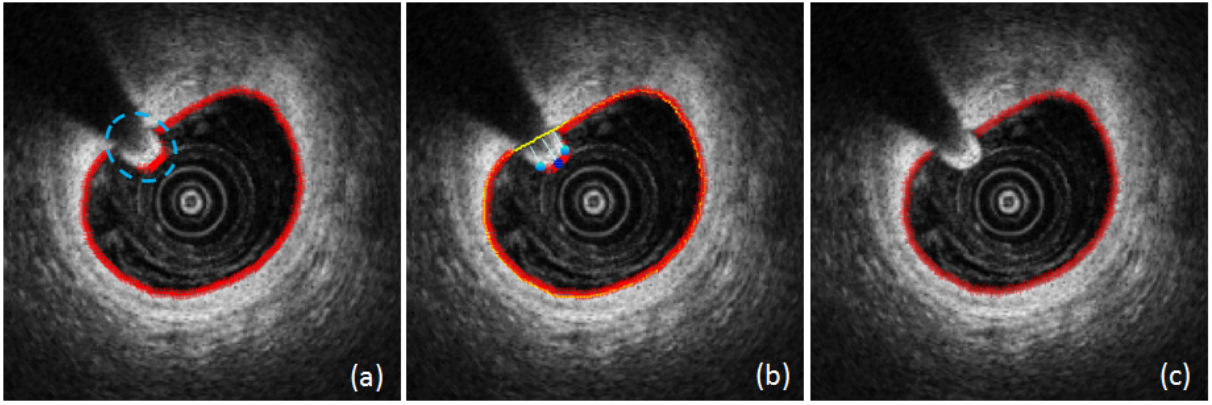
Figure 4.7: From left to right: (a) an result of initial lumen border detection that contains artifacts (marked as light blue circle); (b) convex hull of the initial lumen border points (yellow contour); (c) the updated initial lumen border points without the guided-wire artificial points.

points, a point B where all points lie to the left of line $\overline{AB}$ (by comparing polar angles) can be determined (Figure 4.8(a)). The next point is found by repeating the scanning step. The computation finishes when the end point is the same as the starting point. The convex hull is shown in Figure4.7(b) (yellow contour in (b)) and the illustration of the convex hull is shown in Figure 4.8(a).

From Figure 4.7(a), it is obvious to find that the artifacts appear inside of the lumen border. Thus, it is reasonable to assume that the distances between artifacts and the convex hull of the lumen border are larger than the distances between the lumen border points and the convex hull of the lumen border. We construct a set that contains the distance from each point on the lumen border to the convex hull of the lumen border. The point v that has the maximum distance can be obtained:

$$v = \arg\ \max(H_{convex\_dis}(X)) \tag{4.6}$$

where $H_{convex\_dis}(X)$ is a distance set that records the distances between a convex hull and the initial lumen border points set X. We consider the point v as the seed point of an artifact set S and then perform tracking along the initial lumen border boundary. The neighbouring points of the seed point are placed in the neighbourhood set N. We then examine neighbouring points in the neighbourhood set N. If the distance between a point in the neighbourhood set N and the convex hull is larger than the mean distance, we can assume that this point is an erroneous point resulting from the guide-wire shadow and add this point into the artifacts set
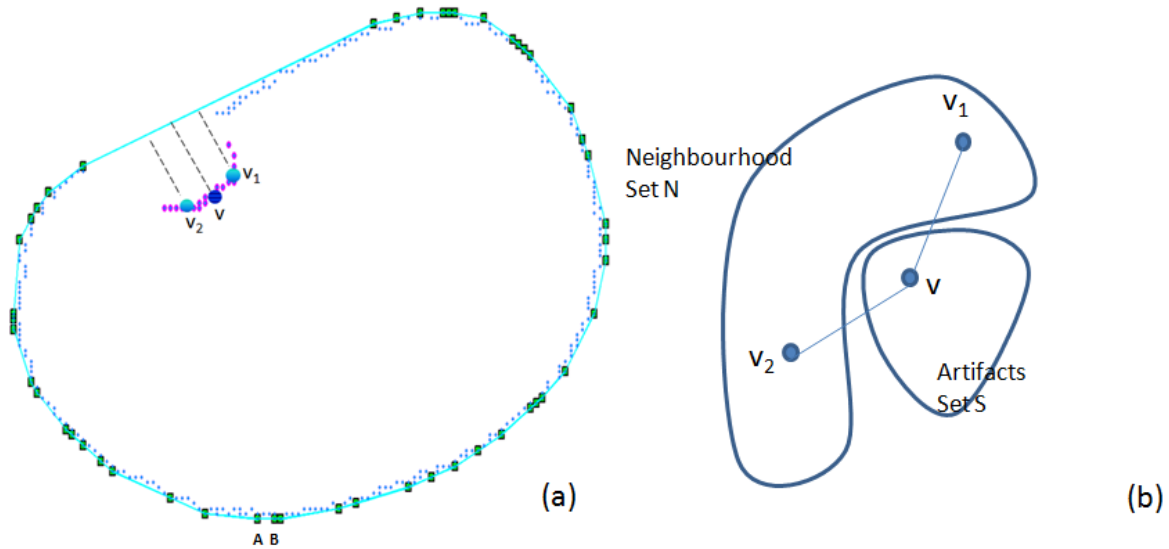
Figure 4.8: (a) shows an illustration of the convex hull and the initial lumen border points of Figure 4.7. Small blue points are the initial lumen border points; purple points are the artifact points; green rectangles are the points used to construct the convex hull calculated by the gift wrapping approach; points A, B are the starting point and the convex hull point; the cyan contour is the convex hull; point v is the point that has maximum distance from the initial lumen border points to the corresponding convex hull point; points v_1, v_2 are the neighbour points of the point v; dashed lines represent the distances between the convex hull and the initial lumen border points and purple points are the guide-wire artificial points. (b) shows an illustration of the iterative guide-wire artificial points elimination. The elimination starts from the seed point v in the artifact set and then performs tracking along the initial lumen border points. The neighbouring points of the seed point v are placed in the neighbourhood set. If the distance between a point in the neighbourhood set and the convex hull is larger than the mean distance, this point is added into the artifact set. The elimination ends when the artifact set is not growing.

S. Figure 4.8(a) shows the point v and its neighbouring points v_1 and v_2 in the initial lumen border points and Figure 4.8(b) illustrate the artifacts set S and its neighbourhood set N. We then iterate this process until the artifacts set S is no longer growing. The final result is shown as Figure 4.7(c).

After the artifacts set has been obtained, we iterate the elimination procedure to verify that the obvious malapposed stent struts (Figure 4.9(a)-(c)) have been eliminated. Malapposed stent struts refer to a separation of the stent struts from the intima surface of the arterial wall that is not present after implantation [Shah et al., 2002]. Identification of malapposed stent struts will be discussed in detail in the next chapter (Chapter 5). After this procedure, a new lumen border point set and artifact point set can be obtained to estimate the correct lumen border

shape. The pseudo-code for this elimination is shown as below (see algorithm 2).

Algorithm 2 Guide-wire artifacts elimination

Input: A point set X of initial lumen border points
Output: A point set Y of lumen border points without artifacts

Set artifacts set $S = \emptyset$
Set $H_{convex\_dis}(X)$ record the distances between X and its convex hull
Set $\overline{H} = \frac{1}{n} \cdot \sum_{i=1}^{n} H_{convex\_dis}(x_i)$, where $x_i \in X$
while $\max(H_{convex\_dis}(X)) > \overline{H}$ **do**
    Set $v = \arg\max(H_{convex\_dis}(X)))$
    Add v into the set S
    Set N denote a set of neighbour points of the seed point v
    for v_i *in* N **do**
        Set $v_{\{i,convexhull\}}$ denote the corresponding convex hull point of v_i
        if $\|v_i - v_{\{i,convexhull\}}\| > \overline{H}$ & $v_i \notin S$ **then**
            Add v_i into S
        end
    end
    Remove v from the initial lumen border point set X;
    Sort and update $H_{convex\_dis}(X)$;
    Update $n = n - 1$;
    Set $\overline{H} = \frac{1}{n} \cdot \sum_{x=1}^{n} H_{convex\_dis}(X)$
end
Set $Y = X - S$

4.2.3   Lumen Border Estimation

After the artifacts have been eliminated, a deformable model (or active contour [Kass et al., 1987]) is used to correct the contour of the lumen border and to extrapolate the contour in the area of the guide-wire shadow. The process of contour correction and extrapolation is implemented frame-by-frame and described in the following.

The active contour model evolves from its initial shape and position as a result of the combined action of external and internal forces. The internal forces lead the snake towards features of the image, whereas internal forces model the elasticity of the curve. In a parametric representation, the contour can be written as a closed curve $v(s) = (x(s), y(s))$, $s \in [0,1]$ with $v(0) = v(1)$. Its
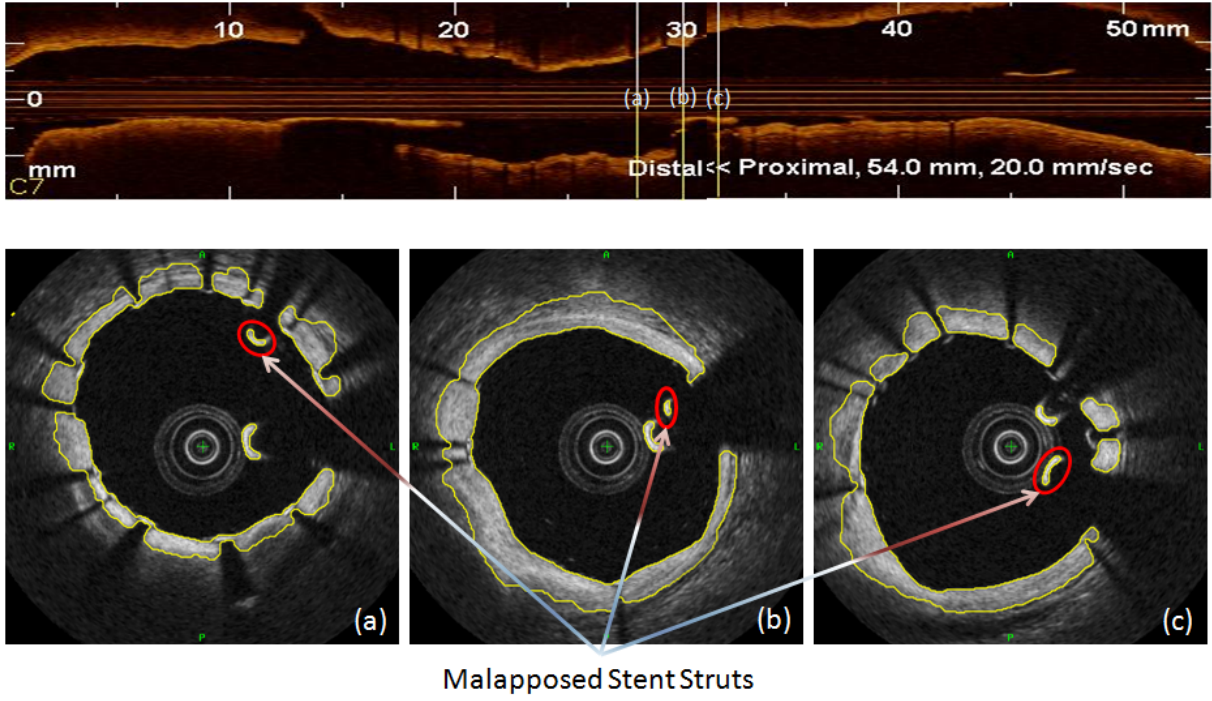
Figure 4.9: The figure shows that malapposed stent struts appear in a patient sequence (P6). Malapposed stent struts are close to the catheter. The iterative elimination approach can discard the artifacts points and malapposed stent strut points that are near the catheter.

internal energy is defined as:

$$E_{int}(v) = \int_0^1 (\alpha|v_s(s)|^2 + \beta|v_{ss}(s)|^2)ds \qquad (4.7)$$

It is made up of two terms: the membrane energy $\alpha|v_s(s)|^2$, which weights its resistance to stretching, and the thin-plate energy, $\beta|v_{ss}(s)|^2$, that weights its resistance to bending. $v_s(s)$ and $v_{ss}(s)$ represent the first and second derivatives of the curve and s is the arc length parametrisation of the curve. The elasticity parameters α and β control the smoothness of the curve.

The external energy is generally defined as a potential field P,

$$E_{ext}(v) = \int_0^1 P(v(s))ds \qquad (4.8)$$

where P ia a combination of energy functions: $\omega_{line}E_{line}$ and $\omega_{edge}E_{edge}$. Since the lumen border is an ellipse-like border, the termination energy term of the external energy is not used. The line energy term E_{line} can be represented as the intensity of the image. The edge energy term

E_{edge} attracts the curve to intensity edges after convolution with a Gaussian kernel (with large image gradients). ω_{line} is the weight which attracts the curve to dark lines or light lines. If it is negative, the curve is attracted to dark lines. Otherwise, the curve is attracted by white lines. ω_{edge} is the weight which adjusts the attraction to edges. The total energy of the snake will be the sum of the external and internal energies along the curve $v(s)$:

$$E_{snake} = E_{int}(v) + E_{ext}(v) \tag{4.9}$$

In the proposed approach, we use the active contour model functions as in [Kroon, 2010]. The functions are implemented in MATLAB. Since the guide-wire artifacts are eliminated, there is a missing region in the initial lumen border points (Figure 4.10(a)). The challenges caused by this missing region are that (1) the positions of lumen border points in the missing region are unknown and (2) the missing region appears in different positions in every frame. Therefore, the first step is to estimate the approximate point positions in the missing region in 2D. Here, we use a MATLAB interpolate function (interp) to upsample the images to higher resolution. The updated initial lumen border points where guide-wire artifacts points and the malapposed struts points have been eliminated (Figure 4.10(a)) are used as initial points to estimate the smooth contour points in the missing region (see Figure 4.10(b)). We then calculate the external energy of the deformable model (Figure 4.10(c)) to estimate the contour of the lumen border by using these estimated positions as the initial contour of the active contour model. With iterative refinement of the current contour, the energy minimisation via gradient descent [Kass et al., 1987] drives the initial contour to fit the the shape of the lumen border (a yellow contour in Figure 4.10(d)).

4.3   Results

4.3.1   Materials
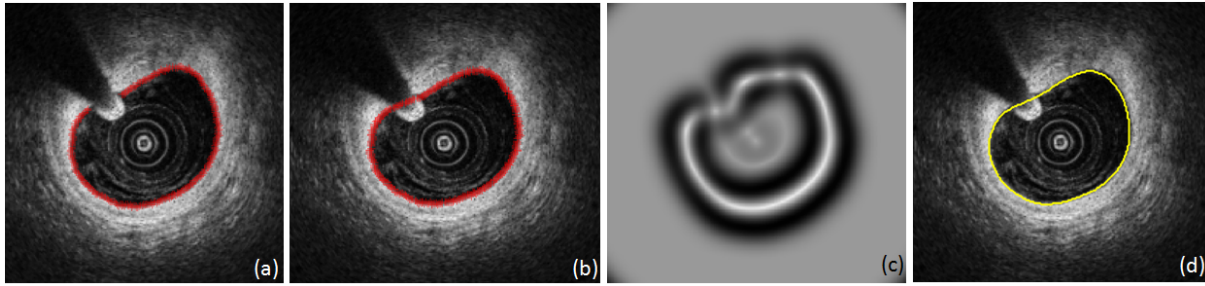
Figure 4.10: From left to right: (a) lumen border points without artifacts are used as initial points of a snake and (b) the estimated positions in the missing region by MATLAB interpolation; (c) the external energy is calculated to estimate the movement of the snake; (d) shows the lumen border estimation (yellow contour).

Table 4.1: This table shows the number of frames of patient data.

Number of frames	Patient ID
271	P1, P2, P5, P6, P7
268	The other 13 patient sequences

The IVOCT image sequences were acquired with a commercial system (the C7-XR system). The number of frames of each sequence varies between 268 and 271 frames (Table 4.1). Since the image sequences were acquired by the FDOCT system (the C7-XR system), the probe and guide-wire artifacts appear in all sequences. To evaluate the segmentation results from the proposed method, the ground truth for all sequences was obtained via the C7-XR system pre-installed software (operated by Dr. Hiroto). In addition, we have tested the results from our method and another commercial software (the Odeirena system (OCT Detecting Instrument for stEnt Reendothelialzation aNd Apposition), designed by [Ughi et al., 2011]) by comparing the accuracy of lumen border segmentation. Finally, the implementation tools (MATLAB and IRTK) of the three-steps lumen border segmentation approach are summarised as Table 4.2.

Table 4.2: This table shows the implementation tools for (1) Initial Lumen Border Detection, (2) Elimination of Guide-Wire Artifacts and (3) Lumen Border Estimation.

Steps	(1)		(2)		(3)
	EM Segmentation	GC Refinement	Convex Hull Construction	Guide-Wire Artifacts Elimination	Active Contours
Tools	IRTK	IRTK	MATLAB	MATLAB+IRTK	MATLAB

4.3.2   Parameter Tuning

Our three-step automatic lumen border segmentation process has been applied to all eighteen IVOCT sequences. In practice, we use four GMM components to perform the EM estimation in the initial lumen border estimation (section 4.2.1). One component of the GMM is used for modeling the background label and three components are used to model the probability of the lumen border tissue. Four GMM components could better present the boundary of the lumen border compared to two components (one component for the background and another one for the lumen border tissue) and three components (one component for the background and the other two components for the lumen border tissue). In addition, there are no obvious differences if more than four components of GMM are used in the EM segmentation. For the graph-based segmentation, we divide an IVOCT sequence into sub-volumes of 64 frames (p=64) because of the memory limitation of our experimental PC (one 24 cores CPU + 64 GB RAM). This value (p=64) has achieved the best performance in our experiments. Subsequent sub-volumes share 2 frames (q=2) in order to guarantee that a segmentation is obtained using 3D GC. There are no differences if the value of sharing frames is larger than 2. Afterwards, we chose 0.5 as the value of λ of the region term weight in the initial lumen border detection step.

In the lumen border estimation (section 4.2.3), we use the active contour model functions as in Kroon [Kroon, 2010]. The number of iterations of the active contour model was set to 100 to avoid over-fitting. The number of the lumen border points obtained by the active contour was set to 200. We have tried the weights of the internal energy function α and β from 0.1 to 1 with step size 0.1 and found the better results are obtained with the value 0.1. The small values of α and β avoid the estimated lumen border contour tending to tense and rigid. In addition, the weights of the external functions (ω_{line} and ω_{edge}) were tested from 0.01 to 0.1 and from 1 to 3. Since the estimated lumen border is determined by the shape of lumen border rather than the intensity of lumen border, the value of ω_{line} is close to zero and found that the value 0.04 yields the desired lumen shape. The value of ω_{edge} was set to 2 since the estimated lumen border contour should be attracted to the lumen border shape edges. All parameters are then applied to all patient sequences. Segmentations are shown in the next subsection.

(a) Peri-Stent Slice (b) Intra-Stent Slice (c) Peri-Stent Slice
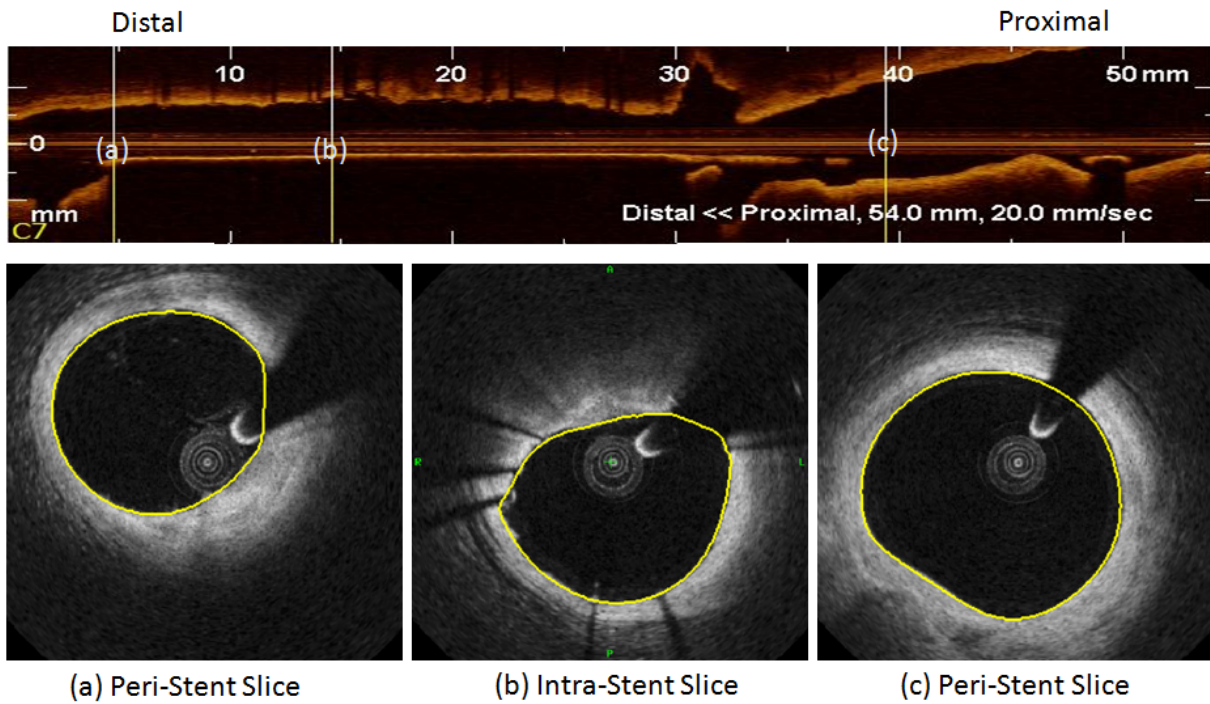
Figure 4.11: The figure shows that (a) and (c) are the lumen border segments in the PSV and (b) is the lumen border segment in the intra-stent volume of a patient sequence (P5).

4.3.3 Segmentation Results

Results of lumen border segmentation are shown in Figure 4.11-4.12. Firstly, our approach can segment the lumen border in the peri-stent volume (PSV) and intra-stent volume of an IVOCT sequence (Figure 4.11). PSV is the volume of plaque and neointima outside the stent. Intra-stent volume is the volume of neointima within the stent [Nakamura et al., 2001]. Examples of lumen border segmentations for wide and narrow lumens are shown in Figure 4.12. In addition, the comparison of the different approaches (EM and EM+GC) used to segment the lumen border are illustrated in Figure 4.14. A longitudinal view of the lumen border segmentation of one patient is shown in Figure 4.13.

We use two measurements to evaluate our results: one is the lumen area measurement (mm^2) and another is the accuracy of the lumen area segmentation (Dice overlap). In the lumen area measurement, we compared the results from our method, the commercial software (the Odeirena system) and the ground truth (the C7-XR system). The Odeirena system provides functions for lumen border segmentation and stent detection. Since it is not an open-source system, we

	(a)	(b)	(c)	(d)
Lumen Area (mm²)	6.58	3.39	2.38	1.24
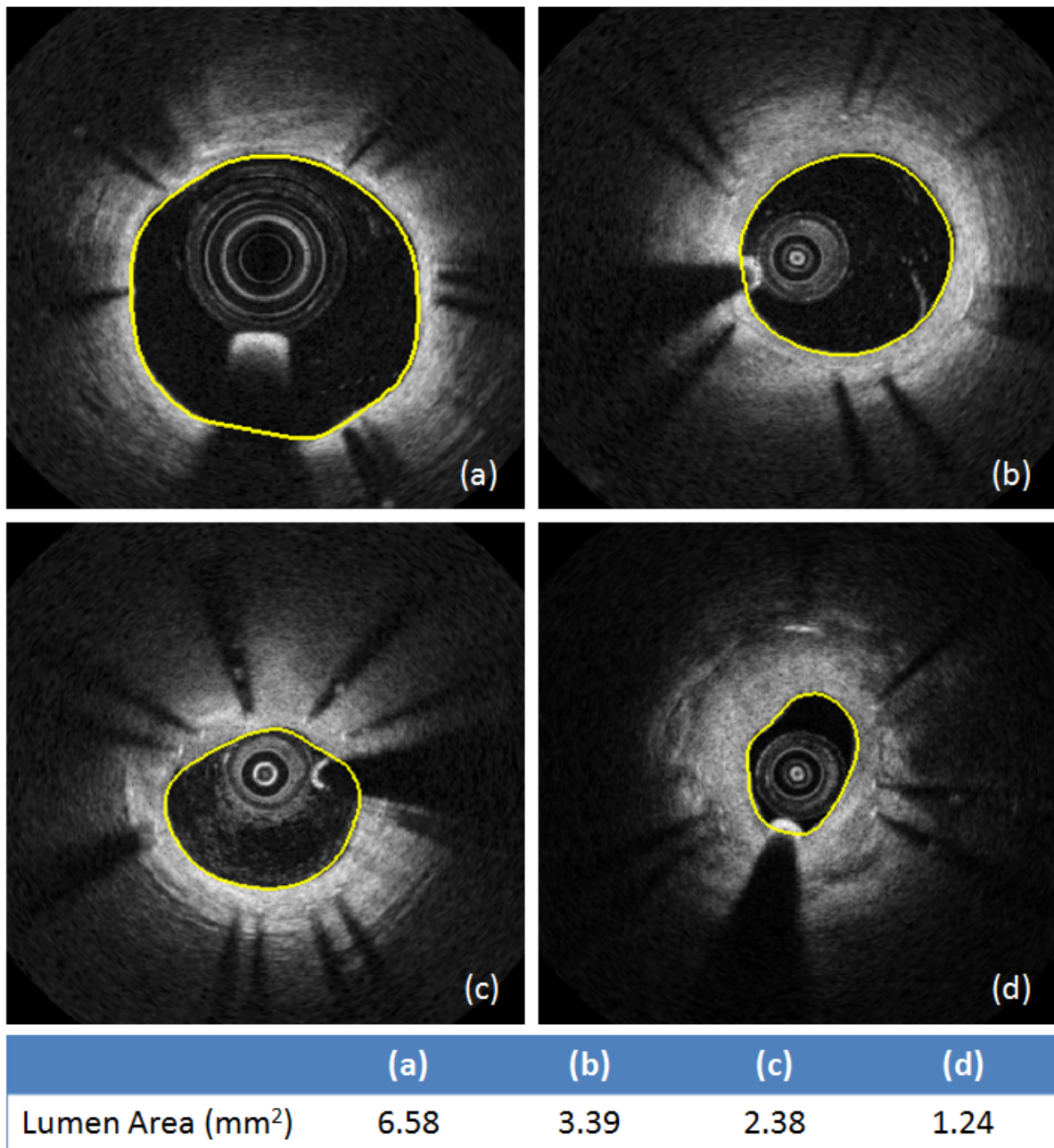
Figure 4.12: This figure shows the lumen borders can be accurately segmented in the wide or narrow vessels. (a) to (d) illustrates the lumen from wide to narrow.

compare segmentations to evaluate the segmentation accuracy between results obtained from our method and the Odeirena system. In practice, we choose 100 continuous slices in one IVOCT image sequence (P15).

In addition, the authors of the Odeirena system only provide information about how the stent detection is performed [Ughi et al., 2011] but not how the lumen segmentation. Therefore, it is difficult to speculate on how the system segment the lumen border. The comparison (Fig-
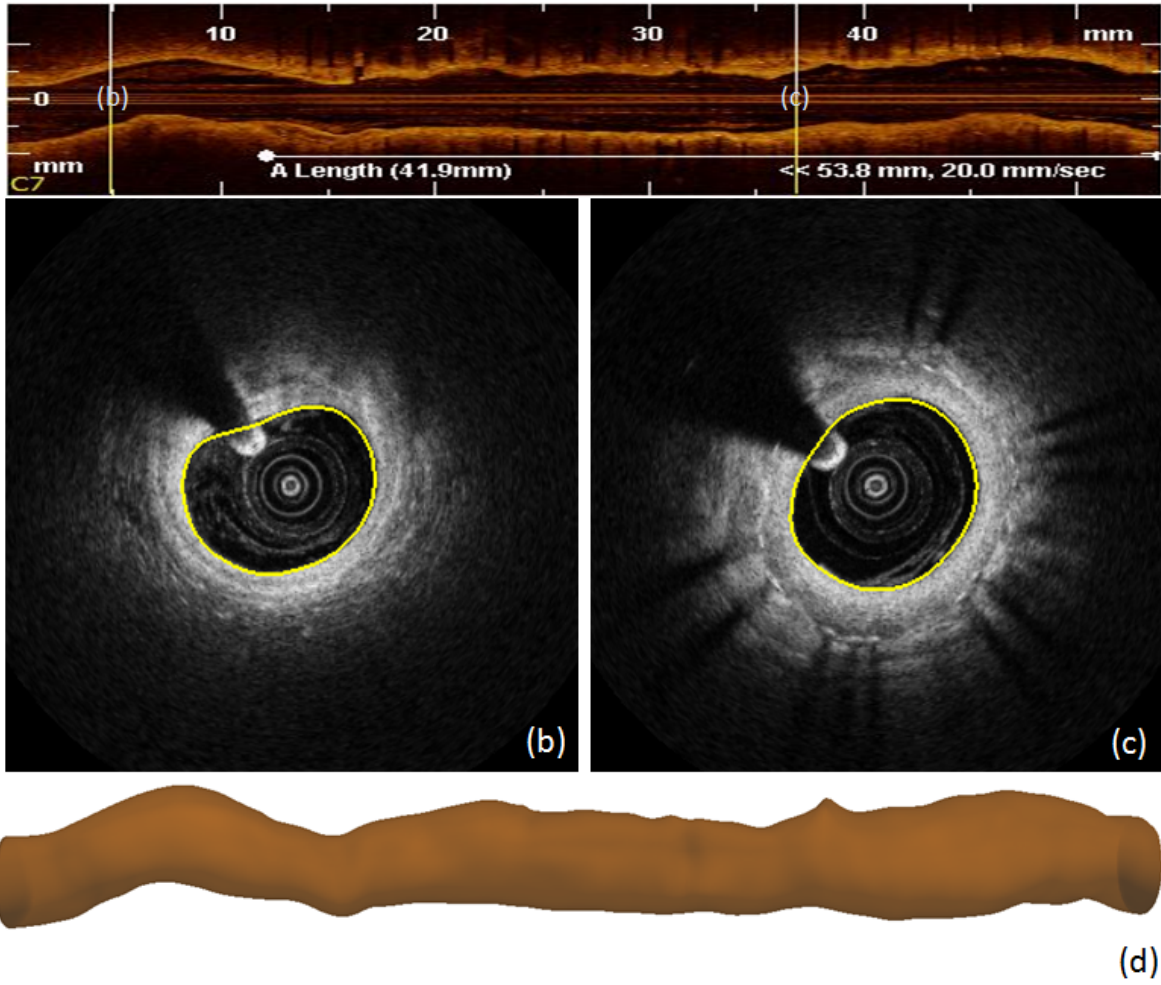
Figure 4.13: This figure shows a 3D longitudinal view of lumen border segmentation of a patient (P15).

ure 4.15) shows that our results are closed to the ground truth.

The second measurement is to compute the accuracy of the lumen area segmentation. The accuracy is estimated using the overlap (Dice) metric between the manual and automatic segmentation:

$$D = \frac{2\|S_a \cap S_b\|}{\|S_a\| + \|S_b\|} \tag{4.10}$$

Here S_a and S_b are the ground truth and the segmentations from EM, EM+GC and our method (Figure 4.16).

Figure 4.17 shows the Dice metrics for EM, EM+GC and our proposed approach of eighteen patients. In our proposed method, the average Dice overlap is 0.985 ± 0.01. Compared with the EM+GC method, our method achieves a high accuracy.
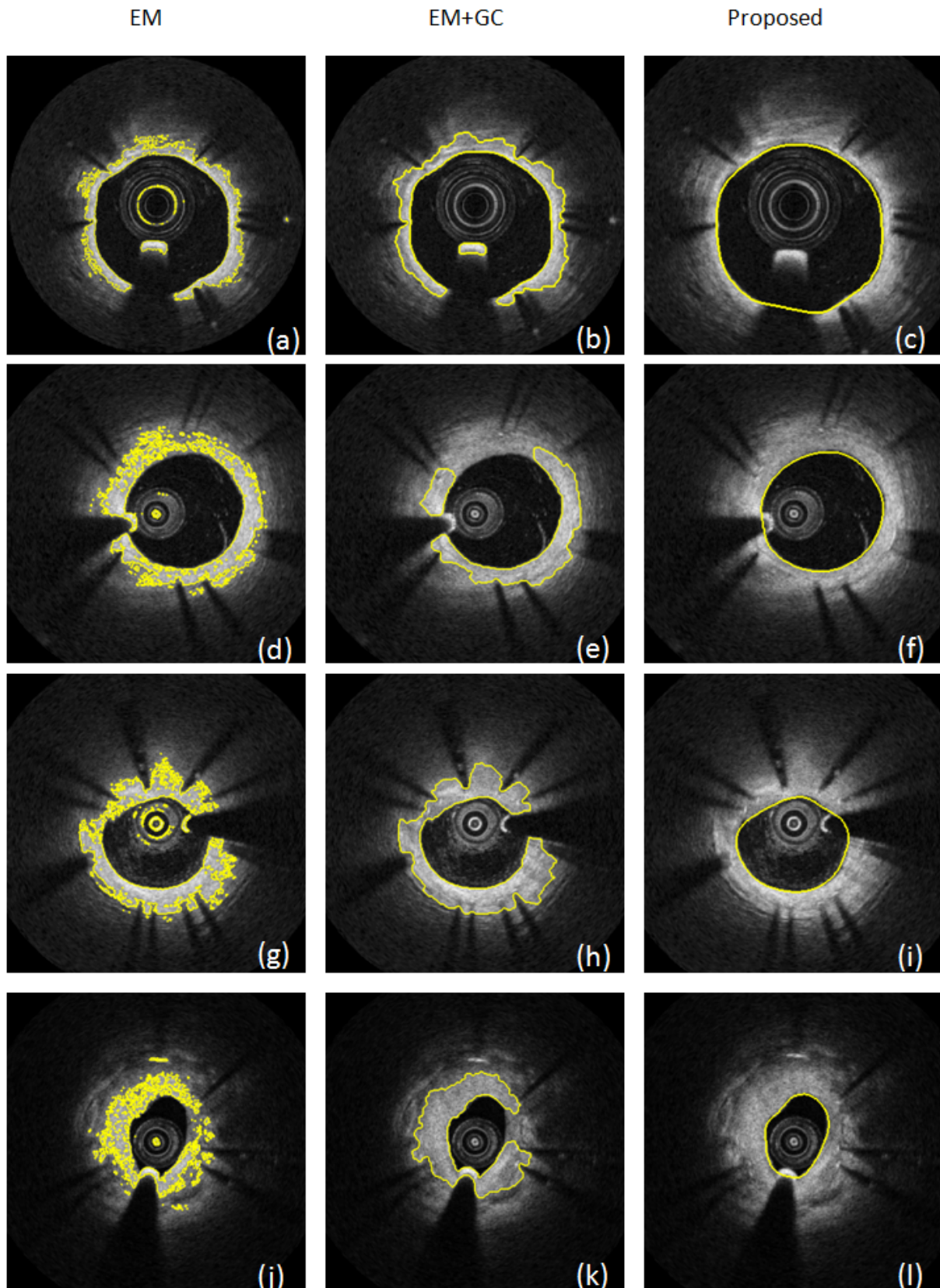
Figure 4.14: From left to right, top to down, each column shows segmentations of EM approach, EM+GC approach and the proposed approach.
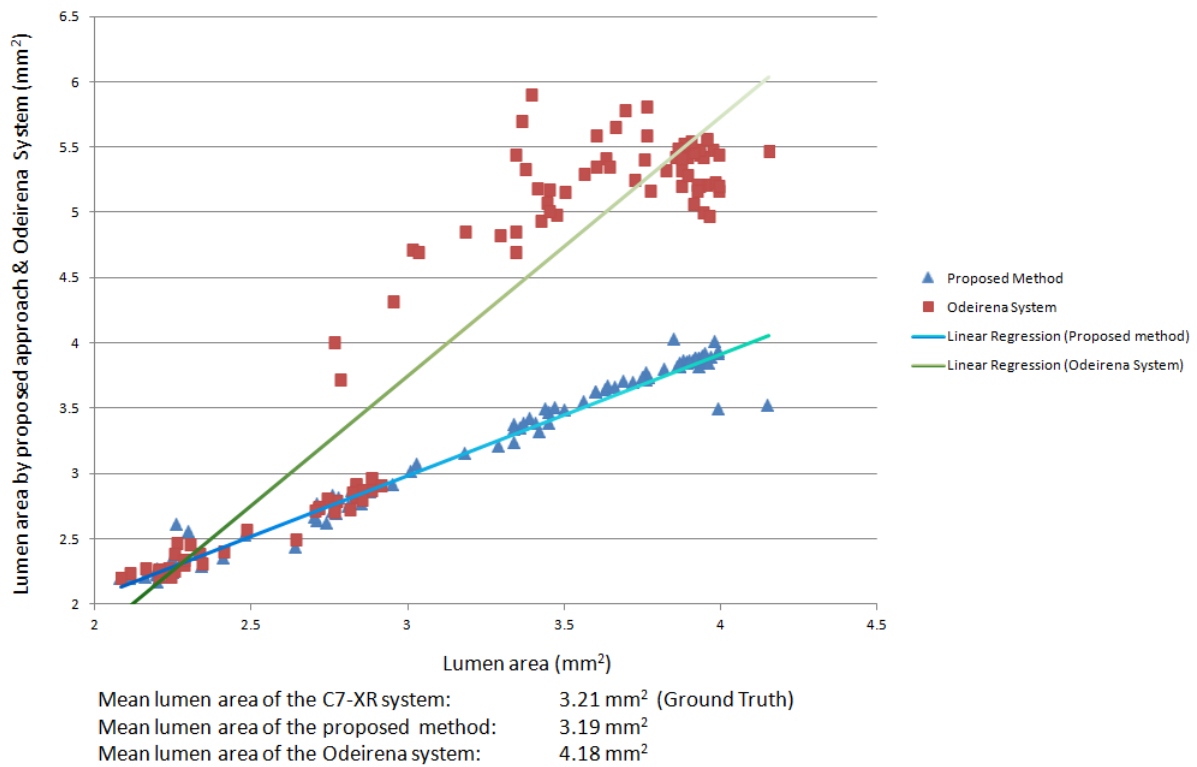
Figure 4.15: A comparison of 100 continues slices segmentations from our method, the Odeirena system and the ground truth (the C7-XR system) in a patient (P15). Our results are better than that obtained from the Odeirena system.
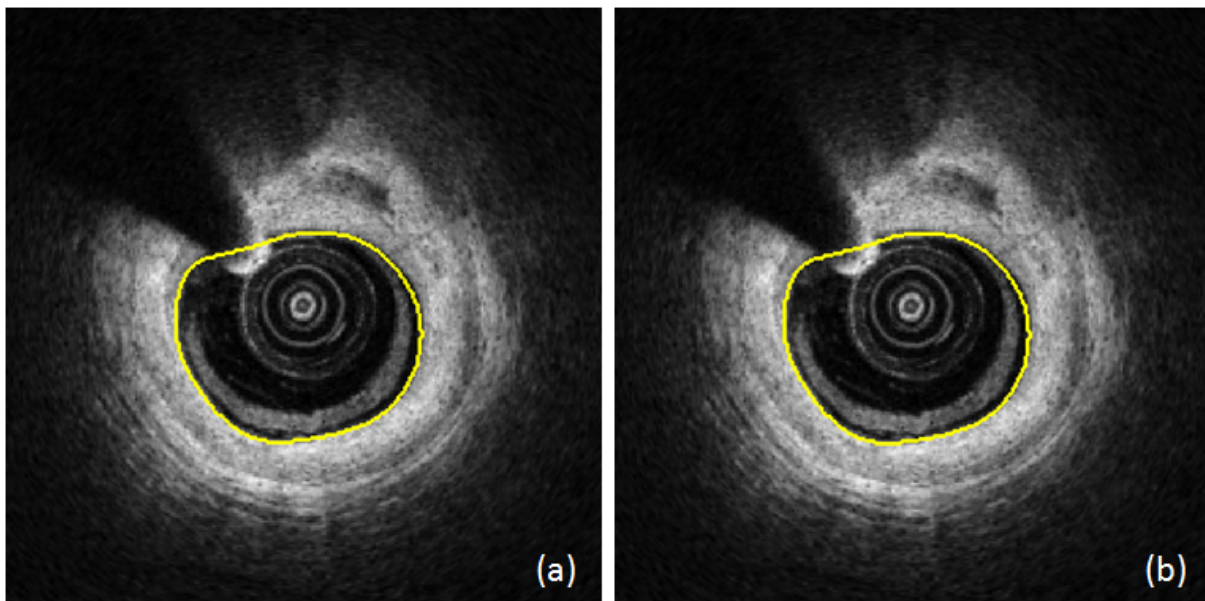
Figure 4.16: This figure shows lumen border segmentations of one slice in (a) the ground truth and (b) the proposed method.

4.4 Summary

In this chapter, we have presented a novel automatic method for the lumen border detection which uses EM&GC-based segmentation, convex hull detection and active contour models to
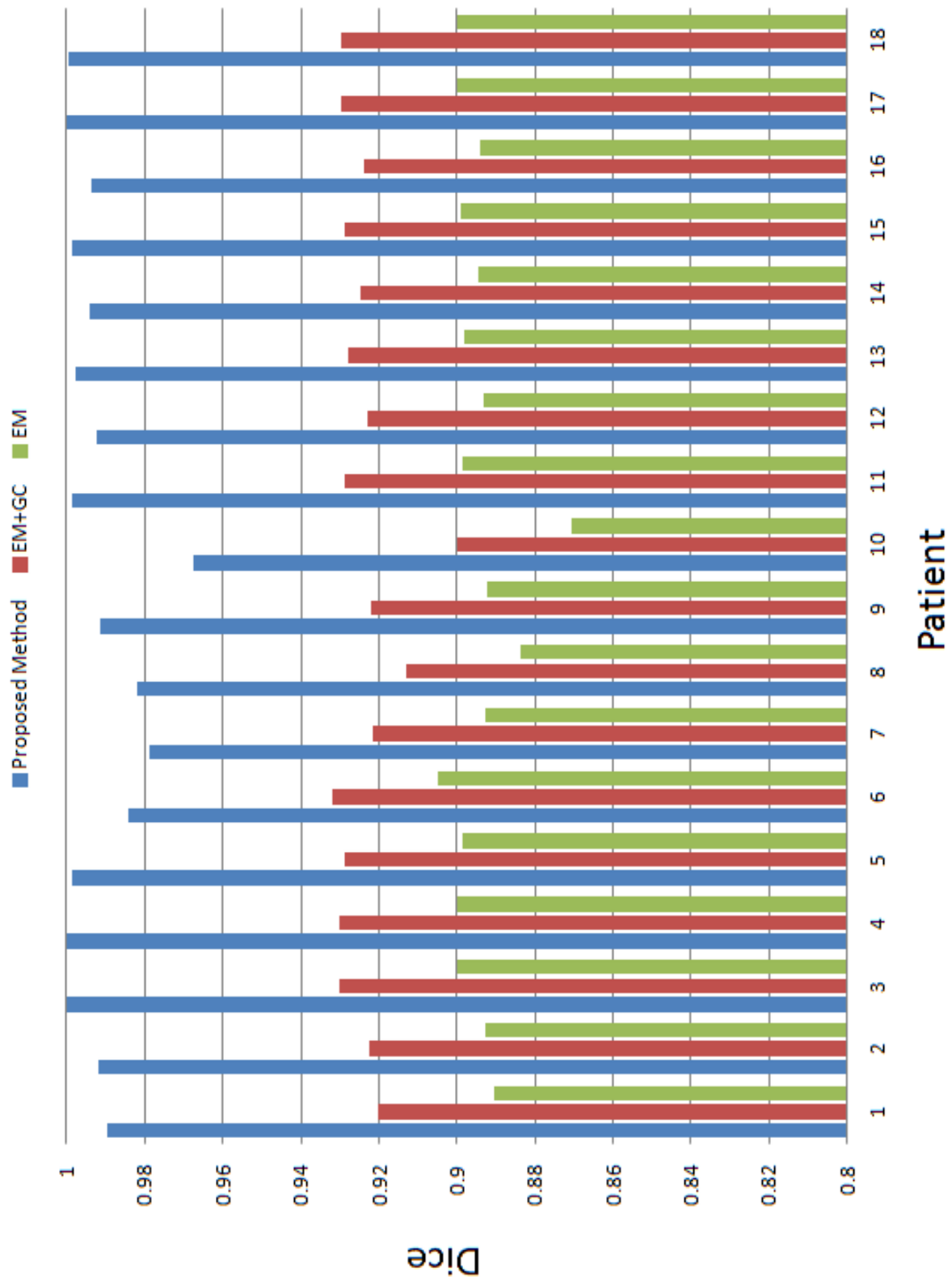
Figure 4.17: This figure shows that our results have achieved the high accuracy in all 18 patients.

obtain accurate segmentations. Our method focuses on images which have guide-wire shadow

artifacts. These artifacts would normally result in inaccurate lumen border segmentation. Our

method therefore estimates the possible lumen border position in the region affected by guide-wire shadows and segments the lumen border accurately.

We evaluate our proposed method using datasets containing lumen image sequences with different narrow severity. In each sequence, lumen border segments in PSV and intra-stent volume can be well represented. The proposed segmentation has been compared to two other segmentation schemes. The results show that our proposed approach achieved high overlap accuracy of lumen border segmentation. We also compare our results with the commercial system and show that our approach can accurately segment a lumen border. In addition, the longitudinal view of 3D lumen border segmentation is also provided. With accurate lumen border segmentation, the stent struts can be precisely segmented. A novel stent struts detection framework is described in the next chapter. In addition, this accurate lumen border segmentation can be an essential preliminary step in the neointima segmentation and the proposed segmentation approach is mentioned in Chapter 6.

Chapter 5

Stent Detection

5.1 Introduction

Treatment options of CHD include a catheter procedure (PTCA/angioplasty or stent implantation) and open-heart bypass surgery. PTCA and stent implantation are minimally invasive procedures performed to improve blood flow in narrow coronary arteries. A PTCA/stenting procedure is performed in a similarly fashion as a cardiac catheterisation, utilising local anaesthesia and sedation. In PTCA, a balloon-tipped tube, or catheter, is transiently inflated within the coronary artery to open the narrowing, or stenosis. The balloon catheter is then removed. Frequently, a stent is implanted during a PTCA procedure. Figure 5.1 illustrates the procedures of PTCA and stent implantation.

A stent is a flexible metal wire mesh tube that holds the newly expanded artery open. It is usually delivered into the lumen in reduced size form using a catheter and engages the lumen wall when it reaches the desired location. Figure 5.2 shows a cross-sectional image combined with stent struts. In general, stent struts typically appear as bright, signal-intense structures with dorsal shadowing (ellipses and rectangles in Figure 5.2(b) and (c)). The stent area is used for analysis of NIH thickness (a circle in Figure 5.2(b)). In addition, the width of stent area can also be used to predict angiographic restenosis [McDaniel and Douglas, 2011].
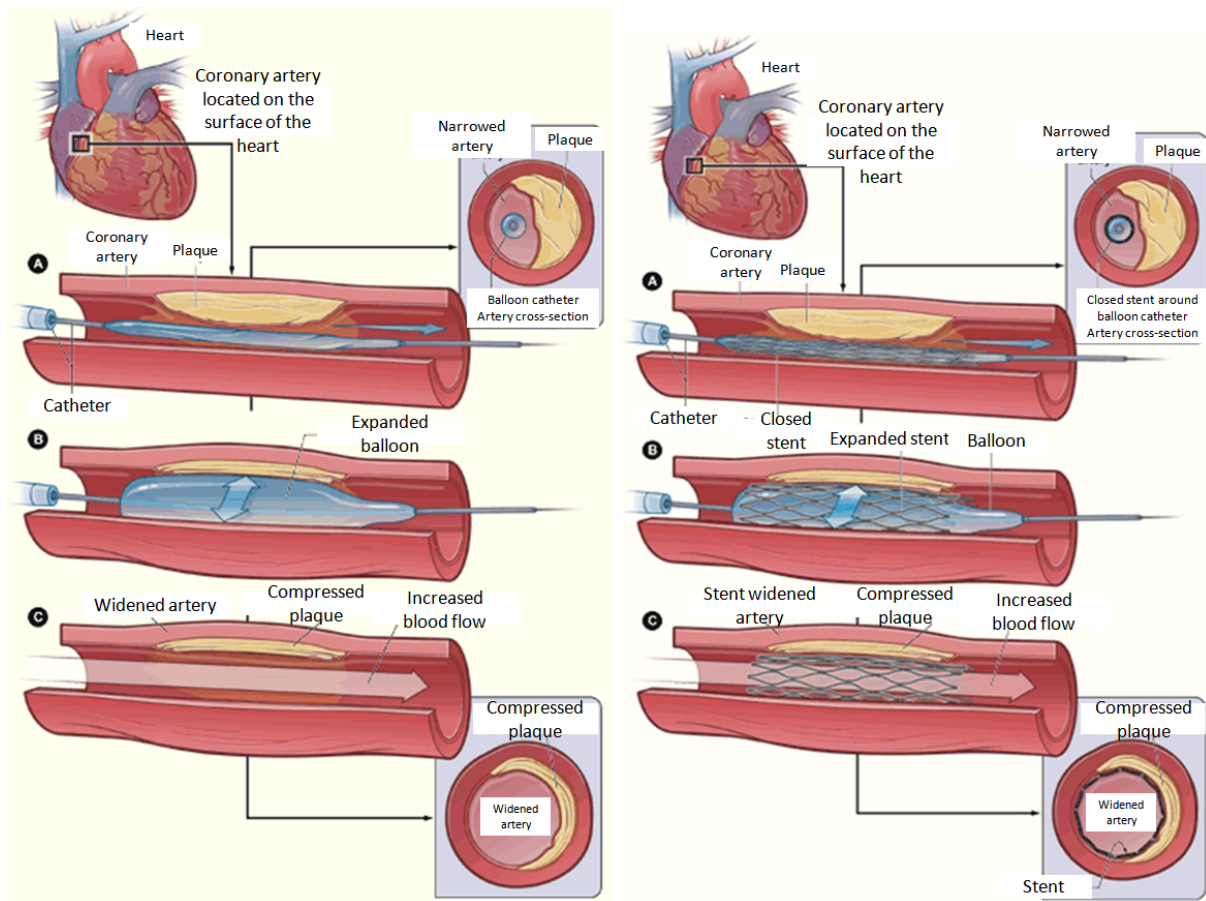
Figure 5.1: This figure shows how PTCA and stent implantation are implemented in the narrowing coronary artery. (A) First, a catheter is delivered to the narrowing vessel segment and (B) inflated to open the narrowing section. (C) Finally, the balloon catheter is removed after balloon expansion (left) and a stent is implanted (right). From [Berke, 2007].
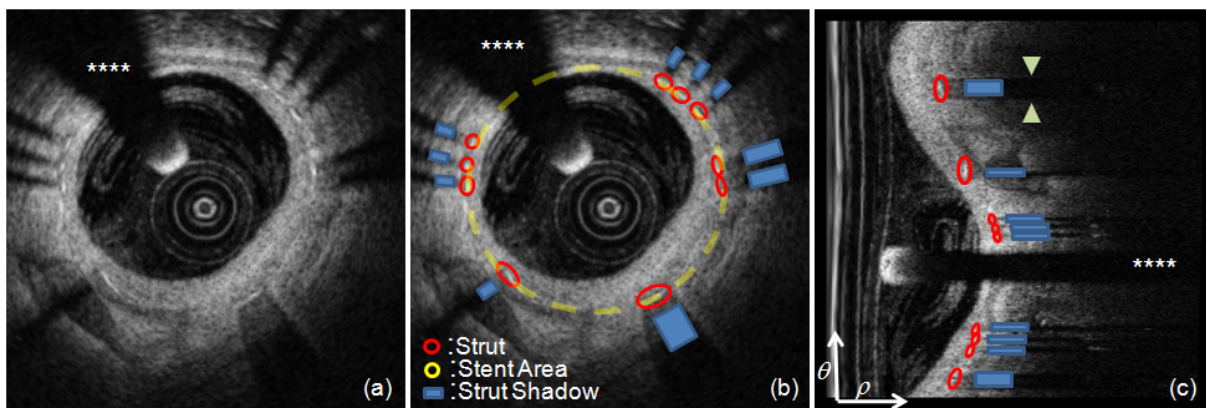
Figure 5.2: This figure shows a cross-sectional image that contains stent struts. (a) and (b) show the images presented in a Cartesian coordinate system and (c) shows the image in polar coordinates. The guide-wire shadow artifact is marked '****'. The stent struts are represented by ellipses and strut shadows are rectangles behind stent struts. The stent area is illustrated by a circle.

Detecting the stent strut position is highly important for stent placement evaluation and its follow-up analysis of CHD. According to the appearance of the struts positions in an image, stent struts can be classified into three categories: coverage, apposition and malapposition. When an implanted stent is located at the lumen boundary without tissue coverage, this is termed stent apposition (Figure 5.3(b)). Following stent implantation, the stent struts which are covered by neointima tissue are referred to as covered stent struts (Figure 5.3(a)). Stent malapposition, or incomplete stent apposition (ISA), refers to the lack of contact between stent struts and the underlying arterial wall and may cause LST (Figure 5.3(c)). It normally happens in a curved vessel section or a branch of the vessel [Mortier et al., 2010]. When a stent strut is classified as malapposed, the distance between the strut and the vessel wall/lumen border is larger than $150\mu m$ [Matsumoto et al., 2007].

Since stent struts are bright reflections followed by dark shadows, recent studies [Dubuisson et al., 2009, Gurmeric et al., 2009, Kauffmann et al., 2010, Unal et al., 2010, Xu et al., 2011, Ughi et al., 2011, Wang et al., 2012, Bonnema et al., 2008, Lu et al., 2012, Tsantis et al., 2012] have proposed several methods for detecting stent struts by incorporating this observation and analysing endovascular IVOCT sequences. Bonnema et al. [Bonnema et al., 2008] used thresholds for strut reflection, shadow darkness, and concentrated energy along single A-line scan to detect stent struts. Dubuisson and Kauffmann [Dubuisson et al., 2009, Kauffmann et al., 2010] proposed that stent struts could be detected by combined morphological, gradient and symmetry operators together with active contour models. Strut shadows and the increasing signal transitions of gradient are the main components of this approach. Gurmeric and Unal [Gurmeric et al., 2009, Unal et al., 2010] used the angular intensity distribution of the image to identify the shadows and to detect the brightest pixels in the shadow region. In their approach, thresholding and Catmull-Rom splines are used to estimate the shape of the lumen border and stent struts. Ughi et al. [Ughi et al., 2011] applied thresholds for peak intensity, shadow intensity and slopes of increasing/decreasing intensity to define a strut. Xu et al. [Xu et al., 2011] employed an improved ridge detector using a steerable filter for computing the local ridge strength and orientation to detect struts with thick tissue coverage. Wang et al. [Wang et al., 2012] detected the brightest pixel in polar coordinates and clusters the candidate pixels
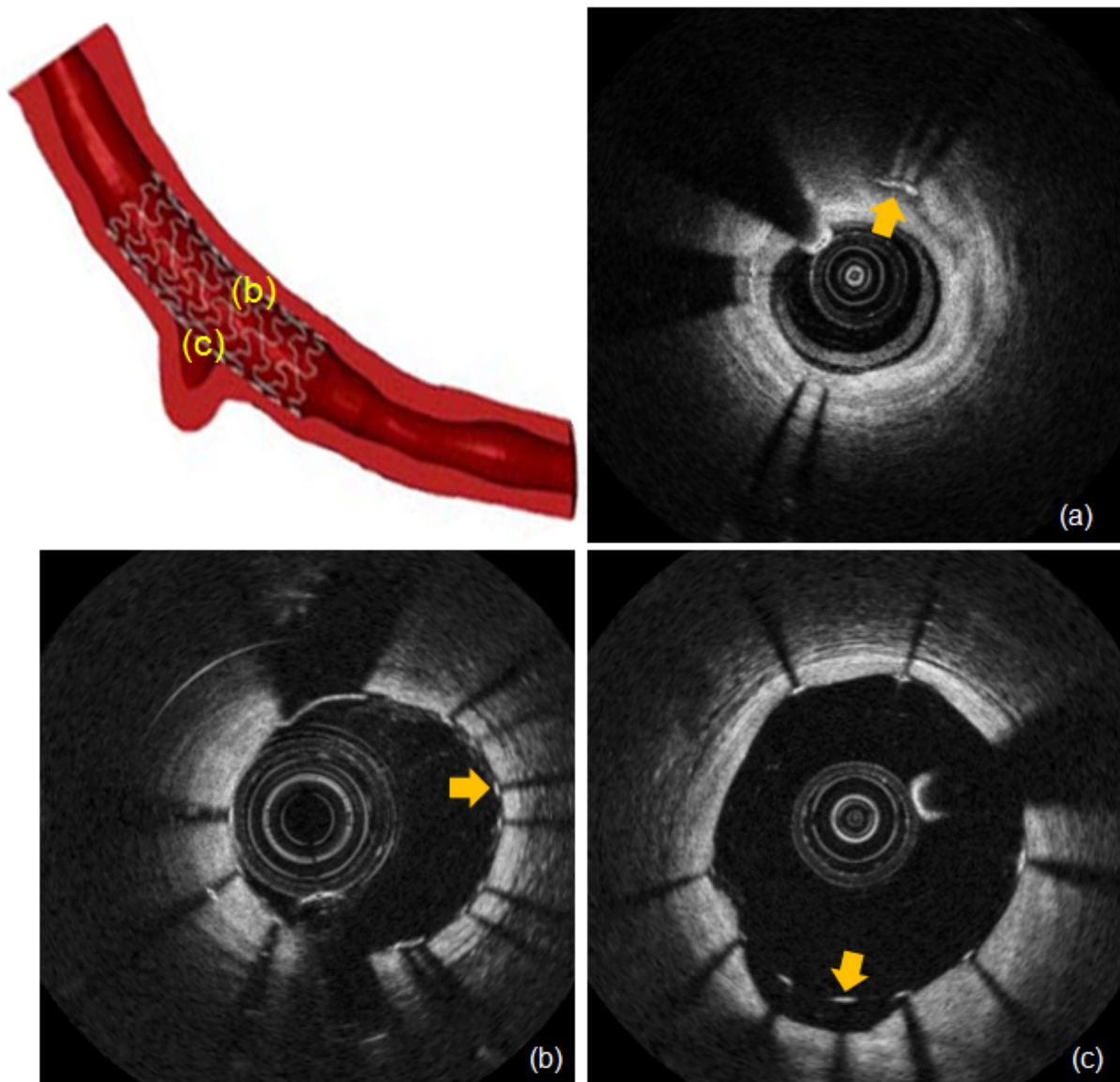
Figure 5.3: This figure shows the three types stent struts: (a) covered stent struts (stent coverage), (b) apposed stent struts (stent apposition) and (c) malapposed stent struts (stent malapposition). The illustration of stent apposition and malapposition can be observed in a stented vessel (top-left).

using edges identified by Prewitt compass filters [Sonka et al., 2007].

Feature extraction and classification methods can also be used in the stent strut detection. Bruining et al. [Bruining et al., 2011] used a basic set of features (mean, maximum and sum of values above mean) of each A-line scan and performed feature-based classification using a k-nearest neighbour classifier. Tsantis et al. [Tsantis et al., 2012] detected struts through introducing each strut wavelet response into a feature extraction and classification scheme in order to optimise the strut position detection. Lu et al. [Lu et al., 2012] detected stent struts by

using bagged decision trees classification which is less sensitive to noise compared to standard decision tree, giving improved accuracy and stability.

However, there were limitations in these early reports. Most of the algorithms only focused on the detection of the stent strut position without consideration of the weak intensity responses of the stent struts. In addition, accuracy of stent area estimation has not been mentioned in these studies even though some of the authors have discussed that the stent area can be estimated by splines [Gurmeric et al., 2009] or ellipsoids [Xu et al., 2011].

In this chapter, we propose an automatic algorithm for identification of the strut and its shadow zone, enabling the accurate and robust segmentation. The estimation of the position of the strut shadow zone is the key step which enables the strut segmentation. After identification of the shadow zone, we use a probabilistic map to estimate the stent strut position. This method can be applied to cross-sectional IVOCT images to detect the struts. The approach will be described in detail in the following sections. Section 5.2 introduces the segmentation framework in more detail. Section 5.3 illustrates the segmentation results from eighteen patients and section 5.4 summarises and concludes this chapter.

5.2   Stent Struts Detection

Our approach consists of two steps: We first detect the strut shadow zone and then segment the struts. A flowchart is presented as Figure 5.4. A cumulative intensity histogram is computed to detect the strut shadow zone. We assume that each stent strut shadow follows a stent strut. Thus, we use a Gaussian probability map to identify the stent strut position in every detected strut shadow zone. These steps will be described in detail in the following subsections. This two-step process is applied to each 2D slice of IVOCT image datasets. To perform our detection method, the image datasets are reformatted from a Cartesian coordinate system to a polar coordinate system (θ, ρ). It is important to mention that before any processing, denoising of the IVOCT images is carried out to improve the signal-to-noise ratio of the images.
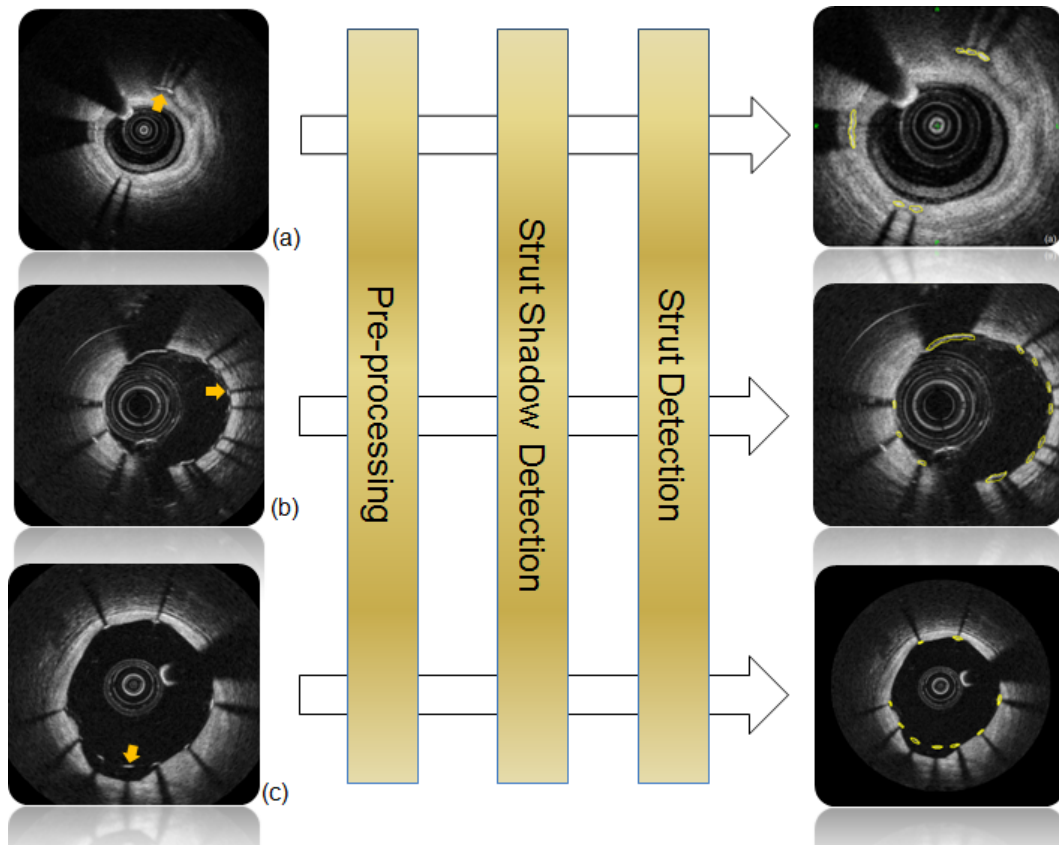
Figure 5.4: Three types of struts: (a) the covered struts, (b) the apposed struts and (c) the malapposed struts are estimated by the strut detection framework.

5.2.1 Preprocessing

The preprocessing facilitates the detection of the shadows and struts. First, image noise is removed. We utilise the transform-based block-matching 3D (BM3D) filter [Dabov et al., 2007] to denoise the images. The BM3D is widely recognised as a state-of-the-art denoising technique. It is based on the fact that an image has a locally sparse representation in the transform domain. This sparsity is enhanced by grouping similar 2D image patches into 3D groups. Due to the similarity between the grouped blocks, it enables a highly sparse representation in 3D transform domain, so that the noise can be well separated by shrinking the coefficients.

After denoising, we utilise a Hessian-based filter [Frangi et al., 1998] to enhance the shadow zone structures since the intensity between shadow zone structures and the surrounding areas is similar in some cases (Fig.5.2(c)). The Hessian-based filter can be used to enhance line- or vessel-like structures and the shadow zone structures are represented as rectangle-like structures
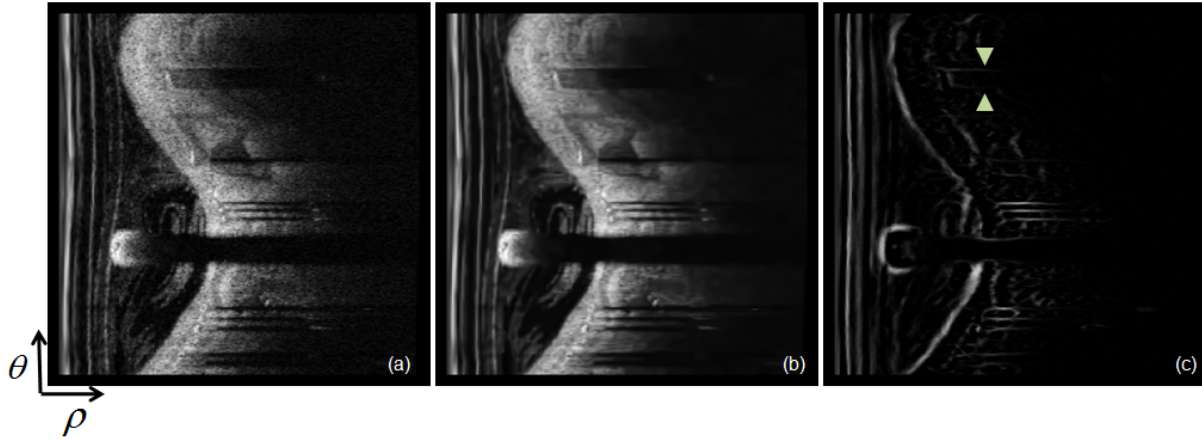
Figure 5.5: This figure shows an example of denoising and strut shadow enhancement in the polar coordinates: (a) the original image; (b) the denoising result using the BM3D filter and (c) the strut shadows enhanced by a Hessian-based filter. Triangles indicate that the intensity between the shadow zone and the background is ambiguous and the Hessian-based filter could enhance the shadow zone structure.

in the polar coordinate. The result after denoising and filtering is shown in Figure 5.5(c) and can be used as *a prior* information in the shadow zone detection.

5.2.2   Strut Shadow Zone Detection

A strut can appear as a high contrast speckle with a variable length depending on the orientation of the IVOCT probe with respect to the stent. When the contrast of the strut is high, it produces a radial shadow zone that can be used to infer the presence or absence of a strut.

To identify the shadow zone, we first compute the cumulative intensity histogram along radius ρ for each angle θ to obtain the positions of the strut shadow zone. For this, we sum the intensity of each pixel along ρ for each θ. If a shadow exists in a column along the θ-axis, its cumulative intensity will be low. A Fourier representation (Fourier transform and inverse Fourier transform) of the cumulative intensity histogram is then computed to smooth the histogram (cyan curve in Figure 5.6).

We locate the valleys in the smoothed cumulative intensity histogram by using the zero-crossings of the histogram's gradient (green curve in Figure 5.6). A point where the sign of a function changes (e.g. from positive to negative), represented by a crossing of the axis in the graph of
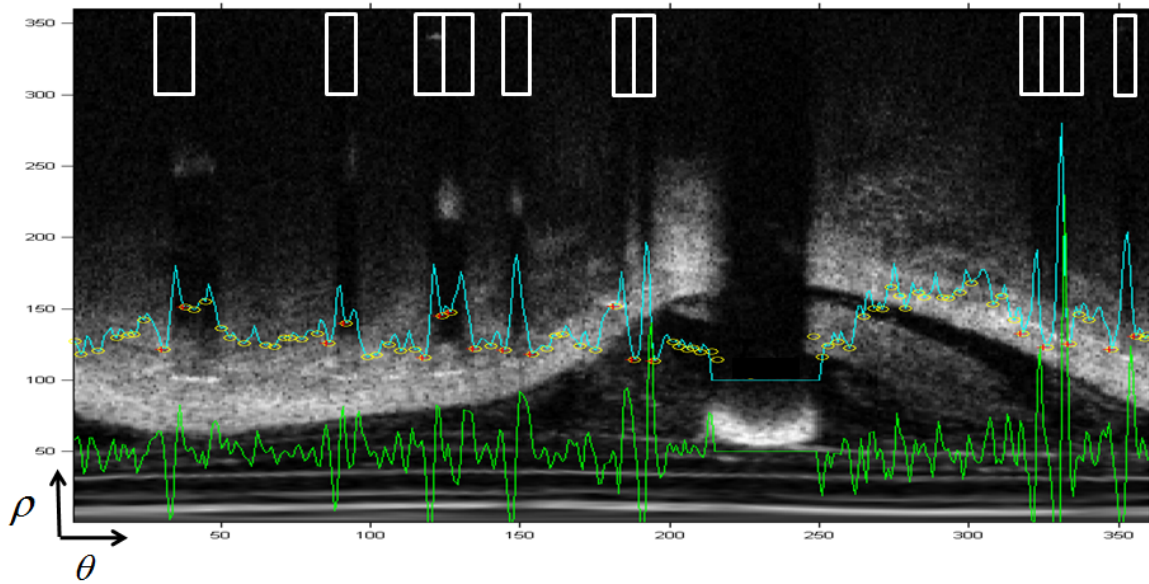
Figure 5.6: The cyan curve is the cumulative intensity histogram of an IVOCT image. The green curve is the first derivative of the histogram. Yellow circles represent the shadow zone candidates and red pluses show the shadow zone positions. A pair of red pluses represents the width of a shadow zone. Detection results of the shadow zone are marked as white rectangles.

the function is called a zero-crossing.

Let $v_i, i = 1, ..., N$ represents the valley points, each pair of valley points (e.g. v_1-v_2, v_2-v_3) describes a potential shadow zone position and the width of the shadow zones sh_{width} (yellow circles in Figure 5.6). $N - 1$ peak amplitudes $p_j, j = 1, ..., N - 1$ exist between N pairs of the valley amplitudes. $l_j = \|p_j - \min(v_i, v_{i+1})\|, i = 1, ..., N - 1, j = 1, ..., N - 1$ denotes the potential amplitude of the shadow zones $sh_{heights}$.

We then identify the shadow zones from the candidate shadow points by thresholding. The process of threshold selection is as follows: Firstly, we randomly select a slice from the IVOCT sequence and calculate its cumulative intensity histogram and the gradient of the cumulative intensity histogram. We then manually label each peak amplitude as $L_{shadow}, L_{non-shadow}$ and calculate the shadow amplitude l_j. We only sum the shadow amplitudes labelled as L_{shadow} and assume an average of the sum is a threshold $\bar{l}$. If a shadow amplitude l_j is larger than the threshold $\bar{l}$, it is labelled as a shadow zone (white rectangles in Figure 5.6) and the corresponding valley points are marked (red crosses in Figure 5.6).

After the threshold selection, we apply the threshold to the whole sequence. We calculate the

cumulative intensity histogram and its gradient in every slice. With the selected threshold, the shadow zones can be detected. The next section explains how these shadow zones can be used to locate the stent struts.

5.2.3   Strut Segmentation

The appearance of a strut in an IVOCT image is not unique and uniform, so it is a challenging task to locate strut positions. A strut in the IVOCT image is located between the lumen border and the shadow zone (a covered strut, an apposed strut) or between the catheter and the lumen border (a malapposed strut). The lumen border can thus be used to differentiate between these three situations and can be estimated by the lumen border detection algorithm proposed in Chapter 4.

We construct a search area consisting of a strut, a shadow, the lumen border related to the shadow and surrounding regions in the θ- and ρ-direction (Figure 5.7 (a)). The width of the search area is the maximum of shadow zone amplitudes of the cumulative intensity histogram in a slice $S_w = \max(sh_{heights})$ and the height of the search area is twice the detected shadow zone width $S_h = 2 * sh_{width}$. This is because the strut shadow detection is performed along radius and angle ρ-θ coordinates not θ-ρ coordinates.

To detect the covered strut and the apposed strut, the task is to recognise a strut in the area where the strut intensity is weak and the intensity of its surrounding region is strong. An example of a wrong strut position (marked by '*') obtained by the highest intensity in the search area is shown in Figure 5.7(a) and (b). Therefore, prior information with respect to the search area is essential.

We build an a-priori probability map for each search area to enhance and locate the strut position. We first compute the cumulative intensity of the search area in the θ- and ρ-direction. We estimate the first potential strut location $p(x, y)$ where y is the peak of the cumulative intensity in the θ-direction and x is initialised as the center of the search area (between the lumen border and the shadow) in the ρ-direction. x is then iteratively updated using the
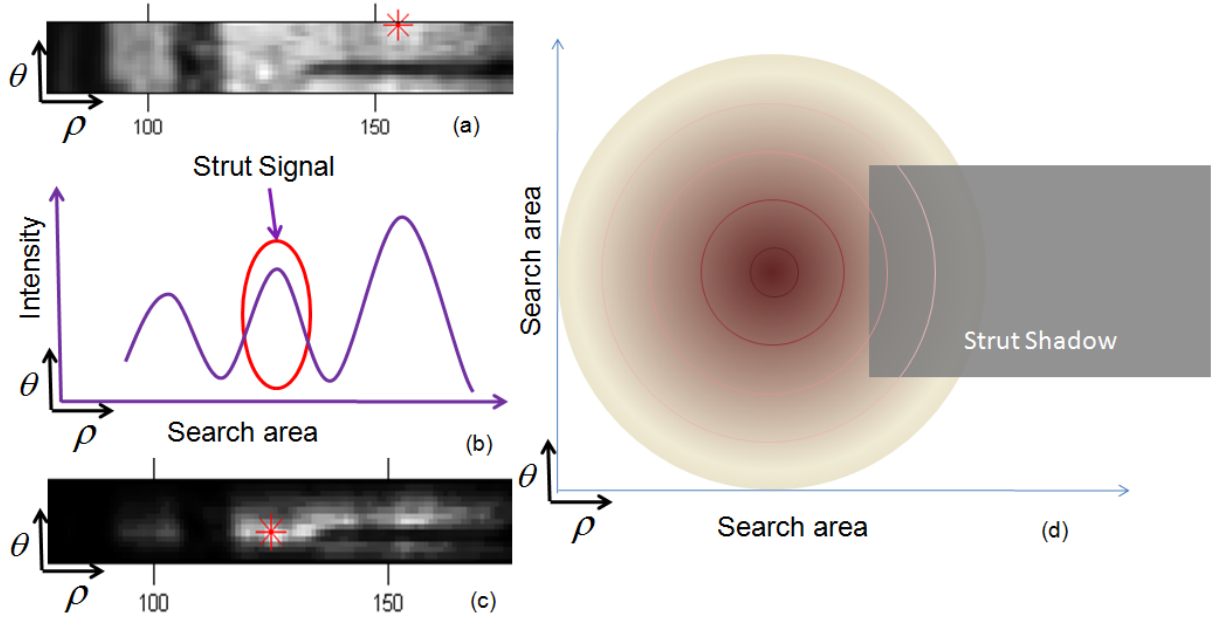
Figure 5.7: (a) a search area that includes a strut, a corresponding strut shadow zone and the surrounding tissues. The wrong strut position obtained by the highest intensity is marked by '*'; (b) the intensity illustration of the search area (a); (c) shows the correct strut position (marked by '*') obtained from the combination of (a) and (d) the prior probability map of the search area.

previously estimated strut position. We use a 2D Gaussian filter $G_{spatial}(p(x,y), \sigma_\theta, \sigma_\rho)$ with $\sigma_\theta = S_w/2$ and $\sigma_\rho = S_h/2$ for modeling the prior probability map. Figure 5.7(d) shows the construction of the prior probability map and it is computed as:

$$W^n(p(x,y)) = \begin{cases} G_{spatial}(p(x,y), \sigma_\theta, \sigma_\rho), & \text{if } n = 1 \\ G_{spatial}(p(x_{pre-strut}, y), \sigma_\theta, \sigma_\rho), & \text{if } n > 1 \end{cases} \tag{5.1}$$

Here $x_{pre-strut}$ is the previous strut's location in the ρ-direction. Thus, the strut probability J (Figure 5.7(c)) can be defined as:

$$J^n(p(x,y)) = I^n(p(x,y)) \cdot W^n(p(x,y)) \tag{5.2}$$

where I^n is the normalised intensity of the search area. The strut position (marked by '*') can be inferred as the highest probability of the output J (Figure 5.7(c)) with the a prior probability map (Figure 5.7(d)).

To identify stent malapposition, a different probability map is required. Since the position of
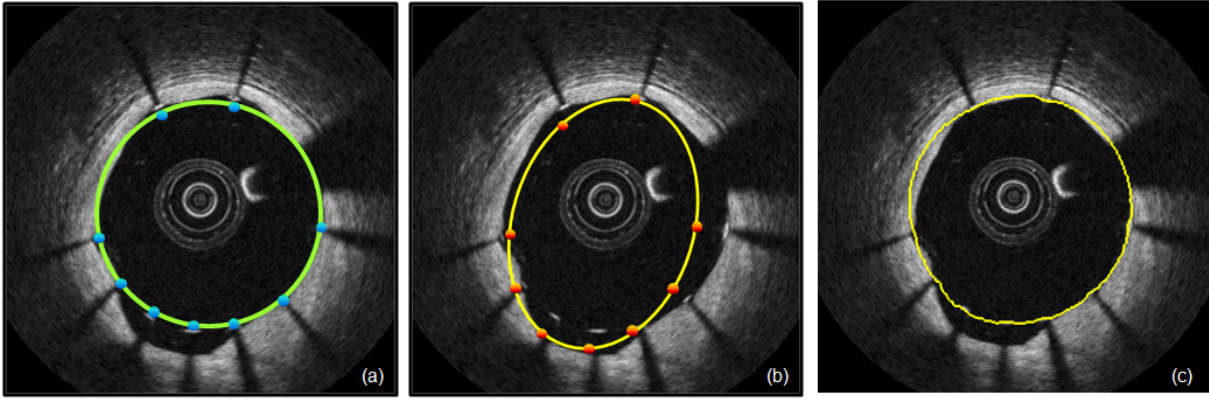
Figure 5.8: (a) Stent area estimation by fitting a circle; (b) stent area estimation by fitting an ellipse; (c) stent area estimation by connecting the stent struts.

a malapposed strut is between the catheter and the lumen border, the first strut is estimated from the stent area. The stent area is the cross-sectional area of stent struts in a 2D image slice and is estimated by ellipse-fitting. We use the estimated elliptic strut position to initialise x and update x from previous strut position and the estimated elliptic strut position iteratively. The probability map is defined as:

$$
W^n(p(x,y)) = \begin{cases} G_{spatial}(p(x_{ellipse}, y_{ellipse}), \sigma_\theta, \sigma_\rho), & \text{if } n = 1 \\ G_{spatial}(p(x_{pre-strut}, y), \sigma_\theta, \sigma_\rho), & \text{if } n > 1 \end{cases} \tag{5.3}
$$

Finally, we use region growing to segment the strut from the strut position (a seed point). Mathematical morphology (dilation) is also used to refine the segmentation.

After the stent struts have been detected, we estimate the stent area by connecting the stent struts in the polar coordinate space. If the stent area is estimated by fitting a circle (Figure 5.8(a)) or an ellipse (Figure 5.8(b)), the stent area estimation is inaccurate (over-estimated or under-estimated). Therefore, we connect the detected stent struts as line segments in the polar coordinates and reformatted these line segments into a Cartesian coordinates (Figure 5.8(c)). This straightforward process can overcome the sensitivity of stent area estimation.

Table 5.1: This table shows the number of stent installed in the patient data.

Number of stent	Patient ID
2	P1
1	The other 17 patient sequences

Table 5.2: This table shows the implementation tools for strut shadow zone detection and strut segmentation.

Steps	Pre-processing		Strut Shadow Zone Detection	Strut Segmentation
	Denoising	Image Enhancement		
Tools	MATLAB	IRTK	IRTK+MATLAB	IRTK+MATLAB

5.3 Results and Discussions

5.3.1 Materials

Eighteen IVOCT image sequences were acquired with the C7-XR commercial system during a pullback rate of 20.0 mm/s. Each sequence has one or two stents installed in the coronary artery (Table 5.1). The lumen border segmentations obtained from Chapter 4 are also used in this chapter. The implementation tools for the strut detection approach based on MATLAB and IRTK (see Table 5.2).

5.3.2 Parameter Tuning

In the pre-processing, the BM3D denoising method [Dabov et al., 2007] works well for images corrupted by Gaussian noise. It uses a parameter σ to adjust the amount of smoothing, i.e. the larger σ the more smoothing is performed in the image. We apply a fixed σ to represent strut structures well and avoid over-smoothing. In practice, the σ is set to 15.

5.3.3   Results

The apposed stent struts, neointima covered stent struts, malapposed stent struts and their 3D reconstructed models are shown in Figure 5.9, Figure 5.10 and Figure 5.11. Our method can distinguish the different types of stent struts that appeared in the eighteen patients. To evaluate the accuracy of stent area, we use the overlap metric (Eq. (4.10)) and a Bland-Altman plot between the stent area of the proposed approach and manual segmentation (see Figure 5.14-Figure 5.19 at the end of this chapter). Manual stent struts and manual stent areas of all patient sequences are labelled by Dr. Hiroto.

The average Dice overlap for all cases is 0.98 but we have noticed that our results tend to over-estimate the stent area since a sensitive shadow zone selection is used. If the intensity between image background and strut shadows is ambiguous, it leads to a sensitive shadow selection threshold which in turn cause inaccurate stent struts segmentations (Figure 5.12). The stent struts appear in a non-stenting area. We will discuss this problem in detail in the next subsection.

5.3.4   Discussion

In the following, we discuss the sensitivity of the shadow detection results for the proposed approach. The sensitivity of the shadow detection is due to the threshold used in the step of shadow detection (subsection 5.2.2). In the proposed approach, the threshold is obtained from one randomly selected slice and applied to whole sequences. However, this threshold results in over- or under-sensitive shadow detections leading to over-estimated stent struts or under-estimated stent struts (see Figure 5.13). For example, if the cumulative intensity of an image is lower than the threshold, the shadow zones are not selected (under-estimate). The inaccurate detection of the shadow zone causes inaccurate strut segments (Figure 5.13).

A possible method to address the sensitivity is to use the stent information such as the stent type used in a patient, the stent diameter, the thickness of the stent struts, and the shape of
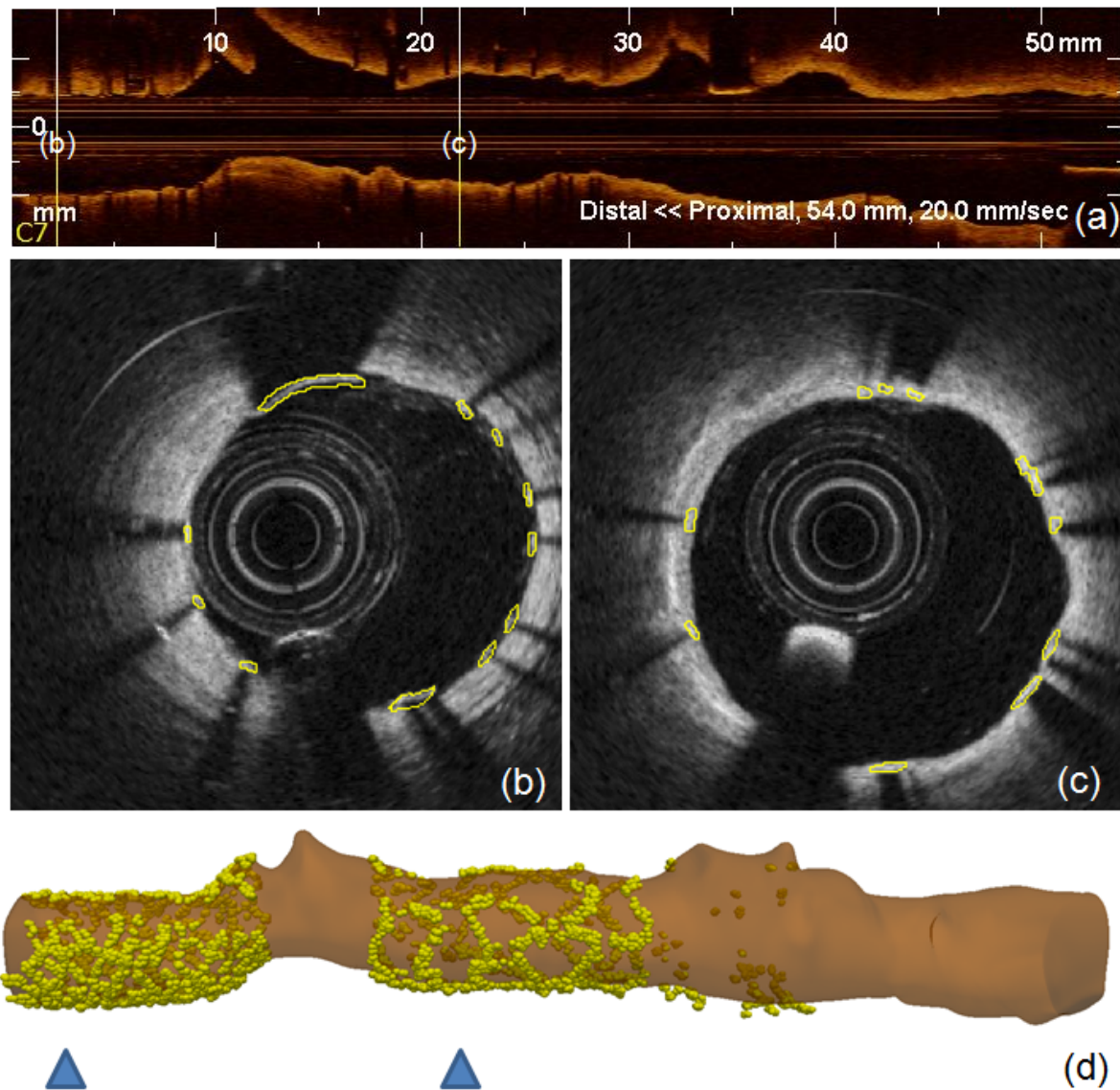
Figure 5.9: (a) shows a longitudinal view of a sequence (P1). Appositional stent struts can be identified in (b) and (c). (d) illustrates the extracted 3D stent model overlapped with the lumen segmentation from previous chapter (Chapter 4) for this patient.

stent struts. With these information, the positions of stent struts can be precisely estimated and the accurate stent area can be obtained.

An alternative method is to obtain the stent area from the neointima area plus the lumen area since neointima area equals to the stent area minus the lumen area. If the neointima area can be accurately estimated, this leads to accurate stent area and the positions of stent struts can be corrected. Therefore, we propose an approach to segment the neointima using multi-atlases without knowledge of stent properties (stent area and stent struts). The details of this method will be discussed in next chapter.
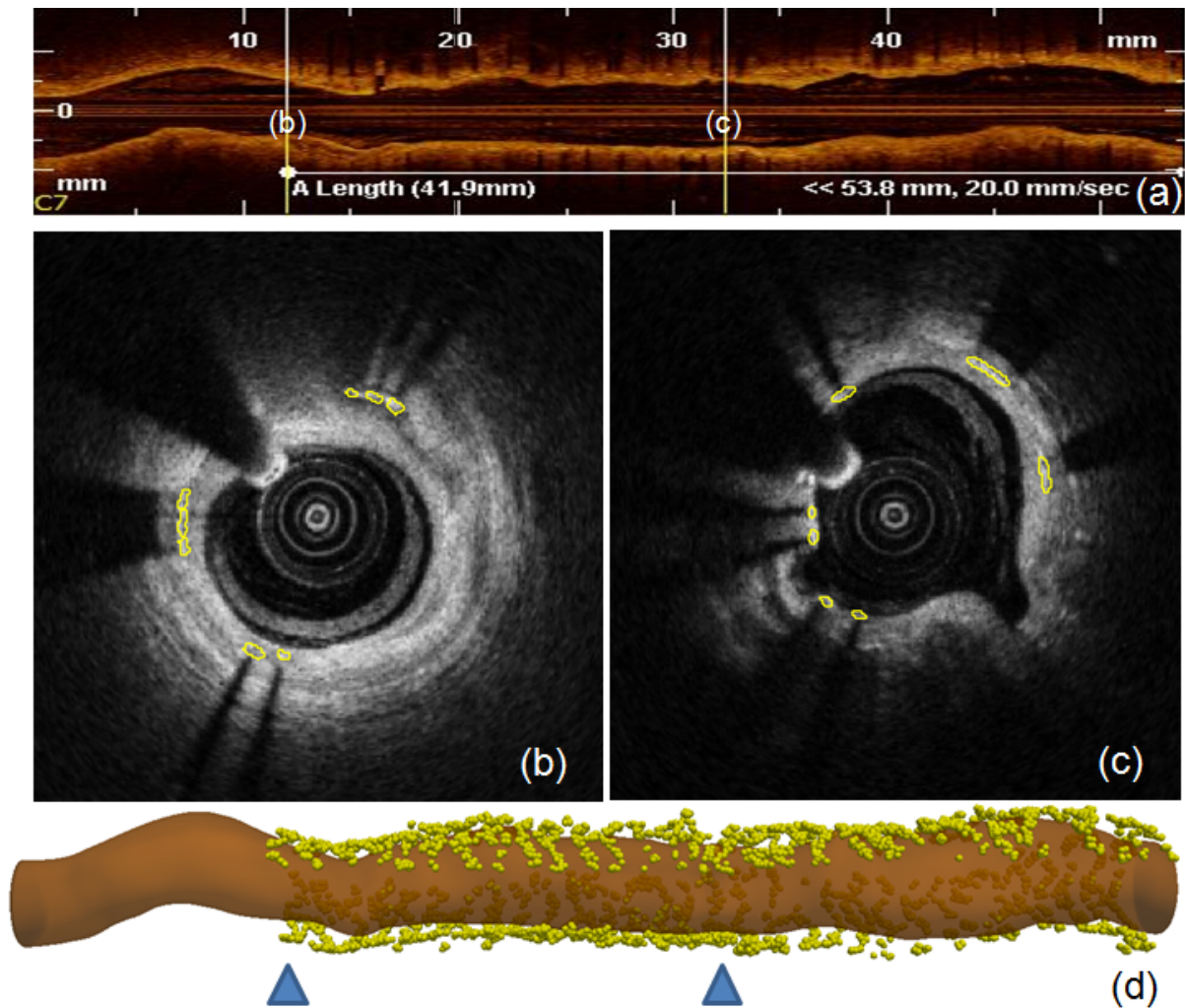
Figure 5.10: This figure shows covered stent struts can be identified in (b) and (c). (a) shows a longitudinal view of a sequence (P15) and (d) illustrates the 3D stent model overlapped with the lumen segmentation from previous chapter (Chapter 4) for this patient.

5.4   Summary

In this chapter, we automatically detected the struts of coronary stents present in IVOCT sequences. We proposed a novel method to detect the strut shadow zone and accurately segment and reconstruct the strut in 3D. The estimation of the position of the strut shadow zone is the key requirement which enables the strut segmentation. After identification of the shadow zone, we used a 2D Gaussian filter as a-priori probability map to estimate stent strut positions. This method can be applied to cross-sectional IVOCT images to detect the struts.

Validation was performed in eighteen in-vivo IVOCT sequences and the strut segments were
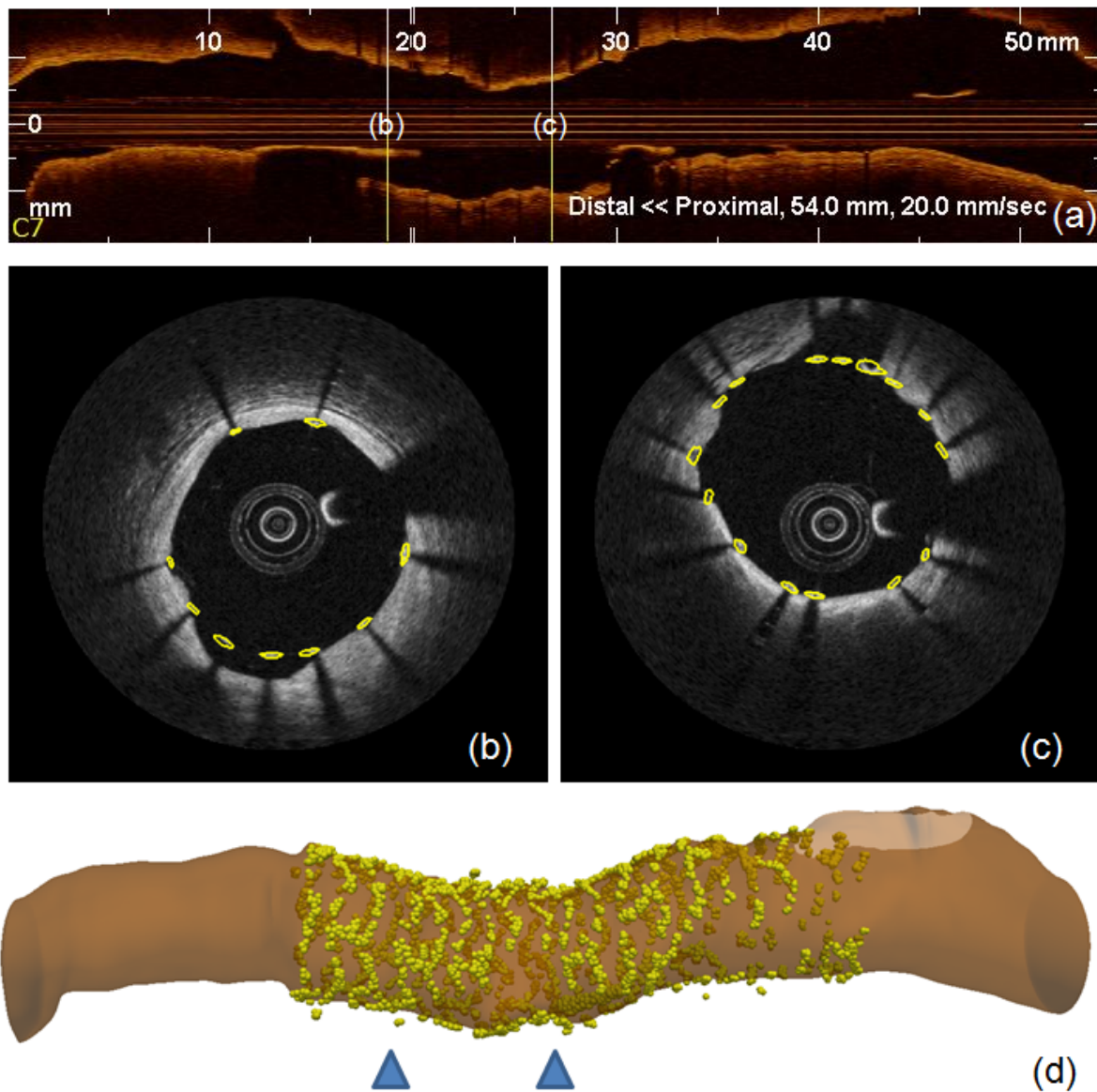
Figure 5.11: This figure shows malapposed stent struts can be identified in (b) and (c). (a) shows a longitudinal view of a sequence (P6) and (d) illustrates the 3D stent model overlapped with the lumen segmentation from previous chapter (Chapter 4) for this patient.

clearly identified in all sequences. Our method can accurately identify all three types of stent struts even though two stents are implanted in a patient. In addition, we evaluated our proposed method for stent area estimation. Compared to the manual segmentation, the results showed that the segmentations of our proposed approach are overestimated in the overlap of stent area, since the sensitive strut shadow selection method was used.

The sensitivity of our proposed method remains a problem since it will cause inaccurate stent area and neointima segmentation. To overcome sensitivity, we propose an atlas-based approach to segment the neointima without information of stent properties (stent area and stent struts).
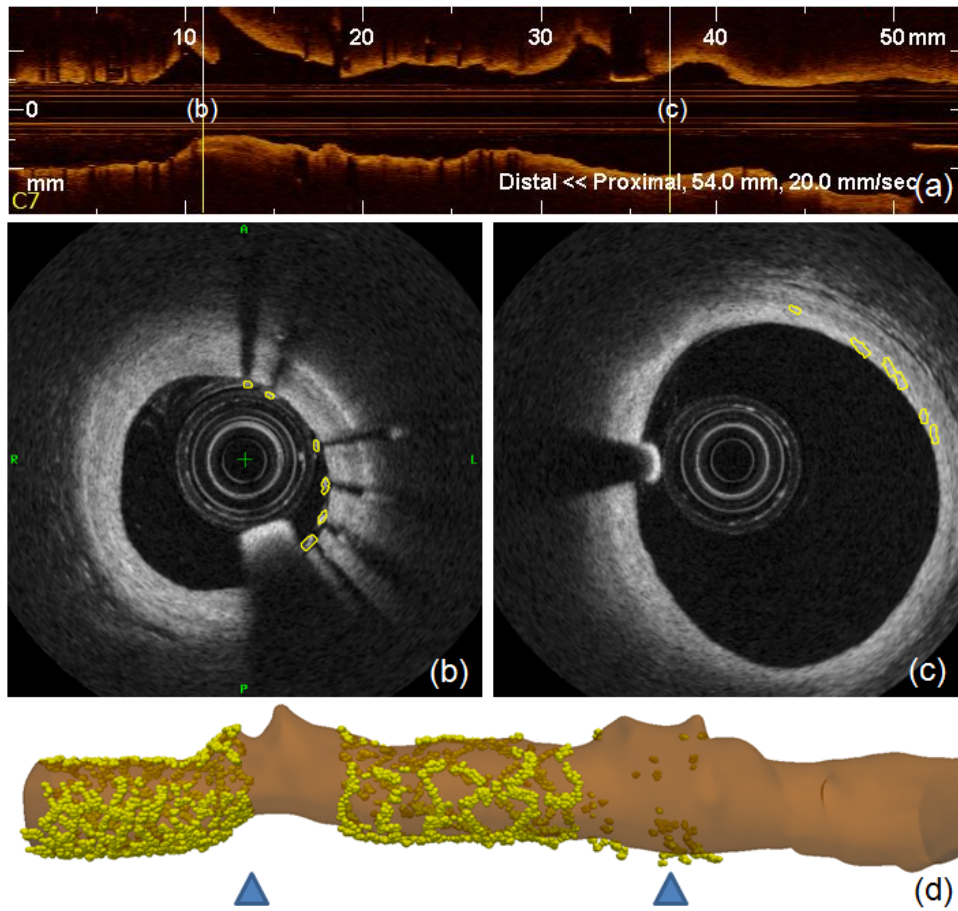
Figure 5.12: (a) a longitudinal view of a sequence where two stents are implanted (P1). (b) stent struts appear at the end of the first stent and (c) inaccurate stent struts appear at in the non-stent volume. (d) illustration of the 3D stent model of this sequence.
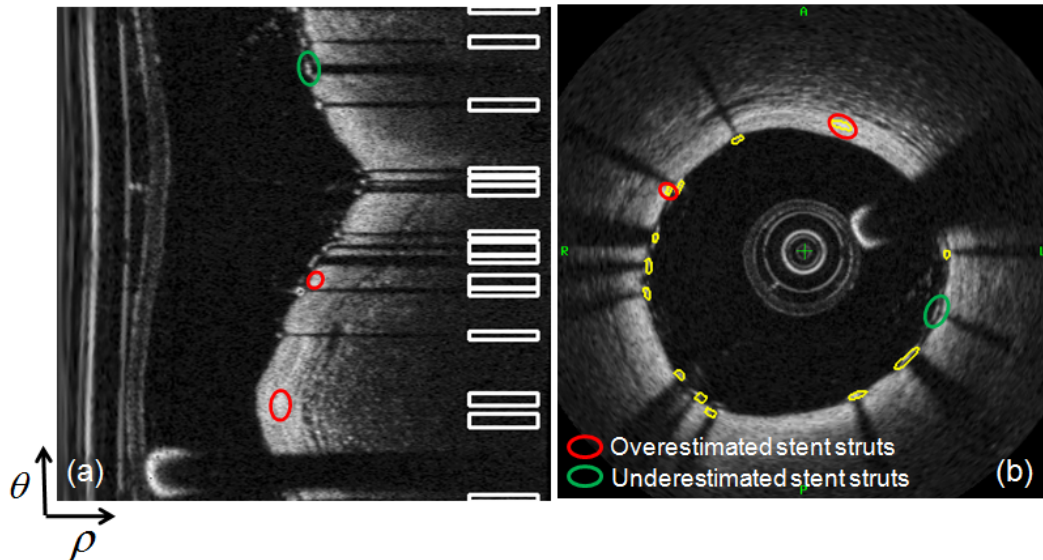
Figure 5.13: This figure shows that the sensitivity threshold causes inaccurate shadow zone detections and strut segmentations in (a) the polar coordinates and (b) the Cartesian coordinates.
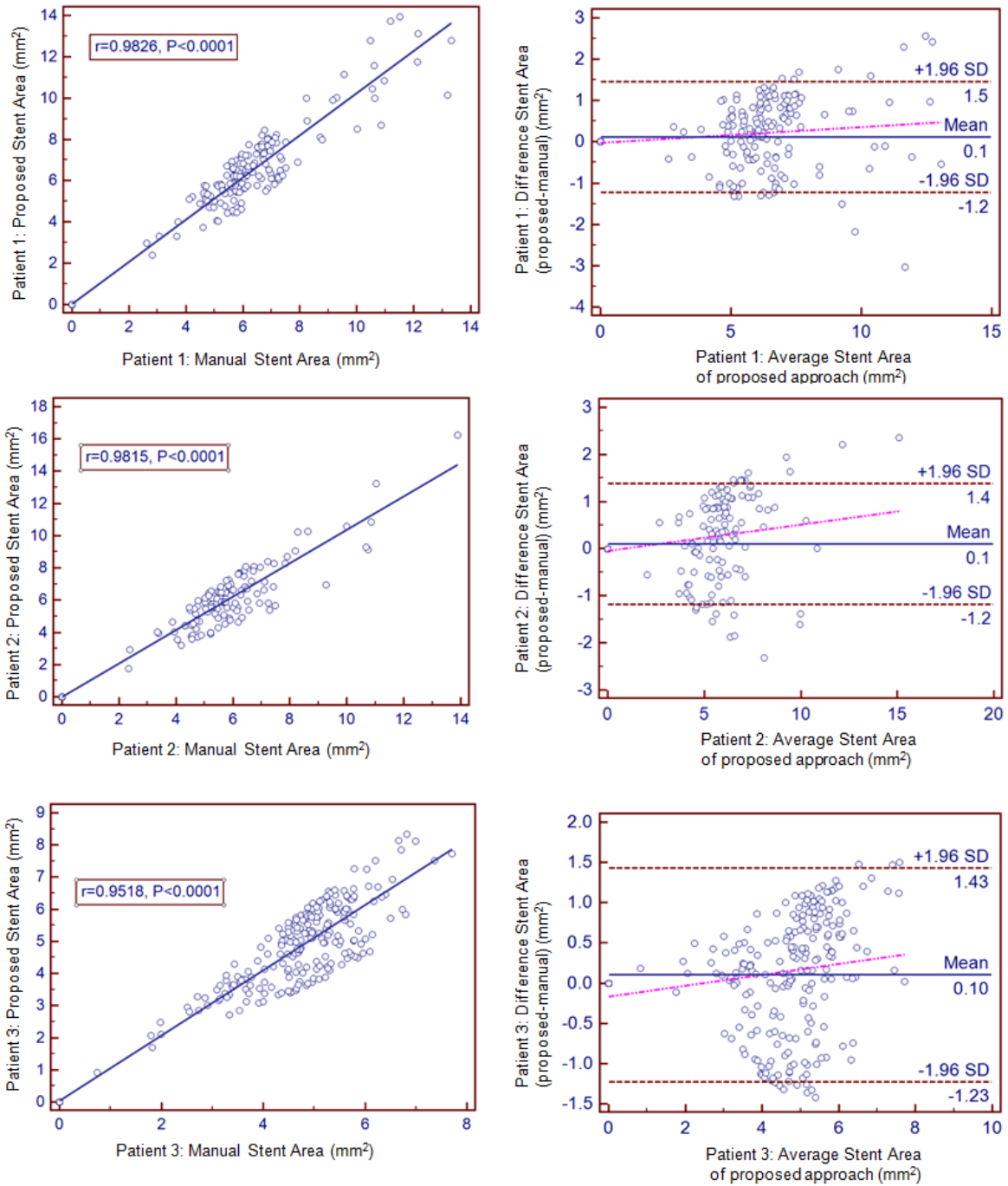
Figure 5.14: This figure shows the results of an evaluation on three patients: The left column shows the overlap metric where r is the correlation coefficient and P is the significance level. The right column shows the differences between the automatic and manual segmentations.

The detail of the proposed approach is discussed in Chapter 6.
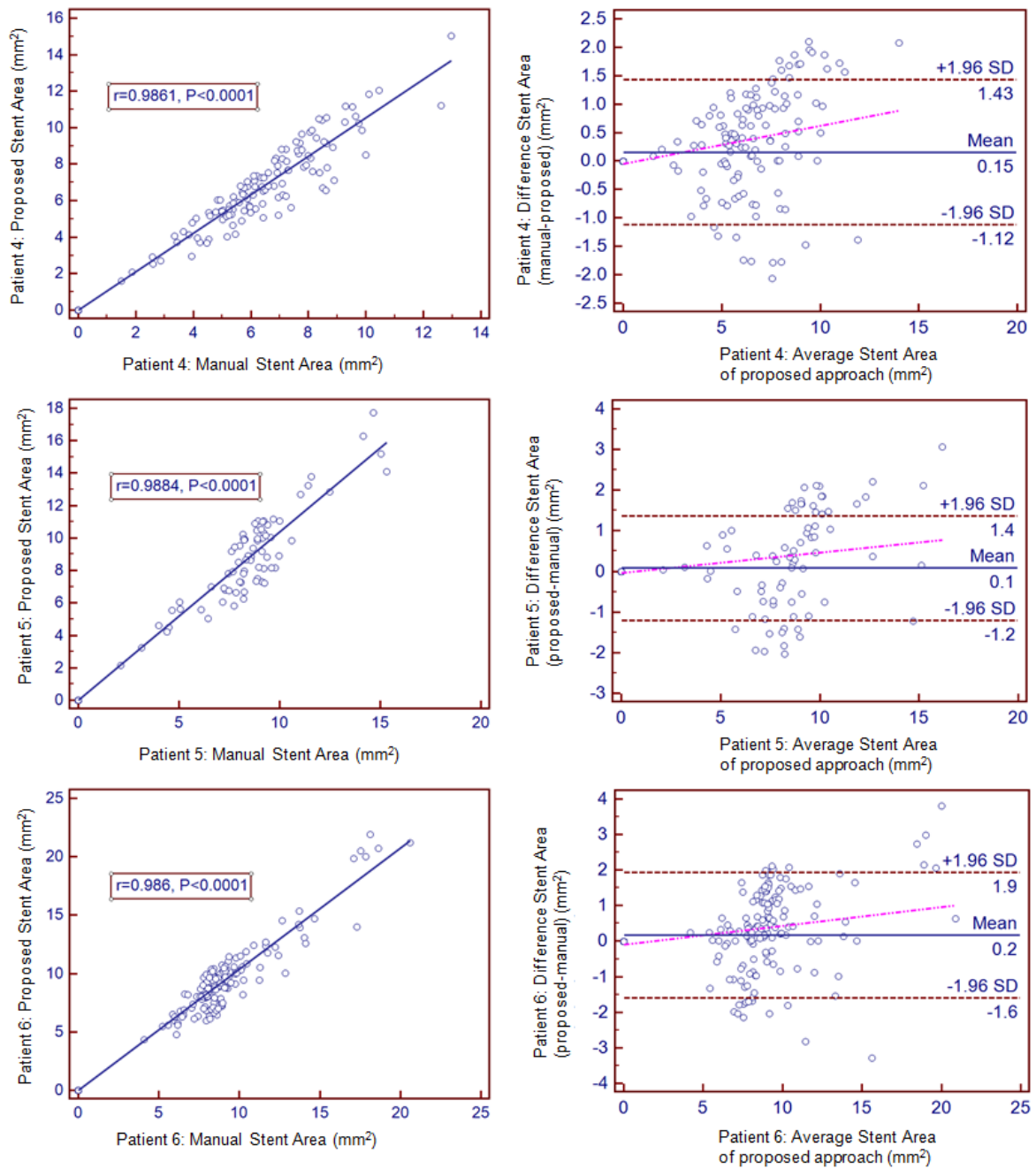
Figure 5.15: This figure shows the results of an evaluation on three patients: The left column shows the overlap metric where r is the correlation coefficient and P is the significance level. The right column shows the differences between the automatic and manual segmentations.
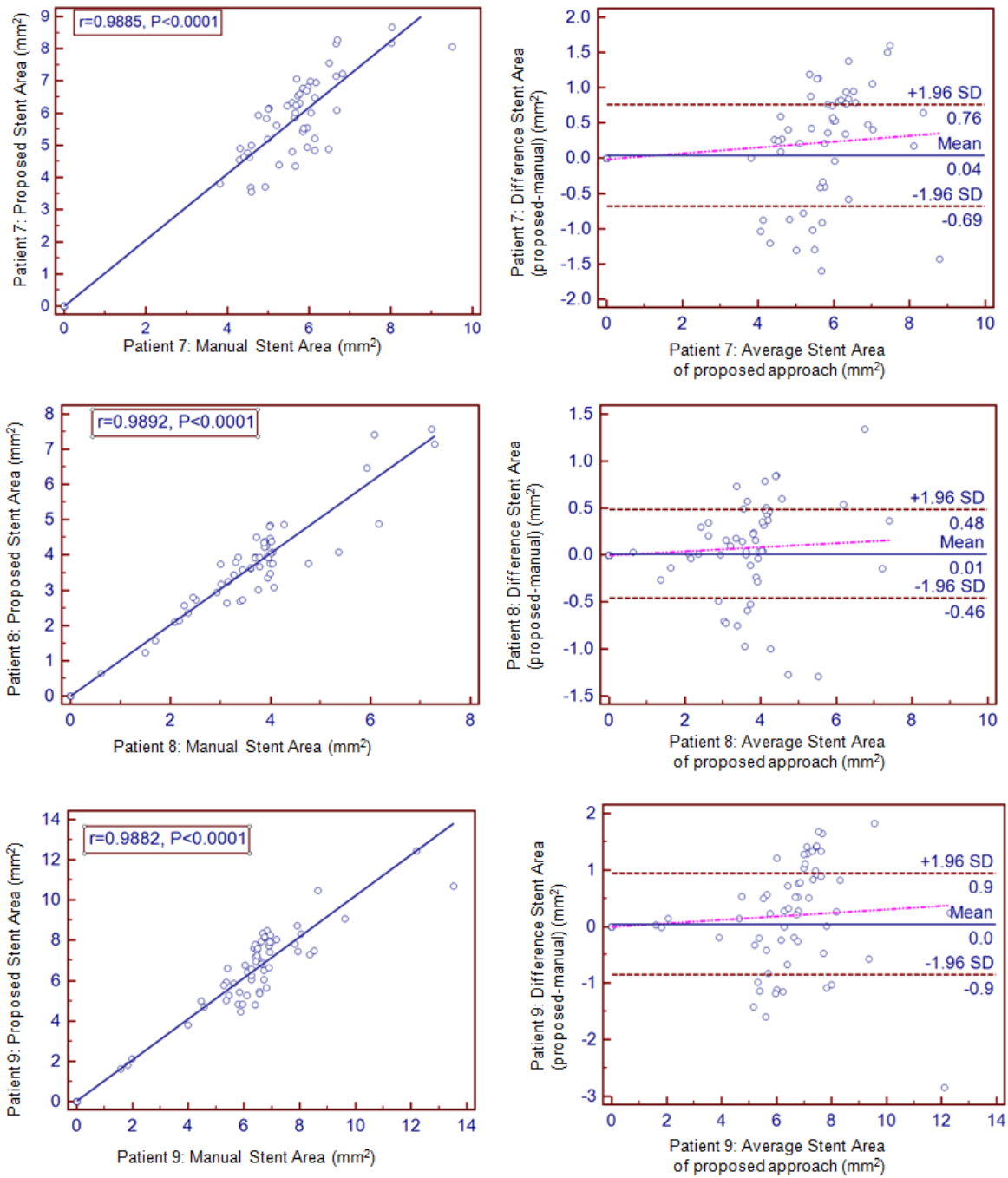
Figure 5.16: This figure shows the results of an evaluation on three patients: The left column shows the overlap metric where r is the correlation coefficient and P is the significance level. The right column shows the differences between the automatic and manual segmentations.
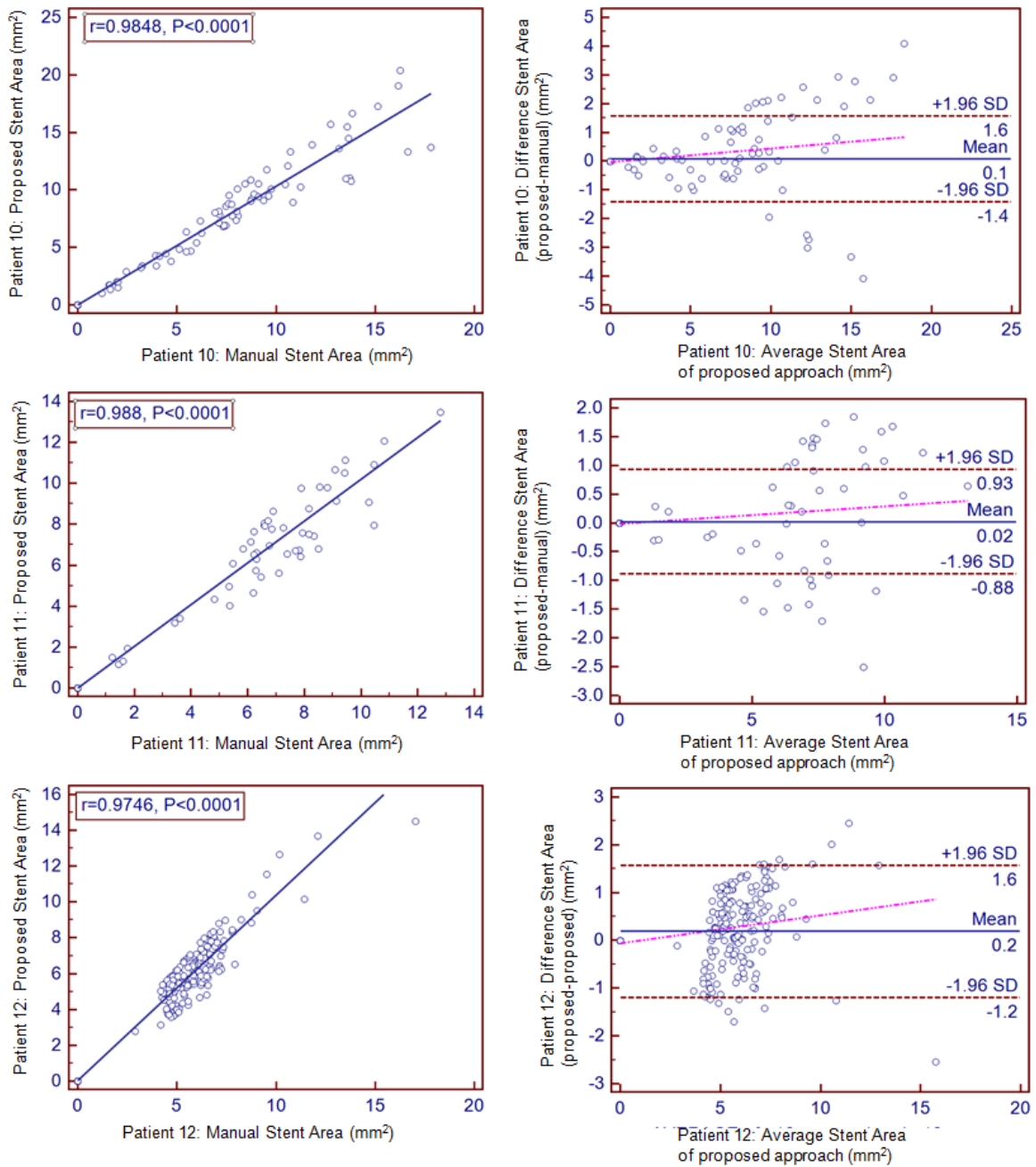
Figure 5.17: This figure shows the results of an evaluation on three patients: The left column shows the overlap metric where r is the correlation coefficient and P is the significance level. The right column shows the differences between the automatic and manual segmentations.
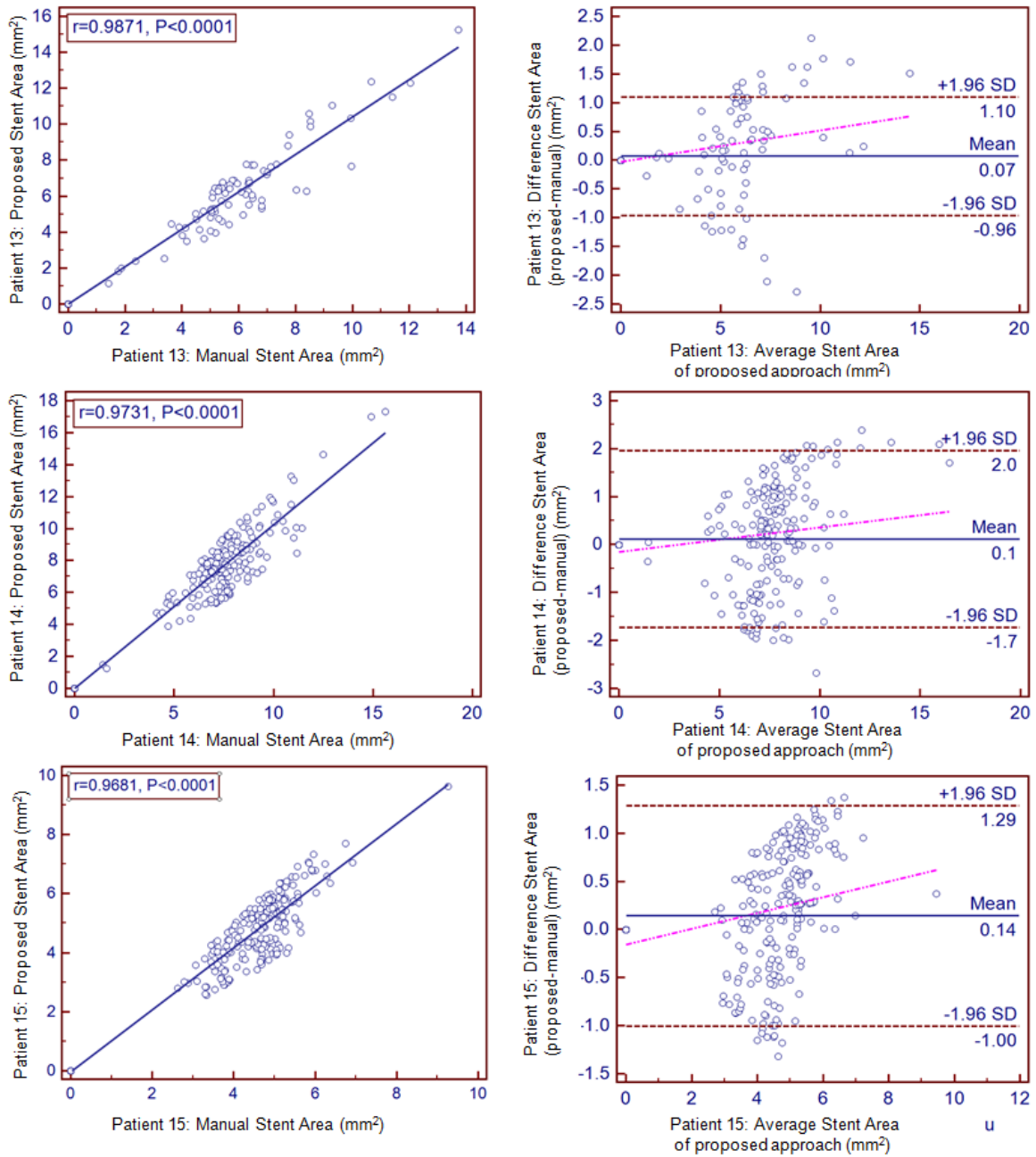
Figure 5.18: This figure shows the results of an evaluation on three patients: The left column shows the overlap metric where r is the correlation coefficient and P is the significance level. The right column shows the differences between the automatic and manual segmentations.
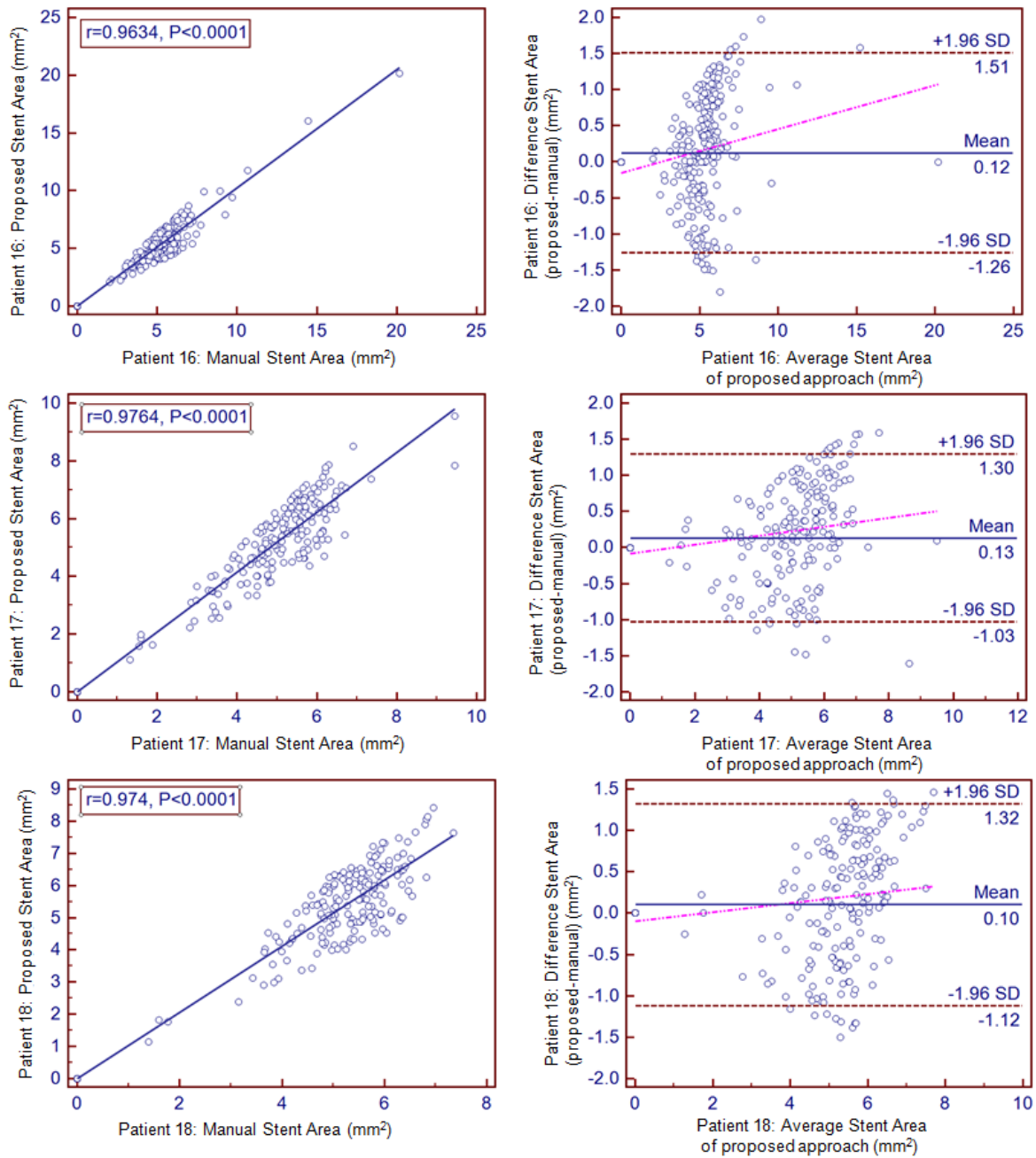
Figure 5.19: This figure shows the results of an evaluation on three patients: The left column shows the overlap metric where r is the correlation coefficient and P is the significance level. The right column shows the differences between the automatic and manual segmentations.

Chapter 6

Neointima Segmentation

6.1 Introduction

Restenosis represents a re-narrowing or blockage of an artery after a previous angioplasty or stent procedure. This is because the artery can react to the stent, perceive it as a foreign body, and respond by mounting an immune system response which leads to further narrowing near to or inside the stent [Denes et al., 2012]. In genral, restenosis remains a recognised clinical problem and is expected to increase in incidence as coronary stenting becomes more frequent [Majesky, 1994]. Two kinds of restenosis are often discussed in the literature: in-stent restenosis (ISR) and post-angioplasty restenosis (PARS). ISR means when a stent is implanted in the artery wall, the artery wall is injured and the growth of tissue across the stent leads to further narrowing near or inside the stent. If restenosis occurs following PTCA, this is referred to as PARS [Bennett, 2003, Hamid and Coltart, 2007].

NIH, or intimal thickening, is considered as the main cause of restenosis after balloon angioplasty [Bult, 2000, Horiba et al., 2000, Zargham, 2008]. Studies of stenting in previous experiments [Schwartz et al., 1992, Kastrati et al., 2001, Hoglund et al., 2010] have reported that there is a linear relationship between neointima growth and restenosis. Thus, suppression of neointima thickening is important from the point of view of prevention of restenosis and atherosclerosis. An example of neointima thickening is shown in Figure 6.1.
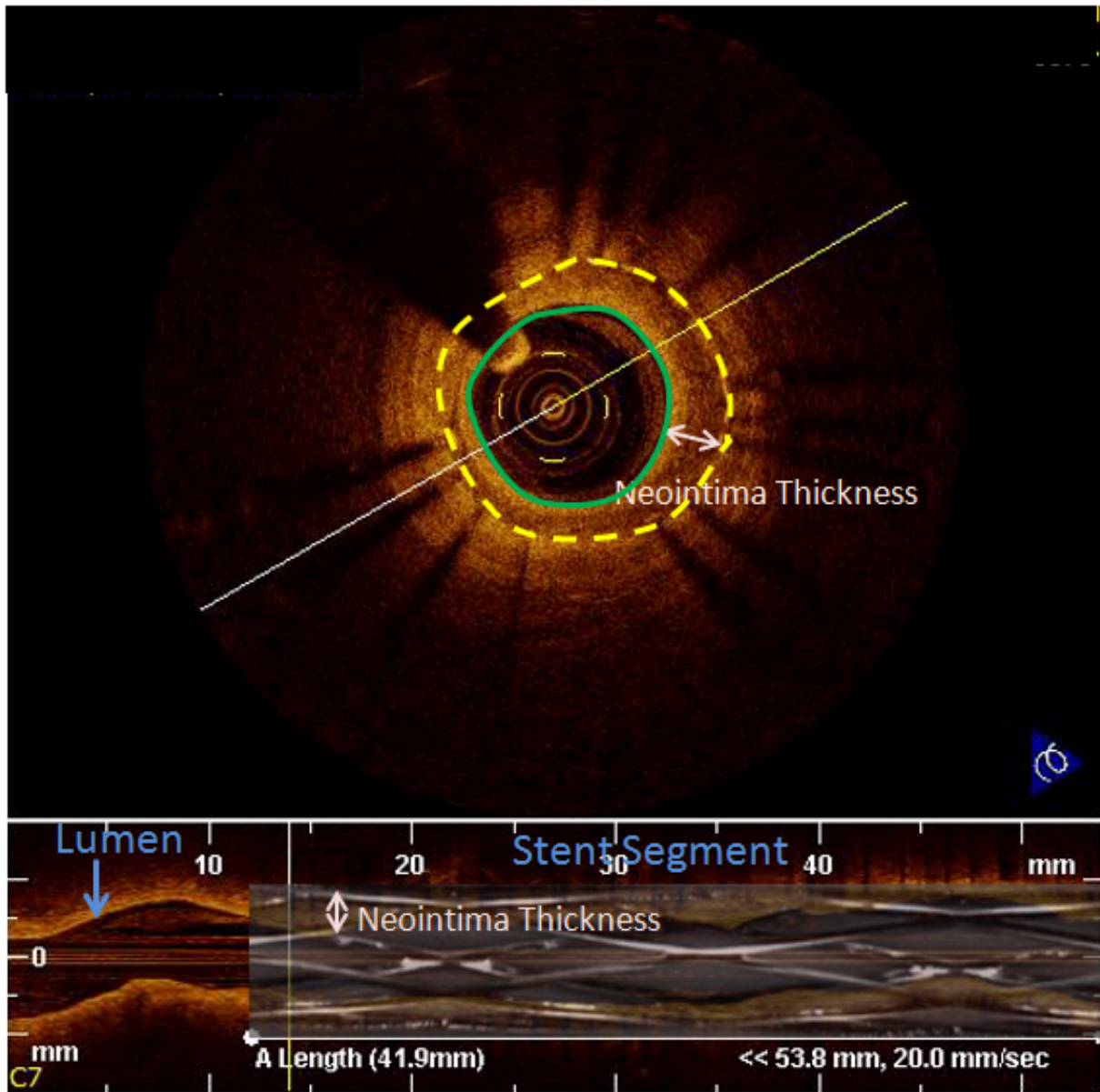
Figure 6.1: From top to bottom: The top figure is the cross-sectional view of a stent segment. Concentric circles represent the stent area (outer circle) and the lumen border (inner circle). The bottom figure is the longitudinal view of the stent segment.

A common method to identify the NIH thickness is based on the lumen border segmentations and stent struts locations [Mintz, 2007]. The lumen border segmentation is used to construct lumen area and stent struts locations are used to estimate the circle-like stent area. NIH is measured by the normalised difference between the stent area and the lumen area in every image as $NIH(\%) = ([St_{area} - Lu_{area}]/St_{area}) \times 100$ [Takano et al., 2007]. However, this method fails when the stent struts are invisible or struts positions are difficult to be recognised. This causes an incorrect stent area calculation and therefore leads incorrect neointima estimation.

Knowledge of neointima thickness and locations is likely to be valuable in the management of severity of restenosis [Nair et al., 2002]. To obtain NIH thickness segmentation, we can construct a classifier using intensity-based plaque classification approaches or plaque boundaries segmentation approaches. These approaches differentiate young stable plaques with low extracellular lipid content that is not dangerous from the unstable and more dangerous plaques. On the other hand, the approaches can assist in distinguishing the layers of plaques.

Intensity-based plaque classification approaches used in IVUS and IVOCT extract features from pixels that belong to the plaque regions. They classify each pixel into its corresponding plaque types using random forest [Athanasiou et al., 2010, Athanasiou et al., 2011], k-nearest neighbour [Tokunaga et al., 2012], texture analysis [Elbasiony and Levkowitz, 2011], acoustic impedance analysis [Bedekar et al., 2003] or boosting schemes [Pujol et al., 2003]. In all of these approaches, feature selection is a key step. Features that are similar to those from pre-defined plaques are selected in the selection phase. To reduce the dimensionality of the features, a dimensionality reduction method (e.g., PCA) can be used. A classifier is then employed to use these features to classify the plaque type. Plaque boundary segmentation approaches [Loizou et al., 2004, Molinari et al., 2007] in ultrasound images are used to determine the size of plaques and vulnerable plaques (plaques with high risk to rupture). Furthermore, histogram of plaque regions and a deformable parameter model (i.e. a snake) can be used to identify the plaque thickness [Loizou et al., 2004].

All of these methods require pre-defined plaques, neointima and other components (e.g. intima, media and adventitia) as training features to build a classifier for plaque classification. If the types of neointima and positions of stent struts are pre-indicated, a classifier for neointima segmentation can be implemented. However, if this information is not available or an inexact estimation of the stent area is obtained, this can cause an inaccurate NIH thickness estimation. In order to overcome the erroneous NIH estimation caused by the inaccurate estimate of the stent area, an approach that segments neointima without information of stent struts will be considered in the following.

Atlas-based approaches are widely used for cardiac segmentation [Lorenzo-Valdes et al., 2004,

Zhuang et al., 2010]. Using one single atlas for any patient may be satisfactory if the atlas is a good representation of the population. However, a drawback of a single atlas is that it may be very similar to some patients, but very different from others.

To address this shortcoming, multi-atlas based segmentation approaches have been proposed as solutions. The approaches consist of selecting the most appropriate images among the atlas database (atlas selection step) and fusing their segmentations [Rohlfing et al., 2004, Aljabar et al., 2007, Aljabar et al., 2009, Commowick et al., 2009] (atlas fusion step). These multi-atlas approaches can be regarded as classifier ensembles where each atlas acts as a classifier and the votes from all the classifiers are fused.

In this chapter, we propose a multi-atlas based segmentation approach to detect the neointima in coronary arteries without knowledge about stent struts positions. To detect neointima tissues, we first select atlases that are similar to the unseen image. In the atlas selection process, we use the LPDS and the lumen cross-sectional area (LCSA) to pre-select the potential atlas candidates from the coronary arteries with narrow lumen area. We then select the atlases by measuring the cross-correlation between an unseen image and the candidates. After the atlases are selected, we use a non-rigid free-form registration [Rueckert et al., 1999] to propagate the selected atlases to the unseen image. Finally, we fuse atlases and their corresponding neointima tissue labels to obtain the unseen image's neointima tissue label. Registration errors are accounted for by a patch-based label fusion approach [Coupe et al., 2011]. Figure 6.2 shows the flowchart of the proposed algorithm. The propagation and fusion steps are applied to each 2D slice of our eighteen IVOCT image sequences. As before, each IVOCT image is reformatted and interpolated into a polar coordinate system (θ, ρ).

These steps will be described in more detail in the following sections: Section 6.2 introduces the segmentation framework while section 6.3 illustrates the segmentation results from eighteen patients. Section 6.4 summarises and concludes this chapter.
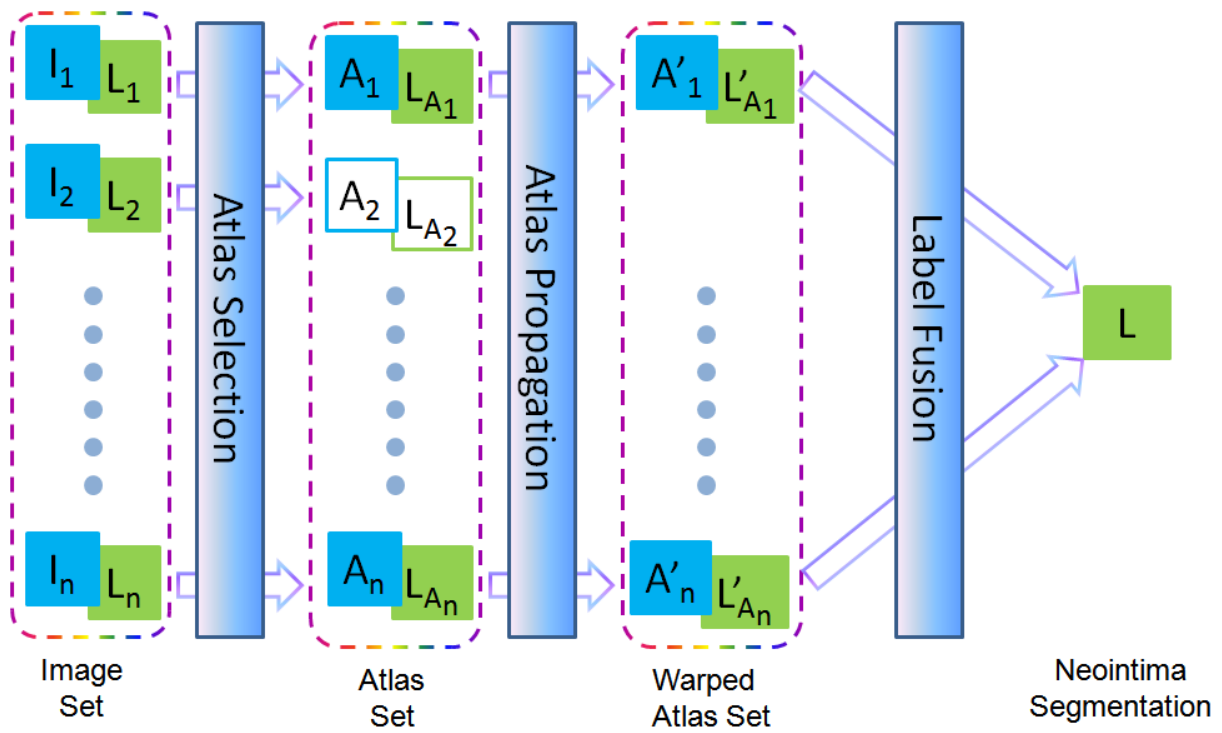
Figure 6.2: Illustration of the neointima segmentation framework that includes atlas selection, atlas propagation and label fusion.

6.2 Multi-atlas based Neointima Segmentation

Neointima thickness is the main measure of coronary restenosis. This section describes the processes of the neointima segmentation without stent area estimation and stent strut definition. The first step is to select atlases which are similar to the unseen image. After atlas selection, we use a non-rigid free-form registration algorithm [Rueckert et al., 1999] to propagate the selected atlases to the unseen image. Finally, we use the patch-based fusion approach to fuse atlases and their neointima tissue labels to obtain the unseen image's neointimal label. The three-step approach is implemented frame by frame. In addition, the lumen border segmentation used in the label fusion step is estimated by the lumen border segmentation algorithm proposed in Chapter 4.

Table 6.1: This table shows the stenosis severity based on percent diameter stenosis.

LPDS (%)	<20%	20%-35%	35%-50%	>50%
Narrow	no	mild	moderate	severe

6.2.1   Atlas Selection

In general, thick NIH causes higher restenosis severity [Meijboom et al., 2008]. Since neointima exists when the coronary artery has become narrow, we perform a pre-selection of the images to select the coronary images with narrow lumen area. The first step is to determine the severity level of stenosis in the artery. We measure the lumen percent area stenosis (LPAS), which is used to validate IVUS for the assessment of lesion severity as the measure of the narrow of the artery in IVOCT imaging [Abizaid et al., 1998, Briguori et al., 2001, Nishioka et al., 1999, Gutierrez-Chico et al., 2012]. This measure can be obtained from the lumen area (mm^2) calculation. In addition, assuming that the coronary lumen is circular, the LPDS of the lesion is also calculated as:

$$LPAS(\%) = \frac{\overline{LArea} - \min(LArea)}{\overline{LArea}} \times 100$$
$$LPDS(\%) = (1 - \sqrt{1 - LPAS/100}) \times 100$$

$$(6.1)$$

Here $\overline{LArea}$ is the average of lumen area and $\min(LArea)$ denotes the narrowest segment of lumen area.

As in the experiments [Vos et al., 1997, Pitt et al., 2000] using IVUS, the stenosis severity can also be divided into four groups by LPDS (Table 6.1).

We use the absolute LCSA to select neointimal tissue images from the arteries which are measured as the narrow arteries. This measure has been used in IVUS experiments to distinguish plaques and also applied in IVOCT imaging [Abizaid et al., 1998, Gutierrez-Chico et al., 2012]. If an image is picked from the narrow artery (LPDS is larger than 20%) and its LCSA is less than $4mm^2$, this image is considered as a neointimal tissue atlas candidate. The candidate can provide information about the neointimal thickness, neointimal location and neointimal shape.
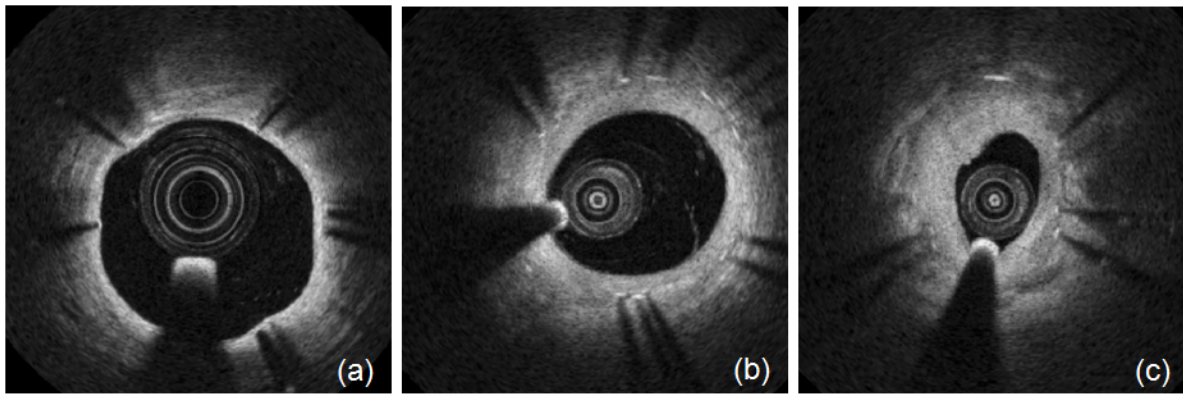
Types	PID	LCSA(mm²)	LPDS(%)	Narrow
(a)	1	6.58	26.04	Mild
(b)	3	3.38	40.24	Moderate
(c)	10	1.27	51.27	Severe

Figure 6.3: From left to right: mild narrowing, moderate narrowing and severe narrowing. PID denotes the patient identify. LCSA is a measure of the lumen cross-sectional area and LPDS refers to the percentage of diameter stenosis.

Fig 6.3 shows examples of images with different severity of narrowing that are in the atlas pool.

If all atlases are used in the next stage, the computation will become expensive and time consuming. It has been suggested by [Aljabar et al., 2009] that a few atlases can achieve a similar accuracy compared to a large number of atlases. A common way to reduce the number of atlases is to perform an atlas selection [Aljabar et al., 2009]. The selection framework relies on evaluating the similarity of a pair of images (the atlas and the unseen image). The image similarity can be expressed using a variety of metrics including SSD, CC, MI and NMI. A detailed review of similarity measures in the literature can be found in [Hajnal et al., 2001].

In this section, CC is used to select atlases from those images with narrow lumen. CC assumes that a linear relationship exists between the intensity values of corresponding pixels in the two images. The most similar atlases of the unseen image are selected and used in the next stage of non-rigid free form registration and label fusion. A flowchart of the proposed atlas selection is shown as Figure 6.4.
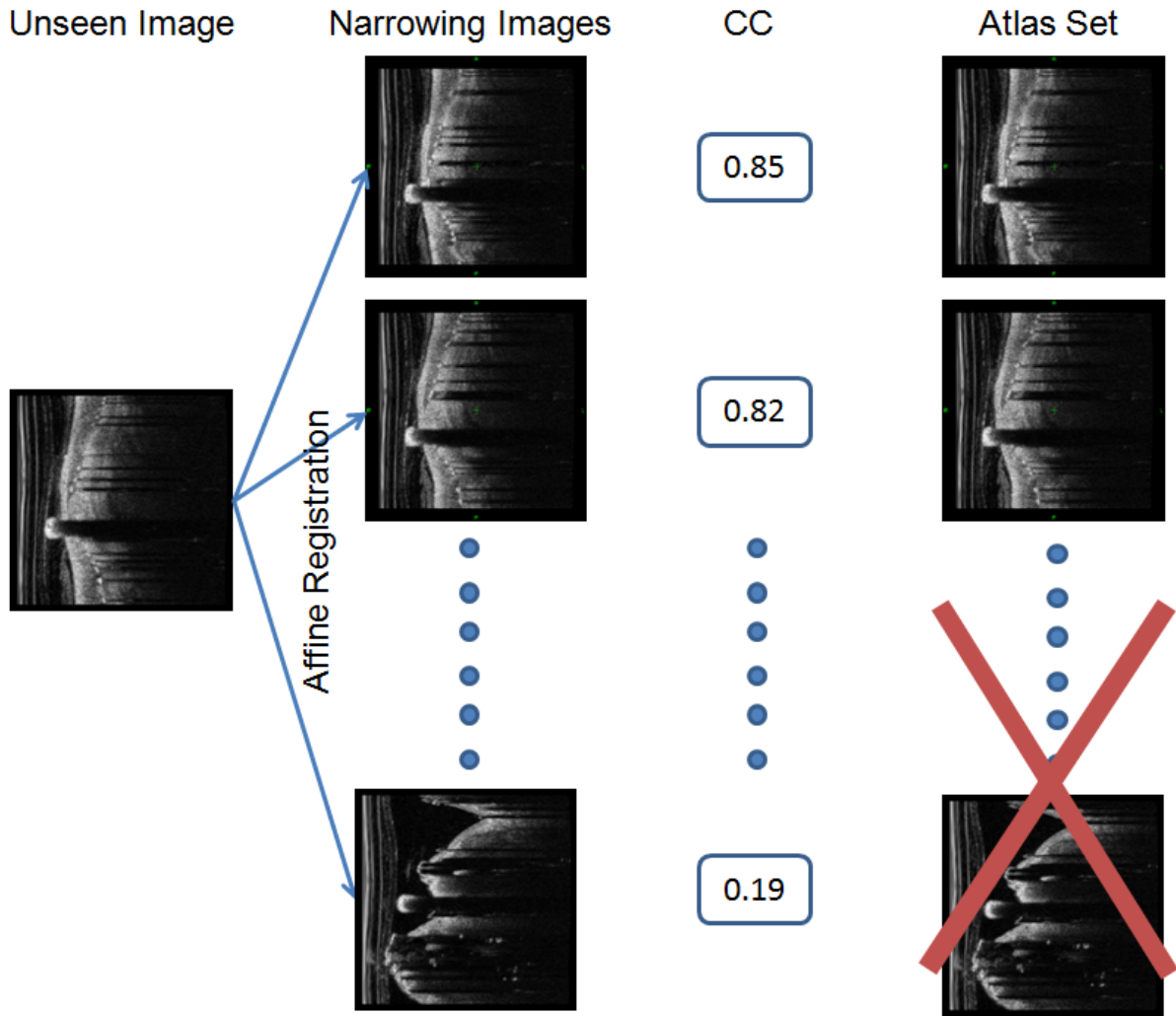
Figure 6.4: Atlas selection. Similar images are selected by using cross-correlation.

6.2.2   Propagation by Non-Rigid Registration

In this section, we describe the registration method that estimates the transformation between an atlas and the unseen image. Since the atlas may not be perfectly aligned with the unseen image, the subsequent non-rigid image registration using a free-form deformation model based on cubic B-splines [Rueckert et al., 1999] can provide a better matching between the unseen image and the atlas image.

Assuming that a free-form deformation is parametrised by a set of control point vectors Φ, each vector $\phi_{i,j}$ denotes a control point that is arranged on a regular lattice size $n_x \times n_y$ with uniform spacing of δ along each dimension. The index i,j denotes the location of its associated control point within the lattice. By using cubic B-spline basis functions to blend the control point

vectors, a continuously varying displacement is defined at each point of the image domain. The free-form deformation for a pixel $x = (x, y)$ can be formulated as the 2D tensor product of the 1D cubic B-splines:

$$T(x, y) = \sum_{l=0}^{2} \sum_{m=0}^{2} B_l(q) B_m(s) \phi_{i+l, j+m} \tag{6.2}$$

where $i = \lfloor \frac{x}{n_x} \rfloor - 1$, $j = \lfloor \frac{y}{n_y} \rfloor - 1$, $q = \frac{x}{n_x} - \lfloor \frac{x}{n_x} \rfloor$, $s = \frac{y}{n_y} - \lfloor \frac{y}{n_y} \rfloor$. The function B_l represents the l-th basis function of the B-spline:

$$\begin{aligned} B_0(u) &= \frac{(1-u)^3}{6} \\ B_1(u) &= \frac{3u^3 - 6u^2 + 4}{6} \\ B_0(u) &= \frac{-3u^3 + 3u^2 + 3u + 1}{6} \\ B_0(u) &= \frac{u^3}{6} \end{aligned} \tag{6.3}$$

After the registration, the transformations between the unseen image and atlases is obtained. We warp the atlases and their corresponding labels to the unseen image and fuse this new atlas set to obtain the label estimation for the unseen image.

6.2.3   Local Patch-based Label Fusion

Due to the difference in the severity of stenosis, an unseen image's neointimal tissue might not be exactly the same as any of the atlases. In addition, the unseen image's neointima might not be exactly aligned with the atlas because of registration errors. Therefore, an approach that can reduce the sensitivity to registration error is important. We proposed a combined probabilistic model as the core of our algorithm which leads to a more flexible label fusion and tolerates registration errors.

Our method is inspired by Sabuncu [Sabuncu et al., 2010] and Coupe [Coupe et al., 2011]. In Sabuncu's local label voting model, the label of a voxel x in the unseen image is determined by the corresponding voxel in atlases. However, the unseen's label estimated from a single voxel in the atlas might result in a wrong vote when there is a misregistration between the unseen

and atlas images. Thus, we use a patch-based scheme proposed by Coupe [Coupe et al., 2011] instead of a single voxel to estimate the tissue label.

Let $I = \{I(x) \in \Omega\}$ be a unseen image to be segmented where $\Omega \subset \Re^2$ denotes the lattice on which the image is defined and x denotes a pixel in the unseen image. The goal of segmentation is to estimate a label map L associated with the image I where each pixel is assigned a discrete label. The label L is classified into binary labels: $L(x) = \{L_{background}, L_{foreground}\}$. The probability of patch-based label fusion model in the unseen image is estimated by the fusion of a weighted patch label integration (P_1) and a weighted patch location (P_2). The combined probability for label L is

$$\hat{P}(L|x, I) = C \cdot P_1(x) + (1 - C) \cdot P_2(x) \tag{6.4}$$

where C is a fusion factor that aligns the weights between the weighted patch label integration and the weighted patch location. $\hat{P}(L|x, I)$ represents the probability of label L.

We assume that the transformation Φ_n between the image I and an atlas A_n has been computed in the section 6.2.2. We warp the atlas image A_n and its corresponding label L_n to the unseen image space. Let $A'_n = A_n(\Phi_n)$ denotes the warped atlas image and $L'_{A_n} = L_{A_n}(\Phi_n)$ denotes the warped label map. $At'_1 = (A'_1, L'_{A_1}), ..., At'_n = (A'_n, L'_{A_n})$ are a set of N warped atlases and labels. Each L'_{A_n} is a candidate segmentation for the label of the unseen image.

The weighted patch label integration P_1 is used to perform the weighted averaging of atlas labels. For all pixels x of the image to be segmented, the probability of the final label is based on a weighted label fusion of all labeled samples inside a patch k for the n selected atlases:

$$P_1(x) = \frac{\sum_{n=1}^{N} \sum_{k=1}^{K} \omega_{n,k} \cdot L'_{A_n}(x_k)}{\sum_{n=1}^{N} \sum_{k=1}^{K} \omega_{n,k}} \tag{6.5}$$

where x_k is the pixel x at k-th patch in the n-th atlas.

The probability of a pixel x in the unseen image is estimated from a weighted fusion of spatial neighbourhood with K patches and N atlases. During the voting, the weight $\omega_{n,k}$ is determined

by the distance between the k-th patch in the n-th atlas and the patch centered around x. We assume that the differences between patches can be modeled by a Gaussian distribution with zero mean. The model is described as:

$$\omega_{n,k} = \frac{1}{\sqrt{2\pi\sigma_1^2}} exp\{-\frac{1}{2\sigma_1^2}[I(x) - A'_n(x + \Delta_k)]^2\} \tag{6.6}$$

Here Δ_k denotes the distance between the centre pixel x and the k-th candidate pixel. $I(x)$ and $A'_n(x + \Delta_k)$ respectively denote the intensities of the pixel in the unseen image and the corresponding atlas pixel. σ_1 is the standard deviation of the Gaussian distribution. We use a small patch instead of a single pixel and the weight $\omega_{n,k}$ can then be estimated as:

$$\omega_{n,k} = \frac{1}{\sqrt{2\pi\sigma_1^2}} exp\{-\frac{1}{2\sigma_1^2|S(x)|} \sum_{y \in S(x)} [I(y) - A'_n(y + \Delta_k)]^2\} \tag{6.7}$$

where $S(x)$ denotes a patch centred at x and $|S(x)|$ denotes the number of voxels in $S(x)$. The intensity difference of a single pixel in Eq. (6.6) is replaced by the mean squared difference in the patch $S(x)$ (Eq. (6.7)).

The weighted patch location P_2 is used to estimate the location of a patch in the unseen image. We assume that the weighting of the location obeys a normal distribution and the probability can be written as Eq. (6.8) and Eq. (6.9):

$$w_{patch\_pos}(x) = \begin{cases} \frac{1}{\sqrt{2\pi\sigma_2^2}} exp\{-\frac{1}{2\sigma_2^2}[x_k - x_{lb}]^2\}, & \text{if } x_k \geq x_{lb} \\ \\ 0, & \text{otherwise} \end{cases} \tag{6.8}$$

$$P_2(x) = \frac{w_{patch\_pos}(x)}{\sum w_{patch\_pos}(x)} \tag{6.9}$$

Here x_{lb} is the corresponding lumen border location of the pixel x at k-th patch. If x_k is the inner of the lumen border, the probability is set to zero. σ_2 is a model parameter that determines the search volume size.

After the weighted label fusion (P_1) and the weighted location (P_2) have been computed, the
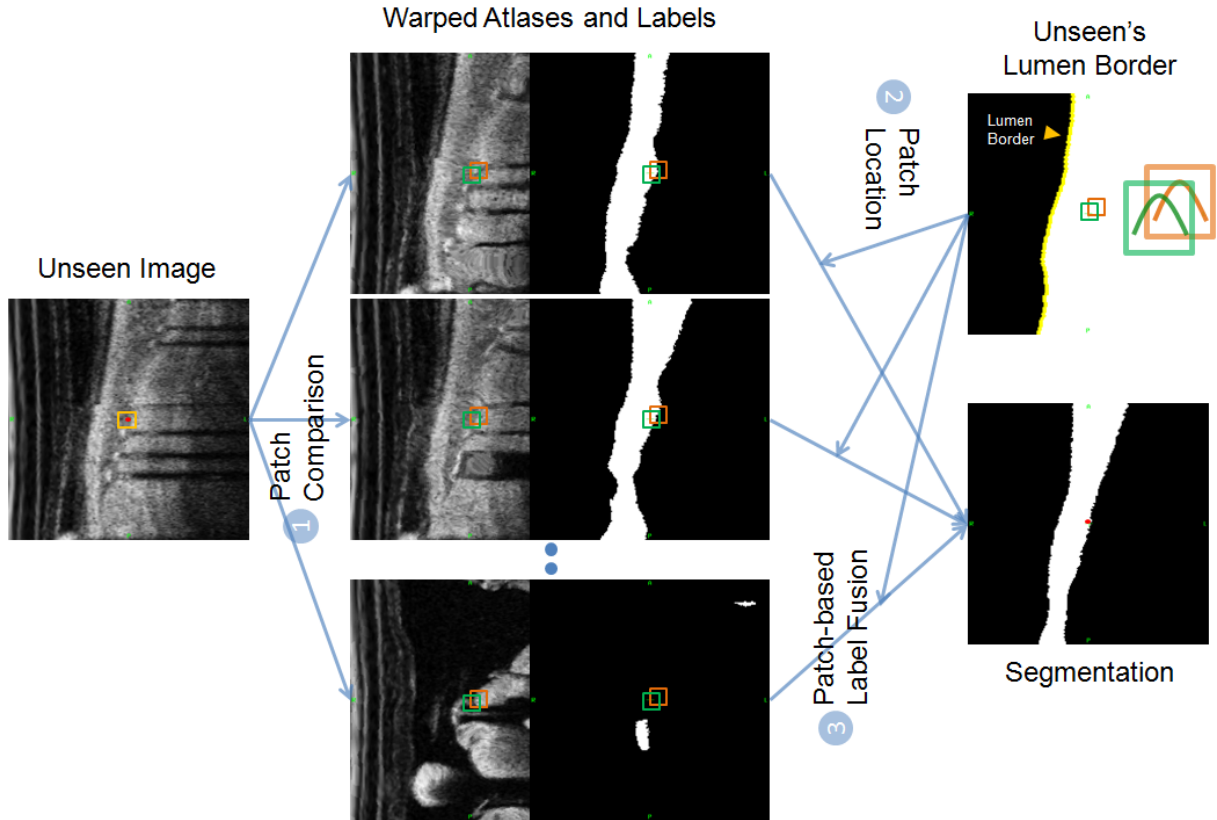
Figure 6.5: To determine the label at a pixel (the red dot), a patch (the yellow rectangle) in the unseen image is compared to a number of patches (the coloured rectangles) in the warped atlases. Each atlas patch is weighted according to its similarity and distance to the target patch (step 1). The labels from all atlas patches are combined to provide the label estimate in the unseen image. In addition, each atlas patch location is compared to its corresponding lumen border segment location in the unseen image. With the combined probability of patch voting weight and patch location weight, the unseen's neointimal segment can be obtained when the probability is larger than the threshold (Step 3).

combined probability for label L of the unseen image ($\hat{P}(L|x, I)$) is determined. Since P_1, P_2 and $\hat{P}(L|x, I)$ are defined as $\{0, 1\}$, the final label can be computed as:

$$L(x) = \begin{cases} 1, & \text{if } \hat{P}(L|x, I) \geq th \\ 0, & \text{otherwise} \end{cases} \tag{6.10}$$

Here if the combined probability $\hat{P}(L|x, I)$ is higher than the threshold th, the label of the pixel x can be marked as neointima. Figure 6.5 illustrates the procedure of patch-based label fusion.

Finally, we apply a Gaussian smoothing to refine our segmentation. If the combined probability

Table 6.2: This table shows the implementation tools for (1) Atlas selection, (2) Atlas propogation and (3) Label fusion.

Steps	Atlas Selection	Atlas Propagation	Label Fusion
Tools	IRTK	IRTK	IRTK

is lower than the threshold, this causes image noise. For examples, holes appear in Figure 6.8(c), (d), (e), (g), (h). The Gaussian smoothing can fill in the holes in the segmentation results. An example is shown in Figure 6.8(f).

6.3 Results and Discussions

6.3.1 Testing Datasets

A commercial C7-XR system is used to acquire the IVOCT image sequences. Images were acquired during a pullback rate of 20.0 mm/s. All sequences are the cases of in-stent-restenosis with different severity of narrowing (see Table 1.2). The lumen border segmentations obtained by our lumen border estimation method proposed in Chapter 4 are used as preliminaries. The implementation tool of each step of the neointima segmentation approach is based on IRTK (Table 6.2).

6.3.2 Parameter Estimation

In the atlas selection step, we implement an atlas pre-selection to select images with narrow lumen area as potential atlases since neointima exists in the narrow lumen images. To identify the narrow images, we calculate the LPDS and LCSA for each slice of each patient sequence. The number of atlas candidates for every patient is shown as Table 6.3.

After the pre-selection, we use the atlas selection strategy as proposed in [Aljabar et al., 2009] to select the similar atlases. We register all candidates to the unseen image using affine reg-

Table 6.3: This table shows the number of potential atlases have been used in the experiments.

Patient ID	Total slices	Narrowing slices	Number of atlas candidates
P1	271	0	756
P2	271	0	756
P3	268	202	554
P4	268	4	752
P5	271	2	754
P6	271	11	745
P7	271	0	756
P8	268	47	709
P9	268	0	756
P10	268	0	756
P11	268	0	756
P12	268	0	756
P13	268	0	756
P14	268	0	756
P15	268	94	662
P16	268	67	689
P17	268	64	692
P18	268	65	691

istration. Atlases are selected by the similarity (CC) between the candidates and the unseen image.

We reduce the number of atlases to improve the performance of computation. Figure 6.6 shows the impact of the size of atlases on segmentation accuracy. It shows that, for the training set, more than 100 atlases result in trivial improvement or even decrease of segmentation performance. Therefore, in the following experiments, we select 100 atlases for label fusion. Since 100 atlases still represents a large atlas set, we define a threshold to pick the most similar images to further reduce the computational cost. In our experiments, this threshold is set to half of the highest similarity. Thus, 100 atlases can be considered as an upper bound for the label fusion step. In practice, the average atlases number is between 20-50.

After atlas selection, we determine the parameters for registration. During the registration, we use a hierarchical optimisation with three levels. At the coarsest level, the image resolution and control point spacing are 4x4*mm* and 32x32*mm*, respectively. We use CC as the similarity
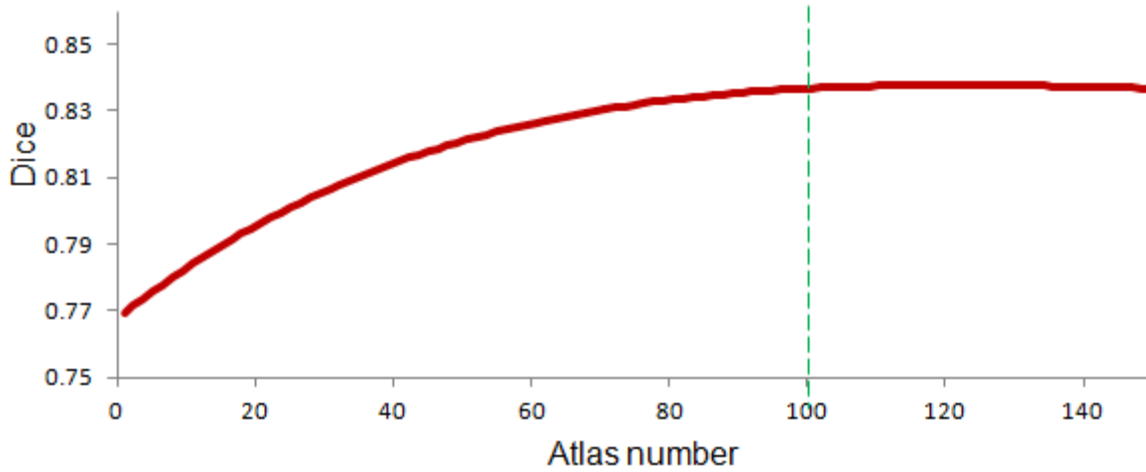
Figure 6.6: This figure shows the effect of the number of atlases on the segmentation accuracy. The accuracy is evaluated using the Dice overlap between the results of our proposed approach and manual neointimal segments.

measure in the registration procedure.

In the label fusion step, we use Gaussian distributions to estimate the probability of the patch-based label fusion model. This model is a combination of the weighted patch label integration (P_1) and the weighted patch location (P_2). The weighted patch label integration (P_1) is an intensity-based image likelihood term that follows a Gaussian distribution and the likelihood term of the weighted patch location also follows a Gaussian distribution. The standard deviation σ_1 of the Gaussian distribution in the weighted patch label integration (P_1) is used to group pixels since the intensities between neointimal tissues are similar. In practice, we have tried values of σ_1 between 10 and 70. We found that $\sigma_1 = 50$ yields best results.

In addition, the standard deviation σ_2 of the Gaussian distribution in the weighted patch location (P_2) is used to restrict the search area since neointima is close to the lumen border. Therefore, we have tried values of σ_2 between 0.5mm and 2mm and found that $\sigma_2 = 1.5mm$ provides best results. These two values are then applied to all patient sequences. The neighbourhood for searching for atlas patches is set to $\pm 2\sigma_2$ around the centre pixel and the patch size in the unseen image is 5x5. The fusion factor C (Eq. (6.4)) is set to 0.5. Finally, the threshold used to determine the binary label of the unseen image (Eq. (6.10)) is 0.5. After label fusion, we have applied a Gaussian smoothing with $\sigma = 1$ to refine the segmentation.

6.3.3   Results

The proposed neointima detection method has been applied to eighteen IVOCT sequences. We use a leave one out cross-validation to evaluate the segmentation. The atlases used for segmenting the left-out test subject are obtained from the other seventeen patient sequences. Examples of the neointima segmentations for different degrees of narrow severity are shown in Figure 6.7. We then compare the segmentation of a random slice in one patient sequence by using different fusion approaches with different registration strategies. The comparison is shown in Figure 6.8. Examples of the 3D neointima reconstruction with the different severity of narrowing (mild, moderate and serve narrow) are shown in Figure 6.9, Figure 6.10 and Figure 6.11.

In general, severe degree of stenosis causes severe restenosis. However, in some cases, a mild/moderate narrow artery (grouped by LPDS) may have moderate/serve narrow restenosis slices (Figure 6.9 and Figure 6.10). Similarly, slices showing a mild narrowing of the artery may appear in a serve narrow artery (see Figure 6.11). To evaluate the accuracy, we used the Dice overlap (Eq. (4.10)) to evaluate the neointimal area between our segmentations, manual segmentations and other segmentations obtained from different fusion approaches (majority voting [Kittler et al., 1998] and multi-atlas local fusion [Sabuncu et al., 2010]). The manual neointima segmentations are obtained by two trainees (Paul Huang and Larry Lin) and verified by Dr. Zhang. Our method has achieved the average score of Dice 0.92 ± 0.02. A detailed comparison is shown in Figure 6.12. The verification between our result and manual segmentation is discussed in next subsection (section 6.3.4).

In addition, we utilise a Bland-Altman plot to show the differences between the neointima area detected by the proposed approach and manual segmentation (Figure 6.14-Figure 6.16 at the end of this chapter). Our results show a trend of slight under-estimation. This may be due to the lower weighted patch location (P_2) and the lower weighted patch label integration (P_1) of a pixel that is close to the neointima boundary. Another possible reason is that the similarity between atlases and the unseen image is too low. The means that the neointimal tissue label

	(a)	(b)	(c)
LCSA (mm²)	5.59	2.62	1.27
PDS (%)	26.2	39.9	50.2
Narrow	①	②	③
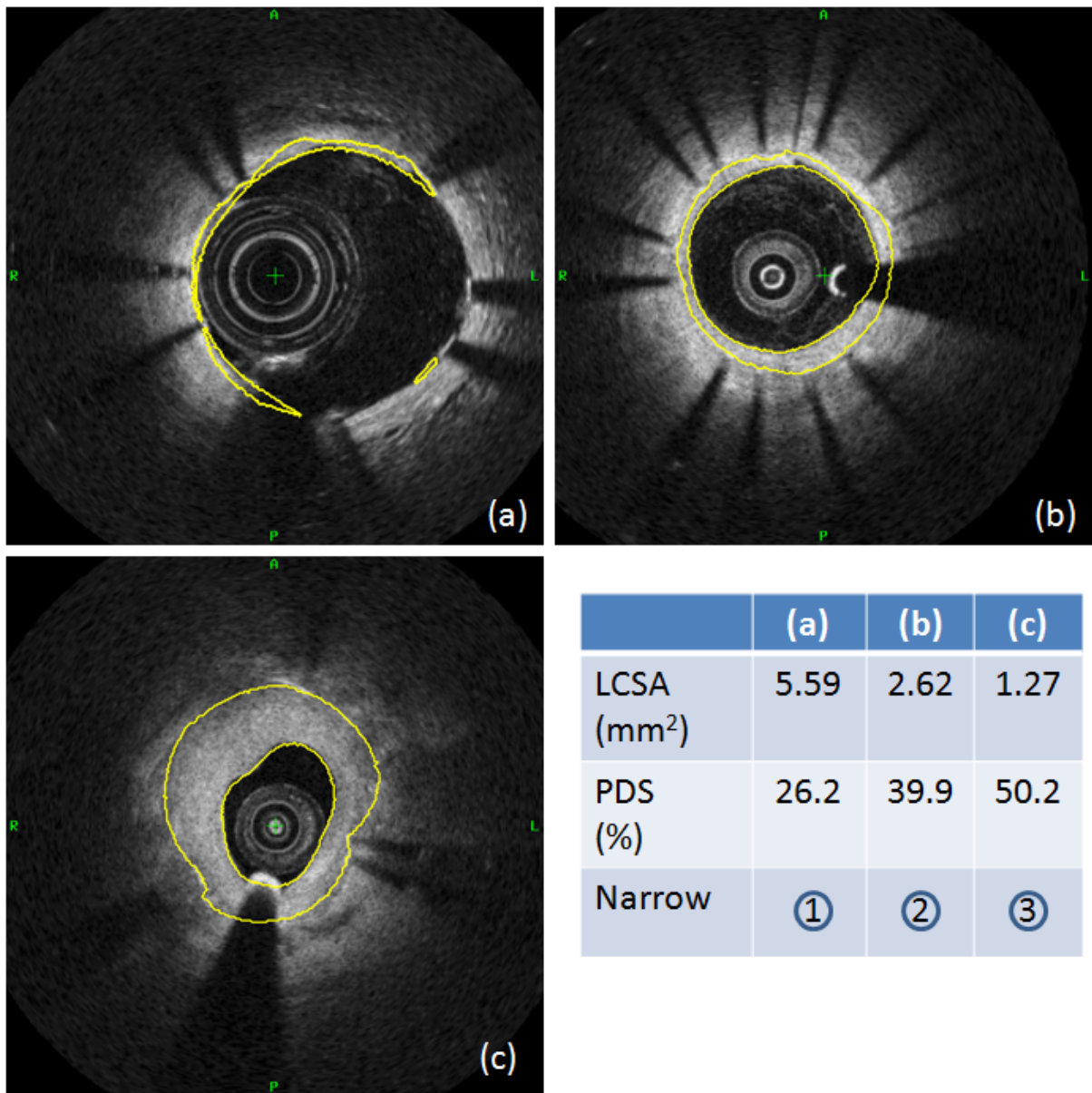
Figure 6.7: This figure shows neointima segmentations for different severity of restenosis: (1) mild narrow, (2) moderate narrow and (3) severe narrow.

of the unseen image is hard to obtain from the atlases.

6.3.4 Discussion

In this subsection, we compare neointima segmentations with (1) ones obtained from the previous chapters (Chapter 4 and Chapter 5), (2) manual neointima segmentation and (3) outer circle neointima segmentation. The outer circle neointima segmentation can be obtained as the estimated circle stent area minus the lumen border area (Figure 6.13(c)). In our experiments,
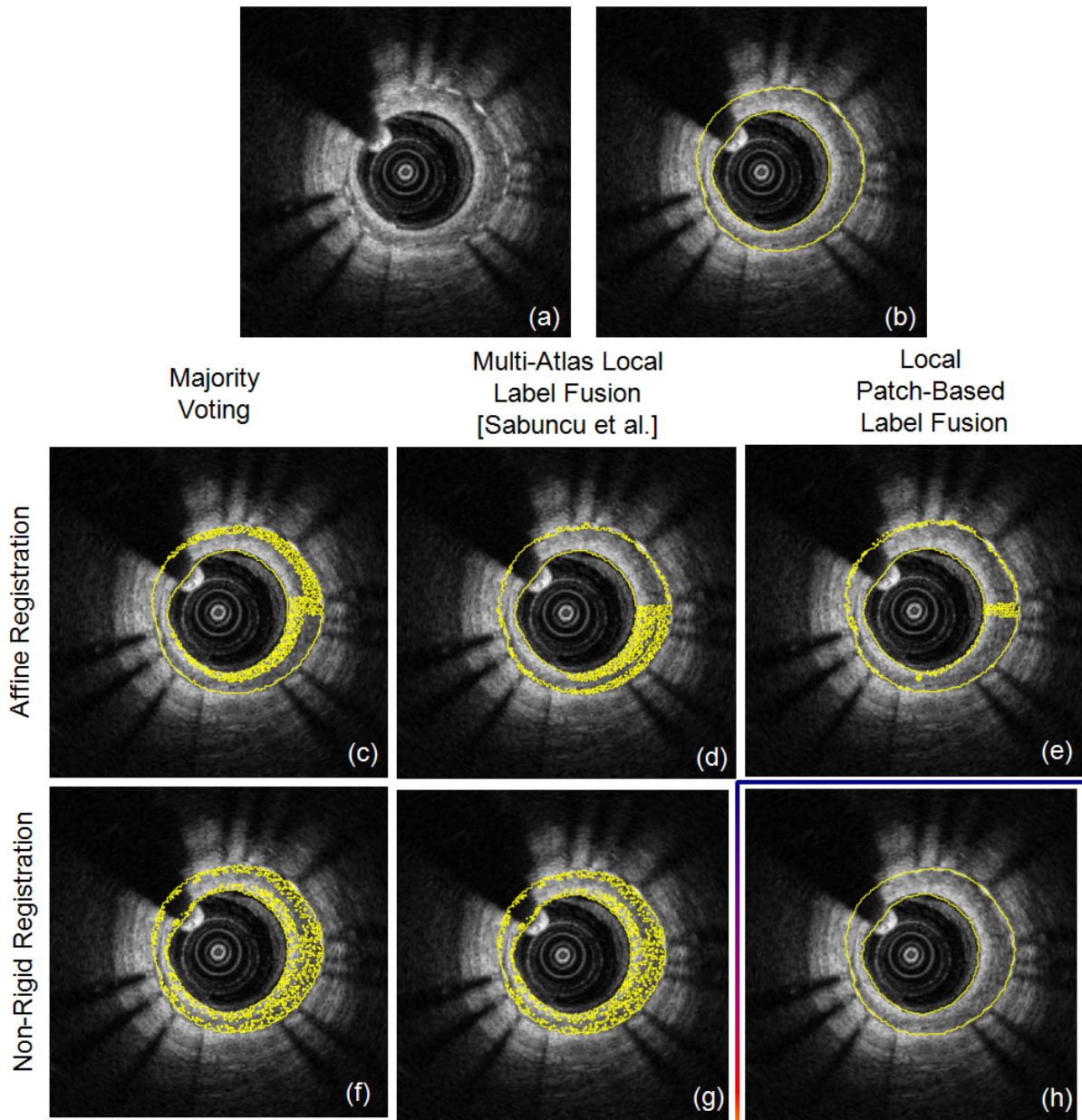
Figure 6.8: This figure shows neointima segmentations with different label fusion approaches and different registration strategies. (a) shows the original image and (b) its manual neointimal segmentation. Each row ((c)-(e) and (f)-(h)) represents each of the different registration strategies: affine registration and non-rigid registration [Rueckert et al., 1999]. Each column ([(c),(f)];[(d),(g)];[(e),(h)]) shows each of the different fusion approaches: local patch-based label fusion, majority voting and multi-atlas label fusion [Sabuncu et al., 2010]. The segment with local patch-based label fusion and non-rigid registration has performed better than the other approaches.

the lumen border area is calculated by the proposed method (Chapter 4). The estimated circle stent area was obtained by fitting a circle to the manual stent struts segmentation. This measure was inspired by [Murata et al., 2002] as the authors mention that the stent area is equal to the area of the hypothetical circle. This outer circle neointima segmentation overestimates
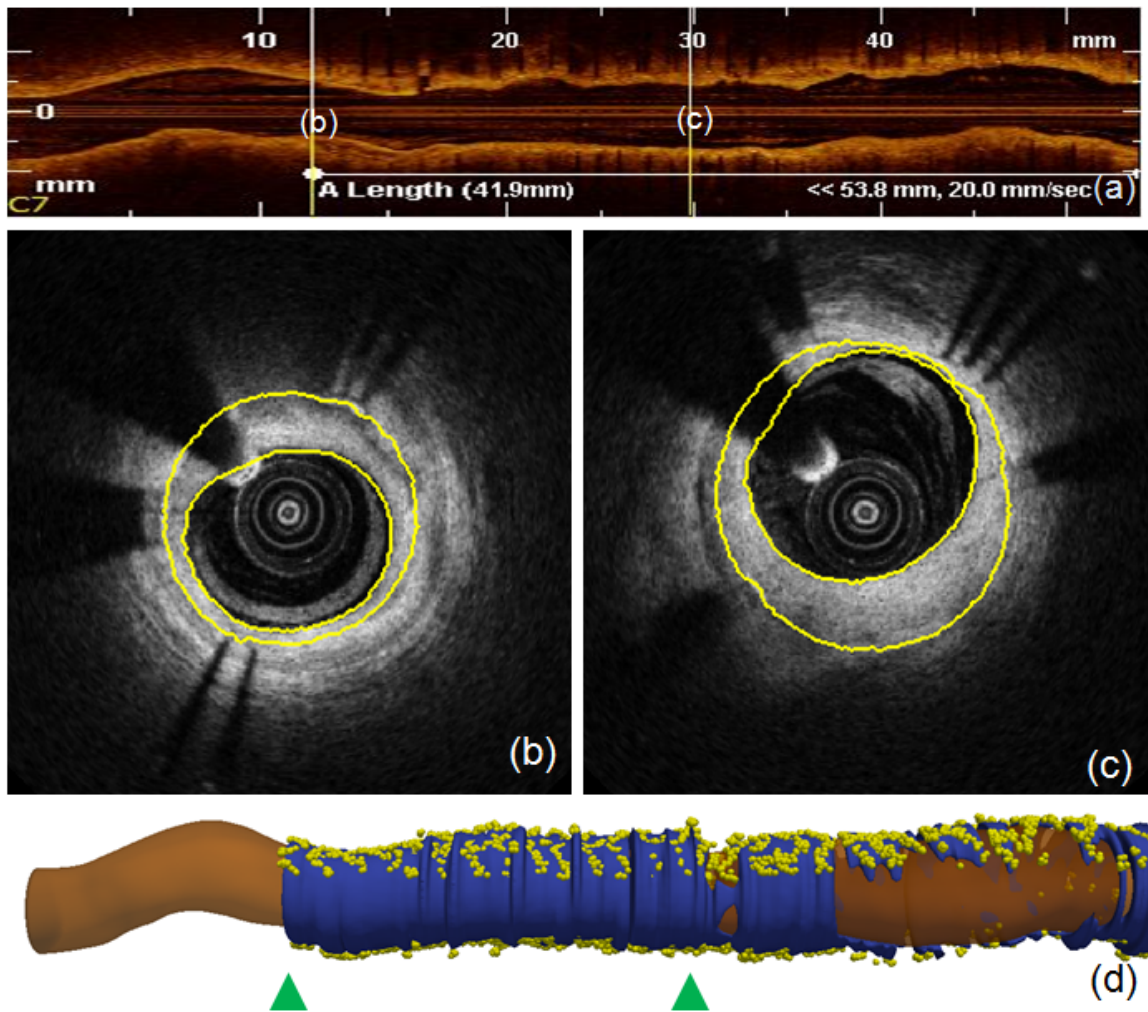
Figure 6.9: This figure shows an example of the 3D neointima reconstruction (case with mild narrowing). (a) the longitudinal view of the mild narrow patient sequence (P15). (b) and (c) are the random selected slices in the sequence. (d) the 3D longitudinal view. Blue regions are neointima segmentations. Yellow spheres are the stent struts detected from Chapter 5 and lumen border segmentations (brown color) are extracted from Chapter 4.

the area since the shape of the stent area is a circle-like structure but not a circle. However, an advantage of this outer circle neointima segmentation is that the measure is straightforward to calculate and implement while the manual stent struts segmentation and manual neointima segmentation are time-consuming. Therefore, the outer circle neointima segmentation can be used to assist the restenosis diagnosis [Lemos et al., 2011] even though it is an over-estimat.

With the over-estimated/under-estimated stent struts (Figure 6.13(a)), the inaccurate stent area estimation is obtained in Figure 6.13(d) (see Chapter 5). The manual neointima segmentation is shown in Figure 6.13(b). Finally, the proposed multi-atlas neointima segmentation is shown in the Figure 6.13(e). Our proposed method has achieved results which are close to
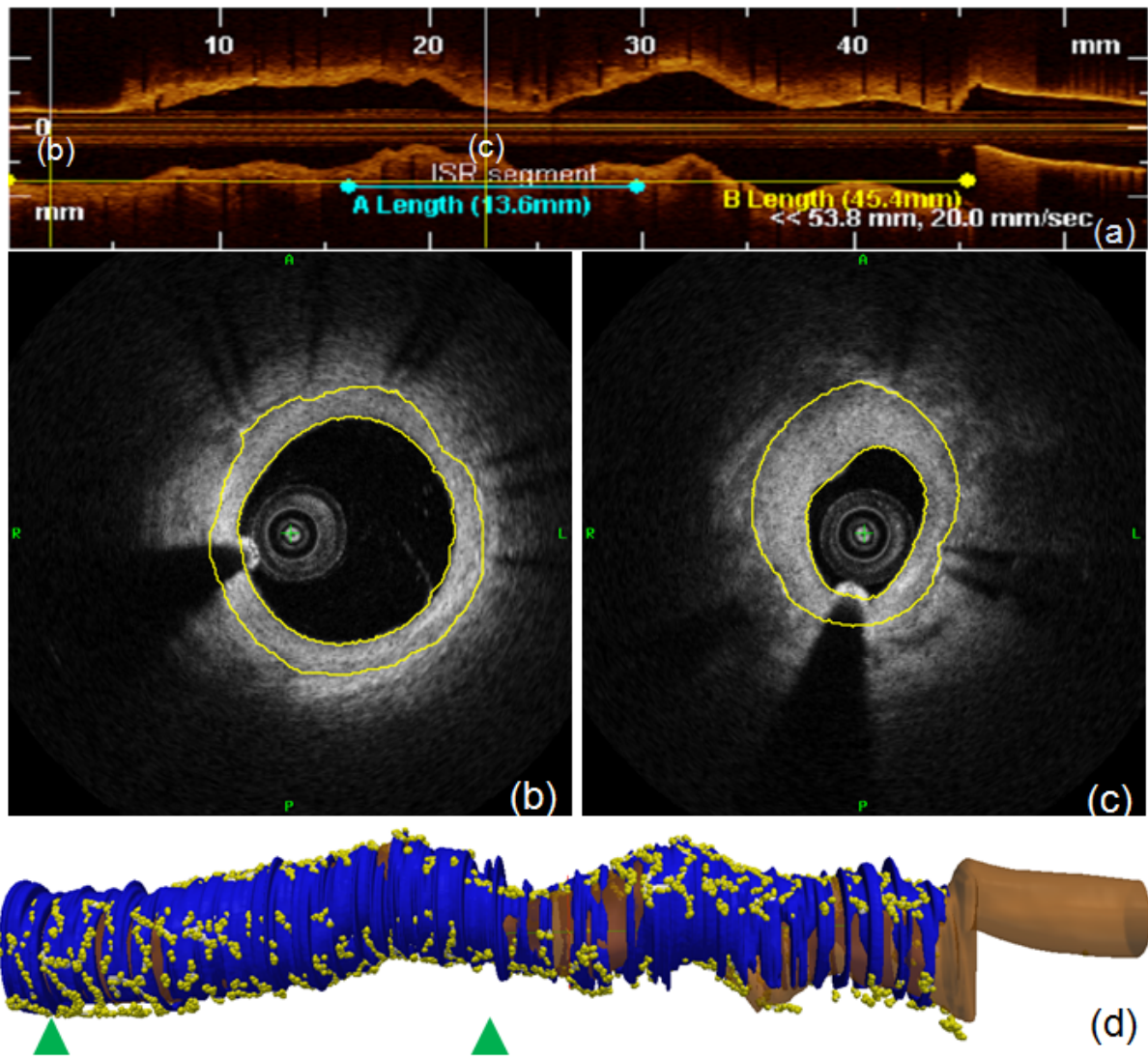
Figure 6.10: This figure shows an example of 3D neointima reconstruction (case with moderate narrowing). (a) the longitudinal view of the moderate narrow patient sequence (P16). (b) and (c) are the random selected slices in the sequence. (d) the 3D longitudinal view. Blue regions are neointima segmentations.Blue regions are neointima segmentations. Yellow spheres are the stent struts detected from Chapter 5 and lumen border segmentations (brown color) are extracted from Chapter 4.

the manual neointima segmentations and provide highly accurate results even though the stent

properties (such as stent position, stent strut thickness and stent shape) are unavailable.
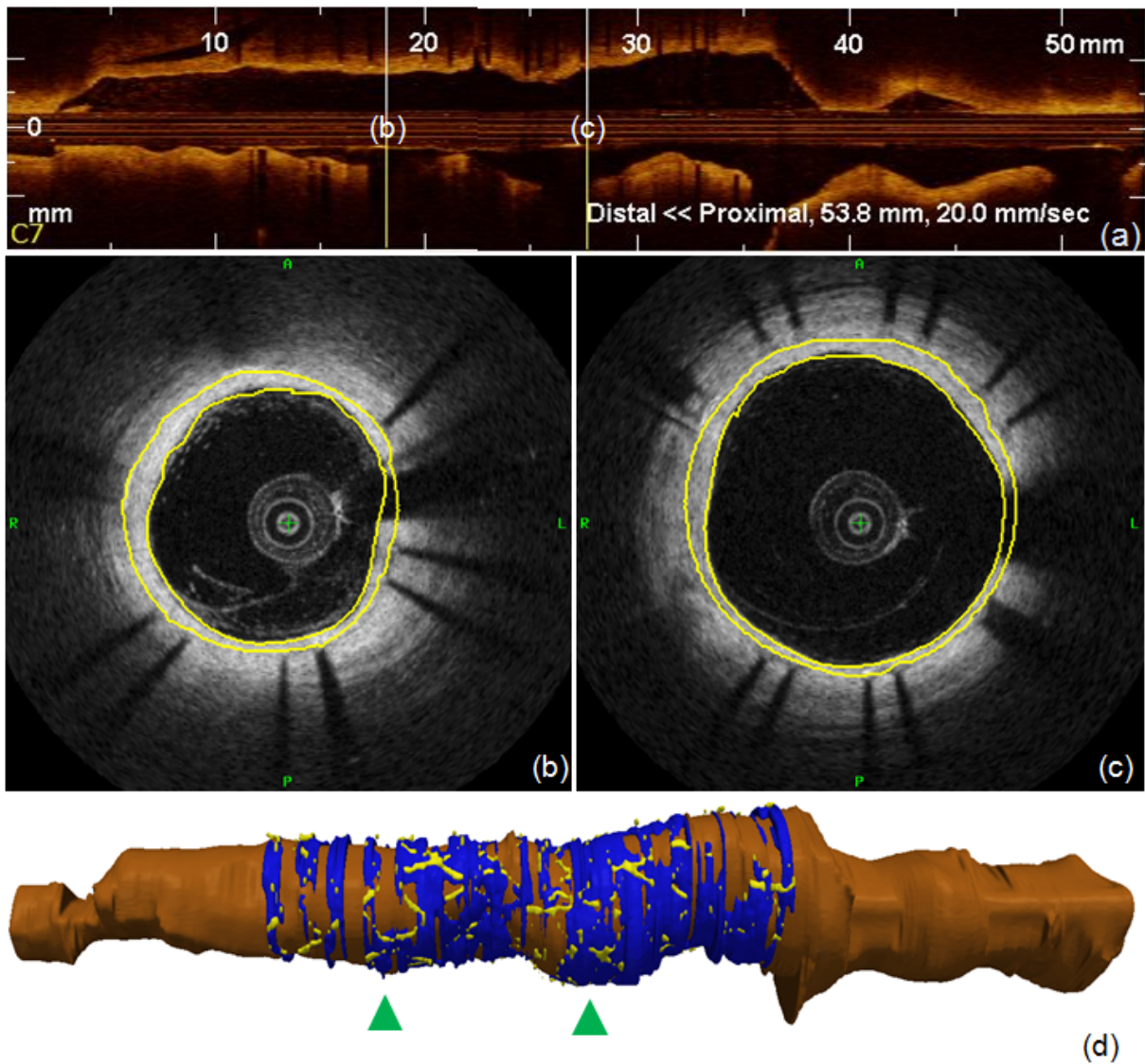
Figure 6.11: This figure shows an example of 3D neointima reconstruction (case with serve narrowing). (a) the longitudinal view of the serve narrow patient sequence (P4). (b) and (c) are the random selected slices in the sequence. (d) the 3D longitudinal view. Blue regions are neointima segmentations. Yellow spheres are the stent struts detected from Chapter 5 and lumen border segmentations (brown color) are extracted from Chapter 4.

6.4 Summary

In this chapter, we have presented a patch-based label fusion method based on a multi-atlas approach to detect neointimal tissue in IVOCT sequences. The approach consists of an atlas selection step, propagation step and label fusion step. In the atlas selection, measurements, LPDS and LCSA, are used to select the images with narrow lumen area. This step excludes the light restenosis cases since the thick neointima results in the severe restenosis. Atlases are
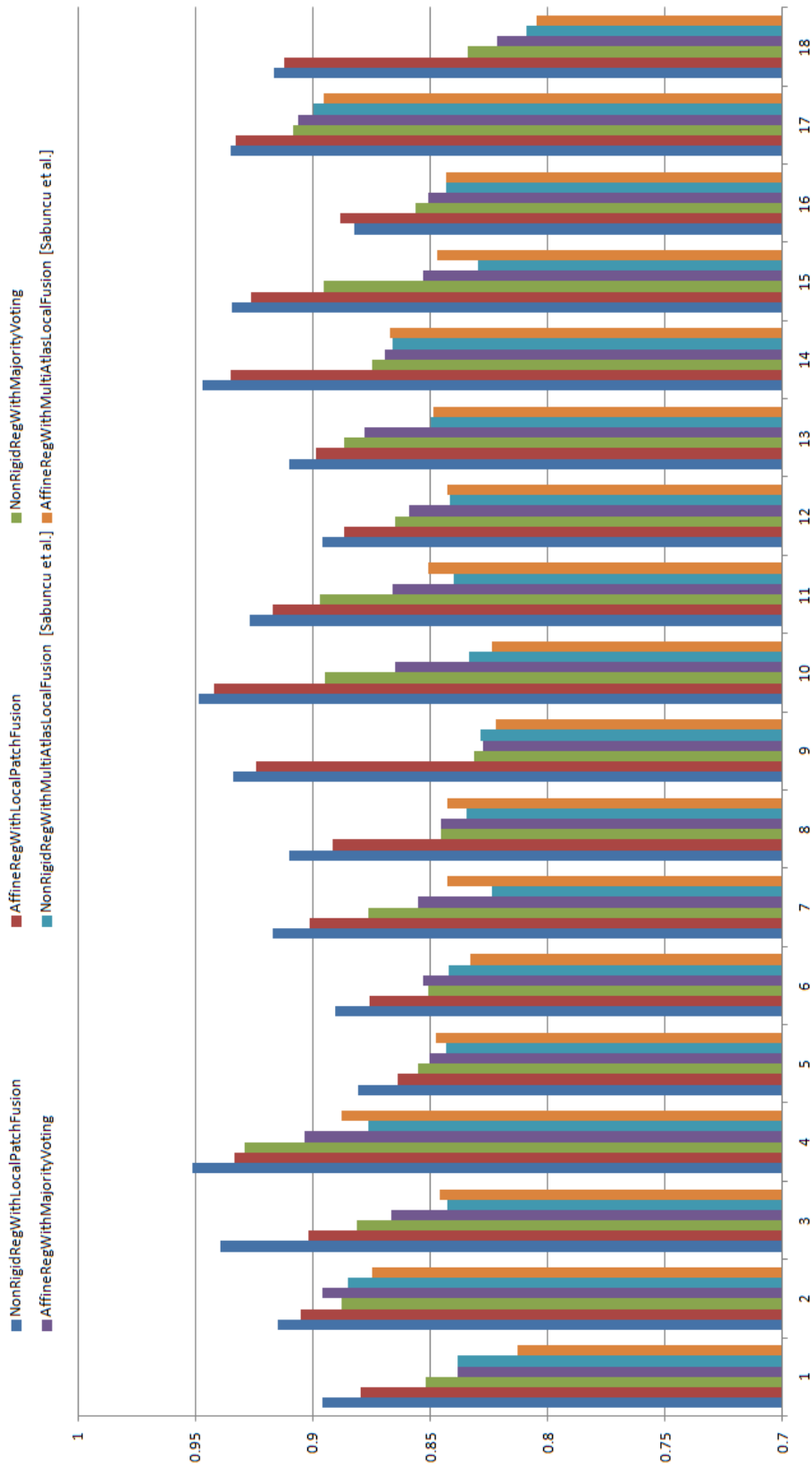
Figure 6.12: This figure shows the comparison of approaches with different registration strategies on different patients. Our proposed approach performs well in all patient sequences.
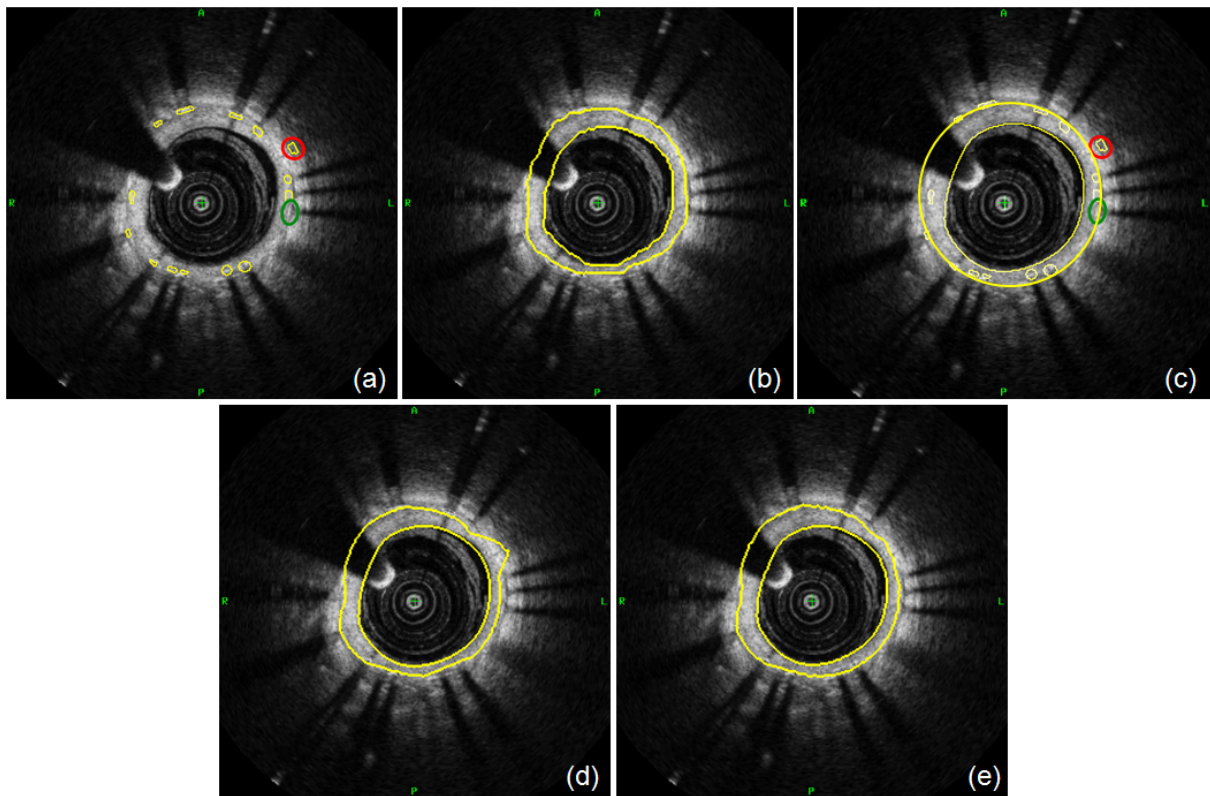
Figure 6.13: (a) represents the over-estimate/under-estimate stent struts (red/green circle) from Chapter 5; (b) the manual neointima segmentation; (c) the outer circle neointima segmentation. the over-estimate stent strut (red circle) is excluded from the circle stent area; (d) the neointima segmentation is calculated by the stent area segmentation (obtained by the proposed stent area estimation (Chapter 5)) and the lumen area segmentation (obtained by the proposed lumen area estimation (Chapter 4)). (e) the neointima segmentation is obtained by the proposed multi-atlas based method (Chapter 6).

then selected by the similarity between artery images with narrow lumen area and the unseen image. These atlases are then used in the propagation and label fusion steps.

In the label fusion step, we apply a patch-based model formulated in a probabilistic framework to extract the neointima label segmentation from each atlas. We use multiple neighbouring patches instead of a single pixel from the atlases to account for the registration errors. Lumen border information is added to improve the accuracy of the segmentation. Our method has focused on images in which stent struts are hard to be recognised or the property of the stent is not available. The results can provide useful information for clinicians and aid in the diagnosis of cardiac diseases.

We use the Dice overlap to evaluate our proposed method and some other fusion approaches compared to manual segmentations. The results showed that our proposed approach achieves
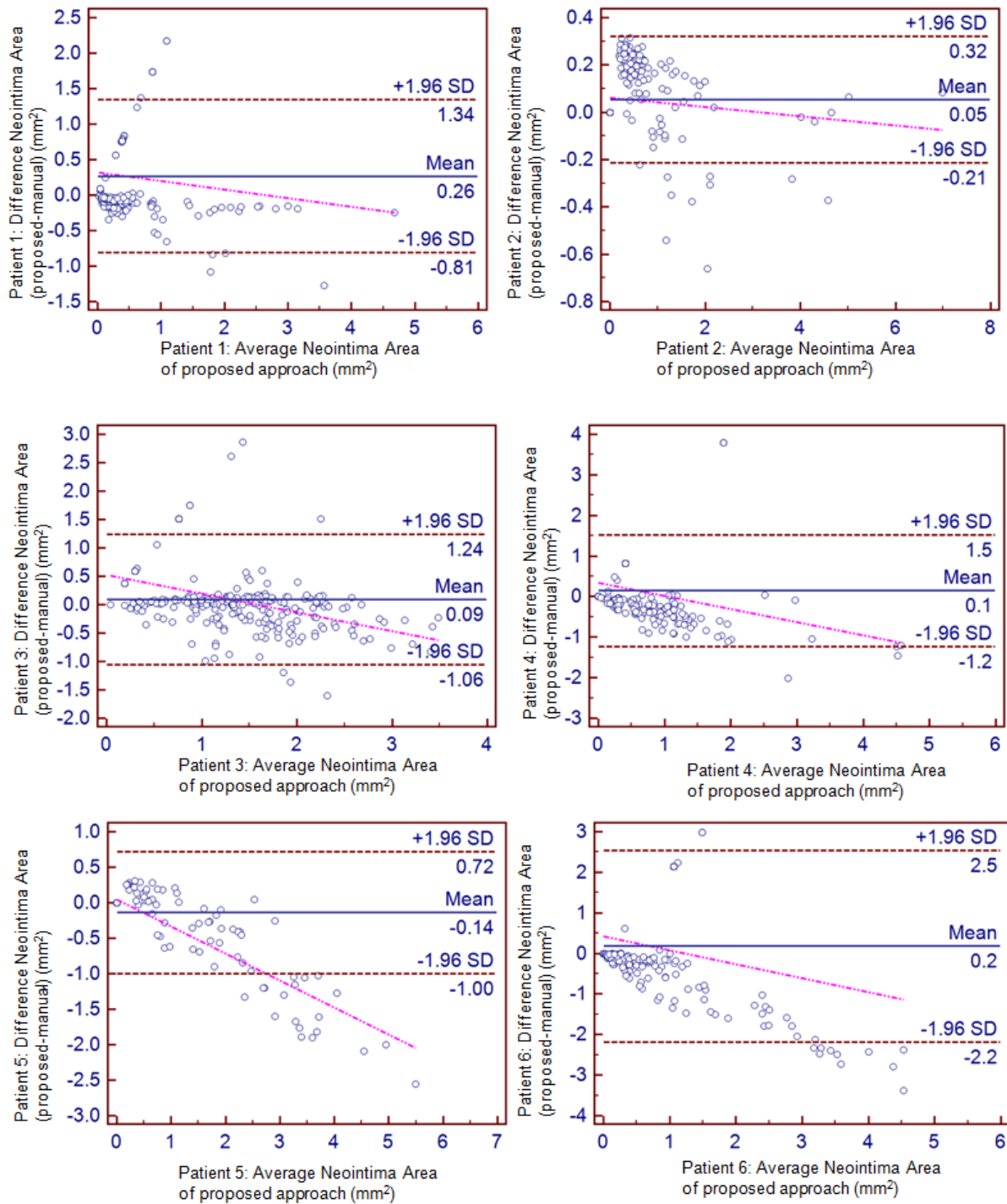
Figure 6.14: This figures shows Bland-Altman plots of 6 patients. Each plot shows differences between the proposed segmentation and manual segmentation.

high accuracy (over 90%) in the neointima overlap measurements. The comparison against manual expert segmentation demonstrates that the proposed neointima segmentation is accurate.
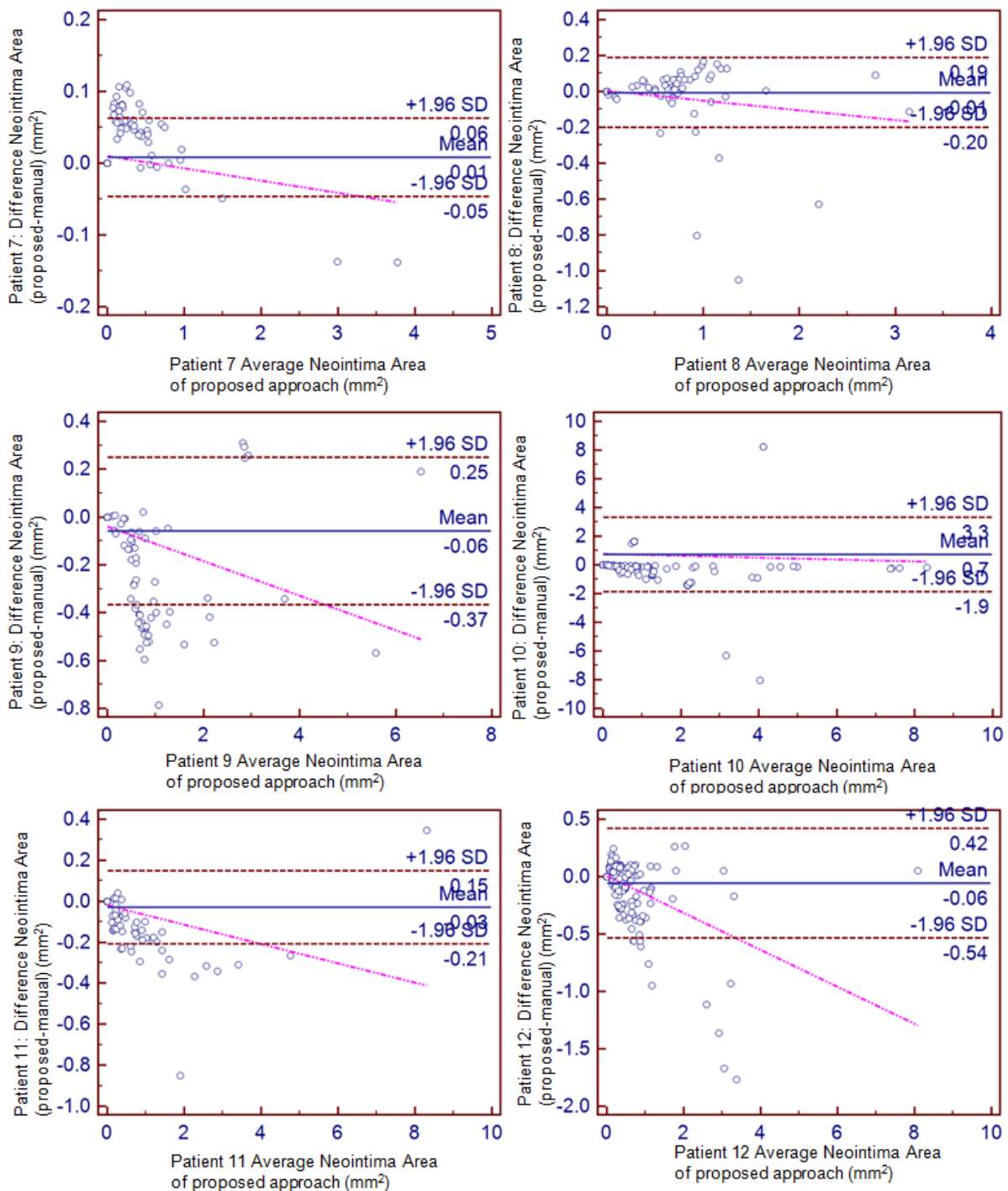
Figure 6.15: This figures shows Bland-Altman plots of 6 patients. Each plot shows differences between the proposed segmentation and manual segmentation.
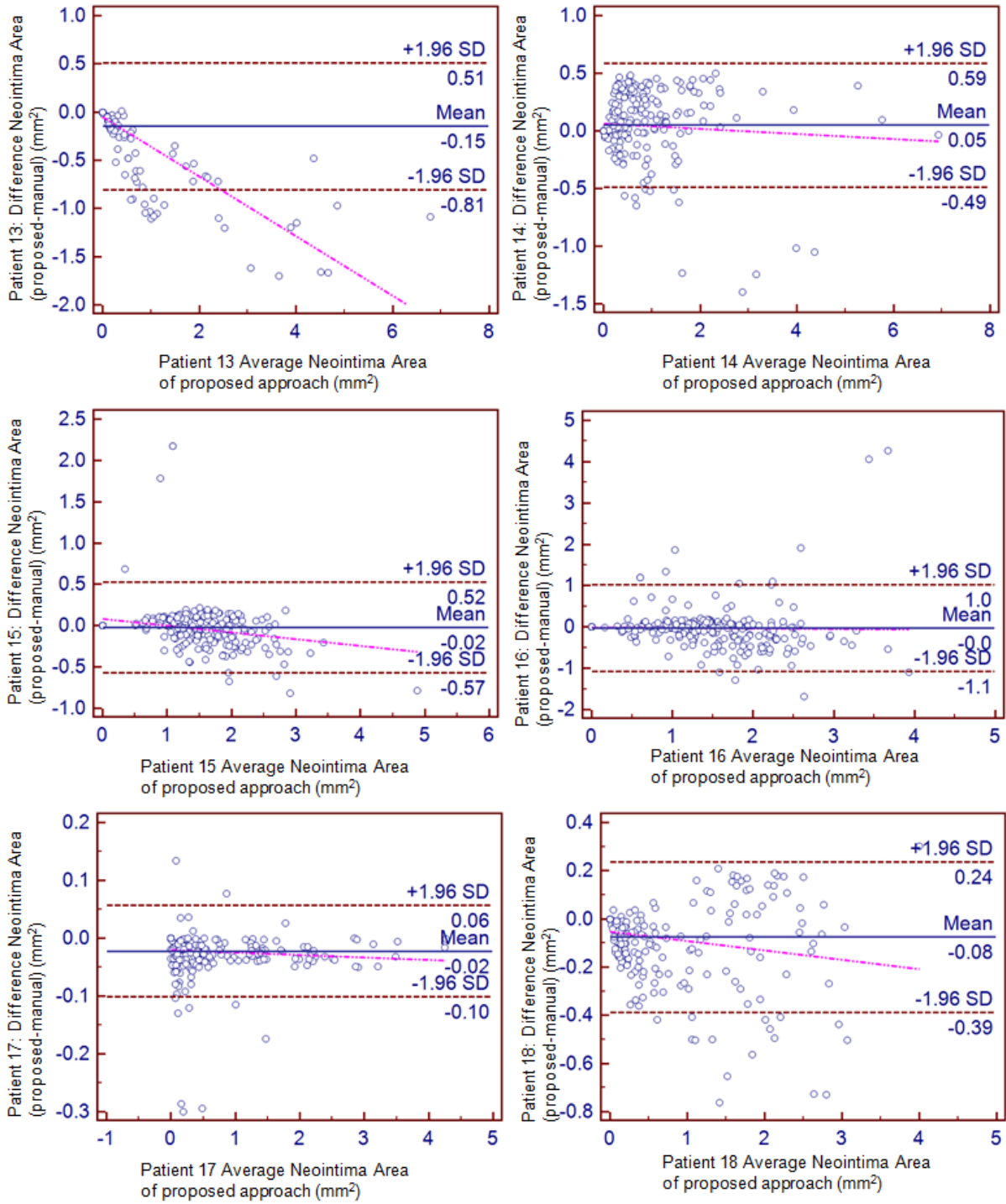
Figure 6.16: This figures shows Bland-Altman plots of 6 patients. Each plot shows differences between the proposed segmentation and manual segmentation.

Chapter 7

Conclusion

7.1 Summary

CHD is characterised by thickening of the arterial vessel wall due to atheromatous plaque. The thickening of the plaque not only narrows the arterial lumen but also leads to immediate blood clotting at the site of the artery. When the artery is seriously clotted, it can lead to heart attacks. Invasive image modalities such as IVUS and IVOCT can provide invasive information to well prevent CHD or the treatment of CHD since IVOCT permits direct tomographic visualisation of cross-sectional images of lumen border, stent struts and neointima. However, the spatial resolution of IVUS is inadequate to quantify the thickness of plaque and neointima accurately. Therefore, IVOCT has been chosen as the image modality used in this thesis as it provides high-resolution images with micrometer resolution. With IVOCT techniques, stenosis and restenosis caused by plaques and neointima can be detected and analysed.

The work in this thesis has focused on the development of a fully automatic coronary image analysis framework using segmentation techniques for IVOCT sequences. This framework can lead to comprehensive understanding of CHD and analysis of restenosis. Furthermore, the framework consists of lumen border segmentation, stent struts detection and neointima segmentation.

137

When IVOCT sequences are acquired, a guide-wire runs in parallel to the catheter outside and results in shadow artifacts in every slice of the sequence. If guide-wire shadow artifacts are not eliminated, these artifacts will lead to inaccurate lumen segmentations. However, most existing approaches do not explicitly address the guide-wire shadow artifacts elimination.

A fully automatic segmentation technique which is capable of generating an accurate lumen border segmentation from IVOCT image sequences is proposed. This technique can eliminate guide-wire shadow artifacts and accurately estimates the lumen borders. The segmentation approach is based on a novel combination of EM framework and GC based optimisation. This combination provides initial estimates of the boundaries of lumen border and positions of guide-wire artifacts. After identification of the artifacts, a geometrically-based method is proposed to remove them. Finally, the initial lumen border points are connected by a deformable method to estimate the lumen border. Compared to the commercial system (the C7-XR system) the approach has achieved high overlap accuracy in terms of lumen area estimation.

After the lumen border has been segmented, the next step is to identify the coronary stents. In general, after stent implantation, stent struts can be classified into covered stent struts, apposed stent struts and malapposed stent struts according to the appearance of the strut positions in cross-sectional images. When a stent is placed well at the site of blockage of a coronary artery, this is referred to as stent apposition. If it does not reach the arterial wall, stent malapposition occurs and may cause LST. Covered stent struts are stent struts covered by neointima tissue which can provide information about restenosis. Most existing algorithms focus on the detection of the strut position without considering the weak intensity responses of stent struts.

A novel automatic stent struts detection method which detects the strut shadow zone and accurately segments and reconstructs the stent strut in 3D is proposed. The position of the strut shadow zone is a key requirement which enables the strut segmentation. After identification of the shadow zone, an a-priori Gaussian probability map for every detected shadow is built to estimate the probable stent strut position. This probability map can be used to estimate not only malapposed struts but also apposed and covered struts when their intensity response

is weak. With the detected stent struts, the stent area can be estimated. The stent area is used for analysis of neointima coverage. The segmentation results demonstrate that three types of stent struts can be accurately segmented but the stent area is overestimate. This is because sensitive thresholds are used to identify the strut shadow zones and stent struts. With inaccurate stent strut identification, the inaccurate stent can be estimated and this leads to inaccurate neointima segmentations. To reduce the sensitivity, an alternative neointima segmentation approach (multi-atlas based neointima segmentation) has been proposed.

The thickness of the neointima is the main measurement for the analysis of the severity of stenosis/restenosis. Since the accurate segmented lumen border and stent area segmentation are obtained, the NIH can be estimated. However, if the estimation of stent area is inaccurate, the neointima segmentation can fail. Inaccurate stent area estimation often occurs when the stent struts are invisible or struts positions are difficult to recognise. Existing algorithms do not deal with this inaccurate neointima estimation caused by the inaccurate stent area estimation.

To overcome the problem caused by the stent area estimation, a multi-atlas based segmentation method that segments NIH with information about the lumen border instead of the stent area has been developed. The approach can be regarded as a classifier ensemble in which each atlas acts as a classifier and the opinions from all atlases are fused. Atlases are selected by measurements of stenosis and a similarity measure, CC. A probabilistic patch-based label fusion model is then developed to estimate neointima tissue in the unseen image. The label at a pixel in the unseen image is determined by fusing the labels at the corresponding pixels from each atlas. Before label fusion, each atlas is registered via non-rigid registration [Rueckert et al., 1999]. To account for registration errors, multiple neighbouring patches are extracted from each atlas instead of a single pixel as proposed in [Sabuncu et al., 2010, Coupe et al., 2011]. In addition, the location of the patch in the unseen image also contributes to the label fusion. Compared to other label fusion approaches, a significant increase in segmentation accuracy has been observed.
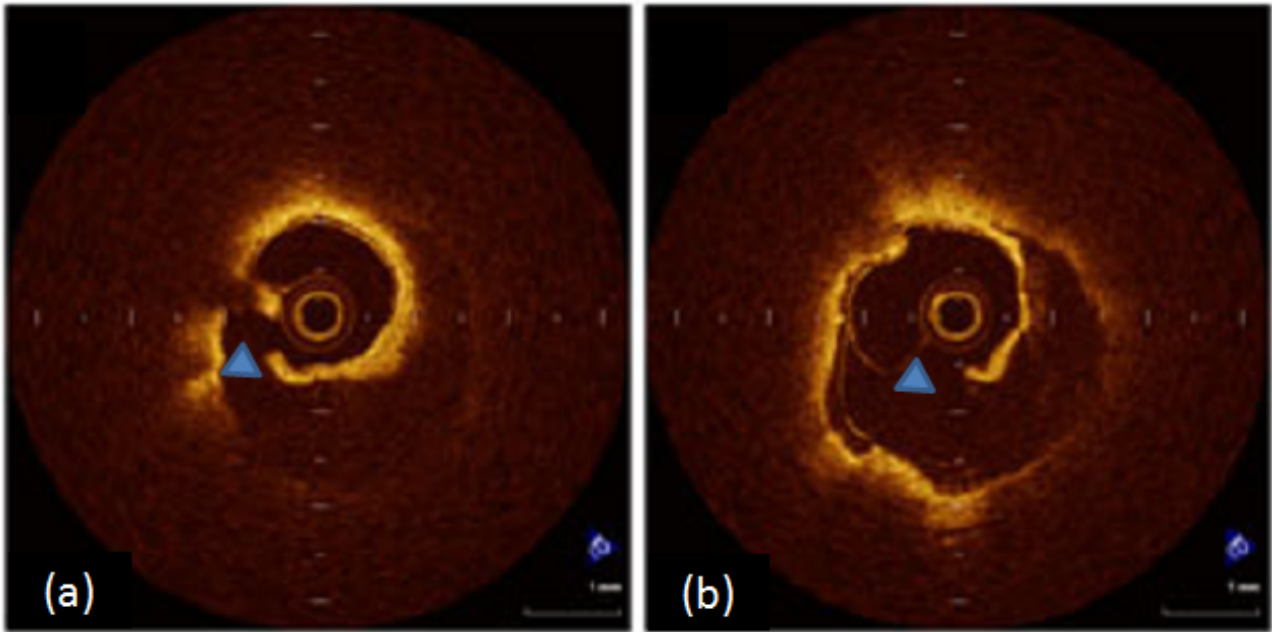
Figure 7.1: Examples of plaque rupture. Triangles highlight the plaque rupture positions. From [Kubo et al., 2011].

7.2   Limitations and Future Work

The thesis has focused on using image segmentation for coronary stent detection and coronary restenosis analysis in IVOCT sequences. We have proposed an automatic approach to segment the lumen border. Future work will investigate how to extend this framework to estimate lumen border in the case of plaque rupture (Figure 7.1) which is the main cause of heart attacks [Hong et al., 2004].

When plaque rupture occurs, the lumen border is difficult to segment. A possible solution is to estimate the approximate lumen border from neighbouring slices. The guide-wire elimination method can be extended from 2D to 3D to estimate the approximate lumen diameter. With the approximate lumen diameter and a 3D deformable model, i.e. [Caselles et al., 1996], the lumen border can be obtained in the presence of plaque rupture.

Our stent strut detection method can detect a stent well in IVOCT sequences. However, our method cannot deal with cases in which multiple stents are implanted. If multiple stents exist (Figure 7.2), the assumption that a stent strut shadow follows a stent strut is violated.
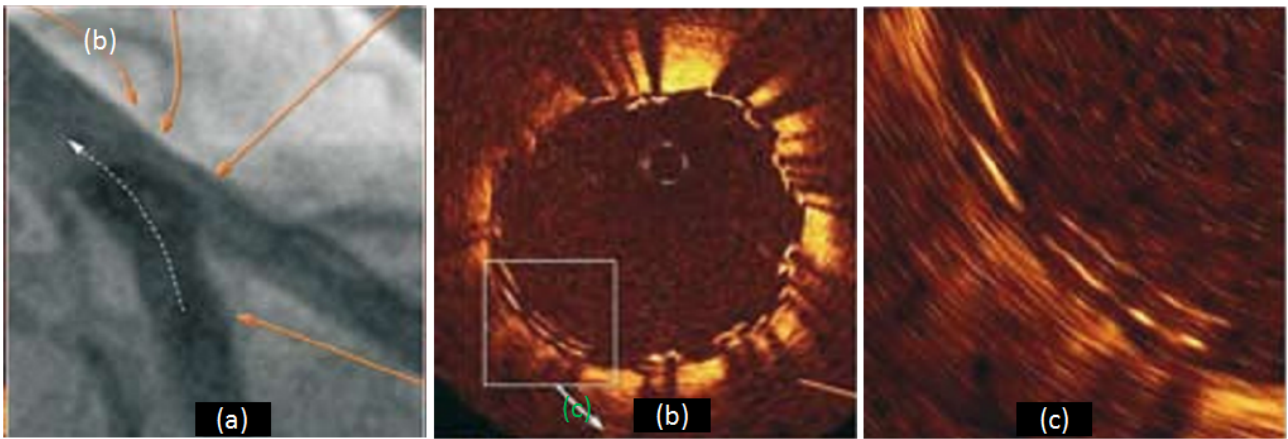
Figure 7.2: (a) angiographic result after implantation of two stents into the left anterior descending artery and diagonal branch. The white arrow indicates the optical coherence tomography imaging wire. (b) Well apposed two layers of struts in the proximal segment. (c) Magnification of the two layers of struts from image (b). From [Tyczynski et al., 2010].

This means multiple stent struts might share one strut shadow (see Figure 7.2(b) and (c)). A steerable filter [Freeman and Adelson, 1991] may offer a solution in this case. A steerable filter is an orientation-selective convolution kernel used for image enhancement and feature extraction that can be expressed via a linear combination of a small set of rotated versions of itself. The first oriented derivative of a 2D Gaussian can be used to recognise possible strut shape edges. With the probability map used in our proposed method for identification of a stent strut, the locations of multiple stent struts can be estimated.

With accurate lumen border segmentations and stent segmentations, the final goal of the CHD analysis is to perform true 3D lumen reconstruction of a coronary vessel by a fusion of x-ray angiography (XA) and IVOCT images. IVOCT provides cross-sectional information of the coronary but it lacks information about the curvature of the coronary. An additional image modality, such as XA, can be used to overcome this shortage since XA provides the information about vessel curvature. Therefore, by fusing these two modalities, a 3D coronary model that provides the curvature estimation and cross-sectional information can be reconstructed.

The first step of the 3D model reconstruction is to reconstruct the 3D catheter path from biplane angiograms [Wahle et al., 1995, Molina et al., 1998, Yang et al., 2009]. Reconstruction of the trajectory in the 3D space is based on the corresponding points on the two angiographic views using epipolar geometry [Hartley and Zisserman, 2004]. Alternatively, it is possible

to reconstruct the 3D catheter path via motion compensation [Perrenot et al., 2006]. The method uses markers on a device or guide-wire to identify and estimate the motion of an object or region of interest in order to register and motion compensate the projection images to generate a motion-free reconstruction [Schoonenberg et al., 2008, Schoonenberg, 2010]. Only frames in which markers were identified can be motion compensated and will be used in the reconstruction process. Motion compensation, in general, is achieved by generating a static 3D model of the markers, forward projecting the 3D marker positions to all projection images and warping the images using an affine transformation from the detected marker positions to the forward projected positions. These motion compensated images are used as input for a Feldkamp (FDK) [Feldkamp et al., 1984] reconstruction instead of the original acquired images.

After the 3D catheter path has been reconstructed from two angiographic views, this path can be considered as the pullback trajectory so that cross-sectional images (IVUS or IVOCT) can be aligned along the trajectory. [Tu et al., 2011, Tu et al., 2012] proposed an approach that estimates the corresponding IVUS/IVOCT image from the reconstructed vessel centerline based on the vessel curvature where the vessel deviates from being a straight tube. To determine the curvature at each position along the vessel, the reconstructed arterial centerline is approximated by a parameterised Bezier curve [Bartels et al., 1996] and the curvature is calculated using the first and second derivatives.

By indicating baseline positions (anatomical or mechanical landmarks visualised in both angiographic and IVUS/IVOCT images) along the reconstructed arterial centerline, the corresponding axial positions in the cross-sectional images can be obtained via registration approaches [Rotger et al., 2001, Wahle et al., 2006, Schuurbiers et al., 2009]. After the registration, point-to-point correspondences between the XA and IVOCT images are established and markers superimposed on different image views are synchronised. Thus, the 3D model of the coronary vessel is fully reconstructed. In clinic, this model can not only assist the diagnosis of CHD but also analyse of the severity of restenosis. With the information from the 3D model, suggestions of treatments (from doctors) can be given to patients who have in-stent restenosis or the related diseases.

Bibliography

[Abizaid et al., 1998] Abizaid, A., Mintz, G. S., Pichard, A. D., Kent, K. M., Satler, L. F., Walsh, C. L., Popma, J. J., and Leon, M. B. (1998). Clinical, intravascular ultrasound, and quantitative angiographic determinants of the coronary flow reserve before and after percutaneous transluminal coronary angioplasty. *The American Journal of Cardiology*, 82(4):423 – 428.

[Aljabar et al., 2007] Aljabar, P., Heckemann, R., Hammers, A., Hajnal, J., and Rueckert, D. (2007). Classifier selection strategies for label fusion using large atlas databases. *Medical Image Computing and Computer-Assisted Intervention*, 4791:523–531.

[Aljabar et al., 2009] Aljabar, P., Heckemann, R. A., Hammers, A., Hajnal, J. V., and Rueckert, D. (2009). Multi-atlas based segmentation of brain images: Atlas selection and its effect on accuracy. *NeuroImage*, 46(3):726–738.

[Arjomand et al., 2003] Arjomand, H., Turi, Z. G., McCormick, D., and Goldberg, S. (2003). Percutaneous coronary intervention: historical perspectives, current status, and future directions. *American Heart Journal*, 146(5):787 – 796.

[Artaechevarria et al., 2008] Artaechevarria, X., Munoz-Barrutia, A., and de Solorzano, C. O. (2008). Efficient classifier generation and weighted voting for atlas-based segmentation: Two small steps faster and closer to the combination oracle. *SPIE Medical Imaging*, 6914(3):69141W–1.

[Artaechevarria et al., 2009] Artaechevarria, X., Munoz-Barrutia, A., and de Solorzano, C. O. (2009). Combination strategies in multi-atlas image segmentation: Application to brain mr data. *IEEE Transactions on Medical Imaging*, 28(8):1266–1277.

[Athanasiou et al., 2011] Athanasiou, L. S., Exarchos, T. P., Naka, K. K., Michalis, L. K., Prati, F., and Fotiadis, D. I. (2011). Atherosclerotic plaque characterization in optical coherence tomography images. *IEEE Engineering in Medicine and Biology Society*, pages 4485 –4488.

[Athanasiou et al., 2010] Athanasiou, L. S., Karvelis, P. S., Tsakanikas, V. D., Stefanou, K. A., Naka, K. K., Michalis, L. K., Rigas, G. A., and Fotiadis, D. I. (2010). Atherosclerotic plaque characterization using geometrical features from virtual histology intravascular ultrasound images. *Information Technology and Applications in Biomedicine (ITAB)*, pages 1 –4.

[Bai et al., 2012] Bai, W. J., Shi, W. Z., Wang, H. Y., Peters, N. S., and Rueckert, D. (2012). Multi-atlas based segmentation with local label fusion for right ventricle mr images. *MICCAI 2012 - 3D Cardiovascular Imaging Segmentation Challenge*, pages 137–144.

[Bartels et al., 1996] Bartels, R., Beatty, J. C., and Barsky, B. A. (1996). *An Introduction to Splines for Use in Computer Graphics and Geometric Modeling*. Morgan Kaufmann Publishers.

[Bedekar et al., 2003] Bedekar, D., Nair, A., and Vince, D. G. (2003). Atherosclerotic plaque characterization by acoustic impedance analysis of intravascular ultrasound data. *IEEE Symposium on Ultrasonics*, 2:1524 – 1527.

[Bennett, 2003] Bennett, M. R. (2003). In-stent stenosis: Pathology and implications for the development of drug eluting stents. *Heart*, 89(2):218–224.

[Berke, 2007] Berke, A. D. (2007). ptca and stent implantation. http://www.cardiology.md/procedures.htm.

[Besag, 1974] Besag, J. (1974). Spatial interaction and the statistical analysis of lattice systems. *Journal of the Royal Statistical Society. Series B (Methodological)*, 36(2):192–236.

[Bezerra et al., 2009] Bezerra, H. G., Costa, M. A., Guagliumi, G., Rollins, A. M., and Simon, D. I. (2009). Intracoronary optical coherence tomography: A comprehensive reviewclinical and research applications. *JACC: Cardiovascular Interventions*, 2(11):1035–1046.

[Binder, 2002] Binder, T. (2002). three-dimensional echocardiography - principles and promises. *Journal of clinical and basic cadiology*, 5(2):149–152.

[Bluemke et al., 2008] Bluemke, D. A., Achenbach, S., Budoff, M., Gerber, T. C., Gersh, B., Hillis, L. D., Hundley, W. G., Manning, W. J., Printz, B. F., Stuber, M., and Woodard, P. K. (2008). Noninvasive coronary artery imaging. magnetic resonance angiography and multidetector computed tomography angiography. *Circulation*, 118(5):586–606.

[Bonnema et al., 2008] Bonnema, G. T., Cardinal, K. O., Williams, S. K., and Barton, J. K. (2008). An automatic algorithm for detecting stent endothelialization from volumetric optical coherence tomography datasets. *physics in Medicine and Biology*, 53(12):3083–3098.

[Boykov et al., 2001a] Boykov, Y., Lee, V. S., Rusinek, H., and Bansal, R. (2001a). Segmentation of dynamic n-d data sets via graph cuts using markov models. *Medical Image Computing and ComputerAssisted Intervention*, 2208:1058–1066.

[Boykov et al., 2001b] Boykov, Y., Veksler, O., and Zabih, R. (2001b). Fast approximate energy minimization via graph cuts. *IEEE Transactions on Pattern Analysis and Machine Intelligence*, 23(11):1222–1239.

[Boykov and Jolly, 2001] Boykov, Y. Y. and Jolly, M. P. (2001). Interactive graph cuts for optimal boundary & region segmentation of objects in n-d images. *IEEE International Conference on Computer Vision*, 1:105–112.

[Briguori et al., 2001] Briguori, C., Anzuini, A., Airoldi, F., Gimelli, G., Nishida, T., Adamian, M., Corvaja, N., Mario, C. D., and Colombo, A. (2001). Intravascular ultrasound criteria for the assessment of the functional significance of intermediate coronary artery stenoses and comparison with fractional flow reserve. *The American Journal of Cardiology*, 87(2):136 – 141.

[Bruining et al., 2011] Bruining, N., Sihan, K., Ligthart, J., de Winter, S., and Regar, E. (2011). Automated three-dimensional detection of intracoronary stent struts in optical coherence tomography images. *Computing in Cardiology*, pages 221 –224.

[Brusseau et al., 2004] Brusseau, E., de Korte, C. L., Mastik, F., Schaar, J., and van der Steen, A. F. W. (2004). Fully aautomatic luminal contour segmentation in intracoronary ultrasound imaging - a statistical approach. *IEEE Transactions on Medical Imaging,*, 23(5):554 –566.

[Buckley, 2011] Buckley, C. J. (2011). Intravascular ultrasound is critical to insuring long-term stent performance. *Vascular Disease Management*, pages 87–92.

[Bult, 2000] Bult, H. (2000). Restenosis: a challenge for pharmacology. *Trends in Pharmacological Sciences*, 21(7):274 – 279.

[Cabrera-Fernandez, 2005] Cabrera-Fernandez, D. (2005). Delineating fluid-filled region boundaries in optical coherence tomography images of the retina. *IEEE Transactions on Medical Imaging*, 24(8):929 –945.

[Cabrera-Fernandez et al., 2005] Cabrera-Fernandez, D., Salinas, H. M., and Puliafito, C. A. (2005). Automated detection of retinal layer structures on optical coherence tomography images. *Optics Express*, 13(25):10200–10216.

[Camilus and Govindan, 2012] Camilus, K. S. and Govindan, V. K. (2012). A review on graph based segmentation. *International Journal of Image, Graphics and Signal Processing (IJIGSP)*, 5:1–13.

[Caramori et al., 1999] Caramori, P. R. A., Lima, V. C., Seidelin, P. H., Newton, G. E., Parker, J. D., and Adelman, A. G. (1999). Long-term endothelial dysfunction after coronary artery stenting. *Journal of the American College of Cardiology*, 34(6):1675 – 1679.

[Cardinal et al., 2005] Cardinal, M., Meunier, J., Soulez, G., Maurice, R., Therasse, E., and Cloutier, G. (2005). Automatic 3d segmentation of intravascular ultrasound images using region and contour information. *Medical Image Computing and Computer-Assisted Intervention*, 3749:319–326.

[Cardinal et al., 2006] Cardinal, M. H. R., Meunier, J., Soulez, G., Maurice, R. L., Therasse, E., and Cloutier, G. (2006). Intravascular ultrasound image segmentation: a three-dimensional fast-marching method based on gray level distributions. *IEEE Transactions on Medical Imaging*, 25(5):590 –601.

[Caselles et al., 1996] Caselles, V., Kimmel, R., Sapiro, G., and Sbert, C. (1996). 3d active contours. *Lecture Notes in Control and Information Sciences*, 219:43–49.

[Catmull and Rom, 1974] Catmull, E. and Rom, R. (1974). A class of local interpolating splines. *Computer aided geometric design. Academic Press.*, pages 317–326.

[Chen et al., 2012] Chen, X., Nacif, M. S., Liu, S., Sibley, C., Summers, R. M., Bluemke, D. A., and Yao, J. (2012). A framework of whole heart extracellular volume fraction estimation for low-dose cardiac ct images. *IEEE Transactions on Information Technology in Biomedicine*, 16(5):842 –851.

[Chiu et al., 2010] Chiu, S. J., Li, X. T., Nicholas, P., Toth, C. A., Izatt, J. A., and Farsiu, S. (2010). Automatic segmentation of seven retinal layers in sdoct images congruent with expert manual segmentation. *Optics Expresst*, 18(18):19413–19428.

[Cohen et al., 1992] Cohen, I., Cohen, L., and Ayache, N. (1992). Using deformable surfaces to segment 3-d images and infer differential structures. *European Conference on Computer Vision*, 588:648–652.

[Collignon et al., 1995] Collignon, A., Maes, F., Delaere, D., Vandermeulen, P., Suetens, P., and Marchal, G. (1995). automated multimodality image registration based on information theory. *Information Processing in Medical Imaging*, 3:263–274.

[Commowick et al., 2009] Commowick, O., Warfield, S. K., and Malandain, G. (2009). Using frankenstein's creature paradigm to build a patient specific atlas. *Medical Image Computing and Computer Assisted Intervention*, 5762:993–1000.

[Cootes et al., 1995] Cootes, T., Taylor, C., Cooper, D., and Graham, J. (1995). Active shape models-their training and application. *Computer Vision and Image Understanding*, 61(1):38 – 59.

[Cormen et al., 2001] Cormen, T. H., Leiserson, C. E., Rivest, R. L., and Stein, C. (2001). *Introduction to Algorithms, Second Edition*. The MIT Press, 2 edition.

[Coupe et al., 2011] Coupe, P., Manjon, J. V., Fonov, V., Pruessner, J., Robles, M., and Collins, D. L. (2011). Patch-based segmentation using expert priors: Application to hippocampus and ventricle segmentation. *NeuroImage*, 54(2):940 – 954.

[Cour et al., 2005] Cour, T., Benezit, F., and Shi, J. (2005). Spectral segmentation with multiscale graph decomposition. *Computer Vision and Pattern Recognition*, 2:1124–1131.

[Dabov et al., 2007] Dabov, K., A.Foi, V.Katkovnik, and Egiazarian, K. (2007). Image denoising by sparse 3d transform-domain collaborative filtering. *IEEE Transactions on Image Processing*, 16(8):2080–2095.

[de Berg et al., 1997] de Berg, M., van Kreveld, M., Overmars, M., and Schwarzkopf, O. (1997). *Computational Geometry: Algorithms and Applications*. Springer.

[DeBuc, 2011] DeBuc, D. C. (2011). *Image Segmentation*, chapter A Review of Algorithms for Segmentation of Retinal Image Data Using Optical Coherence Tomography, pages 15–54. InTech Europe.

[Dempster et al., 1977] Dempster, A. P., Laird, N. M., and Rubin, D. B. (1977). Maximum likelihood from incomplete data via the em algorithm. *JOURNAL OF THE ROYAL STATISTICAL SOCIETY, SERIES B*, 39(1):1–38.

[Denes et al., 2012] Denes, L., Entz, L., and Jancsik, V. (2012). Restenosis and therapy. *International Journal of Vascular Medicine*, 2012:1–9.

[Dice, 1945] Dice, L. R. (1945). Measures of the amount of ecologic association between species. *Ecology*, 26(3):297–302.

[Dikici and Orderud, 2010] Dikici, E. and Orderud, F. (2010). Graph-cut based edge detection for kalman filter based left ventricle tracking in 3d+t echocardiography. *Computing in Cardiology*, pages 205 –208.

[Dubuisson et al., 2009] Dubuisson, F., Kauffmann, C., Motreff, P., and Sarry, L. (2009). In vivo oct coronary imaging augmented with stent reendothelialization score. *Medical Image Computing and Computer-Assisted Intervention*, 5761:475–482.

[Elbasiony and Levkowitz, 2011] Elbasiony, A. and Levkowitz, H. (2011). Characterization of atherosclerosis plaque in oct images using texture analysis and parametric equations. *Information Visualisation*, pages 237 –240.

[Feldkamp et al., 1984] Feldkamp, L. A., Davis, L. C., and Kress, J. W. (1984). Practical cone-beam algorithm. *Journal of the Optical Society of America A: Optics, Image Science, and Vision,*, 1(6):612–619.

[Fercher et al., 2003] Fercher, A. F., Drexler, W., Hitzenberger, C. K., and Lasser, T. (2003). Optical coherence tomographyprinciples and applications. *Reports on Progress in Physics*, 66(2):239–303.

[Fitzgibbon et al., 1998] Fitzgibbon, A., Pilu, M., and Fisher, R. B. (1998). Direct least square fitting of ellipses. *IEEE Transactionson Pattern Analysis and Machine Intelligence*, 1(7):476–480.

[Frangi et al., 1998] Frangi, A., Niessen, W., Vincken, K., and Viergever, M. (1998). Multiscale vessel enhancement filtering. *Medical Image Computing and Computer-Assisted Interventation*, pages 130–137.

[Freeman and Adelson, 1991] Freeman, W. T. and Adelson, E. H. (1991). The design and use of steerable filters. *IEEE Transactions on Pattern Analysis and Machine Intelligence*, 13(9):891 –906.

[Fuller et al., 2007] Fuller, A. R., Zawadzki, R. J., Choi, S., Wiley, D. F., Werner, J. S., and Hamann, B. (2007). Segmentation of three-dimensional retinal image data. *IEEE Transactions on Visualization and Computer Graphics*, 13(6):1719 –1726.

[Funka-Lea et al., 2006] Funka-Lea, G., Boykov, Y., Florin, C., Jolly, M. P., Moreau-Gobard, R., Ramaraj, R., and Rinck, D. (2006). Automatic heart isolation for ct coronary visualization

using graph-cuts. *IEEE International Symposium on Biomedical Imaging: Nano to Macro*, pages 614 –617.

[Garvin et al., 2008] Garvin, M. K., Abramoff, M. D., Kardon, R., Russell, S. R., Wu, X., and Sonka, M. (2008). Intraretinal layer segmentation of macular optical coherence tomography images using optimal 3-d graph search. *IEEE Transactions on Medical Imaging*, 27(10):1495 –1505.

[Gawaz et al., 1996] Gawaz, M., Neumann, F.-J., Ott, I., May, A., and Schomig, A. (1996). Platelet activation and coronary stent implantation. *Circulation*, 94(3):279–285.

[German and German, 1984] German, S. and German, D. (1984). Stochastic relaxation, gibbs distribution aand the bayesian restoration of images. *IEEE Transactions on Pattern Analysis and Machine Intelligence*, 6(6):721–741.

[Gil et al., 2000a] Gil, D., Radeva, P., and Saludes, J. (2000a). Segmentation of artery wall in coronary ivus images: a probabilistic approach. *International Conference on Pattern Recognition*, 4:352 –355.

[Gil et al., 2000b] Gil, D., Radeva, P., Saludes, J., and Mauri, J. (2000b). Automatic segmentation of artery wall in coronary ivus images: a probabilistic approach. *Computers in Cardiology*, pages 687 –690.

[Gilboa et al., 2004] Gilboa, G., Sochen, N., and Zeevi, Y. Y. (2004). Image enhancement and denoising by complex diffusion processes. *IEEE Transactions on Pattern Analysis and Machine Intelligence*, 26(8):1020 –1036.

[Gonzalo, 2010] Gonzalo, N. (2010). *Optical Coherence Tomography for the Assessment of Coronary Atherosclerosis and Vessel Response after Stent Implantation*. PhD thesis, Erasmus University Rotterdam.

[Gurmeric et al., 2009] Gurmeric, S., Isguder, G. G., Carlier, S., and Unal, G. (2009). A new 3-d automated computational method to evaluate in-stent neointimal hyperplasia in in-vivo intravascular optical coherence tomography pullbacks. *Medical Image Computing and Computer-Assisted Intervention*, 5762:776–785.

[Gutierrez-Chico et al., 2012] Gutierrez-Chico, J. L., Alegria-Barrero, E., Teijeiro-Mestre, R., Chan, P. H., Tsujioka, H., de Silva, R., Viceconte, N., Lindsay, A., Patterson, T., Foin, N., Akasaka, T., and di Mario, C. (2012). Optical coherence tomography: from research to practice. *European Heart Journal Cardiovascular Imaging*, 13(5):370–84.

[Haas et al., 2000] Haas, C., Ermert, H., Holt, S., Grewe, P., Machraoui, A., and Barmeyer, J. (2000). Segmentation of 3d intravascular ultrasonic images based on a random field model. *Ultrasound in Medicine Biology*, 26(2):297 – 306.

[Haeker et al., 2006] Haeker, M., Abramoff, M., Kardon, R., and Sonka, M. (2006). Segmentation of the surfaces of the retinal layer from oct images. *Medical Image Computing and Computer Assisted Intervention*, 9:800–807.

[Hajnal et al., 2001] Hajnal, J. V., Hill, D. L., and Hawkes, D. J., editors (2001). *Medical Image Registration*. CRC Press.

[Hamid and Coltart, 2007] Hamid, H. and Coltart, J. (2007). Miracle stents - a future without restenosis. *McGill Journal of Medicine*, 10(2):105–111.

[Han et al., 2008] Han, X., Hoogeman, M., Levendag, P., Hibbard, L., Teguh, D., Voet, P., Cowen, A., and Wolf, T. (2008). Atlas-based auto-segmentation of head and neck ct images. *Medical Image Computing and Computer Assisted Intervention (MICCAI)*, pages 434–441.

[Hartley and Zisserman, 2004] Hartley, R. I. and Zisserman, A. (2004). *Multiple View Geometry in Computer Vision*. Cambridge University Press, ISBN: 0521540518, second edition.

[Heckemann et al., 2006] Heckemann, R. A., Hajnal, J. V., Aljabar, P., Rueckert, D., and Hammers, A. (2006). Automatic anatomical brain mri segmentation combining label propagation and decision fusion. *NeuroImage*, 33(1):115 – 126.

[Hegadi et al., 2010] Hegadi, R., Kop, A., and Hangarge, M. (2010). A survey on deformable model and its applications to medical imaging. *Internal Journal of Computer Applications, Special Issue on RTIPPR*, 2(2):64–75. Published By Foundation of Computer Science.

[Herrington et al., 1992] Herrington, D. M., Johnson, T., Santago, P., and Snyder, W. E. (1992). Semi-automated boundary detection for intravascular ultrasound. *Proceedings of Computers in Cardiology*, pages 103 –106.

[Herzog et al., 2004] Herzog, A., Boyer, K., and Roberts, C. (2004). Robust extraction of the optic nerve head in optical coherence tomography. *Computer Vision and Mathematical Methods in Medical and Biomedical Image Analysis*, 3117:395–407.

[Hoffmann et al., 1999] Hoffmann, K. R., Wahle, A., Pellot-Barakat, C., Sklansky, J., and Sonka, M. (1999). Biplane x-ray angiograms, intravascular ultrasound, and 3d visualization of coronary vessels. *The International Journal of Cardiac Imaging*, 15:495–512.

[Hoglund et al., 2010] Hoglund, V. J., Dong, X. R., and Majesky, M. W. (2010). Neointima formation : A local affair. *American Heart Association*, 30:1877–1879.

[Hong et al., 2004] Hong, M.-K., Mintz, G. S., Lee, C. W., Kim, Y.-H., Lee, S.-W., Song, J.-M., Han, K.-H., Kang, D.-H., Song, J.-K., Kim, J.-J., Park, S.-W., and Park, S.-J. (2004). Comparison of coronary plaque rupture between stable angina and acute myocardial infarction: A three-vessel intravascular ultrasound study in 235 patients. *Circulation*, 110(8):928–933.

[Horiba et al., 2000] Horiba, M., Kadomatsu, K., Nakamura, E., Muramatsu, H., Ikematsu, S., Sakuma, S., Hayashi, K., Yuzawa, Y., Matsuo, S., Kuzuya, M., Kaname, T., Hirai, M., Saito, H., and Muramatsu, T. (2000). Neointima formation in a restenosis model is suppressed in midkine-deficient mice. *The Journal of Clinical Investigation*, 105(4):489–495.

[Huang et al., 1991] Huang, D., Swanson, E. A., Lin, C. P., Schuman, J. S., Stinson, W. G., Chang, W., Hee, M. R., Flotte, T., Gregory, K., and Puliafito, C. A. (1991). Optical coherence tomography. *Science*, 254(5035):1178–1181.

[Ikenaga et al., 2010] Ikenaga, H., Dai, K., and Ishihara, M. (2010). Very late stent thrombosis after sirolimus-eluting stent implantation observed using optical coherence tomography and coronary angioscopy. *the journal of invasive cardiology*, pages 557–558.

[Isgum et al., 2009] Isgum, I., Staring, M., Rutten, A., Prokop, M., Viergever, M. A., and van Ginneken, B. (2009). Multi-atlas-based segmentation with local decision fusion–application

to cardiac and aortic segmentation in ct scans. *IEEE Transactions on Medical Imaging*, 28(7):1000–1010.

[Ishikawa et al., 2005] Ishikawa, H., Stein, D. M., Wollstein, G., Beaton, S., Fujimoto, J. G., and Schuman, J. S. (2005). Macular segmentation with optical coherence tomography. *Investigative Ophthalmology and Visual Science (IOVS)*, 46(6):2012–2017.

[Jang et al., 2002] Jang, I.-K., Bouma, B. E., Kang, D.-H., Park, S.-J., Park, S.-W., Seung, K.-B., Choi, K.-B., Shishkov, M., Schlendorf, K., Pomerantsev, E., Houser, S. L., Aretz, H. T., and Tearney, G. J. (2002). Visualization of coronary atherosclerotic plaques in patients using optical coherence tomography: comparison with intravascular ultrasound. *Journal of the American College of Cardiology*, 39(4):604 – 609.

[Kass et al., 1987] Kass, M., Witkin, A., and Terzopoulos, D. (1987). Snakes: Active contour models. *International Journal of Computer Vision*, 1(4):321–331.

[Kastrati et al., 2001] Kastrati, A., Mehilli, J., Dirschinger, J., Pache, J., Ulm, K., Schuhlen, H., Seyfarth, M., Schmitt, C., Blasini, R., Neumann, F.-J., and Schomig, A. (2001). Restenosis after coronary placement of various stent types. *The American Journal of Cardiology*, 87(1):34 – 39.

[Katouzian, 2011] Katouzian, A. (2011). *Quantifying atherosclerosis: IVUS imaging for lumen border detection and plaque characterization.* PhD thesis, Columbia University, New York.

[Katouzian et al., 2012] Katouzian, A., Angelini, E. D., Carlier, S. G., Suri, J. S., Navab, N., and Laine, A. F. (2012). A state-of-the-art review on segmentation algorithms in intravascular ultrasound (ivus) images. *IEEE Transactions on Information Technology in Biomedicine*, 16(5):823–834.

[Katouzian et al., 2009] Katouzian, A., Angelini, E. D., Lorsakul, A., Sturm, B., and Laine, A. F. (2009). Lumen border detection of intravascular ultrasound via denoising of directional wavelet representations. *Functional imaging and modeling of the heart*, pages 104–113.

[Katouzian et al., 2010] Katouzian, A., Angelini, E. D., Sturm, B., and Laine, A. F. (2010). Automatic detection of luminal borders in ivus images by magnitude-phase histograms of

complex brushlet coefficients. *IEEE Engineering in Medicine and Biology Society (EMBC)*, pages 3073 –3076.

[Katz, 2005] Katz, A. (2005). *Physiology of the Heart.* Lippincott Williams & Wilkins.

[Kauffmann et al., 2010] Kauffmann, C., Motreff, P., and Sarry, L. (2010). In vivo supervised analysis of stent reendothelialization from optical coherence tomography. *IEEE Transactions on Medical Imaging*, 29(3):807–818.

[Kimura et al., 1995] Kimura, B. J., Bhargava, V., and DeMaria, A. N. (1995). Value and limitations of intravascular ultrasound imaging in characterizing coronary atherosclerotic plaque. *American Heart Journal*, 130(2):386 – 396.

[Kittler et al., 1998] Kittler, J., Hatef, M., Duin, R. P. W., and Matas, J. (1998). On combining classifiers. *IEEE Transactions on Pattern Analysis and Machine Intelligence*, 20:226–239.

[Koozekanani et al., 2001] Koozekanani, D., Boyer, K., and Roberts, C. (2001). Retinal thickness measurements from optical coherence tomography using a markov boundary model. *Medical Imaging, IEEE Transactions on*, 20(9):900 –916.

[Kovalski et al., 2000] Kovalski, G., Beyar, R., Shofti, R., and Azhari, H. (2000). Three-dimensional automatic quantitative analysis of intravascular ultrasound images. *Ultrasound in Medicine Biology*, 26(4):527 – 537.

[Kroon, 2010] Kroon, D.-J. (2010). Snake : Active contour. http://www.mathworks.com/matlabcentral/fileexchange/28149.

[Kubo et al., 2011] Kubo, T., Ino, Y., Tanimoto, T., Kitabata, H., Tanaka, A., and Akasaka, T. (2011). Optical coherence tomography imaging in acute coronary syndromes. *Cardiology Research and Practice*, 2011:s:1–5.

[Lang et al., 2011] Lang, P., Rajchl, M., Li, F., and Peters, T. M. (2011). Towards model-enhanced real-time ultrasound guided cardiac interventions. *Intelligent Computation and Bio-Medical Instrumentation (ICBMI)*, pages 89 –92.

[Lee et al., 2010] Lee, K., Abramoff, M. D., Niemeijer, M., Garvin, M. K., and Sonka, M. (2010). 3-d segmentation of retinal blood vessels in spectral-domain oct volumes of the optic nerve head. *Proceedding of SPIE Medical Imaging: Biomedical Applications in Molecular, Structural, and Functional Imaging*, 7626,:76260V.

[Lee et al., 1995] Lee, M. R., Izatt, J. A., Swanson, E. A., Huang, D., Schumun, J. S., Lin, C. P., Puliafito, C. A., and Fujimoto, J. G. (1995). Optical coherence tomography for ophthalmic imaging: new technique delivers micron-scale resolution. *IEEE Engineering in Medicine and Biology Magazine*, 14(1):67 –76.

[Lemos et al., 2011] Lemos, P. A., Takimura, C. K., Laurindo, F. R. M., Gutierrez, P. S., and Aiello, V. D. (2011). A histopathological comparison of different definitions for quantifying instent neointimal tissue: Implications for the validity of intracoronary ultrasound and optical coherence tomography measurements. *Cardiovascular Diagnosis and Therapy*, 1(1).

[Lerme et al., 2010] Lerme, N., Malgouyres, F., and Letocart, L. (2010). Reducing graphs in graph cut segmentation. *IEEE International Conference on Image Processing (ICIP)*, pages 3045 –3048.

[Li et al., 1994] Li, W., Birgelen, C. V., Mario, C. D., Boersma, E., Gussenhoven, E. J., Putten, N. V. D., and Bom, N. (1994). Semi-automatic contour detection for volumetric quantification of intracoronary ultrasound. *in Proceedings Computers in Cardiology*, pages 277 –280.

[Li et al., 2004] Li, Y., Sun, J., Tang, C.-K., and Shum, H.-Y. (2004). Lazy snapping. *Association for Computing Machinery*, pages 303–308.

[Lin et al., 2005] Lin, X., Cowan, B., and Young, A. (2005). Model-based graph cut method for segmentation of the left ventricle. *International Conference of the Engineering in Medicine and Biology Society*, pages 3059 –3062.

[Lobregt and Viergever, 1995] Lobregt, S. and Viergever, M. A. (1995). A discrete dynamic contour model. *IEEE Transactions on Medical Imaging*, 14(1):12 –24.

[Loizou et al., 2004] Loizou, C., Pattichis, C. S., Istepanian, R. S. H., Pantziaris, M., and Nicolaides, A. (2004). Atherosclerotic carotid plaque segmentation. *IEEE Engineering in Medicine and Biology Society*, 1:1403 –1406.

[Lombaert and Cheriet, 2010] Lombaert, H. and Cheriet, F. (2010). Spatio-temporal segmentation of the heart in 4d mri images using graph cuts with motion cues. *IEEE International Symposium on Biomedical Imaging: From Nano to Macro*, pages 492 –495.

[Lombaert et al., 2005] Lombaert, H., Sun, Y., Grady, L., and Xu, C. (2005). A multilevel banded graph cuts method for fast image segmentation. *IEEE International Conference on Computer Vision*, 1:259 – 265.

[Lorenz et al., 1997] Lorenz, C., Carlsen, I., Buzug, T., Fassnacht, C., and Weese, J. (1997). Multi-scale line segmentation with automatic estimation of width, contrast and tangential direction in 2d and 3d medical images. *Proceedings of the First Joint Conference Computer Vision, Virtual Reality and Robotics in Medicine and Medical Robotics and Computer-Assisted Surgery*, 1205:233–242. 10.1007/BFb0029242.

[Lorenzo-Valdes et al., 2004] Lorenzo-Valdes, M., Sanchez-Ortiz, G., Elkington, A., Mohiaddin, R., and Rueckert, D. (2004). Segmentation of 4d cardiac mr images using a probabilistic atlas and the em algorithm. *Medical Image Analysis*, 8(3):255–265.

[Lorenzo-Valdes et al., 2002] Lorenzo-Valdes, M., Sanchez-Ortiz, G., Mohiaddin, R., and Rueckert, D. (2002). Atlas-based segmentation and tracking of 3d cardiac mr images using non-rigid registration. *Medical Image Computing and Computer Assisted Intervention (MICCAI)*, pages 642–650.

[Lorenzo-Valdes et al., 2003] Lorenzo-Valdes, M., Sanchez-Ortiz, G., Mohiaddin, R., and Rueckert, D. (2003). Segmentation of 4d cardiac mr images using a probabilistic atlas and the em algorithm. *Medical Image Computing and Computer Assisted Intervention (MICCAI)*, pages 440–450.

[Lotjonen et al., 2010] Lotjonen, J. M. P., Wolz, R., Koikkalainen, J. R., Thurfjell, L., Waldemar, G., Soininen, H., and Rueckert, D. (2010). Fast and robust multi-atlas segmentation of brain Magnetic Resonance images. *Neuroimage*, 49(3):2352–2365.

[Lu et al., 2012] Lu, H., Gargesha, M., Wang, Z., Chamie, D., Attizzani, G. F., Kanaya, T., Ray, S., Costa, M. A., Rollins, A. M., Bezerra, H. G., and Wilson, D. L. (2012). Automatic stent detection in intravascular oct images using bagged decision trees. *Biomedical Optical Express*, 3(11):2809–2824.

[Majesky, 1994] Majesky, M. W. (1994). Neointima formation after acute vascular injury. role of counteradhesive extracellular matrix proteins. *Texas Heart Institute Journal*, 21(1):78–85.

[Malladi et al., 1995] Malladi, R., Sethian, J. A., and Vemuri, B. C. (1995). Shape modeling with front propagation: a level set approach. *IEEE Transactions on Pattern Analysis and Machine Intelligence*, 17(2):158 –175.

[Marr and Hildreth, 1980] Marr, D. and Hildreth, E. (1980). Theory of edge detection. *Proceedings of the Royal Society of London. Series B. Biological Sciences*, 207(1167):187–217.

[Matsumoto et al., 2007] Matsumoto, D., Shite, J., Shinke, T., Otake, H., Tanino, Y., Ogasawara, D., Sawada, T., Paredes, O. L., Hirata, K., and Yokoyama, M. (2007). Neointima coverage of sirolimus-eluting stents at 6-month follow-up: Evaluated by optical coherence tomography. *European Heart Journal*, 28:961–967.

[McDaniel and Douglas, 2011] McDaniel, M. C. and Douglas, J. S. (2011). Stent area by intravascular ultrasound and outcomes in left main intervention with drug-eluting stents. *Circulation: Cardiovascular Interventions*, 4(6):542–544.

[Meier et al., 1997] Meier, D. S., Cothren, R. M., Vince, D. G., and Cornhill, J. F. (1997). Automated morphometry of coronary arteries with digital image analysis of intravascular ultrasound. *American Heart Journal*, 13(5):267.

[Meijboom et al., 2008] Meijboom, W. B., Mieghem, C. A. G. V., van Pelt, N., Weustink, A., Pugliese, F., Mollet, N. R., Boersma, E., Regar, E., van Geuns, R. J., de Jaegere, P. J.,

Serruys, P. W., Krestin, G. P., and de Feyter, P. J. (2008). Comprehensive assessment of coronary artery stenoses: Computed tomography coronary angiography versus conventional coronary angiography and correlation with fractional flow reserve in patients with stable angina. *Journal of the American College of Cardiology*, 52(8):636 – 643.

[Mendizabal-Ruiz et al., 2008] Mendizabal-Ruiz, G., Rivera, M., and Kakadiaris, I. A. (2008). A probabilistic segmentation method for the identification of luminal borders in intravascular ultrasound images. *IEEE Conference on Computer Vision and Pattern Recognition*, pages 1 –8.

[Mintz, 2007] Mintz, G. S. (2007). Features and parameters of drug-eluting stent deployment discoverable by intravascular ultrasound. *The American Journal of Cardiology*, 100(8):S26 – S35. ¡ce:title¿Integrating Safety into the Practice of Drug-Eluting Stent Deployment¡/ce:title¿.

[Mishra et al., 2009] Mishra, A., Wong, A., Bizheva, K., and Clausi, D. A. (2009). Intra-retinal layer segmentation in optical coherence tomography images. *Optics Express*, 17(26):23719– 23728.

[Molina et al., 1998] Molina, C., Prause, G., Radeva, P., and Sonka, M. (1998). 3-d catheter path reconstruction from biplane angiograms. *Proceeding of SPIE: Medical Imaging*, 3338:504–512.

[Molinari et al., 2007] Molinari, F., Liboni, W., Pavanelli, E., Giustetto, P., Badalamenti, S., and Suri, J. S. (2007). Accurate and automatic carotid plaque characterization in contrast enhanced 2-d ultrasound images. *IEEE Engineering in Medicine and Biology Society*, pages 335 –338.

[Moliterno, 2005] Moliterno, D. J. (2005). Healing achilles sirolimus versus paclitaxel. *New England Journal of Medicine*, 353(7):724–727.

[Moon, 1996] Moon, T. K. (1996). The expectation-maximization algorithm. *IEEE Signal Processing Magazine*, 13(6):47 –60.

[Moraes et al., 2012] Moraes, M. C., Cardenas, D. A. C., and Furuie, S. S. (2012). Automatic ioct lumen segmentation using wavelet and mathematical morphology. *Computing in Cardiology*, 39:545–548.

[Mortier et al., 2010] Mortier, P., Holzapfel, G., Beule, M., Loo, D., Taeymans, Y., Segers, P., Verdonck, P., and Verhegghe, B. (2010). A novel simulation strategy for stent insertion and deployment in curved coronary bifurcations: Comparison of three drug-eluting stents. *Annals of Biomedical Engineering*, 38(1):88–99.

[Mujat et al., 2005] Mujat, M., Chan, R., Cense, B., Park, B., Joo, C., Akkin, T., Chen, T., and de Boer, J. (2005). Retinal nerve fiber layer thickness map determined from optical coherence tomography images. *Optics Express*, 13(23):9480–9491.

[Murata et al., 2002] Murata, T., Hiro, T., Fujii, T., Yasumoto, K., Murashige, A., Kohno, M., Yamada, J., Miura, T., and Matsuzaki, M. (2002). Impact of the cross-sectional geometry of the post-deployment coronary stent on in-stent neointimal hyperplasia. *Circulation*, 66:489–493.

[Nair et al., 2002] Nair, A., Kuban, B. D., Tuzcu, E. M., Schoenhagen, P., Nissen, S. E., and Vince, D. G. (2002). Coronary plaque classification with intravascular ultrasound radiofrequency data analysis. *Circulation.*, 106(17):2200–2206.

[Nakamura et al., 2001] Nakamura, M., Yock, P. G., Bonneau, H. N., Kitamura, K., Aizawa, T., Tamai, H., Fitzgerald, P. J., and Honda, Y. (2001). Impact of peri-stent remodeling on restenosis. *Circulation*, 103(17):2130–2132.

[NHLBI, 2008] NHLBI (2008). Overview of atherosis. http://www.nhlbi.nih.gov/health/health-topics/topics/hbc/.

[NHLBI, 2012a] NHLBI (2012a). coronary heart disease. http://www.nhlbi.nih.gov/health/dci/Diseases/Cad/CADSignsAndSymptoms.html.

[NHLBI, 2012b] NHLBI (2012b). Overview of restenosis. http://www.nhlbi.nih.gov/health//dci/Diseases/Angioplasty/.

[Nishioka et al., 1999] Nishioka, T., Amanullah, A. M., Luo, H., Berglund, H., Kim, C. J., Nagai, T., Hakamata, N., Katsushika, S., Uehata, A., Takase, B., Isojima, K., Berman, D. S., and Siegel, R. J. (1999). Clinical validation of intravascular ultrasound imaging for assessment of coronary stenosis severity: Comparison with stress myocardial perfusion imaging. *Journal of the American College of Cardiology*, 33(7):1870 – 1878.

[OBEL, 2012] OBEL (2012). Comparsion of oct and other image modalities. http://obel.ee.uwa.edu.au/research/oct/intro/.

[Olabarriaga et al., 2003] Olabarriaga, S., Breeuwer, M., and Niessen, W. (2003). Evaluation of hessian-based filters to enhance the axis of coronary arteries in ct images. *Computer Assisted Radiology and Surgery*, 1256(0):1191 – 1196. ¡ce:title¿CARS 2003. Computer Assisted Radiology and Surgery. Proceedings of the 17th International Congress and Exhibition¡/ce:title¿.

[Orderud and Rabben, 2008] Orderud, F. and Rabben, S. I. (2008). Real-time 3d segmentation of the left ventricle using deformable subdivision surfaces. *IEEE Conference on Computer Vision and Pattern Recognition*, pages 1 –8.

[Orlowski and Orkisz, 2009] Orlowski, P. and Orkisz, M. (2009). Efficient computation of hessian-based enhancement filters for tubular structures in 3d images. *IRBM*, 30(3):128 – 132.

[Osher and Sethian, 1988] Osher, S. and Sethian, J. (1988). Fronts propagating with curvature-dependent speed: algorithms based on hamilton-jacobi formulations. *Journal of Computation Physics*, 79:12–49.

[Otsu, 1979] Otsu, N. (1979). A threshold selection method from gray-level histograms. *IEEE Transactions on Systems, Man and Cybernetics*, 9(1):62 –66.

[Paragios and Deriche, 2002] Paragios, N. and Deriche, R. (2002). Geodesic active regions and level set methods for supervised texture segmentation. *International Journal of Computer Vision*, 46:223–247.

[Pearson, 1994] Pearson, J. D. (1994). Vessel wall interactions regulating thrombosis. *British Medical Bulletin*, 50(4):776–788.

[Peng and Veksler, 2008] Peng, B. and Veksler, O. (2008). Parameter selection for graph cut based image segmentation. *British Machine Vision Conference*, pages 1–10.

[Perk et al., 2012] Perk, J., Backer, G. D., Gohlke, H., Graham, I., Reiner, Z., Verschuren, M., Albus, C., Benlian, P., Boysen, G., Cifkova, R., Deaton, C., Ebrahim, S., Fisher, M., Germano, G., Hobbs, R., Hoes, A., Karadeniz, S., Mezzani, A., Prescott, E., Ryden, L., Scherer, M., Syvanne, M., Reimer, W. J. M. S. O., Vrints, C., Wood, D., Zamorano, J., and Zannad, F. (2012). European guidelines on cardiovascular disease prevention in clinical practice (version 2012). *European Heart Journal*, 33:1635–1701.

[Perrenot et al., 2006] Perrenot, B., Vaillant, R., Prost, R., Finet, G., Douek, P., and Peyrin, F. (2006). Motion compensation for 3d tomographic reconstruction of stent in x-ray cardiac rotational angiography. *IEEE International Symposium on Biomedical Imaging: Nano to Macro*, pages 1224 –1227.

[Pfisterer et al., 2006] Pfisterer, M., Rocca, H. P. B.-L., Buser, P. T., Rickenbacher, P., Hunziker, P., Mueller, C., Jeger, R., Bader, F., Osswald, S., and Kaiser, C. (2006). Late clinical events after clopidogrel discontinuation may limit the benefit of drug-eluting stents: An observational study of drug-eluting versus bare-metal stents. *Journal of the American College of Cardiology*, 48(12):2584 – 2591.

[Pitt et al., 2000] Pitt, B., Byington, R. P., Furberg, C. D., Hunninghake, D. B., Mancini, G. B. J., Miller, M. E., and Riley, W. (2000). Effect of amlodipine on the progression of atherosclerosis and the occurrence of clinical events. *Circulation*, 102(13):1503–1510.

[Pluim et al., 2003] Pluim, J. P. W., Maintz, J. B. A., and Viergever, M. A. (2003). Mutual-information-based registration of medical images: a survey. *IEEE Transactions on Medical Imaging*, 22(8):986 –1004.

[Pujol and Radeva, 2002] Pujol, O. and Radeva, P. (2002). Lumen detection in ivus image using snakes in a statistical framework. *XX Congreso Annual de la Sociedad Espanola de Ingeneria Biomedica*, pages 27–29.

[Pujol et al., 2003] Pujol, O., Rotger, D., Radeva, P., Rodriguez, O., and Mauri, J. (2003). Near real-time plaque segmentation of ivus. *Computers in Cardiology*, pages 69 – 72.

[Roger et al., 2012] Roger, V. L., Go, A. S., Lloyd-Jones, D. M., Benjamin, E. J., Berry, J. D., Borden, W. B., Bravata, D. M., Dai, S., Ford, E. S., Fox, C. S., Fullerton, H. J., Gillespie, C., Hailpern, S. M., Heit, J. A., Howard, V. J., Kissela, B. M., Kittner, S. J., Lackland, D. T., Lichtman, J. H., Lisabeth, L. D., Makuc, D. M., Marcus, G. M., Marelli, A., Matchar, D. B., Moy, C. S., Mozaffarian, D., Mussolino, M. E., Nichol, G., Paynter, N. P., Soliman, E. Z., Sorlie, P. D., Sotoodehnia, N., Turan, T. N., Virani, S. S., Wong, N. D., Woo, D., and Turner, M. B. (2012). Heart disease and stroke statistics-2012 update. *Circulation*, 125(1):e2–e220.

[Rohlfing et al., 2004] Rohlfing, T., Brandt, R., Menzel, R., and Jr., C. R. M. (2004). Evaluation of atlas selection strategies for atlas-based image segmentation with application to confocal microscopy images of bee brains. *NeuroImage*, 21(4):1428 – 1442.

[Rohlfing et al., 2005] Rohlfing, T., Brandt, R., Menzel, R., Russakoff, D. B., and Maurer, C. R. (2005). Quo vadis, atlas-based segmentation? *Handbook of Biomedical Image Analysis*, pages 435–486.

[Ross, 1993] Ross, R. (1993). The pathogenesis of atherosclerosis: a perspective for the 1990s. *Nature*, 362(6423):801–809.

[Rotger et al., 2001] Rotger, D., Radeva, P., Canero, C., Villanueva, J., Mauri, J., Fernandez, E., Tovar, A., and Valle, V. (2001). Corresponding ivus and angiogram image data. *Computers in Cardiology*, pages 273 –276.

[Rueckert et al., 2007] Rueckert, D., Schnabel, J., and Group, B. I. A. (2007). Irtk. http://biomedic.doc.ic.ac.uk/uploads/Internal/rviewManual.pdf.

[Rueckert et al., 1999] Rueckert, D., Sonoda, L. I., Hayes, C., Hill, D. L. G., Leach, M. O., and Hawkes, D. J. (1999). Nonrigid registration using free-form deformations: application to breast mr images. *IEEE Transactions on Medical Imaging*, 18(8):712 –721.

[Sabuncu et al., 2010] Sabuncu, M. R., Yeo, B. T. T., Leemput, K. V., Fischl, B., and Golland, P. (2010). A generative model for image segmentation based on label fusion. *Medical Imaging, IEEE Transactions on*, 29(10):1714 –1729.

[Saeed et al., 1998] Saeed, M., Karl, W. C., Nguyen, T. Q., and Rabiee, H. R. (1998). A new multiresolution algorithm for image segmentation. *IEEE International Conference on Acoustics, Speech and Signal Processing*, 5:2753–2756 vol.5.

[Sampson and Hillman, 2004] Sampson, D. D. and Hillman, T. R. (2004). *Lasers and Current Optical Techniques in Biology*. Royal Society of Chemistry.

[Sato et al., 1998] Sato, Y., Nakajima, S., Shiraga, N., Atsumi, H., Yoshida, S., Koller, T., Gerig, G., and Kikinis, R. (1998). Three-dimensional multi-scale line filter for segmentation and visualization of curvilinear structures in medical images. *Medical Image Analysis*, 2(2):143 – 168.

[Schoonenberg et al., 2008] Schoonenberg, G., Lelong, P., Florent, R., Wink, O., and Romeny, B. H. (2008). The effect of automated marker detection on in vivo volumetric stent reconstruction. *Medical Image Computing and Computer-Assisted Intervention MICCAI*, 5242:87–94.

[Schoonenberg, 2010] Schoonenberg, G. A. F. (2010). *3D reconstruction for percutaneous interventions*. PhD thesis, Eindhoven: Technische Universiteit Eindhoven.

[Schuijf et al., 2006] Schuijf, J. D., Bax, J. J., Shaw, L. J., de Roos, A., Lamb, H. J., van der Wall, E. E., and Wijns, W. (2006). Meta-analysis of comparative diagnostic performance of magnetic resonance imaging and multislice computed tomography for noninvasive coronary angiography. *American Heart Journal*, 151(2):404 – 411.

[Schuurbiers et al., 2009] Schuurbiers, J. C. H., Lopez, N. G., Ligthart, J., Gijsen, F. J. H., Dijkstra, J., Serruys, P. W., der Steen, A. F. V., and Wentzel, J. J. (2009). In vivo validation of caas qca-3d coronary reconstruction using fusion of angiography and intravascular ultrasound (angus). *Catheterization and Cardiovascular Interventions*, 73(5):620–626.

[Schwartz et al., 1992] Schwartz, R. S., Huber, K. C., Murphy, J. G., Edwards, W. D., Camrud, A. R., Vlietstra, R. E., and Holmes, D. R. (1992). Restenosis and the proportional neointimal

response to coronary artery injury: Results in a porcine model. *Journal of the American College of Cardiology*, 19(2):267 – 274.

[Serruys et al., 2006] Serruys, P. W., Kutryk, M. J. B., and Ong, A. T. L. (2006). Coronary-artery stents. *New England Journal of Medicine*, 354(5):483–495.

[Shah et al., 2002] Shah, V. M., Mintz, G. S., Apple, S., and Weissman, N. J. (2002). Background incidence of late malapposition after bare-metal stent implantation. *Circulation*, 106(14):1753–1755.

[Shahidi et al., 2005] Shahidi, M., Wang, Z., and Zelkha, R. (2005). Quantitative thickness measurement of retinal layers imaged by optical coherence tomography. *American Journal of Ophthalmology*, 139(6):1056 – 1061.

[Shekhar et al., 1999] Shekhar, R., Cothren, R., Vince, D., Chandra, S., Thomas, J., and Cornhill, J. (1999). Three-dimensional segmentation of luminal and adventitial borders in serial intravascular ultrasound images. *Computerized Medical Imaging and Graphics*, 23(6):299 – 309.

[Shi, 2012] Shi, W. Z. (2012). *An image segmentation and registration approach to cardiac function analysis using MRI*. PhD thesis, Imperial College London.

[Sifakis et al., 2002] Sifakis, E., Garcia, C., and Tziritas, G. (2002). Bayesian level sets for image segmentation. *Journal of Visual Communication and Image Representation*, 13:44–64.

[Sinop and Grady, 2006] Sinop, A. K. and Grady, L. (2006). Accurate banded graph cut segmentation of thin structures using laplacian pyramids. *Medical Image Computing and Computer-Assisted Intervention*, pages 896–903.

[Sonka et al., 2007] Sonka, M., Hlavac, V., and Boyle, R. (2007). *Image Processing, Analysis and Machine Vision*. CL Engineering.

[Sonka et al., 1995] Sonka, M., Xiangmin, Z., Siebes, M., Bissing, M. S., Dejong, S. C., Collins, S. M., and McKay, C. R. (1995). Segmentation of intravascular ultrasound images a knowledge-based approach. *IEEE Transactions on Medical Imaging*, 14(4):719 –732.

[Stenhning et al., 2007] Stenhning, C., Boernert, P., and Nehrke, K. (2007). Advances in coronary mra from vessel wall to whole heart imaging. *Magnetic Resonance in Medical Sciences*, 6(3):157–170.

[Studholme et al., 1999] Studholme, C., Hill, D., and Hawkes, D. (1999). An overlap invariant entropy measure of 3d medical image alignment. *Pattern Recognition*, 32(1):71 – 86.

[Takano et al., 2007] Takano, M., Inami, S., Jang, I., Yamamoto, M., Murakami, D., Seimiya, K., Ohba, T., and Mizuno, K. (2007). Evaluation by optical coherence tomography of neointimal coverage of sirolimus-eluting stent three months after implantation. *The American Journal of Cardiology*, 99(8):1033 – 1038.

[Taki et al., 2008] Taki, A., Najafi, Z., Roodaki, A., Setarehdan, S. K., Zoroofi, R. A., Konig, A., and Navab, N. (2008). Automatic segmentation of calcified plaques and vessel borders in ivus images. *International Journal of Computer Assisted Radiology and Surgery*, 3:347–354.

[Tan et al., 2008] Tan, O., Li, G., Lu, A. T., Varma, R., and Huang, D. (2008). Mapping of macular substructures with optical coherence tomography for glaucoma diagnosis. *Ophthalmology*, 115(6):949 – 956.

[Terashima et al., 2012] Terashima, M., Kaneda, H., and Suzuki, T. (2012). The role of optical coherence tomography in coronary intervention. *The Korean Journal of Internal Medicine*, 27(1):1–12.

[Toennies, 2012] Toennies, K. D. (2012). *Guide to Medical Image Analysis: Methods and Algorithms*. Springer-Verlag London Limited.

[Tokunaga et al., 2012] Tokunaga, K., Uchino, E., Tanaka, H., and Suetake, N. (2012). Tissue classification of coronary plaque using intravascular ultrasound method by extended multiple k-nearest neighbor. *International MultiConference of Engineers and Computer Scientists*, 1:1–4.

[Tsantis et al., 2012] Tsantis, S., Kagadis, G. C., Katsanos, K., Karnabatidis, D., Bourantas, G., and Nikiforidis, G. C. (2012). Automatic vessel lumen segmentation and stent strut detection in intravascular optical coherence tomography. *Medical Physics*, 39(1):503–513.

[Tsimikas, 2006] Tsimikas, S. (2006). Drug-eluting stents and late adverse clinical outcomes-lessons learned, lessons awaited. *Journal of the American College of Cardiology*, 47(10):2112–2115.

[Tu et al., 2011] Tu, S., Holm, N. R., Koning, G., Huang, Z., and Reiber, J. H. C. (2011). Fusion of 3d qca and ivus/oct. *The International Journal of Cardiovascular Imaging*, 27:197–207.

[Tu et al., 2012] Tu, S., Xu, L., Ligthart, J., Xu, B., Witberg, K., Sun, Z., Koning, G., Reiber, J., and Regar, E. (2012). In vivo comparison of arterial lumen dimensions assessed by co-registered three-dimensional (3d) quantitative coronary angiography, intravascular ultrasound and optical coherence tomography. *The International Journal of Cardiovascular Imaging*, 28:1315–1327.

[Tvanbr, 2010] Tvanbr   (2010).   Anatomy   of   the   human   heart. http://www.tiesworks.nl/mywork.php?view=preview&category=5&image=12.

[Tyczynski et al., 2010] Tyczynski, P., Ferrante, G., Moreno-Ambroj, C., Kukreja, N., Barlis, P., Pieri, E., Silva, R. D., Beatt, K., and Mario, C. D. (2010). Simple versus complex approaches to treating coronary bifurcation lesions: direct assessment of stent strut apposition by optical coherence tomography. *Revista Espanola de Cardiologia*, 63(8):904–914.

[Ughi et al., 2011] Ughi, G. J., Adriaenssens, T., Onsea, K., Kayaert, P., Dubois, C., Sinnaeve, P., Coosemans, M., Desmet, W., and D'hooge, J. (2011). Automatic segmentation of in-vivo intra-coronary optical coherence tomography images to assess stent strut apposition and coverage. *International Journal Cardiovasc Imaging.*, 28(2):229–241.

[Unal et al., 2008] Unal, G., Bucher, S., Carlier, S., Slabaugh, G., Fang, T., and Tanaka, K. (2008). Shape-driven segmentation of the arterial wall in intravascular ultrasound images. *IEEE Transactions on Information Technology in Biomedicine*, 12(3):335 –347.

[Unal et al., 2010] Unal, G., Gurmeric, S., and Carlier, S. (2010). Stent implant follow-up in intravascular optical coherence tomography images. *The International Journal of Cardiovascular Imaging*, 26:809–816.

[USFDA, 2012] USFDA (2012). Taxus express2 drug-eluting stent. http://www.medicalsunited.com/lightbox/photos/Drug

[Viola and Wells, 1995] Viola, P. and Wells, W. M. (1995). Alignment by maximization of mutual information. *In Proceeding of the 5th International Conference on Computer Vision*, pages 16 –23.

[Virmani et al., 2004] Virmani, R., Guagliumi, G., Farb, A., Musumeci, G., Grieco, N., Motta, T., Mihalcsik, L., Tespili, M., Valsecchi, O., and Kolodgie, F. D. (2004). Localized hypersensitivity and late coronary thrombosis secondary to a sirolimus-eluting stent. *Circulation*, 109(6):701–705.

[von Birgelen et al., 1996] von Birgelen, C., Mario, C. D., Li, W., Schuurbiers, J. C. H., Slager, C. J., de Feyter, P. J., Roelandt, J. R. T. C., and Serruys, P. W. (1996). Morphometric analysis in three-dimensional intracoronary ultrasound: an in vitro and in vivo study performed with a novel system for the contour detection of lumen and plaque. *American Heart Journal*, 132(3):516–527.

[Vos et al., 1997] Vos, J., de Feyter, P. J., Kingma, J. H., Emanuelsson, H., Legrand, V., Winkelmann, B., Dumont, J. M., and Simoons, L. M. (1997). Evolution of coronary atherosclerosis in patients with mild coronary artery disease studied by serial quantitative coronary angiography at 2 and 4 years follow-up. *European Heart Journal*, 18(7):1081–1089.

[Wagner et al., 1983] Wagner, R. F., Smith, S. W., Sandrik, J. M., and Lopez, H. (1983). Statistics of speckle in ultrasound b-scans. *IEEE Transactions on Sonics and Ultrasonics*, 30(3):156 –163.

[Wahle et al., 2006] Wahle, A., Lopez, J. J., Olszewski, M. E., Vigmostad, S. C., Chandran, K. B., Rossen, J. D., and Sonka, M. (2006). Plaque development, vessel curvature, and wall shear stress in coronary arteries assessed by x-ray angiography and intravascular ultrasound.

Medical Image Analysis, 10(4):615 – 631. ¡ce:title¿Special Issue on Functional Imaging and Modelling of the Heart (FIMH 2005)¡/ce:title¿.

[Wahle et al., 1995] Wahle, A., Wellnhofer, E., Mugaragu, I., Saner, H. U., Oswald, H., and Fleck, E. (1995). Assessment of diffuse coronary artery disease by quantitative analysis of coronary morphology based upon 3-d reconstruction from biplane angiograms. *IEEE Transactions on Medical Imaging*, 14(2):230 –241.

[Wang et al., 2012] Wang, A., Eggermont, J., Dekker, N., Garcia-Garcia, H. M., Pawar, R., Reiber, J. H. C., and Dijkstra, J. (2012). A robust automated method to detect stent struts in 3d intravascular optical coherence tomographic image sequences. *SPIE Medical Imaging 2012: Computer-Aided Diagnosis*, 8315:83150L–83150L–9.

[Williams and Shah, 1997] Williams, D. and Shah, M. (1997). A fast algorithm for active contours. *Third International Conference on Computer Vision*, pages 592 –595.

[Wink et al., 2002] Wink, O., Frangi, R., Verdonck, B., Viergever, M., and Niessen, W. (2002). 3d mra coronary axis determination using a minimum cost approach. *Magnetic Resonance in Medicine*, pages 1169–1175.

[Wolz et al., 2010] Wolz, R., Heckemann, R. A., Aljabar, P., Hajnal, J. V., Hammers, A., Lotjonen, J., and Rueckert, D. (2010). Measurement of hippocampal atrophy using 4d graph-cut segmentation: Application to adni. *NeuroImage*, 52(1):109–118.

[Xu and Prince, 1998] Xu, C. and Prince, J. (1998). Snakes, shapes and gradient vector flow. *IEEE Transactions on Image Processing*, 7:359–369.

[Xu et al., 2011] Xu, C., Schmitt, J. M., Akasaka, T., Kubo, T., and Huang, K. (2011). Automatic detection of stent struts with thick neointimal growth in intravascular optical coherence tomography image sequences. *Physics in Medicine and Biology*, 56(20):6655.

[Yabushita et al., 2002] Yabushita, H., Bouma, B. E., Houser, S. L., Aretz, H. T., Jang, I.-K., Schlendorf, K. H., Kauffman, C. R., Shishkov, M., Kang, D.-H., Halpern, E. F., and Tearney, G. J. (2002). Characterization of human atherosclerosis by optical coherence tomography. *Circulation*, 106(13):1640–1645.

[Yang et al., 2009] Yang, J., Wang, Y., Liu, Y., Tang, S., and Chen, W. (2009). Novel approach for 3-d reconstruction of coronary arteries from two uncalibrated angiographic images. *IEEE Transactions on Image Processing*, 18(7):1563 –1572.

[Zargham, 2008] Zargham, R. (2008). Preventing restenosis after angioplasty: a multistage approach. *Clinical Science*, 114(4):257–264.

[Zhang, 2010] Zhang, D. P. (2010). *Coronary Artery Segmentation and Motion Modelling*. PhD thesis, Imperial College London.

[Zhang et al., 2001] Zhang, Y., Brady, M., and Smith, S. (2001). Segmentation of brain mr images through a hidden markov random field model and the expectation-maximization algorithm. *IEEE Transactions on Medical Imaging*, 20(1):45 –57.

[Zhu et al., 2002] Zhu, H., Liang, Y., and Friedman, M. H. (2002). Ivus image segmentation based on contrast. *in Proceedings SPIE*, pages 1727–1733.

[Zhuang et al., 2010] Zhuang, X., Rhode, K. S., Razavi, R. S., Hawkes, D. J., and Ourselin, S. (2010). A registration-based propagation framework for automatic whole heart segmentation of cardiac mri. *IEEE Transactions on Medical Imaging,*, 29(9):1612 –1625.

Appendix A

Implementation Tools and Overview of Image Sequences

A.1 Implementation Tools

The algorithms developed in the thesis are implemented by C++, MATLAB and IRTK. MATLAB is a numerical computing environment developed by MathWorks Inc. It allows matrix calculations, functions and data plotting, user interfaces design and program binding with other languages (C, C++, Java and so on).

IRTK is a cross-platform software tool for image analysis developed by Professor Daniel Rueckert and the Biomedical Image Analysis (BioMedIA) group at Imperial College London. It provides an extensive suite for image analysis (e.g. image registration and image segmentation). Developers are free to add functions to achieve the tasks of segmentation or registration. The resulting images can be viewed in RView which is a viewer for medical images (NIfTI image format) (Figure A.1). The manual and binaries of the IRTK are available online [Rueckert et al., 2007].
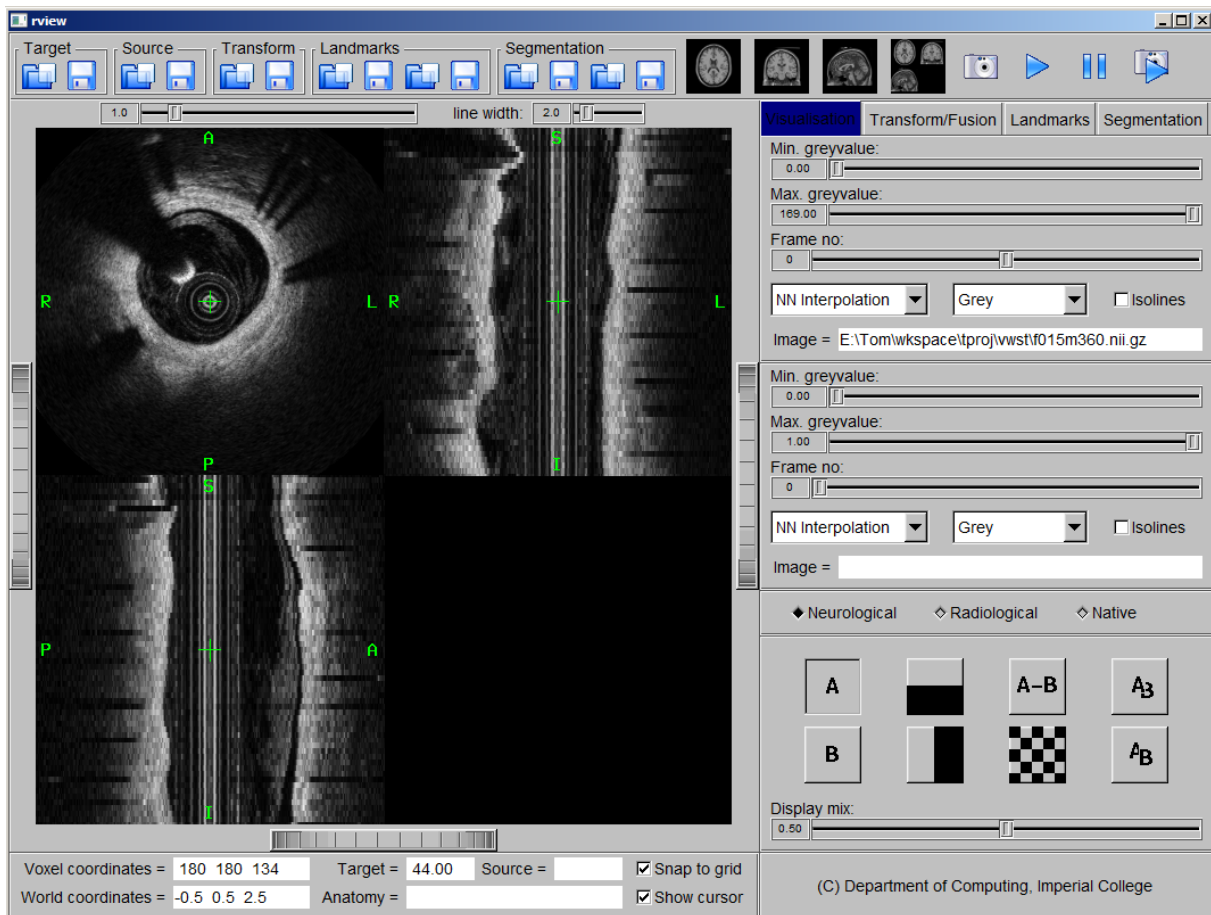
Figure A.1: This figure shows the interface of RView and some functions of image registration and segmentation. An image can be viewed in axial view (top-left image), coronal view (top-right image), sagital view (bottom-left image) and both directions image in one slice of a sequence. Here, the ID of the image sequence is the sequence 15 (P15).

A.2 Overview of Image Sequences

The image sequences used in the thesis and the acquisition time of the sequences are shown below. Every sequence is considered as an independent patient sequence and the longitudinal-view of every sequence is shown. In addition, the image sequence have been acquired between 2009 and 2011.
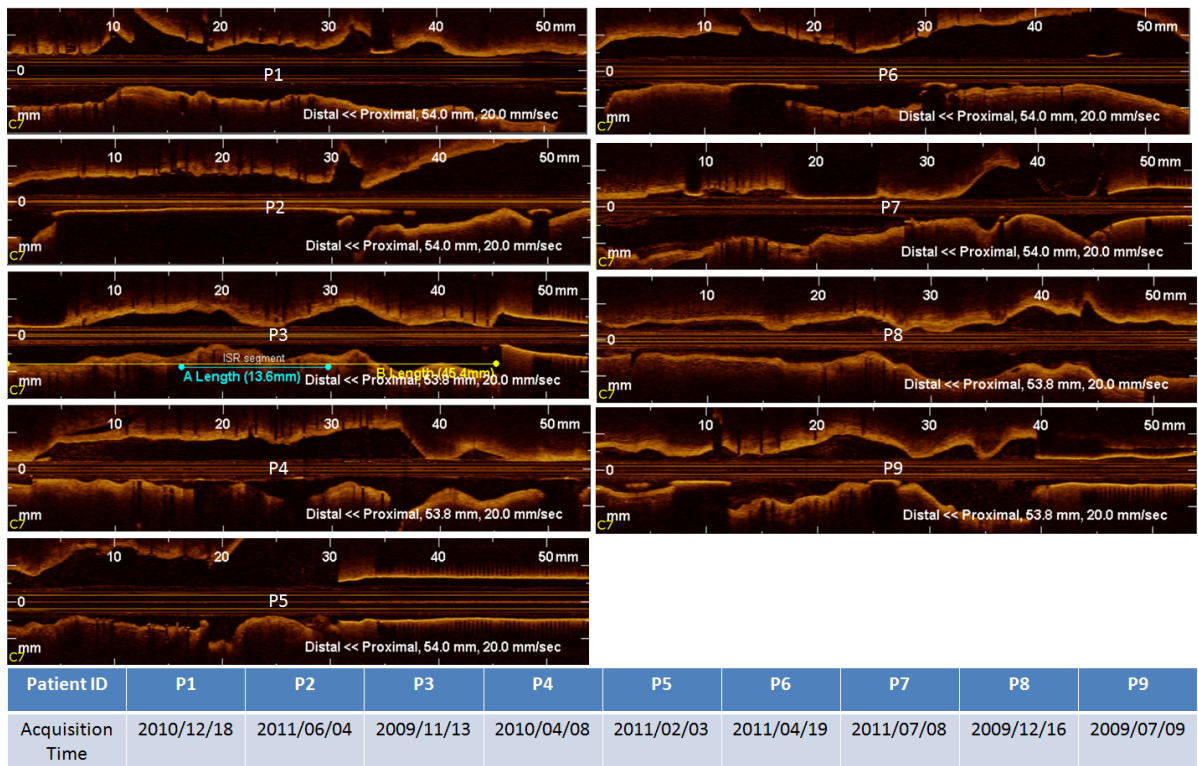
Patient ID	P1	P2	P3	P4	P5	P6	P7	P8	P9
Acquisition Time	2010/12/18	2011/06/04	2009/11/13	2010/04/08	2011/02/03	2011/04/19	2011/07/08	2009/12/16	2009/07/09

Figure A.2: A longitudinal-view of patient sequences (P1-P9). The table shows the acquisition time of image sequences.

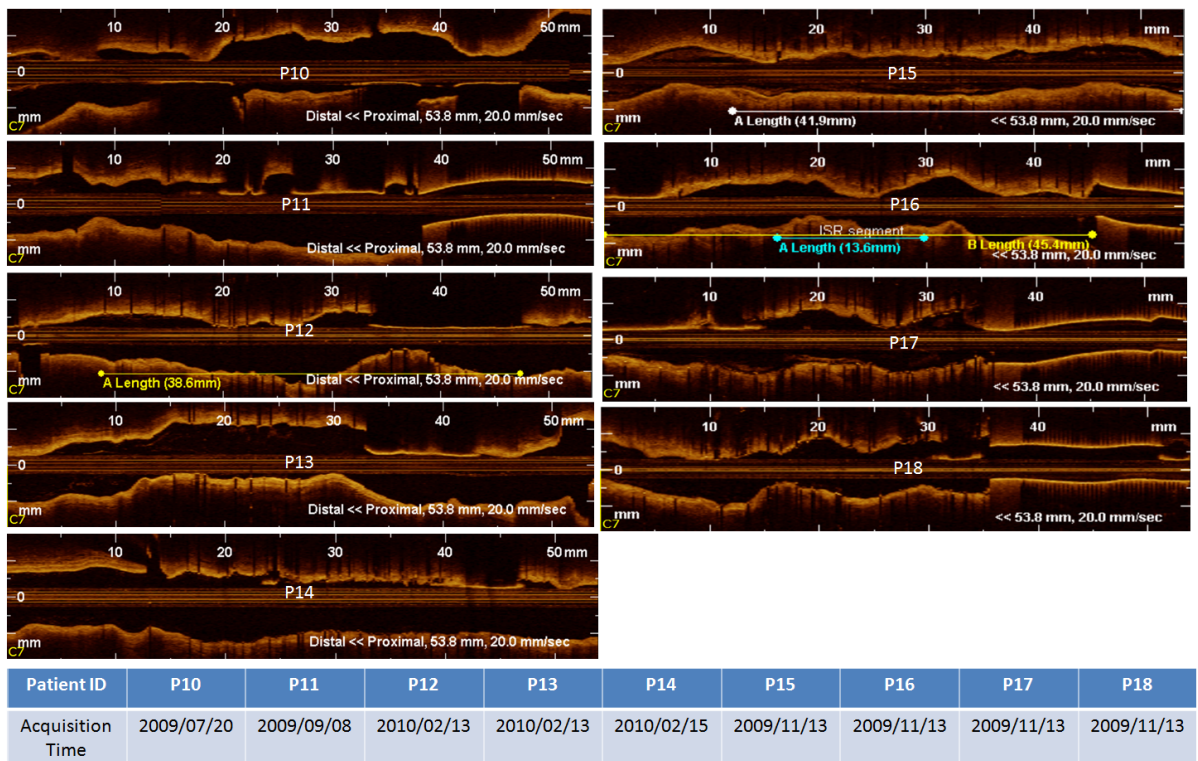| Patient ID	P10	P11	P12	P13	P14	P15	P16	P17	P18
Acquisition Time	2009/07/20	2009/09/08	2010/02/13	2010/02/13	2010/02/15	2009/11/13	2009/11/13	2009/11/13	2009/11/13

Figure A.3: A longitudinal-view of patient sequences (P10-P18). The table shows the acquisition time of image sequences.

Appendix B

Publications

- Kai-Pin Tung, Wenjia Bai, WenZhe Shi, HaiYan Wang, Tong Tong, Ranil de Silva, Eddie Edwards, Daniel Rueckert. (2013). Multi-Atlas Based Neointima Segmentation in Intravascular Coronary OCT. IEEE International Symposium on Biomedical Imaging: From Nano to Macro (ISBI), pages 1268-1271.

- Kai-Pin Tung, WenZhe Shi, Luis Pizarro Quiroz, HaiYan Wang, Ricardo Guerrero Moreno, Ranil De Silva, Philip Edwards, Daniel Rueckert. (2012). Automatic Detection of Coronary Stent Struts in Intravascular OCT imaging. Proceedings of SPIE Medical Imaging: Computer-Aided Diagnosis, Vol. 8315, pages 83150K-83150K-8.

- Kai-Pin Tung, WenZhe Shi, Ranil de Silva, Eddie Edwards, Daniel Rueckert. (2011). Automated Segmentation of Coronary Vessel Wall in OCT Imaging. Medical Image Analysis and Understanding (MIUA), pages 299-303.

- Kai-Pin Tung, WenZhe Shi, Ranil de Silva, Eddie Edwards, Daniel Rueckert. (2011). Automatical Vessel Wall Detection in Intravascular Coronary OCT. IEEE International Symposium on Biomedical Imaging: From Nano to Macro (ISBI), pages 610-613.

- Wenzhe Shi, Xiahai Zhuang, Luis Pizarro, Wenjia Bai, Haiyan Wang, Kai-Pin Tung, Philip Edwards, Daniel Rueckert. (2012). Registration using sparse free-form deformations. Medical Image Computing and Computer Assisted Intervention (MICCAI), pages

173

695-666.

- Wenzhe Shi, Xiahai Zhuang, Haiyan Wang, Simon Duckett, Duy V.N. Luong, Catalina Tobon-Gomez, KaiPin Tung, Philip Edwards, Kawal Rhode, Reza Razavi, Sebastien Ourselin, Daniel Rueckert. (2012). A comprehensive cardiac motion estimation framework using both untagged and 3D tagged MR images based on non-rigid registration. IEEE Transactions on Medical Imaging, 31(6), pages 1263-1275.

- Wenzhe Shi, Xiahai Zhuang, Robin Wolz, Duckett Simon, KaiPin Tung, Haiyan Wang, Sebastien Ourselin, Philip Edwards, Reza Razavi, and Daniel Rueckert. (2011). A multi-image graph cut approach for cardiac image segmentation and uncertainty estimation. Statistical Atlases and Computational Models of the Heart: Imaging and Modelling Challenges (STACOM), pages 178-187.

- Haiyan Wang, Wenzhe Shi, Xiahai Zhuang, Xiangliang Wu, Kai-Pin Tung, Sebastien Ourselin, Philip Edwards, Daniel Rueckert. (2013). Landmark Detection and Coupled Patch Registration for Cardiac Motion Tracking. Proceedings of SPIE Medical Imaging: Image Processing, Vol. 8669, pages 86690J-1-J-6.

- Haiyan Wang, Wenzhe Shi, Xiahai Zhuang, Simon Duckett, Kai Pin Tung, Philip Edwards, Reza Razavi, Sebastien Ourselin, and Daniel Rueckert. (2011). Automatic cardiac motion tracking using both untagged and 3D tagged MR images. Statistical Atlases and Computational Models of the Heart: Imaging and Modelling Challenges (STACOM), pages 45-56.